Nonequilibrium aspects in strongly correlated one-dimensional quatum systems

Mario Collura

To cite this version:

Mario Collura. Nonequilibrium aspects in strongly correlated one-dimensional quatum systems. Other [cond-mat.other]. Université de Lorraine, 2012. English. NNT : 2012LORR0009 . tel-01749155

HAL Id: tel-01749155
https://hal.univ-lorraine.fr/tel-01749155

Submitted on 29 Mar 2018

U.F.R. Sciences & Technologies
Ecole Doctorale Energie Mécanique et Matériaux
Formation Doctorale Physique et Chimique de la Matière et des Matériaux

THÈSE

présentée pour l'obtention du titre de

Docteur de l'Université de Lorraine, Nancy

Discipline: Sciences Physiques
Spécialité: Physique Statistique

par **Mario Collura**

Aspects hors de l'équilibre de systèmes quantiques unidimensionnels fortement corrélés

Nonequilibrium aspects in strongly correlated one-dimensional quantum systems

Soutenance publique prévue le 23 Février 2012

Membres du Jury:

Président:	Christophe Salomon	Directeur de Recherches CNRS, Laboratoire Kastler Brossel, Paris
Rapporteurs:	Anna Minguzzi	Chargé de Recherche CNRS, LPMMC, Grenoble
	Giovanna Morigi	Professor, Universität des Saarlandes, Saarbrücken, Germany
Examinateurs:	Bertrand Berche	Professeur, Université de Lorraine, Nancy
	Rosemary J. Harris	Lecturer, Queen Mary, University of London, England
	Dragi Karevski	Professeur, Université de Lorraine, Nancy (Directeur de Thèse)

Institut Jean Lamour
Faculté des Sciences et Techniques - 54500 Vandœuvre-lès-Nancy

U.F.R. Sciences & Technologies
Ecole Doctorale Energie Mécanique et Matériaux
Formation Doctorale Physique et Chimique de la Matière et des Matériaux

THÈSE

présentée pour l'obtention du titre de

Docteur de l'Université de Lorraine, Nancy

DISCIPLINE: SCIENCES PHYSIQUES
SPÉCIALITÉ: PHYSIQUE STATISTIQUE

par **Mario COLLURA**

Aspects hors de l'équilibre de systèmes quantiques unidimensionnels fortement corrélés

Nonequilibrium aspects in strongly correlated one-dimensional quantum systems

Soutenance publique prévue le 23 Février 2012

Membres du Jury:

Président:	Christophe SALOMON	Directeur de Recherches CNRS, Laboratoire Kastler Brossel, Paris
Rapporteurs:	Anna MINGUZZI	Chargé de Recherche CNRS, LPMMC, Grenoble
	Giovanna MORIGI	Professor, Universität des Saarlandes, Saarbrücken, Germany
Examinateurs:	Bertrand BERCHE	Professeur, Université de Lorraine, Nancy
	Rosemary J. HARRIS	Lecturer, Queen Mary, University of London, England
	Dragi KAREVSKI	Professeur, Université de Lorraine, Nancy (Directeur de Thèse)

Institut Jean Lamour
Faculté des Sciences et Techniques - 54500 Vandœuvre-lès-Nancy

Ἀστέρας εἰσαθρεῖς, Ἀστὴρ ἐμός· εἴθε γενοίμην
οὐρανός, ὡς πολλοῖς ὄμμασιν εἰς σὲ βλέπω.

Plato

Contents

Ringraziamenti / Remerciements

Concepire queste righe di ringraziamenti come apertura a questo lavoro di tesi è stata cosa affatto semplice. Non tanto perché coloro i quali tenevo a ringraziare sarebbero stati in troppi, ché una selezione bisogna pur farla, quanto piuttosto, poiché non è mai semplice esprimere gratitudine con parole appropriate e senza scivolare nelle ovvietà.

Voglio ringraziare i miei genitori, mio fratello, i miei famigliari tutti, per essermi sempre stati vicino, se non fisicamente, quantomeno col cuore. Per avermi incondizionatamente sostenuto nel mio percorso, anche quando questo mi ha visto allontanarmi da loro.

Ringrazio Valeria, per essermi stata accanto in ogni momento, brutto o bello che fosse; per avermi sopportato e per aver coraggiosamente sopportato più d'ogni altra persona la mia assenza. Non c'è giorno che non passi pensando al momento in cui tale distanza verrà colmata.

Esprimo tutta la mia più profonda gratitudine a Dragi, il mio direttore di tesi, per avermi accolto e per la fiducia che mi ha costantemente testimoniato. La sua esperienza nella ricerca, unita ai suoi consigli e incoraggiamenti, ma sopratutto la sua amicizia, mi è stata estremamente preziosa e mi ha permesso di gestire al meglio il mio lavoro. Infine, un caloroso grazie va anche a Caroline.

Ancora, quando penso agli anni trascorsi qui in Francia, penso inevitabilmente ai miei soggiorni parigini. Penso a Pony, il mio amico da sempre. Penso a Riccardo e ai suoi preziosi suggerimenti. E ancora, un anno a Lipsia, i miei coinquilini, ma sopratutto, la venuta di Michele... grazie. E poi, il resto dei miei amici. Non mi è possibile elencarvi tutti, così, non me ne abbiate a male.

Un sentito grazie va a tutto il gruppo di fisica statistica. Ognuno di loro mi ha dato qualcosa. E poi, Jean-Charles, Sophie, Nelson, Xavier, Pierre... grazie a tutti voi per le giornate passate piacevolmente assieme.

Ringrazio Guillaume per le piacevoli e utili discussioni e per il suo continuo supporto per tutto il periodo in cui abbiamo collaborato.

Infine, ringrazio calorosamente i membri della commissione, per aver accettato di presenziare alla discussione.

Concevoir ces lignes de remerciements comme ouverture de ce travail de thèse n'a pas du tout été facile. Pas tellement parce que ceux que je tenais à remercier auraient été trop nombreux, car il faut quand même faire un choix, mais plutôt parce qu'il n'est jamais facile d'exprimer sa gratitude avec les mots appropriès et sans tomber dans la banalité.

Je tiens à remercier mes parents, mon frère, toute ma famille, pour avoir toujours été proches, sinon physiquement, du moins avec le cœur. Pour m'avoir soutenu inconditionnellement sur mon chemin, même quand il m'a vu m'éloigner d'eux.

Je remercie Valeria, pour avoir été de mon coté dans tous les moments, laids ou beaux; pour m'avoir supporté et pour avoir courageusement enduré, plus que toutes les autres personnes, mon absence. Pas un jour passe sans penser à quand cette distance sera comblée.

Je tiens à exprimer ma profonde gratitude et mes remerciements les plus sincères à Dragi, mon directeur de thèse, pour son accueil et pour la confiance qu'il m'a toujours témoigée. Son expérience dans la recherche, ses conseils, ses encouragements et surtout son amitié ont été pour moi très précieux, et m'ont permis de bien mener mon travail. Un merci chaleureux va aussi à Caroline.

Pourtant, quand je pense aux années passées ici, en France, je pense inévitablement à mes séjours parisiens. Je pense á Pony, mon ami de toujours. Je pense à Riccardo et à ses précieuses suggestions. Et de nouveau, une année à Leipzig, mes colocataires, mais surtout, la venue de Michele... Merci. Et puis le reste de mes amis. Je ne peux pas vous énumérer tous, alors ne soyez pas en colère avec moi.

Un grand merci va à tout le groupe de physique statistique. Chacun d'entre eux m'a donné quelque chose. Et puis, Jean-Charles, Sophie, Nelson, Xavier, Pierre... Merci à tous pour les jours agréables passés ensemble.

Je remercie Guillaume pour les agréables et utiles discussions et pour son soutien tout au long de la période où nous avons travaillé ensemble.

Enfin, je remercie chaleureusement les membres du jury d'avoir accepté de participer à la soutenance.

Introduction détaillée (en français)

Depuis quelques années, les phénomènes dépendant du temps ont fait l'objet d'un nombre croissant d'expériences, notamment dans le domaine de la physique quantique de la matière condensée et des systèmes optiques. Dans le domaine de la physique de la matière condensée les progrès expérimentaux ont permis d'étudier le comportement de transport sur des systèmes à faible dimensions telles que les boites quantiques ou fils quantiques et d'analyser la réponse de ces systèmes à des potentiels externes. Dans l'optique quantique un exemple célèbre pour des phénomènes dépendant du temps est la réalisation expérimentale de la transition de phase quantique de bosons ultrafroids placés sur un réseau optique [GME+02]; en faisant varier la profondeur du réseau optique on peut faire passe les bosons d'un régime superfluide à un régime isolant de Mott.

Récemment, de nouvelles études ont été menées sur le problème de la thermalisation quantique, c'est-à-dire si un système quantique hors d'équilibre relaxe vers un état stationnaire, et si c'est le cas, comment caractériser ses propriétés physiques après un très long temps. Par ailleurs, il serait intéressant de développer des instruments analytiques pour décrire les propriétés thermiques des systèmes quantiques hors équilibre. Toutes ces questions relèvent de la thermodynamique quantique. Comme on le sait, la thermodynamique est une théorie traitant des systèmes avec une infinité de degrés de liberté. La thermodynamique quantique tente de combiner la thermodynamique et la mécanique quantique dans un ensemble cohérent. Cette recherche est très importante car elle peut nous aider à comprendre comment les lois de la thermodynamique classique dépendent du comportement purement quantique des particules qui constituent la matière [GMM04].

Malgré des progrès expérimentaux récents, la description théorique des phénomènes hors équilibre est encore insuffisante.

À la lumière des discussions précédentes, nous pouvons conclure que la compréhension de la physique des systèmes quantiques hors équilibre représente l'un des problèmes ouverts les plus intrigants de la physique de la matière condensée moderne. Dans cette perspective, un des objectifs de la thèse est de répondre à certaines des questions soulevées dans ce domaine en utilisant des méthodes analytiques et numériques capables de faire face à des fortes corrélations et à des effets de non-équilibre.

Dans ce travail, nous concentrons notre attention sur la dynamique hors équilibre des systèmes quantiques unidimensionnels. Après la préparation du système quantique dans l'état fondamental d'un hamiltonien initiale (ou dans un état excité, ou dans un état canonique à la température inverse β, etc.), une trempe brutale ou quasi-adiabatique conduit le système hors équilibre, en générant des propriétés dynamiques très intéressantes. En effet, les systèmes de faible dimension, malgré leur simplicité, montrent souvent un comportement exotique. Par ailleurs, les caractéristiques unidimensionnelles des systèmes étudiés, comme par example la chaîne XY quantique de spin $1/2$, permetent souvent le développement de méthodes analytiques et numérique puissantes [LSM61, BMD70, BM71a, BM71b, BMA71].

Ces modèles sont largement utilisés comme laboratoire théorique standard pour les questions liées aux phénomènes critiques quantiques, les processus de décohérence et la thermalisation [Sac00].

Néanmoins, la grande partie des modèles quantiques unidimensionnels ne sont pas toujours facilement traitables par des méthodes analytiques (voir par exemple le modèle de Bose-Hubbard). C'est la raison pour laquelle, récemment, un grand effort a été consacré à l'amélioration des algorithmes numériques utilisés pour la simulation des systèmes quantiques unidimensionnels. Un de ces algorithmes, le groupe de renormalisation de la matrice densité en fonction du temps (t-DMRG), se révèle être très bien adapté pour étudier des phénomènes dépendants du temps dans les systèmes unidimensionnels fortement corrélés [Vid03, Vid04, WF04].

Ce rapport est divisé en trois parties. La première partie de la thèse est consacrée à la présentation du contexte dans lequel la partie centrale de notre travail (**Partie II**) peut être inscrite. L'idée principale qui a guidé le développement d'une telle structure était de le rendre "auto-consistent" dans le sens où le lecteur devrait trouver les instruments nécessaires à la compréhension des nouveaux résultats présentés dans les chapitres suivants. Bien sûr, en supposant que le lecteur soit un physicien, nous ne donnons que quelques détails techniques sur les méthodes et les modèles que nous allons utiliser et les analyser après, sans entrer trop dans les bases physiques. Dans un certain sens, avec cette partie, nous tenons à aborder de façon brève, et malheureusement non exhaustive, le cadre théorique qui sera utilisé tout au long du reste de la thèse.

Le **Chapitre 1** est consacré à l'introduction de l'idée de base d'une transition de phase quantique (QPT), en particulier en la comparant avec la transition de phase classique (CPT). Une transition de phase quantique est une transition de phase entre deux phases quantiques différentes (les phases de la matière à température zero). Par conséquent, elle est pilotée non pas par la température, mais par un paramètre physique qui apparaît dans l'hamiltonien. En conséquence de ce qui a été dit précédemment, le comportement du système doit dépendre des propriétés de l'état fondamental. En particulier, en changeant les paramètres, le système présente un comportement qui dépend fortement de la façon dont l'énergie et l'état fondamental dépendent de ces paramètres. Lorsque l'énergie de l'état fondamental est une fonction analytique du paramètre externe, les propriétés du système ne changent pas beaucoup. Par contre, lorsque l'énergie montre quelques points non-analytiques (points critiques quantiques), si le système croise un tel point, il modifie brutalement certaines propriétés, comme les symétries ou d'autres quantités macroscopiques: c'est ce que nous appelons une transition de phase quantique.

En particulier, proche d'un point critique, le système est caractérisé par la divergence de la longueur de corrélation. En général, les valeurs moyennes de certaines observables présentent un comportement de type "loi de puissance", caractérisé par des exposants (appelés exposants critiques) qui prennent des valeurs précises en fonction de la classe d'universalité du système étudié. Les caractéristiques du système au voisinage d'une transition de phase quantique vont aussi affecter son comportement dynamique. C'est ce qui arrive lorsqu'on essaie de traverser de manière adiabatique un point critique. L'échelle de temps sur laquelle un système est capable de répondre à une perturbation de son état est mesurée par l'inverse du gap d'énergie instantané $\tau \sim \Delta^{-1}$.

Il s'avère que ce temps est extrêmement important. Le théorème adiabatique est en fait limitée par cette échelle de temps. Il affirme, en effet, que nous pouvons faire évoluer adiabatiquement un système quantique seulement si le temps caractéristique de variation de l'hamiltonien est beaucoup plus grande que le temps de relaxation maximale que le système montre au cours de toute la dynamique [Mes62]. Par conséquent, au point critique quantique, où l'écart se ferme, la condition adiabatique se casse: il y aura toujours une fenêtre temporelle suffisamment proche du point critique où la dynamique n'est plus adiabatique. De ce point de vue, il est certainement un enjeu très important de savoir comment bien choisir un correct protocole temporelle pour guider le système par une transition de phase quantique. Car le comportement diabatique ne se manifeste qu'à proximité du point critique, il est naturel de se demander si la perte d'adiabaticité peut être décrite en termes de caractéristiques statiques du point critique, par exemple à travers ses exposants critiques. Le mécanisme de Kibble-Zurek [Kib76, Kib80, Zur85] aborde précisément cette question, en fournissant une connexion élégante entre la statique et les propriétés hors équilibre.

Selon le mécanisme de Kibble-Zurek, l'échelle de temps au cours de laquelle le système est capable de réagir à un changement externe diverge au point de transition du fait de la manifestation du "critical slowing down", observée aussi dans le cas classique [ZDZ05]. Tant que le système est suffisamment loin du point critique, son temps de relaxation caractéristique devrait être suffisamment petit pour permettre au système de réagir rapidement à la variation de l'hamiltonien. On suppose que le système a été initialement préparé dans l'état fondamental d'un hamiltonien initiale donnée. Puis, au début de l'évolution (régime adiabatique) l'état du système évolue adiabatiquement, ce dernier étant donné à chaque fois par l'état fondamental adiabatique instantané de l'hamiltonien dépendant du temps. Cependant, comme le système s'approche du QCP son temps de relaxation commence à augmenter dangereusement. Par conséquent, il y aura un instant (le "freeze-out time") à partir duquel le système ne sera plus en mesure de réagir aux changements extérieurs. A ce moment, l'évolution passe du régime adiabatique au régime d'impulsion dans lequel l'état du système est gelé. Selon ce mécanisme, l'adiabaticité est perdue lorsque le temps restant pour attendre la transition est égal au temps de relaxation, donné par l'inverse du gap Δ. Une fois que nous avons passé la zone critique, lorsque le système sera à nouveau assez loin du point critique, la dynamique va retrouver son caractère adiabatique et l'état va redémarrer son évolution adiabatique, mais à partir de l'état gelé.

Enfin, nous introduisons aussi la théorie quantique des perturbations dans la représentation des états propres adiabatiques. L'idée essentielle est très simple. Nous utilisons les états propres instantanés $|k(t)\rangle$ et les énergies propres instantanées $E_k(t)$ de l'hamiltonien dépendant du temps $\mathcal{H}(t)$:

$$\mathcal{H}(t)|k(t)\rangle = E_k(t)|k(t)\rangle. \tag{1}$$

Si l'hamiltonien évolue assez lentement (limite adiabatique), il est utile d'écrire l'état du système comme une série de puissance du nombre de sauts entrepris par le système d'un état propre instantané à l'autre. Ces sauts sont reliés par une évolution adiabatique dans le vecteur dans lequel le système se trouve entre les sauts. Le premier terme de la série donne l'expression habituelle adiabatique pour l'état final, le second est la correction standard pour l'évolution adiabatique. Donc, jusqu'à la contribution "à un seul saut", on a

$$|\Psi(t)\rangle \approx \mathrm{e}^{-i\int_{t_0}^{t} ds E_0(s)} \left[|0(t)\rangle + \sum_{k\neq 0} |k(t)\rangle \int_{t_0}^{t} dt' \langle \dot{k}(t')|0(t')\rangle \mathrm{e}^{-i\int_{t'}^{t} ds \delta\omega_{k0}(s)} \right], \tag{2}$$

avec les fréquences de Bohr $\Delta\omega_{k0}(t) = E_k(t) - E_0(t)$ et les amplitudes adiabatiques $\langle \dot{k}(t)|q(t)\rangle = \langle k(t)|\partial_t \mathcal{H}(t)|q(t)\rangle/(E_k(t) - E_q(t))$. Enfin, en faisant des hypothèses d'échelle pour les énergies et les amplitudes de transition, on retrouve, pour la densité de défauts, le même résultat que celui donné par le mécanisme de Kibble-Zurek.

Dans le **Chapitre 2** nous faison une brève introduction au modèle XY; l'hamiltonien du modèle est donné par

$$H = -\frac{1}{2}\sum_{n=1}^{L-1}\left(J_x\sigma_n^x\sigma_{n+1}^x + J_y\sigma_n^y\sigma_{n+1}^y\right) - \frac{h}{2}\sum_{n=1}^{L}\sigma_n^z, \tag{3}$$

où σ_n^α sont les matrices de Pauli, h est le champ magnétique dans la direction $\hat{z}$, J_x et J_y sont les constantes de couplage

$$J_x = \frac{1+\gamma}{2}, \quad J_y = \frac{1-\gamma}{2}, \quad \gamma \in [0,1], \tag{4}$$

avec γ le paramètre d'anisotropie. La valeur $\gamma = 0$ correspond au modèle XX avec une symètrie $U(1)$. Malgré l'absence d'une transition de phase ordonnée-désordonnée, nous pouvons identifier deux régions différentes: une phase paramagnétique et une phase critique. Dans la phase critique, le modèle présente une divergence de la longueur de corrélation [KT73]. Par ailleurs, dans le modèle XX, l'aimantation totale $M = \sum_n \sigma_n^z$ est conservée. Dans le cas $\gamma = 1$ l'hamiltonien décrit le modèle d'Ising quantique qui correspond à la limite anisotrope extrême du modèle d'Ising classiques à deux dimensions sur réseau carré [FS78, Kog79]. Le modèle d'Ising quantique montre un point critique quantique séparant une phase paramagnétique d'une phase ferromagnétique.

De plus, le modèle XY est intéressant pour différentes raisons: il est un modèle jouet de référence pour la compréhension des modèles plus complexes; il a une loi de dispersion non triviale; il montre un riche diagramme de phase; il est intéressant du point de vue expérimental.

Nous présentons ensuite la diagonalisation canonique de l'hamiltonien. En utilisant la transformation de Jordan-Wigner, en termes des opérateurs de Clifford

$$\Gamma_n^1 = \prod_{j=1}^{n-1}(-\sigma_j^z)\sigma_n^x, \quad \Gamma_n^2 = -\prod_{j=1}^{n-1}(-\sigma_j^z)\sigma_n^y, \tag{5}$$

on peut écrire l'hamiltonien sous la forme quadratique

$$H = \frac{1}{4}\mathbf{\Gamma}^\dagger\mathbf{T}\mathbf{\Gamma}, \tag{6}$$

avec

$$\mathbf{\Gamma}^\dagger = (\mathbf{\Gamma}^{1\dagger}, \mathbf{\Gamma}^{2\dagger}), \quad \mathbf{\Gamma}^{\mu\dagger} = (\Gamma_1^{\mu\dagger}, \cdots, \Gamma_L^{\mu\dagger}), \tag{7}$$

où $\mathbf{T}$ est un matrice hermitienne $2L \times 2L$

$$\mathbf{T} = \begin{pmatrix} \emptyset & \mathbf{C} \\ \mathbf{C}^\dagger & \emptyset \end{pmatrix}, \tag{8}$$

avec des éléments de matrice $C_{mn} = -i[h\delta_{mn} + J_x\delta_{m-1n} + J_y\delta_{mn-1}]$.

Nous introduisons l'entropie d'intrication et, pour le modèle XX, nous donnons le lien explicite avec la matrice de corrélation à deux points. En effet, si l'on divise une chaîne XX en deux parties, $\mathcal{A}$ et $\mathcal{B}$, on a pour l'entropie d'intrication du sous-systéme $\mathcal{A}$

$$S_A = -\sum_k \left[\zeta_k \ln \zeta_k + (1-\zeta_k)\ln(1-\zeta_k)\right], \tag{9}$$

où ζ_k sont les valeurs propres de la matrice de corrélation $\langle c_i^\dagger c_j\rangle$ restreinte à la partie $\mathcal{A}$.

Puis, nous concentrons notre attention sur la dynamique du modèle en donnant la représentation de Heisenberg des opérateurs de Clifford. On trouve que la matrice de corrélation des opérateurs de Clifford évolue comme

$$\langle \mathbf{\Gamma}\mathbf{\Gamma}^\dagger \rangle_t = \mathbf{U}(t)\langle \mathbf{\Gamma}\mathbf{\Gamma}^\dagger \rangle_0 \mathbf{U}^\dagger(t), \tag{10}$$

avec $\mathbf{U}(t) = \mathbf{V}\mathrm{e}^{-it\mathbf{\Lambda}}\mathbf{V}^\dagger$, où $\mathbf{V}$ est la matrice contentant les vecteurs propres de l'hamiltonien apres la trempe et $\mathbf{\Lambda}$ la matrice diagonale contenant les valeurs propres de l'hamiltonien apres la trempe. Enfin, nous considérons le cas où l'hamiltonien dépend explicitement du temps.

Le **Chapitre 3** est consacré à la présentation brève du modèle de Bose-Hubbard. Ce modèle donne une description approximative de la physique des bosons en interaction sur un réseau. Il est étroitement lié au modèle de Hubbard qui provient de la physique du solide comme une description approximative de systèmes supraconducteurs et du mouvement des électrons entre les atomes d'un solide cristallin. Le nom "Bose" fait référence au fait que les particules dans le système sont des bosons. Le modèle de Bose-Hubbard est une simple description des atomes bosoniques sur un réseau optique avec hamiltonien en deuxième quantization

$$H_{BH} = -t\sum_{\langle i,j\rangle}\left(b_i^\dagger b_j + h.c.\right) + \frac{U}{2}\sum_i n_i\left(n_i - 1\right) - \mu\sum_i n_i, \tag{11}$$

en termes des opérateurs bosonique de création et destrution sûr reseau $b_i^\dagger$, b_i et nombre d'occupation $n_i = b_i^\dagger b_i$. Le premier terme représente la contribution cinétiques en décrivant les saut de bosons d'un site à l'autre. Dans le cas le plus simple, le saut est réservé aux plus proches voisins $\langle i,j\rangle$ seulement. Le terme U vient de l'interaction paire et donne le coût d'énergie lorsque les particules n_i sont assis sur le site i. Enfin, le terme μ tient comptes pour un potentiel local externe qui peut être interprétée comme un potentiel chimique essentiel pour fixer le nombre de bosons dans le système.

L'hamiltonien H_{BH} peut être déduit d'une description continue de bosons qui vivent dans un potentiel périodique [JZ05]. A partir de la description continue, dans l'approximation mono-bande et en assumant des fonctions de Wannier bien localisées, on peut remanier la description originale dans la formulation seconde quantifiée (voir [LSA+07, Yuk09] pour plus de détails).

Dans la limite des interactions locales faibles, où le tunnel est dominant $t \gg U$, l'état fondamental de l'hamiltonien est bien décrit par les fonctions d'onde à une particule de N bosons entièrement répartis sur le réseau entier avec L sites. Dans ces conditions, l'état fondamental à plusieurs corps dans un réseau homogène est donnée par

$$|\Phi_{SF}\rangle_{U=0} \sim \left(\sum_i^L b_i^\dagger\right)^N |0\rangle, \tag{12}$$

où $|0\rangle$ est l'état de vide, avec une cohérence de phase evidente des bosons. En d'autres termes, tous les bosons occupent le même état fondamental à une particule, conduisant à la superfluidité du système.

D'autre part, lorsque l'amplitude de saut $t \to 0$, l'hamiltonien de Bose-Hubbard se réduit à une somme directe de Hamiltoniens locaux $H_i = U\sum_i n_i(n_i-1)/2 - \mu\sum_i n_i$. La densité des particules sur chaque site est fixée à une valeur entière par la condition de minimisation de l'énergie. Il n'y a plus de connexions entre les sites voisins et les bosons restent fixe dans l'espace. Dans un tel cas, l'état fondamental à plusieurs corps est un isolant de Mott, et dans un système homogène, il est donné par le produit tensorielle suivant

$$|\Phi_{MI}\rangle_{t=0} = \prod_{i}^{L} \left(b_i^\dagger\right)^n |0\rangle. \tag{13}$$

où n représente le remplissage entier local. Cet état est caractérisé par une corrélation à longue portée dans l'opérateur nombre de particules n_i et, contrairement à la limite précédente, la cohérence de phase a complètement disparu. Enfin, une propriété intéressante de cet état, est la présence d'un gap énergétique de l'ordre de U dans le spectre d'énergie. La présence d'un tel gap énergétique se reflète dans l'absence de compressibilité.

Après l'introduction du diagramme de phase du modèle en regardant particulièrement certaines experiences qui ont montré la transition de phase Mott-Superfluide, nous concentrons notre attention sur une expérience étroitement liée à nos études [DPR+96]. Dans cette expérience, les auteurs présentent des oscillations de Bloch d'atomes de césium ultrafroids dans la bande fondamentale d'énergie d'un potentiel optique périodique. Ils mesurent directement la distribution d'impulsion évoluant dans le temps sous l'influence d'une force d'inertie constante et ce pour diverses profondeurs du potentiel.

La deuxième partie de la thèse contient les principaux résultats de nos études. Toutes les analyses effectuées peuvent être inscrites dans le même sujet général: la dynamique des systèmes quantiques fermés. En effet, les dynamiques de trempe soudaine et adiabatique sont toutes deux étudiées en détail pour différentes chaînes quantiques dans des configurations différentes. En ce qui concerne le processus de croisement d'un point critique quantique, il s'avère que les inhomogénéités, comme des potentiels de confinement, pourraient vraiment affecter la production des défauts [DR10a, CK10, CK11]. De plus, les progrès expérimentaux avec des atomes bosoniques ultra-froids placés dans des réseaux optiques, a conduit la communauté des théoriciens à s'intéresser à la simulation des Hamiltoniens à plusieurs particules type Hamiltonien de Bose-Hubbard avec paramètres ajustables. Des expériences [DPR+96, WBM+96] ont montré des oscillations de Bloch et ont revitalisé la recherche théorique sur la dynamique des modèles bosoniques unidimensionnels. Enfin nous consacrerons une partie de notre étude à la compréhension du mécanisme dynamique de la thermalisation, en particulier en regardant des propriétés locales sur un système quantique étendu dans l'espace.

Avant d'introduire une sorte de résumé de chaque chapitre, nous aimerions dire quelques mots sur les objectifs qui nous ont guidés au cours de l'élaboration des chapitres: dans la pratique, l'idée était de faire chaque chapitre indépendant, en donnant, à chaque fois, une introduction du sujet, bien placée dans la littérature existante, et en développant les outils (éventuellement en se référant à ce qui a déjà été introduit dans la première partie de la thèse) qui conduiront à des résultats nouveaux.

Dans le **Chapitre 4** nous analysons l'évolution cohérente d'un système quantique à plusieurs particules, après le changement lent d'un potentiel de confinement type loi de puissance. L'amplitude du potentiel confinant est variée dans le temps avec une loi de puissance telle que le système à plusieurs particules atteint ou franchit un point critique. Nous supposons que suffisamment proche du point critique quantique, le paramètre de contrôle h s'écarte de la valeur critique h_c en suivant la loi

$$h(x,t) - h_c \simeq g(t)|x|^\omega, \tag{14}$$

avec un exposant $\omega > 0$. L'amplitude $g(t)$ de l'écart spatial à la valeur critique est dirigée depuis une valeur initiale donnée vers une dernière suivant la rampe de temps non linéaire $g(t) = v|t|^\alpha \mathrm{sgn}(t)$.

Tout d'abord, nous analysons en détail la génération cohérente de défauts pendant cette trempe adiabatique inhomogène qui conduit un système quantique unidimensionnel à travers une transition de phase du second ordre. Il s'avére que l'effet des inhomogénéités influence fortement les propriétés d'équilibre et dynamiques d'un système quantique près d'un point critique. Une perturbation pertinente, générée par un potentiel de confinement, par exemple un piège harmonique, change la classe d'universalité du système à proximité du point critique. Plus généralement, le chargement ou la suppression d'un piège, type "loi de puissance", lentement dans le temps et à proximité d'un point critique conduira à un état final avec une densité non triviale de défauts qui dépendra de la forme du piège et du protocole temporel.

Un tel potentiel est relevant surtout dans le contexte des systèmes ultra-froids confinés, où la dynamique est bien décrite par l'évolution unitaire des systèmes fermés. Ainsi, nous développons une théorie d'échelle qui prédit le comportement adiabatique du système après une telle trempe. Nous voyons que l'échelle de longueur typique ℓ diverge, à proximité du point critique, avec un exposant effectif de la longueur de corrélation $\nu_g = \nu/(1+\nu\omega)$. À partir de cette considération, nous trouvons que l'échelle de temp typique τ autour du point critique se comporte comme $\tau \sim v^{-z/y_v}$ où $y_v = z\alpha + 1/\nu_g$ est la dimension RG de la perturbation. Dans notre approche d'échelle, nous analysons comment les propriétés d'échelle sont influencées par une incertitude sur la localisation spatio-temporelle du point critique. Par ailleurs, en utilisant des arguments type Kibble-Zurek, nous calculons les propriétés d'échelle de la densité de défauts $n \sim v^{d/y_v}$ et de l'excès d'énergie $\epsilon \sim v^{(d+z)/y_v}$ générés pendant le chargement ou la suppression du piège. Toutes ces prédictions sont vérifiées sur la chaîne d'Ising quantique. En effet, pour le modèle d'Ising quantique, nous confirmons la prédiction d'échelle pour les niveaux d'énergie ainsi que pour les éléments de matrice de la perturbation (le potentiel de confinement).

Nous trouvons, en utilisant l'approximation adiabatique, une formule analytique pour une trempe d'un piège linéaire qui ne traverse pas le point critique. En branchant la solution exacte dans les amplitudes adiabatiques, on obtient une expression fermée

$$|a_{pq}(t_0,t)|^2 = \left| \frac{\Delta_{pq}}{2\Omega_{pq}} A_{\rho_{pq}}\left(|g_0|, |g(t)|\right) \right|^2 \tag{15}$$

avec

$$\Delta_{pq}(g) = \sqrt{\frac{p+q}{2} + \frac{1+\mathrm{sgn}(g)}{4}}\, \left[\delta_{p\,q-1} - \delta_{p\,q+1}\right] \ , \tag{16}$$

$\Omega_{pq}(g) = |g|^{-1/2}(\epsilon_p(g) + \epsilon_q(g))$ et $\rho_{pq} = -2\Omega_{pq}\frac{v^{-1/\alpha}}{\alpha+2}\mathrm{sgn}(g)$.

La fonction

$$A_\rho(x,y) = \frac{2\alpha}{2+\alpha}\left[\mathrm{E}_1\left(i\rho x^{\frac{2+\alpha}{2\alpha}}\right) - \mathrm{E}_1\left(i\rho y^{\frac{2+\alpha}{2\alpha}}\right)\right] \tag{17}$$

est exprimé en termes d'exponentielle intégrale $\mathrm{E}_1(z) = \int_z^\infty dt\, t^{-1}\mathrm{e}^{-t}$ for $|\mathrm{Arg}(z)| < \pi$.

Dans le cas général, nous effectuons une analyse d'échelle sur les tailles finies. Afin d'extraire le comportement asymptotique, pour une observable générique f, nous supposons le comportement d'échelle de taille finie suivant

$$f(v,L) = f_0(v) + f_1(v)L^{-\lambda_c} + f_2(v)L^{-2\lambda_c} + \dots \tag{18}$$

où λ_c est un exposant de correction d'échelle inconnu.

Nous confirmons cette prediction par la théorie d'échelle générale. Enfin, nous concentrons notre attention sur les propriétés spatiales de la densité de défauts locaux ainsi que sur les effets d'un changement global du point critique. Une fois encore, les prédictions de la théorie d'échelle générale sont confirmées dans le cas du modèle d'Ising quantique.

Dans le **Chapitre** 5 nous analysons l'effet d'une variation soudaine d'un potentiel chimique linéaire sur un gaz de Bose unidimensionnel confiné dans une région finie d'un réseau optique.

Dans un premier temps, dans la limite impénétrable (modèle des bosons Hard-Core), nous dèveloppons une théorie hydrodynamique qui prédit le comportement du condensât piégé ainsi que la densité de bosons éjectés. Deux idées sont sous-jacentes à cette théorie: l'hypothèse d'équilibre local, c'est-à-dire que le système est localement à l'équilibre avec le potentiel local; et le mouvement balistique de chaque point de l'espace de phase (x, q) avec une vitesse qui dépend directement de la loi de dispersion $\epsilon_q = V(x) - \cos q$. Selon cette théorie, l'équation du mouvement pour la densité dans l'espace de phase peut se résumer en

$$\rho^{\pm}(x,q,t) = \frac{1}{2} \iint dq_0 dx_0 \mathcal{G}^{\pm}(x,q,t;x_0,q_0)\rho_0(x_0,q_0), \tag{19}$$

où la densité totale $\rho(x,q,t) = \rho^+(x,q,t) + \rho^-(x,q,t)$ est la somme des densités des particules gauches et droites. Les propagateurs à droite et à gauche $\mathcal{G}^{\pm}$ sont tout simplement donnés par $\mathcal{G}^{\pm}(x,q,t;x_0,q_0) = \delta(x - x^{\pm}(x_0,q_0,t))\delta(q - q^{\pm}(x_0,q_0,t))$, où $x^{\pm}$ et $q^{\pm}$ sont les équations du mouvement pour une seule particule initialement située dans (x_0, q_0).

En utilisant cette théorie, nous reproduisons les oscillations de Bloch bosoniques macroscopiques observées sur la rampe linéaire. Par ailleurs, nous calculons le nombre total de particules éjectées en fonction de la pente du potentiel p, et nous reproduisons exactement l'évolution du profil de la densité et du courant des particules éjectées. On peut résumer quelques résultats généraux que nous observons dans la dynamique d'un tel modèle:

- Pour une petite valeur du potentiel V_A sur le site le plus à gauche (voir Figure 5.1), presque toutes les particules quittent la rampe. En augmentant la pente p, nous observons qu'une partie des particules restent piégées. Ces particules piégées oscillent le long de la rampe lorsque le système est initialement préparé dans une phase superfluide. Au contraire, pour $\rho_0 = 1$, nous n'observons pas ces oscillations. Par ailleurs, lorsque V_A atteint une valeur critique V_A^*, un "plateau", c'est-à-dire une zone avec une densité constante de particules, apparaît au milieu de la rampe.

- La région du plateau au milieu de la rampe devient plus large en augmentant la valeur de la pente du potentiel

$$L_{plat} \simeq A\left(1 - \frac{4}{V_A}\right), \quad \text{pour} \quad \mathrm{V_A} \gtrsim 4. \tag{20}$$

- La période de l'oscillation du profil de la densité est donnée par

$$T = 2\pi \frac{A}{V_A} = \frac{2\pi}{p}. \tag{21}$$

- Dans la région du plateau, le courant de particules est uniforme et montre un comportement parfaitement sinusoïdale dans le temps

$$j(x,t) \propto \sin(2\pi t/T). \tag{22}$$

Enfin, nous analysons la dynamique générée par une trempe soudaine de l'hamiltonien de Bose-Hubbard. Dans ce cas nous utilisons la t-DMRG et l'algorithme de Lanczos. Ces études numériques confirment la présence de deux fréquences principales, la première à la valeur de l'interaction locale U, et la deuxième à la valeur de la rampe externe p du potentiel.

Par ailleurs, lorsque le système est loin des points d'intégrabilité ($U = 0$ et $U = \infty$), nous constatons une perte de cohérence dans l'évolution des bosons piégés.

Dans le **Chapitre 6** nous analysons l'évolution temporelle d'un système quantique étendu, initialement préparé dans un état hors équilibre. En introduisant la matrice densité locale qui dépend du temps, nous définissons correctement un profil de température quantique, par rapport à l'attente classique. En particulier, nous concentrons notre attention sur le comportement d'échelle dynamique du mécanisme de stabilisation thermique pour un système quantique fermé initialement divisé en deux sous-systèmes à des températures différentes.

Ainsi, nous étudions la dynamique d'équilibre thermique après la mise en contact de deux systèmes quantiques étendus d'abord préparés en deux ensembles de Gibbs différents. Nous introduisons la notion de distance $d^n(x, t, \beta) = \mathrm{Tr}_{\mathcal{S}_x} |\rho(x, t) - \rho_x(\beta)|^n$, pour $n = 1, 2$, où la trace est effectuée sur le sous-système locale $\mathcal{S}_x$. Nous comparons cette notion avec une définition globale de distance. On voit que l'equilibre thermique se produit lorsque les variables locales sont prises en compte. De cette façon, nous pouvons introduire un profil de température $\beta(x, t)$ comme dans le cas classique. Après avoir développé cette définition locale de la température pour le modèle unidimensionnel de bosons Hard-Core, nous constatons que, dans la limite de hautes températures, le profil se comporte comme

$$\beta(x, t) = \frac{1}{\sum_q \epsilon_q^2(x)} \sum_q \epsilon_q(x) \ln \frac{1 - \lambda_q(x, t)}{\lambda_q(x, t)}, \tag{23}$$

où $\lambda_q(x, t)$ sont les valeurs propres de la matrice de corrélation locale. Nous étudions numériquement les propriétés d'échelle de tels profils, et nous vérifions que la définition de $\beta(x, t)$ est stable sous différentes tailles des sous-intervalles utilisés pour extraire la température locale. Nous constatons que les observables locales deviennent plus robustes que les globales, montrant, dans les premiers instants de l'évolution, des propriétés thermiques. Enfin, on observe que le profil de température, dans un système quantique étendu, montre le comportement d'échelle

$$\beta(x, t) = \frac{\beta_1 + \beta_2}{2} \left[1 + \frac{\beta_1 - \beta_2}{\beta_1 + \beta_2} \mathcal{B}(x/t, \beta_1/\beta_2) \right] \equiv \bar{\beta} + \delta \mathcal{B}(x/t, \beta_1/\beta_2), \tag{24}$$

avec $\bar{\beta} = (\beta_1 + \beta_2)/2$ et $\delta = (\beta_1 - \beta_2)/2$, similaire à la contrepartie classique.

Dans la dernière partie de la thèse nous compilons des renseignements supplémentaires ne rentrant directement pas dans le corps de la thèse. Comme on l'a dit précédemment, les deux premières annexes donnent des informations supplémentaires en soutenant les chapitres précédents. Plus précisément:

Dans l'**Appendice A** nous donnons une "démonstration" brève et simple de l'expansion perturbative adiabatique en combinant la théorie perturbative quantique indépendante du temps dans la base tournante avec la décomposition de Trotter de l'opérateur d'évolution.

Dans l'**Appendice B** nous présentons, en prenant comme exemple le cas $\omega = 1, \alpha = 2$, les détails du calcul de la prédiction d'échelle dans le cas d'un "changement global du point critique" comme indiqué dans la **Section 4.1.3**.

Dans l'**Appendice C** nous présentons les algorithmes DMRG et t-DMRG utilisés pour simuler les systèmes quantiques étudiés dans cette thèse.

Trois articles scientifiques ont été publiés directement en lien avec les travaux exposés dans ce manuscrit et deux autres articles sont actuellement en préparation. Voici la liste des publications:

The quantum Galileo ramp: entangling many-body bound states with propagative modes
M. Collura, H. Aufderheide, G. Roux and D. Karevski
Soumis à la Physical Review Letters le 23/12/2011.

Nonlinear quenches of power-law confining traps in quantum critical systems
M. Collura and D. Karevski
Physical Review A **83**, 023603 (2011).

Critical Quench Dynamics in Confined Systems
M. Collura and D. Karevski
Physical Review Letters **104**, 200601 (2010).

Gradient critical phenomena in the Ising quantum chain: surface behaviour
M. Collura, D. Karevski and L. Turban
Journal of Statistical Mechanics, P08007 (2009).

Introduction

From some decades to now time-dependent phenomena have been the focus of an increasing number of experiments, especially in the area of condensed matter physics and quantum optical systems. In the area of condensed matter physics the study of these phenomena have made it possible to investigate the transport behavior through low dimensional systems such as quantum dots or quantum wires and to analyze the response of such systems to external potentials. In the quantum optic domains a famous example for time-dependent phenomena is the experimental realization of the quantum phase transition of ultracold bosons loaded in an optical lattice [GME$^+$02]; by varying the optical lattice depth one can drive the bosons from a superfluid to a Mott-insulating regime.

Recently, new attentions was focussed on the quantum thermalization problem, i.e. whether a out-of-equilibrium quantum system relaxes to a stationary state and how to eventually characterize its physical properties at late times. Moreover, it would be interesting to develop analytical instruments for describing thermal properties of out-of-equilibrium quantum systems. All these issues fall in the so-called quantum thermodynamics. Thermodynamics describes systems of infinite degrees of freedom. An interesting question is what will remain of thermodynamics if one goes to the extremely small quantum systems which have only a few degrees of freedom. Quantum thermodynamics is what we need: it tries to combine thermodynamics and quantum mechanics in a coherent way. Therefore, researches in this direction are very important: for example, using quantum thermodynamics we can attempt to understand the essential relation between thermodynamic entropy and entanglement entropy of a quantum system. Moreover, it is very interesting to better understand how the classical laws of thermodynamics depend on the purely quantum nature of the particles that constitute matter [GMM04].

Despite the impressive achievements in the experimental domains, a good theoretical description of most of the out-of-equilibrium phenomena is often incomplete.

In light of the previous discussions we can conclude that understanding the physics of interacting quantum systems out of thermal equilibrium represents one of the most fascinating open problem in modern condensed matter physics. In this perspective, the aim of the present thesis is to address some of these issues arising in this field by means of analytical and numerical methods able to deal with strong correlations and non-equilibrium effects.

In this work we focus our attention on the non-equilibrium dynamics of one-dimensional quantum systems. Indeed, after preparing the quantum system in the ground state of a given initial Hamiltonian (or in a canonical state at β inverse temperature), a sudden or adiabatic quench drives the system out-of-equilibrium, generating very interesting dynamical properties. Indeed, low-dimensional systems, despite there simplicity, often show exotic behavior. Moreover, the one-dimensional characteristics of the systems under investigation often allows the development of analytical methods useful for the simplification of the problem, also from the numerical point of view; this is the case for the XY quantum $1/2$-spin chains

[LSM61, BMD70, BM71a, BM71b, BMA71]. These models are extensively used as a standard theoretical laboratory for issues related to quantum critical phenomena, decoherence and thermalization processes [Sac00].

Nevertheless, the great part of one-dimensional quantum models are still not easily tractable by analytical methods (see for example the Bose-Hubbard model). This is the reason why, recently, a great effort was spent in the improvement of numerical algorithms devoted to the simulation of one-dimensional quantum systems. One of these algorithms, the adaptive time-dependent density-matrix renormalization-group (t-DMRG), is very well suited for investigating time-dependent phenomena in one-dimensional strongly correlated quantum systems [Vid03, Vid04, WF04].

The thesis is divided in three parts. In the first one we briefly introduce the models and the mathematical tools that we will use through the manuscript. The second part of the thesis is focused on the dynamics of closed quantum systems; especially with regards to the one-dimensional XY chain and the Bose-Hubbard model. Finally in the third part we collect all the appendices. For more details on the contents of each chapter, we refer the reader to the introductory sections of each of the parts of the thesis.

Three scientific articles have been published directly related to the PhD studies. Two other papers are currently in preparation. Here is the list of publications:

The quantum Galileo ramp: entangling many-body bound states with propagative modes
M. Collura, H. Aufderheide, G. Roux and D. Karevski
Submitted to Physical Review Letters on 23/12/2011.

Nonlinear quenches of power-law confining traps in quantum critical systems
M. Collura and D. Karevski
Physical Review A **83**, 023603 (2011).

Critical Quench Dynamics in Confined Systems
M. Collura and D. Karevski
Physical Review Letters **104**, 200601 (2010).

Gradient critical phenomena in the Ising quantum chain: surface behaviour
M. Collura, D. Karevski and L. Turban
Journal of Statistical Mechanics, P08007 (2009).

Part I

Context and Models

*This first part of the thesis is devoted to introduce the background in which the central part of our work (***Part II***) can be inscribed. The main idea that guided the development of such manuscript was to make it "self-consistent" in the sense that the reader should find all the tools useful to understand the novel results reported in the following chapters up to the end. Of course, assuming the reader an "expert on physics", we will only give some technical details about the specific methods and models that we will use or analyze after, without going too much inside the physical foundation. In some sense, with this part, we would like to embrace in a brief, and unfortunately non-comprehensive way, the theoretical framework which we will extensively refer to throughout the rest of the work.*

Chapter 1 *is dedicated to introduce the basic idea of a Quantum Phase Transition (QPT) in particular with respect to the Classical Phase Transition (CPT). We will briefly review the level crossing concept and explore the fundamental instruments useful for describing the dynamical behavior of a quantum system adiabatically driven across a Quantum Critical Point (QCP). In particular, we stress the usefulness of the Kibble-Zurek argument which gives an elegant scaling connection between the properties of the critical point and the loss of adiabaticity. Finally, we also introduce the quantum perturbation theory in the adiabatic eigenstate representation.*

In **Chapter 2***, after a brief introduction to the XY model, we give the canonical diagonalization of the Hamiltonian: by using the Jordan-Wigner transformation it is possible to map the XY model to a free-fermion model. We introduce the entanglement entropy and, for the XX model, we give the explicit connection with the two-point correlation matrix. Then, we focus our attention on the dynamics of the model giving the Heisenberg representation of the Clifford operators. Finally, we consider the case in which the Hamiltonian depends explicitly on time.*

Finally **Chapter 3** *is devoted to briefly introduce the Bose-Hubbard model. This model approximatively describes the behavior of interacting bosons on a lattice. It is related to the electronic Hubbard model but, as guessed from the name "Bose", the particles in such a system are bosons. The Bose-Hubbard model turns out to be very important for simulating the dynamics of ultracold atoms on optical lattice lattice. After introducing the phase-diagram of the model especially with regard to some experiments which showed the well-known Mott-Insulating to superfluid phase transition, we focus our attention on an experiment closely related to our studies [DPR+96].*

Chapter 1

Quantum Phase Transition

«Water, water everywhere,
nor any drop to drink.»
S. T. Coleridge

A classical phase transition (CPT) is a dramatic physical phenomenon driven by thermal fluctuations. Beside this well-studied concept of CPT, a similar phenomenon can occur at zero temperature which correspond to a quantum phase transition (QPT) between two macroscopically different states of matter. The QPT is driven by quantum fluctuations whose intensities are controlled by a physical parameter, like an internal interaction coupling or an external field, entering into the Hamiltonian of system. While a classical phase transition is characterized by singularities in the thermodynamic functions of the system under consideration, on the other hand a quantum phase transition manifests itself by singular signatures in the ground state of the many-body quantum system [Sac00], whose macroscopic properties significantly differ on both sides of the transition. In this thesis we will focus our attention only on systems that exhibit (at zero temperature) continuous transitions occurring at a quantum critical point (QCP).

Of course, whenever the temperature is finite, but still sufficiently low, the quantum fluctuations are competing with the thermal ones. As a consequence there would be a certain influence of the quantum transition in a sufficiently small region of the phase space (T, g) (where T is the temperature and g is the Hamiltonian parameter driving the quantum transition) around the QCP located in $(0, g_c)$. Increasing the temperature the system will show a crossover from a purely quantum critical behaviour to a purely classical one (if any, which is not necessary the case as in low-dimensional systems with short range interactions). In Figure 1.1 we show a typical phase diagram in the (T, g) plan, assuming that the system may have a CPT. At high temperatures, the system is completely disordered. In the vicinity of the classical phase transition (the red line in Figure 1.1) the system is governed by classical thermal fluctuations. Decreasing the temperature this transition line converges towards the QCP (the green small circle in Figure 1.1). Furthermore, we have also depicted the ‘quantum critical’ crossover region (the light gray region in Figure 1.1) wherein quantum and thermal fluctuations are of the same order. Finally, the orange thick line at $T = 0$ individuates the pure quantum ordered phase.

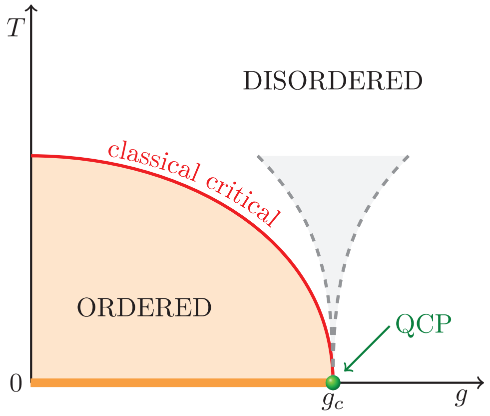

Figure 1.1: Sketch of a quantum phase diagram where transitions are driven by temperature T and a physical parameter g. See the text for more details.

1.1 Level crossing

Let us go more into the details of a quantum phase transition. Whenever we have to study the equilibrium properties of a quantum system at very low temperatures, we have to look at the ground-state properties of the system and as we have already seen, a QPT is related to the non-analytical properties showing up into the ground state of the system for a particular coupling value (which may be an external field or an internal interaction coupling). If the system Hamiltonian $H(h)$ depends on an external parameter h, the ground state $|\Psi_0(h)\rangle$, will 'adiabatically' depend on h. The non-analytic behavior of the system ground state at the QCP should drastically affect the analytical properties of the expectation value $\langle\mathcal{O}(h)\rangle$ of an observable $\mathcal{O}(h)$ (which may or may not depend on h). For example, in the paramagnetic-ferromagnetic transition of the quantum Ising model, the total longitudinal magnetization $M_x = \sum_n \sigma_n^x$ will show non-analytic behavior at the transition point. Incidentally, notice that $\mathcal{O}(h)$ could be the Hamiltonian operator itself and, in this case, its average will be simply the adiabatic ground-state energy $E_0(h)$.

As long as the system will be far away from a QCP, the ground state $|\Psi_0(h)\rangle$ will draw a h-dependent simple curve in the Hilbert space; otherwise, approaching the QCP (h_c in Figure 1.2), the path will be no more analytic, since the ground state may collapse with excited states. The non-analyticity of that curve is connected to the non-analytical behavior of $\frac{\partial_h H(h)}{E_q(h)-E_0(h)}$. Indeed, every time the ground-state energy $E_0(h)$ approaches one of the excited energies, the system will exhibit a fundamental change in its own properties. To be more concrete, suppose that the ground-state is approaching the first-excited state. If we look in a neighborhood of h_c, linearizing $E_0(h)$ and $E_1(h)$, then the level-crossing will show up as a discontinuity in the first derivative of the adiabatic ground-state energy (see the inset of Figure 1.2). Usually (if the perturbation field is not a conserved quantity) the level crossing is forbidden in finite dimensional systems and one has to go to the thermodynamical limit to get a true QPT. Indeed, as we show in Figure 1.3 for the Ising case, in the thermodynamical limit, as the system size L becomes larger and larger, the energetic gap stays finite in the non-critical region, but exactly at the critical point it closes as L^{-1}.

As far as second order quantum phase transitions are concerned, it is natural to use the energy gap $\Delta(h) = |E_1(h) - E_0(h)|$ as the natural energy scale characterizing the system properties near the transition. It turns out that close to the critical value h_c, one has the

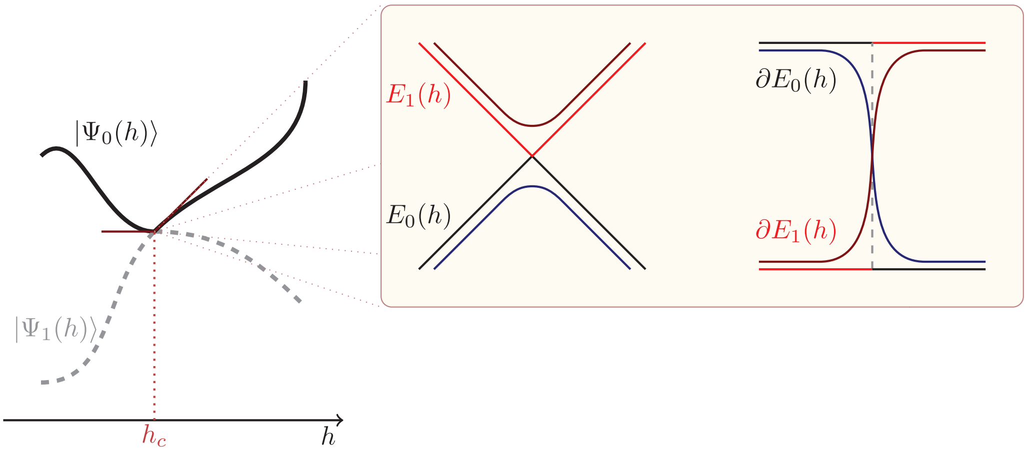

Figure 1.2: Pictorial representation of the ground-state path in the Hilbert space. In such example, the point where the curve is no more derivable represent a QCP. In the inset we inspect some properties of the system near the QCP: in the left figure, the blue and the dark red curves are respectively the energies of the ground state and the first-excitation state for a gapped system. Dark and light red curves represent the energy behavior for a gapless system; notice how level crossing in the energy (gapless system) corresponds to a discontinuity on the first derivative (right part of the inset); nevertheless in a more general setup, e.g. for a finite system, where level crossing is forbidden, the discontinuity is rounded off.

scaling behaviour

$$\Delta(h) \sim J|h - h_c|^{z\nu}, \tag{1.1}$$

with J an energy scale set by a microscopic coupling, z the dynamical critical exponent and ν the correlation length critical exponent. The correlation length diverges at the critical point as

$$\xi \sim a|h - h_c|^{-\nu}, \quad \xi \sim \Delta^{-1/z}, \tag{1.2}$$

where a is a characteristic length (set for example by a lattice spacing). The characteristic time scale of a quantum system is given by the inverse of the minimum instantaneous gap $\tau \sim \Delta^{-1}$, which is the quantum counterpart of the correlation time τ_c associated to a classical transition. In light of what we will see in the next few paragraphs, it turns out that this time is extremely important. The adiabatic theorem is in fact bounded by this time scale. It states, indeed, that we can adiabatically drive a quantum system only if the characteristic time of variation of the Hamiltonian is much larger than the maximum relaxation time the system exhibits during the whole dynamics [Mes62]. Therefore, at the quantum critical point, as the gap closes, the adiabatic condition breaks down: there will be always a temporal window sufficiently close to the critical point where the dynamics is no longer adiabatic. From this point of view, it is definitely a very important issue to know how to properly choose a correct temporal protocol to guide the system through a quantum phase transition.

In order to illustrate what has been said, following the didactical picture originally proposed in [Sac00, Fag08], consider as an example the Ising Hamiltonian (we refer the reader

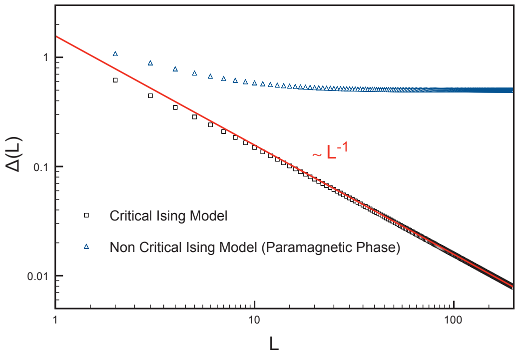

Figure 1.3: Finite-size scaling of the gap Δ for the Ising model. The system is gapped in the paramagnetic phase. Otherwise, at the critical point, the gap closes as L^{-1}.

to the following chapters for more details)

$$H_I = -J \sum_n \sigma_n^x \sigma_{n+1}^x - h \sum_n \sigma_n^z, \tag{1.3}$$

where σ_n^α are the Pauli matrices, $J > 0$ is the characteristic energy scale of the microscopical coupling and h is an external magnetic field applied in the $\hat{z}$ direction. Whenever the Zeeman term is dominating, i.e. when $|h|/J \gg 1$, the spins tend to align in the direction of the field, leading to the many-body ground state

$$|\Psi_0\rangle \xrightarrow{|h|\gg J} \bigotimes_n |\uparrow\rangle_n. \tag{1.4}$$

In this state the σ_n^x operators show the totally uncorrelated behavior

$$\langle\Psi_0|\sigma_m^x \sigma_n^x|\Psi_0\rangle\big|_{|h|/J=\infty} = \delta_{mn}, \tag{1.5}$$

where this short-length correlations should remain exponentially small for sufficiently small $J/|h|$.

In the opposite case, when the longitudinal couplings are dominant, i.e. when $|h|/J \ll 1$, the spins should tend to align in the $\hat{x}$ direction, leading for $h = 0$ to two degenrated ground states:

$$\bigotimes_n |\rightarrow\rangle_n \quad \text{and} \quad \bigotimes_n |\leftarrow\rangle_n, \tag{1.6}$$

where $|\rightarrow\rangle_n$ and $|\leftarrow\rangle_n$ are the eigenvectors of σ_n^x. Of course, in the thermodynamical limit, an infinitesimal magnetic field in the x-direction will bring the system to choose one of the two previous ground states, leading to a spontaneous symmetry breaking. As a consequence, in the thermodynamical limit, the correlation function of the σ_n^x operators will be long-range:

$$\langle\sigma_m^x \sigma_n^x\rangle\big|_{|h|/J=0} = 1. \tag{1.7}$$

Naturally, there should be at least one intermediate value $(|h|/J)_c \sim 1$ of the coupling ratio wherein a QPT occurs. We can take trace the transition by looking at the asymptotic behavior of the σ_n^x correlations

$$\lim_{|m-n|\to\infty} \langle\sigma_m^x \sigma_n^x\rangle. \tag{1.8}$$

Longitudinal correlations will be different from zero only in the ferromagnetic phase, for $|h|/J < (|h|/J)_c$, and vanishe in the paramagnetic phase $|h|/J > (|h|/J)_c$.

1.2 Adiabatic dynamics through a QCP

Suppose we want to prepare a quantum many-body system in a state as close as possible to the ground state $|\Psi_0^{(1)}\rangle$ of a given Hamiltonian H_1 by driving the system at hand from an initial (ground) state $|\Psi_0^{(0)}\rangle$ associated to the initial Hamiltonian H_0 through a QCP. To do that, we can introduce a time dependent Hamiltonian $H(t)$ which connects along a given path the initial and final Hamiltonians, such that

$$H(0) = H_0, \quad H(t_{end}) = H_1, \tag{1.9}$$

where t_{end} represents the duration of the whole evolution starting at $t = 0$. Given the time-dependent Hamiltonian $H(t)$, the time evolution of this closed quantum system can be solved by introducing the evolution operator $U(t)$ satisfying

$$i\hbar \frac{\partial}{\partial t} U(t) = H(t)U(t), \tag{1.10}$$

with initial condition $U(0) = \mathbb{I}$. The formal solution is

$$U(t) = \hat{T} \exp\Big\{ - \frac{i}{\hbar} \int_0^t H(t')dt' \Big\}, \tag{1.11}$$

where $\hat{T}$ denotes time ordering. Now, starting at $t = 0$ from the initial ground state $|\Psi_0^{(0)}\rangle$, the evolved state is given by

$$|\Psi(t)\rangle = U(t)|\Psi_0^{(0)}\rangle. \tag{1.12}$$

Whenever the adiabatic theorem holds, this evolved state $|\Psi(t)\rangle$, would be, at each time, the instantaneous ground state of the time-dependent Hamiltonian $H(t)$, but as soon as we are getting closer and closer to the QCP, since the vanishing of the energy gap leads to a breackdown of the adiabatic theorem, no matter how slow is the driving protocol, eventually

$$|\Psi(t_{end})\rangle \neq |\Psi_0^{(1)}\rangle \tag{1.13}$$

at the end of the whole evolution.

1.2.1 Loss of adiabaticity measures

As we have traced out in the previous section, that the presence of a QCP should completely invalidate the adiabatic theorem and this is actually due to the closure of the gap at the critical point. This implies that the closer the system is driven to the QCP the less its evolved state is able to keep following the corresponding instantaneous ground state. All these considerations appear in a clear and simple fact: during the evolution close to the QCP a production of excitations (with respect to the instantaneous adiabatic ground state) is unavoidable. In other words, the state at the end of the evolution protocol $|\Psi(t_{end})\rangle$ will differ from the target state $|\Psi_0^{(1)}\rangle$. Obviously, the difference between these two states will depend somehow on the choice of the driving protocol as well as on its duration t_{end}.

The first crucial point is to identify appropriate observables suitable to measure the loss of adiabaticity of the system. Obviously, depending on the model we are working with, there may be observables more convenient than other ones. One of the quite natural way to characterize the loss of adiabaticity is by looking at the “heating" of the system, that is simply considering the residual energy

$$E_{res} = E_{end} - E_0^{(1)} \tag{1.14}$$

where $E_0^{(1)}$ is the ground state energy of the final Hamiltonian H_1 and

$$E_{end} = \langle \Psi(t_{end}) | H_1 | \Psi(t_{end}) \rangle \tag{1.15}$$

is the expectation value of the final Hamiltonian in the evolved state $|\Psi(t_{end})\rangle$. It is clear that E_{res} will depend on the evolution protocol and it is easy to guess that the slower is the evolution the smaller the residual energy.

Actually, the introduction of the residual energy as an optimal observable for measuring the loss of adiabaticity is useful from an experimental point of view, where it is often easier to access to the heat pumped into the system during the evolution. However, at least from a theoretical point of view, an obvious and natural way to quantify the deviation from the adiabatic evolution is to compute the so-called fidelity:

$$\mathcal{F} = |\langle \Psi_0^{(1)}(t_{end}) | \Psi(t_{end}) \rangle|^2. \tag{1.16}$$

Obviously $\mathcal{F} \in [0, 1]$ and as long as the evolution is almost adiabatic one has $\mathcal{F} \sim 1$.

The quantities that we have just introduced are quite general and could be used in whatever physical model we want. Nevertheless, we can often get information on the loss of adiabaticity of the system by counting the number of excitations that the evolved state carries with respect to the adiabatic ground state. This is the reason why we finally introduce the so-called density of defects ρ.

In particular, the quantum Ising chain, which is considered in this thesis, is described by a quadratic Hamiltonian which can be diagonalized, at each time, by introducing diagonal quasi-particles excitations $\eta_q^\dagger(t)$ $(\eta_q(t))$[1]. It turns out that, for any value of the driving parameter, i.e. at each time, the adiabatic ground state of the system is the vacuum state of such excitations. In this case the defect density will be simply given by counting the excitations present on the final evolved state:

$$\rho = \frac{1}{L} \sum_{q=1}^{L} \langle \Psi(t_{end}) | \eta_q^\dagger(t_{end}) \eta_q(t_{end}) | \Psi(t_{end}) \rangle \tag{1.17}$$

where L is the size of the chain. It is straightforward to show that for an homogeneous Ising chain, when the ending point is deep in the ferromagnetic phase the defects are simply given by the kinks separating up and down domains. The previous definition reduces to

$$\rho = \frac{1}{L} \sum_{i=1}^{L} \langle \Psi(t_{end}) | \frac{1 - \sigma_i^x \sigma_{i+1}^x}{2} | \Psi(t_{end}) \rangle \tag{1.18}$$

where σ_i^x are the Pauli operators.

We want to stress here that, in the case we have considered in this thesis, since the transverse magnetic field is no more homogeneous, the basic excitations over the ground state are no longer kinks, nevertheless the number of defects is still given by summing over the quasi-particle excitations (see Chapter 4).

1.2.2 Kibble-Zurek Mechanism

The Kibble-Zurek Mechanism (KZM) was originally introduced by Kibble and Zurek in order to describe the defect generation across a classical phase transition [Kib76, Kib80, Zur85]. In

---

[1] Here the time dependence of the creation and annihilation operators is parametric.

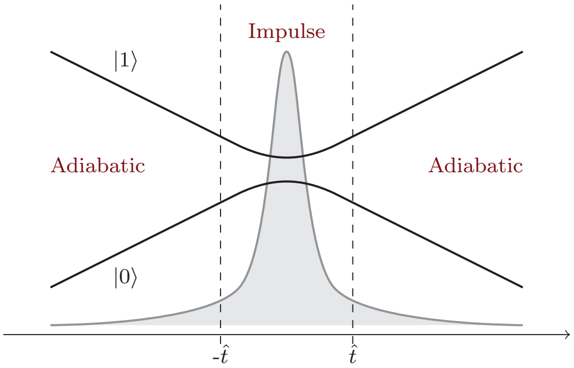

Figure 1.4: Relaxation time scale from KZ theory for a finite-size system; notice that the gap still survives. $\hat{t}$ represents the freeze-out time. Of course, for a gapless system, transition probability diverges and there is no way to completely remove the impulse regime.

particular, it was used in cosmology to describe the generation of defects during the expansion of the universe after the Big-Bang. A few decades after it was also applied to quantum phase transitions [ZDZ05]. Such an argument basically takes its roots on simple scaling considerations and turns out to be an appropriate tool for describing the non-equilibrium properties of a quantum system in terms of its equilibrium scaling properties close to the QCP.

According to KZM, as long as the system is sufficiently far away from the critical point, its characteristic relaxation time should be small enough to allow the system to quickly react to the variation of the Hamiltonian. As we have done in the previous paragraphs, we always assume that the system is initially prepared in the ground state of a given initial Hamiltonian. Then, in the early instants of the evolution (adiabatic regime) the system state evolves adiabatically being given at each time by the instantaneous adiabatic ground state of the time-dependent Hamiltonian. However as the system approaches the QCP its relaxation time starts to dangerously increase *critical slowing down*. Therefore, there will be an instant (the so-called freeze-out time, $\hat{t}$ in Figure 1.4) after which the system will no longer be able to react to the external changes. At that moment the evolution switches from the adiabatic regime to an impulse regime in which the system state freeze out.

Once we have passed the critical region, when the system will be again far enough away from the critical point, the dynamics will regain its adiabatic character and the state will restart its adiabatic evolution, but from the early instant frozen state.

In other words, what KZM suggests is that the adiabatic condition breaks down when the characteristic time of the variations of the Hamiltonian is of the same order of the relaxation time, given by the inverse of the instantaneous gap Δ. Just for specializing what we said, let's suppose a continuum quantum phase transition driven by the dimensionless parameter g. At the QCP ($g = 0$), separating the ordered from the disordered phase, the gap exhibits the scaling behavior $\Delta = |g|^{z\nu}$. Moreover, let's also suppose that we can linearize the time dependence in a neighborhood of the phase transition ($g = 0$):

$$g = vt \tag{1.19}$$

where v represents the evolution rate. Then the freeze-out time is defined by

$$\frac{g(\hat{t})}{\dot{g}(\hat{t})} = \hat{t} \sim \Delta(\hat{t})^{-1} = |g(\hat{t})|^{-z\nu}, \tag{1.20}$$

leading to

$$\hat{t} \sim v^{-z\nu/(1+z\nu)}. \tag{1.21}$$

We can estimate the defect density ρ by using the inverse of the typical volume at the freezing time. One has then

$$\rho \sim \xi(\hat{t})^{-d} \sim |g(\hat{t})|^{d\nu} \sim v^{d\nu/(1+z\nu)} \tag{1.22}$$

where d is the space dimension.

This last formula has been checked on various models, using both analytical and numerical methods [ZDZ05, Pol05, Dzi05, CL06, Dam05, DZ06, DZ07] and has been also verified experimentaly [SHL$^+$06]. Furthermore, a great effort was also spent to generalize and check the KZM in different contexts [DLZ99, DR10b, SSM08, GBP08, BP08]. Part of the work presented in this thesis is devoted to the extension of this formula to inhomogeneous quantum phase transitions (see Chapter 4).

1.2.3 Perturbative approach

In this paragraph we briefly review an alternative scaling analysis of the loss of adiabaticity based on the adiabatic perturbation theory. Such a picture was recently used in the context of defect generation by Polkovnikov in [Pol05]. This approach uses the well-known adiabatic perturbative approximation which was developed at the beginning of quantum mechanics [Mes62]. The essential idea is that a time-dependent Hamiltonian can be diagonalized at each time, obtaining the adiabatic eigenstates $|k(t)\rangle$ and eigenenergies $E_k(t)$, which are the solution of the time-independent Schrödinger equation with $\mathcal{H}(t)$ depending on t like a parameter:

$$\mathcal{H}(t)|k(t)\rangle = E_k(t)|k(t)\rangle. \tag{1.23}$$

Supposing that the system is initially prepared in the instantaneous ground state (the vacuum state in the Ising model) of the Hamiltonian $\mathcal{H}(t_0)$, $|\Psi(t_0)\rangle = |0(t_0)\rangle$, at time $t > t_0$ the unitarily evolved state is then given by $|\Psi(t)\rangle = \mathcal{U}(t,t_0)|0(t_0)\rangle$, where the time evolution operator is

$$\mathcal{U}(t,t_0) = \hat{\mathrm{T}} \exp -i \int_{t_0}^{t} ds \mathcal{H}(s), \tag{1.24}$$

and $\hat{\mathrm{T}}$ denotes time ordering.

If the Hamiltonian evolves slowly enough (adiabatic limit), it is useful to develop the evolved state $|\Psi(t)\rangle$ in a power series in the reference frame of the adiabatic eigenstates of the Hamiltonian; the development is then characterized by the transition amplitudes between different adiabatic eigenstates each of them connected by a true adiabatic evolution in the instantaneous state wherein the system belongs before a transition occurs [MMP06]. Thus, up to the first order correction, one has

$$|\Psi(t)\rangle \approx \mathrm{e}^{-i\int_{t_0}^{t} ds E_0(s)} \left[|0(t)\rangle + \sum_{k\neq 0} |k(t)\rangle \int_{t_0}^{t} dt' \langle \dot{k}(t')|0(t')\rangle \mathrm{e}^{-i\int_{t'}^{t} ds\delta\omega_{k0}(s)} \right], \tag{1.25}$$

with Bohr frequency $\delta\omega_{k0}(t) = E_k(t) - E_0(t)$.

The first term is the usual adiabatic result: the state is the instantaneous ground-state apart from a global dynamical phase factor. The second term contribution represents an adiabatic evolution in the initial ground-state up to the transition $|0\rangle \to |k\rangle$ at time t', followed again by an adiabatic evolution in the state $|k\rangle$ up to the final time t. The result is integrated over all the possible dynamical paths connecting the initial to the final time, by considering also all the possible final states. For a simple derivation of the adiabatic perturbative expansion see Appendix A.

The amplitude $\langle\dot{k}(t)|q(t)\rangle$ can be somehow rewritten in a different way. Indeed, taking the time derivative of the complex conjugate of (1.23) we have $\langle\dot{k}(t)|\mathcal{H}(t) + \langle k(t)|\partial_t\mathcal{H}(t) = \langle\dot{k}(t)|E_k(t) + \langle k(t)|\dot{E}_k(t)$, then projecting on the instantaneous basis vector $|q(t)\rangle$ and using the orthogonality relation $\langle k(t)|q(t)\rangle = \delta_{kq}$, we have

$$\langle\dot{k}(t)|q(t)\rangle = \frac{\langle k(t)|\partial_t\mathcal{H}(t)|q(t)\rangle}{E_k(t) - E_q(t)}, \text{ for } k \neq q. \tag{1.26}$$

From this relation we can argue that the validity of the adiabatic approximation is connected to the scale on which the Hamiltonian varies compared to the instantaneous Bohr frequency.

Now we specialize the calculation to the simplest case of linearly driven quantum system across the QCP (at $t = 0$). We suppose that the evolution goes from $t = -\infty$ to $t = \infty$ with driving parameter $g = vt$, therefore $\partial_t\mathcal{H}(t) = v\partial_g\mathcal{H}(g)$, and after changing the integration variables, in the limit of slow quench ($v \ll 1$), we can keep only the first term in the expansion. The density of defect is simply given by summing the transition probabilities $|\langle k(g)|\Psi(g)\rangle|^2$ over all the adiabatic eigenstates $|k(g)\rangle$ different from the adiabatic ground state; projecting (1.25) on $\langle k(g)|$ and summing over $k \neq 0$ one has

$$\rho \simeq \sum_{k\neq 0} \left| \int_{-\infty}^{\infty} dg \frac{\langle k(g)|\partial_g\mathcal{H}(g)|0(g)\rangle}{\delta\omega_{k0}(g)} \mathrm{e}^{\frac{i}{v}\int^g dg'\delta\omega_{k0}(g')} \right|^2. \tag{1.27}$$

Considering an uniform d-dimensional system, we can recast the previous sum as an integral in the momentum space

$$\rho \simeq \int \frac{d^dk}{(2\pi)^d} \left| \int_{-\infty}^{\infty} dg \frac{\langle k(g)|\partial_g\mathcal{H}(g)|0(g)\rangle}{\delta\omega_{k0}(g)} \mathrm{e}^{\frac{i}{v}\int^g dg'\delta\omega_{k0}(g')} \right|^2. \tag{1.28}$$

Knowing that at the transition the energetic gap behaves as $\Delta \sim |g|^{z\nu}$, from general scaling arguments one has [Sac00]

$$\delta\omega_{k0}(g) = g^{z\nu}\Omega(g^{z\nu}/k^z) \tag{1.29}$$

with

$$\Omega(x) \sim \left\{ \begin{array}{ccc} x^{-1} & \text{for} & x \ll 1 \\ 1 & \text{for} & x \gg 1 \end{array} \right., \tag{1.30}$$

which implies $\delta\omega_{k0} \sim \Delta$ for $k \to 0$, and recasts for $g \ll 1$, the homogeneous critical dispersion relation $\delta\omega_{k0} \sim k^z$ of the lower part of the spectrum [Sac00]. Then, using the rescaled variable $y = g^{z\nu}/k^z$, one has

$$z\nu\frac{dg}{g} = \frac{dy}{y} \Longrightarrow dg = \frac{k^{1/\nu}}{z\nu y^{1+1/z\nu}}dy. \tag{1.31}$$

Thus, we can recast the integral of the phase into

$$\begin{aligned} i\tau\int^g dg'\delta\omega_{k0}(g') &= \frac{i}{v}\int^g dg' g'^{z\nu}\Omega(g'^{z\nu}/k^z) \\ &= \frac{i}{v}\int^y dy' k^z y'\Omega(y')\frac{k^{1/\nu}y'^{-1-1/z\nu}}{z\nu} \\ &= v^{-1}k^{z+1/\nu}f(y). \end{aligned} \tag{1.32}$$

The matrix element, assuming [Sac00] $\langle k(g)|\partial_g \mathcal{H}(g)|0(g)\rangle = g^{z\nu-1}G(g^{z\nu}/k^z)$, is rewritten

$$\frac{\langle k(g)|\partial_g \mathcal{H}(g)|0(g)\rangle}{\delta\omega_{k0}(g)}dg = \frac{G(y)}{\Omega(y)}\frac{dg}{g} = \frac{G(y)}{\Omega(y)}\frac{dy}{z\nu y} \equiv V(y)dy. \tag{1.33}$$

To remove the dependence on v from the exponent one introduces the change of variable $q = kv^{-\nu/(1+z\nu)}$ with $dk = v^{\nu/(1+z\nu)}dq$. Finally one obtains for the defect density

$$\rho \sim Cv^{d\nu/(1+z\nu)} \tag{1.34}$$

where C is a non-universal constant and the scaling of (1.22) is recovered. Power-law quenches was considered in [SSM08] as a generalization of such a perturbative approach. Moreover, this analysis has been properly used to construct an optimal power-law passage across the QCP of the homogeneous Ising model [BP08]. In this thesis we extend such analysis to non-linear adiabatic quenches in inhomogeneous quantum critical systems by using trap-size scaling arguments (see Chapter 4)[PKT07, CV09, CV10, CKT09, CK10, CK11].

1.2.4 Landau-Zener approximation

Both the KZM and the perturbative approach are based on similar scaling assumptions in the vicinity of the gap. The closure of the gap at the QCP is crucial for such arguments. Nevertheless, as we have often repeated throughout this chapter, for a finite-size system the critical gap stays finite. To take that into account, Zurek *et al* proposed in [ZDZ05] to calculate the maximal size $\tilde{L}$ a system can have in order to remain free of defects. The basic idea is then, once we have this maximal size as a function of the evolution rate v, the defect probability should be given by the inverse of the volume $\tilde{L}^d$.

The key point in that treatment is to describe the dynamics close to the avoided level-crossing by means of the Landau-Zener (LZ) approach [Zen32, LL03]. Assuming that the evolution starts at $t_i = -\infty$ and finishes at $t_f = \infty$, the Landau-Zener formula gives the excitation probability

$$P \simeq \exp -\frac{\pi\Delta^2}{2v}, \tag{1.35}$$

where Δ is the critical gap between the two levels. This probability can be connected to the Fidelity $\mathcal{F}$ achieved during the adiabatic evolution: $P \sim 1-\mathcal{F}$. For a fixed small generation of defects, supposing, as shown for the Ising chain in Figure 1.3 the finite-size scaling $\Delta \sim L^{-1}$, they obtained

$$\exp -\frac{\pi\tilde{L}^{-1}}{2v} \sim 1-\mathcal{F} \Rightarrow \tilde{L} \sim \sqrt{\frac{\pi}{2|\ln(1-\mathcal{F})|}}\, v^{-1/2}, \tag{1.36}$$

for the maximal length $\tilde{L}$. Using this result, the density of defects was deduced to be

$$\rho \sim \tilde{L}^{-d} \sim v^{d/2}, \tag{1.37}$$

that is the same result obtained from the KZM for the homogeneous Ising model.

Notwithstanding the previous arguments, the use of the LZ approach for describing the universal adiabatic dynamics near a QCP is a little bit subtler. Indeed, as extensively analyzed in the review [Dzi10], the LZ method has to be handled with more care. The first point is that the excitation probability strongly depends on the dynamical setting we choose: in spite of the previous exponential decay of the excitation probability as a function of the evolution rate, if the evolution starts (or finishes) exactly at the critical point, the probability shows the power-law asymptotic behavior $P \simeq v^2$. Moreover, even assuming that the exponential behavior is appropriate, whenever we are analyzing a homogeneous system of non-interacting fermions (the homogeneous Ising model falls in this category) we can map the dynamics to a set of independent LZ problems. Indeed, the Hamiltonian can be rewritten as a direct sum of two-level Hamiltonians enumerated by the quasimomentum k. Thus, for each k, the LZ formula gives

$$P(k) \simeq \exp -\frac{\pi \Delta^2(k)}{2v}. \tag{1.38}$$

The density of defects is obtained by integrating the previous probability over the quasi-momenta:

$$\rho \simeq \int \frac{d^d k}{(2\pi)^d} P(k). \tag{1.39}$$

If the system crosses an isolated critical point separating two gaped phases, then at the isotropic Fermi point k_F one has

$$\Delta^2(k) \sim |k - k_F|^{z_\Delta}, \tag{1.40}$$

leading, after integration, to

$$\rho \sim v^{d/z_\Delta}. \tag{1.41}$$

Finally, one recovers from this LZ theory the KZM prediction if and only if $z_\Delta = (1 + \nu z)/\nu$, which is actually the case for quenches crossing an isolated critical point [Dzi10].

Chapter 2

The XY quantum model

The homogeneous quantum XY model is an integrable model that was originally treated by Lieb *et al.* [LSM61] in the early 60s. In 1971 Barouch and McCoy, in the thermodynamical limit, determined the behavior of the two-points correlation functions and analyzed some non-equilibrium aspects [BMD70, BM71a, BM71b, BMA71].

Following the same guidelines, we start this chapter by introducing the homogeneous one-dimensional quantum XY model, and by looking at some interesting properties of such a model. The XY-model Hamiltonian for L interacting 1/2-spins, with open boundary conditions, is

$$H = -\frac{1}{2}\sum_{n=1}^{L-1}\left(J_x\sigma_n^x\sigma_{n+1}^x + J_y\sigma_n^y\sigma_{n+1}^y\right) - \frac{h}{2}\sum_{n=1}^{L}\sigma_n^z, \tag{2.1}$$

where σ_n^α are the Pauli matrices, h is the magnetic field in the $\hat{z}$ direction, J_x and J_y are the coupling constants parametrized as

$$J_x = \frac{1+\gamma}{2}, \quad J_y = \frac{1-\gamma}{2}, \quad \gamma \in [-1,1], \tag{2.2}$$

with the anisotropy parameter γ. The value $\gamma = 0$ corresponds to the XX-model with continuum $U(1)$ symmetry where the total magnetization $M = \sum_n \sigma_n^z$ is a conserved quantity. It do not show an ordered-disordered phase transition, nevertheless, we can identify two different regions: a paramagnetic phase and a critical phase. In the critical phase the model exhibits a divergency of the correlation length [KT73]. In the opposite case ($\gamma = 1$) the Hamiltonian describes the quantum Ising model that corresponds to the extreme anisotropic limit of the classical two-dimensional Ising model on the square lattice [FS78, Kog79]. The quantum Ising model shows a quantum critical point separating a paramagnetic phase from a ferromagnetic one.

2.1 Generalities

Now, we will briefly review some properties of the homogeneous XY-model summarized in its phase diagram (see Figure 2.1). We will relate the peculiarities of the different regions of the phase diagram to the one-particle dispersion law of the system.

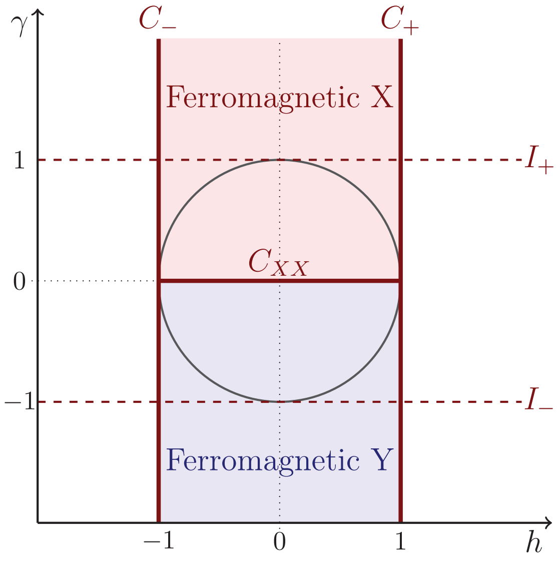

Figure 2.1: Phase diagram for the XY-model: we show with straight lines the XX critical regions (C_{XX}) and $|h| = 1$ ($C\pm$). The dotted lines $I_\pm$ indicate the Ising region.

As we already said, the XY-model is analytically solvable and the positive branch of its one-particle energy spectrum is given by [LSM61, Kar06, Pla08, Fag08]

$$\epsilon_q = \sqrt{(h + \cos q)^2 + \gamma^2 \sin^2 q}, \tag{2.3}$$

where the quasi-fermion momentum q is restricted in $[0, \pi]$. Indeed, as we will briefly see in the next section, the ground state of the XY-model is the vacuum state of the diagonal quasi-fermion annihilation operators, and the complete spectrum exhibits the symmetry $\epsilon_{q+\pi} = -\epsilon_q$.

The XY-model is gapless if an excited many-body state appears with the same energy as the ground state. This statement is equivalent to saying that there must be at least a quasi-momentum q^* for which $\epsilon_{q^*} = 0$. By exploiting the dispersion law we can reconstruct the phase diagram as we have depicted in Figure 2.1.

The two dashed red lines I_+ and I_- correspond both to the Ising quantum model ($\gamma = \pm 1$). In the I_+ the spin-spin couplings are in the $\hat{x}$ direction, while in the I_- spins are coupled along the $\hat{y}$ direction. Obviously, by varying the parameter γ, we can change the global behavior of the system which could eventually show a preference for $\hat{x}$ or $\hat{y}$ direction.

More important, analyzing the excitation spectrum, we can identify two different critical regions: the $C_\pm$ regions and the C_{XX} region (full red lines on Figure 2.1). The regions $C_\pm$, corresponding to $|h| = 1$, are the one-dimensional quantum Ising critical regions. Indeed, it is straightforward to show that, in this region, the gap closes. Moreover, in these regions the absolute value of the velocity of the quasi-particle $|v| = |\partial\epsilon/\partial q|$ depends on h and shows one maximum for $\gamma \in [-1, 1]$. The regions $C_\pm$ belong to the same universality class of free massless fermions in $1+1$ dimensions and are characterized by the correlation length critical exponent $\nu = 1$ and the dynamical critical exponent $z = 1$[1].

---

[1] Indeed, for $\gamma = 1$, at the critical quasi-momentum $q^* = \pi$, one has $\epsilon_\pi(h) = |h - 1|$ giving $z\nu = 1$; then, exactly at the critical point $h = 1$ and developing the dispersion relation around $q^* = \pi$ one obtains $\epsilon_q(h = 1) \simeq |q - \pi|$, therefor $z = 1$, and consequently $\nu = 1$.

The two lines $C_\pm$ separate the paramagnetic region ($|h| > 1$) from the ferromagnetic one (|h|<1). For distinguishing this two phases (wherein spins behave differently, preferring to align along the magnetic field ($|h| > 1$), or along the direction of the microscopical couplings ($|h| < 1$)) we can introduce the order parameter $\lim_{n\to\infty}\langle\sigma_l^x\sigma_{l+n}^x + \sigma_l^y\sigma_{l+n}^y\rangle$ which is different from zero only when $|h| < 1$. If we want to distinguish the X-ferromagnetism from the Y-ferromagnetism, we can introduce $\lim_{n\to\infty}\langle\sigma_l^x\sigma_{l+n}^x\rangle$ which is non vanishing only for $\gamma > 0$ (Ferromagnetic X region), and $\lim_{n\to\infty}\langle\sigma_l^y\sigma_{l+n}^y\rangle$ which is different from zero only for $\gamma < 0$ (Ferromagnetic Y region).

The C_{XX} is a continuous transition line wherein the system exhibits a critical behavior. Indeed, on this line the system is gapless. This region is the so-called XX quantum critical region and belongs to the universality class of free bosons in 1+1 dimension. The critical exponent characterizing the C_{XX} line are $\nu = 1/2$ and $z = 2$[2]. Furthermore, unlike the previous critical lines $C_\pm$, here the absolute value of the velocity $|v|$ does not depend on h.

In Figure 2.1 we have also depicted the region inside the circle $|h|^2 + |\gamma|^2 = 1$. The peculiarity of this region sits in the particular representation of the many-body ground state: it turns out that the ground state factorizes completely into the tensorial product of local spin states. An example is the point $h = 0, \gamma = 1$ which we have yet considered in the previous chapter: in this case the Hamiltonian reduces to $H = -(1/4)\sum_n \sigma_n^x\sigma_{n+1}^x$ leading to the two possible ground state $\bigotimes_n |\rightarrow\rangle_n$ or $\bigotimes_n |\leftarrow\rangle_n$. Another example could be the point $h = 1, \gamma = 0$ wherein the Hamiltonian reduces to $H \propto -(1/4)\sum_n \sigma_n^x\sigma_{n+1}^x + \sigma_n^y\sigma_{n+1}^y - (1/2)\sum_n \sigma_n^z$ where the ground state is the perfect Mott-Insulating state $\bigotimes_n |\uparrow\rangle_n$. This special circle indicates a transition from an ordinary ferromagnetic phase (outside the circle) to an oscillatory one (inside the circle) [BM71a, BM71b, Ovc07]. Exactly at the boundary $|h|^2 + |\gamma|^2 = 1$ the correlation functions have been analytically calculated [FA05].

Experimental evidences — The XY-model is a simple good theoretical laboratory for understanding more complex models as well as for giving explanations to some experimental realizations. For example, the insulators $CsCoBr_3$ and $CsCoCl_3$ have been extensively studied as examples of one-dimensional Ising magnets. Indeed, in these systems the Co atoms behave in such a way as to recreate an antiferromagnetic Ising spin chain [Sac00]. Although the effective Hamiltonian of these systems is not exactly the Ising Hamiltonian, these systems exhibit many properties quite identical to those exhibited by the Ising model. More recently, experimental evidence of magnetic properties on $CsCoCl_4$ materials [KCT+02] have been understood by means of the XY-model.

2.2 Canonical diagonalization

Now we come back to the XY-model Hamiltonian and we briefly sketch the canonical diagonalization. Indeed, the Hamiltonian (2.1) can be exactly mapped on a free fermion model [LSM61, Kar06, Pla08]. The first step consists in introducing the ladder operators

$$\sigma_n^\pm = \frac{\sigma_n^x \pm i\sigma_n^y}{2}, \tag{2.4}$$

that satisfy, at the same site, the anticommutation rules $\{\sigma_n^+, \sigma_n^-\} = 1$, otherwise, by construction, they commute at different sites. The second step consists in using the Jordan-

---

[2] In this case, for $\gamma = 0$, the dispersion relation reads $\epsilon_q(h) = |h + \cos q|$ and it shows that for each $h \in [-1, 1]$ there is a critical quasi-momentum q^* wherein $h = h^* \equiv -\cos q^*$. Once again, near a given h^* the dispersion relation predicts $z\nu = 1$. Now, looking at the transition point $h = 1$ from the pamagnetic to the C_{XX} phase and developing the dispersion relation around $q^* = \pi$ one founds $\epsilon_q \simeq |q - \pi|^2$ giving $z = 2$ and therefore $\nu = 1/2$.

Wigner transformation [JW28] in oder to obtain a description in terms of true fermionic operators. To do that, one can introduce the Clifford operators

$$\begin{aligned} \Gamma^1_n &= \prod_{j=1}^{n-1}(-\sigma^z_j)\sigma^x_n, \\ \Gamma^2_n &= -\prod_{j=1}^{n-1}(-\sigma^z_j)\sigma^y_n, \end{aligned} \tag{2.5}$$

generating a real ($(\Gamma^\mu_n)^\dagger = \Gamma^\mu_n$) Clifford algebra:

$$\{\Gamma^\mu_n, \Gamma^\nu_m\} = 2\delta_{\mu\nu}\delta_{nm}, \quad \forall\,\nu,\mu = 1,2; \quad \forall\,n,m = 1,\ldots,L. \tag{2.6}$$

Notice that the Clifford operators are un-normalised Majorana fermions. The different terms in the original Hamiltonian are re-expressed in terms of Clifford operators as

$$\begin{aligned} \sigma^z_n &= i\Gamma^1_n\Gamma^2_n, \\ \sigma^x_n\sigma^x_{n+1} &= -i\Gamma^2_n\Gamma^1_{n+1}, \\ \sigma^y_n\sigma^y_{n+1} &= i\Gamma^1_n\Gamma^2_{n+1}. \end{aligned} \tag{2.7}$$

The quadratic form of the Hamiltonian in terms of Clifford operators ensures the integrability of the model. Actually this approach is not useful for handling more general quantum spin chains. For example, in the Heisenberg model, interaction terms in the z direction $\sigma^z_n\sigma^z_{n+1} \propto \Gamma^1_n\Gamma^2_n\Gamma^1_{n+1}\Gamma^2_{n+1}$ lead to interacting fermions. Moreover, due to the non-locality of the Jordan-Wigner transformations, longer range interactions, such as $\sigma^x_n\sigma^x_{n+p}$, or magnetic fields in the $\hat{x}$ or $\hat{y}$ directions break the integrability of the model.

Now, introducing the $2L$-components row vector operator

$$\mathbf{\Gamma}^\dagger = \begin{pmatrix} \mathbf{\Gamma}^{1\dagger} & \mathbf{\Gamma}^{2\dagger} \end{pmatrix}, \quad \mathbf{\Gamma}^{\mu\dagger} = (\Gamma^{\mu\dagger}_1 \cdots \Gamma^{\mu\dagger}_L) \tag{2.8}$$

one can write the Hamiltonian in the form

$$H = \frac{1}{4}\mathbf{\Gamma}^\dagger\mathbf{T}\mathbf{\Gamma}, \tag{2.9}$$

which defines a $2L \times 2L$ Hermitian matrix $\mathbf{T}$:

$$\mathbf{T} = \begin{pmatrix} \emptyset & \mathbf{C} \\ \mathbf{C}^\dagger & \emptyset \end{pmatrix}, \tag{2.10}$$

with $\mathbf{C}$ given by

$$\mathbf{C} = -i\begin{pmatrix} h & J_y & & & \\ J_x & h & J_y & & \\ & J_x & \ddots & \ddots & \\ & & \ddots & \ddots & J_y \\ & & & J_x & h \end{pmatrix}. \tag{2.11}$$

Introducing the unitary matrix ($\mathbf{V}^\dagger\mathbf{V} = \mathbb{I}_{2L\times 2L}$)

$$\mathbf{V} = \begin{pmatrix} V_1 & \cdots & V_{2L} \end{pmatrix}, \tag{2.12}$$

with the parametrization

$$V_q = \frac{1}{\sqrt{2}} \begin{pmatrix} \phi_q \\ -i\psi_q \end{pmatrix} \tag{2.13}$$

we obtain from the eigenvalue equation $\mathbf{T}V_q = \epsilon_q V_q$ the following coupled equations[3]:

$$\begin{aligned} -i\mathbf{C}\psi_q &= \epsilon_q \phi_q, \\ \mathbf{C}^\dagger \phi_q &= -i\epsilon_q \psi_q. \end{aligned} \tag{2.14}$$

We can notice here that these equations are invariant under the simultaneous change $\epsilon_q \to -\epsilon_q$ and $\psi_q \to -\psi_q$. So, to each positive eigenvalue, $\epsilon_q \geqslant 0$, corresponds a negative eigenvalue $\epsilon_{q'} = -\epsilon_q$ with the associated eigenvector $V_{q'} = (\sigma^{\mathbf{z}} \otimes \mathbb{I}_{L\times L})V_q$. In practice, due to the symmetry properties of the matrix $\mathbf{T}$, its diagonal form is

$$\mathbf{\Lambda} \equiv \mathbf{V}^\dagger \mathbf{T} \mathbf{V} = \sigma^{\mathbf{z}} \otimes \mathbf{E}, \tag{2.15}$$

where

$$\sigma^{\mathbf{z}} = \begin{pmatrix} 1 & 0 \\ 0 & -1 \end{pmatrix}, \quad \text{and} \quad \mathbf{E} = \begin{pmatrix} \epsilon_1 & & \\ & \ddots & \\ & & \epsilon_L \end{pmatrix}. \tag{2.16}$$

From the Majorana field one can go to the diagonal Fermi representation thanks to the Bogoliubov transformation

$$\frac{1}{\sqrt{2}} \begin{pmatrix} \mathbf{\Gamma}^1 \\ \mathbf{\Gamma}^2 \end{pmatrix} = \mathbf{V} \begin{pmatrix} \eta \\ \eta^{\dagger T} \end{pmatrix}, \tag{2.17}$$

with

$$\eta = \begin{pmatrix} \eta_1 \\ \vdots \\ \eta_L \end{pmatrix}, \quad \eta^\dagger = \begin{pmatrix} \eta_1^\dagger & \cdots & \eta_L^\dagger \end{pmatrix}, \tag{2.18}$$

where the fermionic creation and annihilation operators $\eta_q^\dagger$, η_q satisfy the canonical anticommutation rules $\{\eta_q^\dagger, \eta_p\} = \delta_{qp}$. More explicitly, one has

$$\begin{aligned} \Gamma_n^1 &= \sum_{q=1}^{L} \phi_q(n) \left[\eta_q + \eta_q^\dagger\right], \\ \Gamma_n^2 &= -i\sum_{q=1}^{L} \psi_q(n) \left[\eta_q - \eta_q^\dagger\right], \end{aligned} \tag{2.19}$$

and the inverse relation

$$\begin{aligned} \eta_q &= \frac{1}{2}\sum_{n=1}^{L} \left\{\phi_q(n)\Gamma_n^1 + i\psi_q(n)\Gamma_n^2\right\}, \\ \eta_q^\dagger &= \frac{1}{2}\sum_{n=1}^{L} \left\{\phi_q(n)\Gamma_n^1 - i\psi_q(n)\Gamma_n^2\right\}, \end{aligned} \tag{2.20}$$

---

[3] From these equations it is straightforward to obtain two decoupled eigenvalue equations $\mathbf{C}\mathbf{C}^\dagger\phi_q = \epsilon_q^2\phi_q$, $\mathbf{C}^\dagger\mathbf{C}\psi_q = \epsilon_q^2\psi_q$; since $\mathbf{C}\mathbf{C}^\dagger$ and $\mathbf{C}^\dagger\mathbf{C}$ are real symmetric matrices, their eigenvectors can be chosen real and they satisfy completeness and orthogonality realtions.

that explicitly recast the Hamiltonian (2.9) in diagonal form. Indeed, from (2.9), using (2.17) one obtains

$$H = \frac{1}{2} \begin{pmatrix} \eta^\dagger & \eta^T \end{pmatrix} \mathbf{V}^\dagger \mathbf{T} \mathbf{V} \begin{pmatrix} \eta \\ \eta^{\dagger T} \end{pmatrix}, \tag{2.21}$$

and exploiting the diagonal form (2.15),

$$H = \frac{1}{2} \begin{pmatrix} \eta^\dagger & \eta^T \end{pmatrix} \begin{pmatrix} \mathbf{E} & \emptyset \\ \emptyset & -\mathbf{E} \end{pmatrix} \begin{pmatrix} \eta \\ \eta^{\dagger T} \end{pmatrix} = \frac{1}{2}\Big[\eta^\dagger \mathbf{E}\, \eta - \eta^T \mathbf{E}\, \eta^{\dagger T}\Big], \tag{2.22}$$

which can be explicitly rewritten, due to the anti-commutation relations, as

$$H = \sum_{q=1}^{L} \epsilon_q [\eta_q^\dagger \eta_q - 1/2] \tag{2.23}$$

where ϵ_q are the positive eigenvalues of $\mathbf{T}$. The ground state of H is consequently given by the η's vacuum state $|0\rangle$, with the usual properties $\eta_q|0\rangle = 0$, $\langle 0|\eta_q^\dagger = 0$, $q = 1 \dots L$ and with energy $E_0 = -\frac{1}{2}\sum_{q=1}^{L} \epsilon_q$.

2.3 Entanglement entropy

Before turning on the dynamical aspects of the XY model, we briefly introduce the concept of entanglement entropy in a bipartite system. Then, we specialize this concept to the XX spin chain, needed in Chapter 5.

Let us suppose a closed quantum system composed by two parts $\mathcal{A}$ and $\mathcal{B}$ with Hilbert space $\mathcal{H}_\mathcal{A}$ and $\mathcal{H}_\mathcal{B}$ respectively. The total Hilbert space in which the whole system lives is given by the tensorial product $\mathcal{H} = \mathcal{H}_\mathcal{A} \otimes \mathcal{H}_\mathcal{B}$. The pure bipartite state is not entangled if and only if it can be written as a tensor product of pure states of the parts

$$|\Psi_{AB}\rangle = |\Psi_A\rangle \otimes |\Psi_B\rangle. \tag{2.24}$$

Otherwise, for a generic pure state, one has the bipartite decomposition

$$|\Psi_{AB}\rangle = \sum_{\alpha,\beta} \varphi_{\alpha\beta} |\phi_\alpha^A\rangle |\phi_\beta^B\rangle, \tag{2.25}$$

where $\{|\phi_\alpha^A\rangle\}$ and $\{|\phi_\beta^B\rangle\}$ are two orthonormal basis of the Hilbert spaces $\mathcal{H}_\mathcal{A}$ and $\mathcal{H}_\mathcal{B}$ respectively. The state (2.25) is generally entangled and the measure of this entanglement can be extracted by introducing the von Neumann entropy S_A of the part $\mathcal{A}$

$$S_A = -\mathrm{Tr}\{\rho_A \ln \rho_A\}, \tag{2.26}$$

where ρ_A is the reduced density matrix of the system $\mathcal{A}$

$$\rho_A = \mathrm{Tr}_B\{|\Psi_{AB}\rangle\langle\Psi_{AB}|\}. \tag{2.27}$$

Notice that, whenever O_A is a local observable acting only in $\mathcal{A}$, the expectation value is given by $\langle O_A \rangle = \mathrm{Tr}\{O_A \rho_A\}$.

Now we specialize to the XX-model case. Instead of using the Majorana operators, the XX-model Hamiltonian can be rewritten by means of the real lattice fermion operators

$$c_i = \prod_{j=1}^{i-1} (-\sigma_j^z)\sigma_i^-, \quad c_i^\dagger = \prod_{j=1}^{i-1} (-\sigma_j^z)\sigma_i^+, \tag{2.28}$$

leading to

$$H_{XX} = \sum_{i,j} c_i^\dagger T_{ij} c_j. \tag{2.29}$$

The eigenstates of this Hamiltonian are Slater determinants. Denoting $|\Psi\rangle$ one of such states and $C_{nm} = \langle c_n^\dagger c_m \rangle$ the two-point correlation matrix in this state, since $|\Psi\rangle$ is a Slater determinant, all the higher correlation functions can be expressed in terms of the two-point correlation functions [Pes03]. For example

$$\langle c_n^\dagger c_m^\dagger c_k c_l \rangle = \langle c_n^\dagger c_l \rangle \langle c_m^\dagger c_k \rangle - \langle c_n^\dagger c_k \rangle \langle c_m^\dagger c_l \rangle. \tag{2.30}$$

Now, if one considers a subsystem $\mathcal{A}$ with A sites, by definition the reduce density matrix has to reproduce all the expectation values of local operators acting in the subsystem. Thus, the two-point correlation matrix has to satisfy the equivalence

$$C_{nm} = \mathrm{Tr}\{c_n^\dagger c_m \rho_A\}, \quad \forall\, n, m \in \mathcal{A}, \tag{2.31}$$

and the higher correlations must factorize as before. It is possible to show that, according to Wick's theorem, this property holds if ρ_A is the exponential of a free-fermion operator [Pes03, CP01, LRV04, CH04], i.e.

$$\rho_A = \frac{1}{Z} \exp\Big\{ - \sum_{i,j} c_i^\dagger A_{ij} c_j \Big\}, \tag{2.32}$$

where Z is a normalization constant such that $\mathrm{Tr}\{\rho_A\} = 1$. Introducing the eigenfunctions $\phi_k(i)$ of A_{ij} with eigenvalues λ_k, the transformations to diagonal fermion operators ξ_k read

$$c_i = \sum_k \phi_k(i) \xi_k, \tag{2.33}$$

and ρ_A becomes

$$\rho_A = \frac{1}{Z} \exp\Big\{ - \sum_k \lambda_k \xi_k^\dagger \xi_k \Big\}. \tag{2.34}$$

Using (2.34) in (2.31) yields

$$C_{nm} = \sum_{k,q} \phi_k^*(n) \frac{\delta_{kq}}{1 + \mathrm{e}^{\lambda_k}} \phi_q(m) = \sum_k \frac{\phi_k^*(n) \phi_k(m)}{1 + \mathrm{e}^{\lambda_k}}. \tag{2.35}$$

Therefore, the eigenvalues of the matrix A_{ij} are related to the eigenvalues ζ_k of the correlation matrix restricted to the part $\mathcal{A}$ by

$$\zeta_k = \frac{1}{1 + \mathrm{e}^{\lambda_k}}. \tag{2.36}$$

Once the exponential form of ρ_A is known, it is straightforward to calculate the entanglement entropy. Indeed, one has

$$\begin{aligned} S_A &= -\mathrm{Tr}\{\rho_A \ln \rho_A\} = -\mathrm{Tr}\{\rho_A \ln \frac{1}{Z} \mathrm{e}^{-\sum_k \lambda_k n_k}\} \\ &= \sum_k \lambda_k \mathrm{Tr}\{n_k \rho_A\} + \ln Z, \end{aligned} \tag{2.37}$$

where $n_k = \xi_k^\dagger \xi_k$. Now, using $Z = \mathrm{Tr}\{\mathrm{e}^{-\sum_k \lambda_k n_k}\} = \prod_k (1+\mathrm{e}^{-\lambda_k})$ and $\mathrm{Tr}\{n_k \rho_A\} = \langle n_k \rangle = 1/(1+\mathrm{e}^{\lambda_k})$, one obtains

$$S_A = \sum_k \left[\frac{\lambda_k}{1+\mathrm{e}^{\lambda_k}} + \ln(1+\mathrm{e}^{-\lambda_k}) \right], \tag{2.38}$$

which, rewritten in terms of the eigenvalues of the restricted correlation matrix, reads

$$S_A = -\sum_k \left[\zeta_k \ln \zeta_k + (1-\zeta_k) \ln(1-\zeta_k) \right], \tag{2.39}$$

where ζ_k are interpreted as the diagonal occupation numbers. Finally, if we are interested in the temporal evolution of the entanglement entropy, the only thing one needs to do is to perform the evolution of the correlation matrix, as explained in the following sections. Then, $S_A(t)$ will be still given by the previous formula, but now, with eigenvalues $\zeta_k(t)$ calculated from the reduced correlation matrix at time t.

2.4 Dynamics

Now, we turn to the out-of-equilibrium dynamical behavior of the free fermionic chains. It is well known that in quantum mechanics the temporal evolution of a closed system is governed by the Schrödinger equation

$$i\frac{d}{dt}|\Psi(t)\rangle = H|\Psi(t)\rangle, \tag{2.40}$$

where H is the Hamiltonian of the system (henceforth we assume $\hbar = 1$). In this representation the time dependence is explicitly carried out by the state vector $|\Psi(t)\rangle$. Moreover, if the closed system is described by the density operator $\rho(t)$, the Schrödinger equation leads to

$$i\partial_t \rho(t) = [H, \rho(t)]. \tag{2.41}$$

Whenever the Hamiltonian is time independent, the evolution operator is given by

$$U(t) = \exp(-iHt), \quad U(t)U^\dagger(t) = U^\dagger(t)U(t) = \mathbb{I}, \tag{2.42}$$

and we can define, in the Scrhödinger representation, the time dependent density matrix

$$\rho(t) = U(t)\rho(0)U^\dagger(t), \tag{2.43}$$

generated from an initial state $\rho(0)$. Now, let us consider a time independent operator $\mathcal{A}$. By definition, the expectation value of such an operator at time t is given by

$$\langle \mathcal{A}(t) \rangle \equiv \mathrm{Tr}\{\rho(t)\mathcal{A}\} = \mathrm{Tr}\{\rho(0)\mathcal{A}(t)\}, \tag{2.44}$$

where the last equality comes from the cyclic property of the trace. In this way we have defined the Heisenberg representation of the operator $\mathcal{A}$:

$$\mathcal{A}(t) \equiv U^\dagger(t)\mathcal{A}\,U(t). \tag{2.45}$$

In the following we will use the Heisenberg representation in order to calculate the time evolution of the operators describing the XY-model.

Dynamics of Clifford operators — The XY Hamiltonian is diagonal using the η_q ($\eta_q^\dagger$) operators and, in the Heisenberg representation, the time evolution of such operators is given by

$$\eta_q(t) = U_q^\dagger(t)\eta_q U_q(t), \tag{2.46}$$

with $U_q(t) = \exp(-i\epsilon_q \eta_q^\dagger \eta_q t)$, and leads to

$$\begin{aligned} \eta_q(t) &= \mathrm{e}^{-i\epsilon_q t}\eta_q, \\ \eta_q^\dagger(t) &= \mathrm{e}^{i\epsilon_q t}\eta_q^\dagger. \end{aligned} \tag{2.47}$$

Since the Clifford operators Γ_n^μ are given by a linear combination of the fermionic operators η_q ($\eta_q^\dagger$), their temporal evolution is simply given through the transformation (2.17). At time t one has:

$$\frac{1}{\sqrt{2}}\left(\begin{array}{c} \mathbf{\Gamma}^1(t) \\ \mathbf{\Gamma}^2(t) \end{array}\right) = \mathbf{V}\left(\begin{array}{c} \eta(t) \\ \eta^{\dagger T}(t) \end{array}\right). \tag{2.48}$$

Using the matrix representation of (2.47) one obtains

$$\left(\begin{array}{c} \mathbf{\Gamma}^1(t) \\ \mathbf{\Gamma}^2(t) \end{array}\right) = \mathbf{V}\mathrm{e}^{-it\mathbf{\Lambda}}\mathbf{V}^\dagger \left(\begin{array}{c} \mathbf{\Gamma}^1 \\ \mathbf{\Gamma}^2 \end{array}\right) = \mathrm{e}^{-it\mathbf{T}}\left(\begin{array}{c} \mathbf{\Gamma}^1 \\ \mathbf{\Gamma}^2 \end{array}\right), \tag{2.49}$$

where $\mathbf{T}$ is given by (2.10). Explicitly, the components of (2.49) are given by the linear decomposition [Kar06]

$$\Gamma_n^\mu(t) = \sum_{\nu,m} \langle \Gamma_m^\nu | \Gamma_n^\mu \rangle \Gamma_m^\nu, \tag{2.50}$$

with the time-dependent contractions

$$\begin{aligned} \langle \Gamma_m^1 | \Gamma_n^1 \rangle_t &= \sum_q \phi_q(m)\phi_q(n)\cos(\epsilon_q t), \\ \langle \Gamma_m^1 | \Gamma_n^2 \rangle_t &= -\sum_q \phi_q(m)\psi_q(n)\sin(\epsilon_q t), \\ \langle \Gamma_m^2 | \Gamma_n^1 \rangle_t &= \sum_q \psi_q(m,)\phi_q(n)\sin(\epsilon_q t), \\ \langle \Gamma_m^2 | \Gamma_n^2 \rangle_t &= \sum_q \psi_q(m)\psi_q(n)\cos(\epsilon_q t). \end{aligned} \tag{2.51}$$

2.4.1 Time-dependent Hamiltonian

In Chapter 4 we focus our attention on the Ising spin chain driven in time across the critical point. In that case the Hamiltonian will explicitly depend on time. Thus, an interesting question is how to calculate, at least numerically, the time evolution of an observable when the Hamiltonian depends on time.

It turns out, of course, that also for time-dependent Hamiltonian we can numerically solve the Schrödinger equation. Suppose we prepare the chain in the ground state of $H(g(t))$ at time t_0, where the Hamiltonian depends on time through the parameter $g(t)$. We can extract many information (magnetization, energy profile, spin correlations) by using the Clifford operator correlation matrix. The usefulness of this representation stands in the independence of these operators from time (like a parameter). Then, assuming that the system, at time t_0, is in its ground state, we have

$$\langle \mathbf{\Gamma}\mathbf{\Gamma}^\dagger \rangle_{t_0} = \left(\begin{array}{cc} \langle \Gamma_m^1 \Gamma_n^1 \rangle_{t_0} & \langle \Gamma_m^1 \Gamma_n^2 \rangle_{t_0} \\ \langle \Gamma_m^2 \Gamma_n^1 \rangle_{t_0} & \langle \Gamma_m^2 \Gamma_n^2 \rangle_{t_0} \end{array}\right) = \mathbb{I} + i\left(\begin{array}{cc} \emptyset & \mathbf{G} \\ -\mathbf{G}^\dagger & \emptyset \end{array}\right) \tag{2.52}$$

where the matrix elements of $\mathbf{G}$ are

$$G_{mn} = \sum_q \phi_q(m, g(t_0))\psi_q(n, g(t_0)), \tag{2.53}$$

with $\phi_q(g(t_0))$ and $\psi_q(g(t_0))$ the Bogoliubov coefficients that diagonalize the Hamiltonian $H(g(t_0))$ at time t_0[4]. Splitting the continuum time evolution into N infinitesimal sudden quenches, the expectation of the Clifford correlation matrix at time t is given by

$$\langle \mathbf{\Gamma}\mathbf{\Gamma}^\dagger \rangle_t = \prod_{i=N}^{0} \mathcal{R}^T(dt; t_i)\, \langle \mathbf{\Gamma}\mathbf{\Gamma}^\dagger \rangle_{t_0} \prod_{i=0}^{N} \mathcal{R}(dt; t_i) \tag{2.54}$$

where the infinitesimal evolution matrix for the time interval $[t_i, t_{i+1}]$ is

$$\mathcal{R}(dt; t_i) = \begin{pmatrix} \langle \Gamma^1_m | \Gamma^1_n \rangle_{t_i} & \langle \Gamma^1_m | \Gamma^2_n \rangle_{t_i} \\ \langle \Gamma^2_m | \Gamma^1_n \rangle_{t_i} & \langle \Gamma^2_m | \Gamma^2_n \rangle_{t_i} \end{pmatrix}, \tag{2.55}$$

with the time-dependent contractions

$$\begin{aligned} \langle \Gamma^1_m | \Gamma^1_n \rangle_{t_i} &= \sum_q \phi_q(m, t_i)\phi_q(n, t_i) \cos[\epsilon_q(t_i) dt], \\ \langle \Gamma^1_m | \Gamma^2_n \rangle_{t_i} &= -\sum_q \phi_q(m, t_i)\psi_q(n, t_i) \sin[\epsilon_q(t_i) dt], \\ \langle \Gamma^2_m | \Gamma^1_n \rangle_{t_i} &= \sum_q \psi_q(m, t_i)\phi_q(n, t_i) \sin[\epsilon_q(t_i) dt], \\ \langle \Gamma^2_m | \Gamma^2_n \rangle_{t_i} &= \sum_q \psi_q(m, t_i)\psi_q(n, t_i) \cos[\epsilon_q(t_i) dt]. \end{aligned} \tag{2.56}$$

Taking the limit $N \to \infty$, $dt = t_i - t_{i-1} \to 0$, we recover the continuous time evolution.

Using the time evolution equation (2.54) and the mapping for each value of $g(t)$ between Clifford operators and free-fermion operators we can easily write the evolution of the free-fermion correlation matrix. Indeed, as we will see in Chapter 4, whenever we are interested on the correlation matrix of the fermion operators $\eta_q^\dagger(g)$ ($\eta_q(g)$) which diagonalize the Hamiltonian $H(g)$, what we need is to calculate the expectation value of the free-fermion correlation matrix in the final state $|\Psi(t)\rangle$:

$$\langle \Psi(t) | \begin{pmatrix} \eta(g) \\ \eta^{\dagger T}(g) \end{pmatrix} \cdot \begin{pmatrix} \eta^\dagger(g) & \eta^T(g) \end{pmatrix} | \Psi(t) \rangle. \tag{2.57}$$

Introducing the g-dependent Bogoliubov transformation (2.17), with the specific unitary matrix $\mathbf{V}(g)$ diagonalizing $H(g)$,

$$\frac{1}{\sqrt{2}} \begin{pmatrix} \mathbf{\Gamma}^1 \\ \mathbf{\Gamma}^2 \end{pmatrix} = \mathbf{V}(g) \begin{pmatrix} \eta(g) \\ \eta^{\dagger T}(g) \end{pmatrix}, \tag{2.58}$$

we can rewrite the evolution of the free-fermion correlation matrix as

$$\langle \Psi(t) | \begin{pmatrix} \eta(g) \\ \eta^{\dagger T}(g) \end{pmatrix} \cdot \begin{pmatrix} \eta^\dagger(g) & \eta^T(g) \end{pmatrix} | \Psi(t) \rangle = \frac{1}{2} \mathbf{V}^\dagger(g) \langle \Psi(t) | \mathbf{\Gamma}\mathbf{\Gamma}^\dagger | \Psi(t) \rangle \mathbf{V}(g), \tag{2.59}$$

---

[4] Obviously we could have prepared the initial correlation matrix $\langle \mathbf{\Gamma}\mathbf{\Gamma}^\dagger \rangle_{t_0}$ in any other way, without modifying the protocol of the temporal evolution.

that is

$$\left\langle \begin{pmatrix} \eta\eta^{\dagger}(g) & \eta\eta^{T}(g) \\ \eta^{\dagger T}\eta^{\dagger}(g) & \eta^{\dagger T}\eta^{T}(g) \end{pmatrix} \right\rangle_t = \frac{1}{2}\mathbf{V}^{\dagger}(g)\langle \mathbf{\Gamma}\mathbf{\Gamma}^{\dagger}\rangle_t \mathbf{V}(g), \tag{2.60}$$

where $\langle \mathbf{\Gamma}\mathbf{\Gamma}^{\dagger}\rangle_t$ is given by (2.54). Notice that the real temporal evolution of the diagonal fermion operators is encoded in (2.60) and it is due to the temporal evolution of the Clifford correlation matrix and to the parametric dependence on time, through $\mathbf{V}(g)$, of the unitary diagonalization procedure at parameter value $g(t)$.

Chapter 3

The Bose-Hubbard model

The first experimental realization of a Bose-Einstein Condensate (BEC) with atoms goes back to the nineties. Indeed, at the University of Colorado, Eric Cornell and Carl Wieman, using a gas of Rubidium atoms cooled at 170nK, produced for the first time a new exotic state of matter predicted many years ago by Bose and Einstein [CW98, Bos24, Ein25].

In the following years, progress at the experimental level, the ability to reach lower and lower temperatures, the introduction of efficient laser sources, have allowed to investigate experimentally a countless number of quantum phenomena, some of which were predicted in the early years of quantum mechanics. Among them, the experiment of Greiner *et al* [GME+02] where they explored the Mott Insulator to superfluid quantum phase transition in an experimental realization of a Bose-Hubbard model is a milestone. The Bose-Hubbard model is a simple description of interacting bosons on a lattice [FWGF89, JBC+98] with second quantized hamiltonian

$$H_{BH} = -t \sum_{\langle i,j \rangle} \left(b_i^\dagger b_j + h.c. \right) + \frac{U}{2} \sum_i n_i \left(n_i - 1 \right) - \mu \sum_i n_i, \tag{3.1}$$

in terms of lattice bosonic creation and destruction operators $b_i^\dagger$, b_i and occupation number operator $n_i = b_i^\dagger b_i$. The first term represents a kinetical contribution describing the hopping of bosons from one site to another. In the simplest case, the hopping is restricted to nearest neighbours $\langle i, j \rangle$ only. The U-term comes from a pair interaction and gives the energy cost when n_i particles are sitting at site i. Finally, the μ term accounts for a local external potential which may be interpreted as a chemical potential essentially fixing the number of bosons in the system.

The H_{BH} Hamiltonian can be deduced from a continuum quantum effective field description of bosons living in a periodic potential [JZ05]. Starting from the continuum description, in the single-band approximation and assuming well-localized Wannier functions, one can recast the original continuum description into the second quantized formulation (3.1) (see [LSA+07, Yuk09] for details).

The H_{BH} Hamiltonian is not analytically solvable, nevertheless we can extract useful informations in both limiting cases $t/U \to \infty$ and $t/U \to 0$. Indeed, in both cases, the Bose-Hubbard Hamiltonian reduces to a quadratic form of creation and annihilation operators. In the limit of vanishing boson-boson interactions, i.e. $t \gg U$, the N boson many-body ground state is given by a product of N identical single-particle wave functions each of them

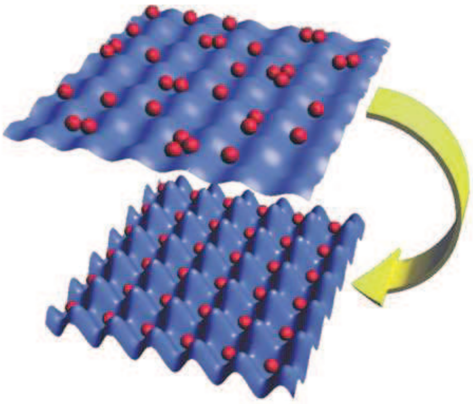

Figure 3.1: Pictorial representations of the superfluid (above) and Mott-Insulating (below) phases of bosons on an optical lattice. (Figure taken from `http://www.uibk.ac.at`)

describing a boson completely delocalized over the whole lattice. Under these conditions, one gets

$$|\Phi_{SF}\rangle_{U=0} = \left(\sum_i b_i^\dagger\right)^N |0\rangle, \tag{3.2}$$

where $|0\rangle$ is the vacuum state, with a manifest phase-coherence of the bosons. In other words, all bosons occupy the same one-particle ground state of the limiting Hamiltonian, leading to the system superfluidity.

On the other hand, when the hopping amplitude $t \to 0$, the Bose-Hubbard Hamiltonian reduces to a direct sum of local Hamiltonians $H_i = U\sum_i n_i(n_i-1)/2 - \mu\sum_i n_i$. The particle density on each site is fixed to an integer value by the minimization condition. There is no more connections between neighboring sites and the bosons stay fixed in space. In such a case, the many-body ground state is a so-called Mott-Insulating state, and in a homogeneous system, it is given by the following local tensorial product

$$|\Phi_{MI}\rangle_{t=0} = \prod_i \left(b_i^\dagger\right)^n |0\rangle, \tag{3.3}$$

where n represent the local integer filling. This state is characterized by long range correlation in the boson local number operator and, unlike the previous limit, the phase coherence has completely disappeared. Finally, an interesting property of this state, is the presence of an energy gap of order U in the energy spectrum. The presence of such an energy gap is reflected in the absence of compressibility.

The Bose-Hubbard model has been extensively studied by Fischer *et al* in [FWGF89] where they also considered the effect of disorder. In the following, referring to their analysis, we will briefly sketch the main properties of the homogeneous Bose-Hubbard model phase-diagram reported in Figure 3.2.

Let us suppose that we initially prepare the system in a perfect Mott-Insulating state at vanishing hopping amplitude $t = 0$ and where, just to fix the idea, we chose the ratio μ/U in such a way that the system is exactly at half integer local filling condition. Then, we turn on a small probability for bosons to jump from one site to a neighboring site (small finite t/U). Under such a condition, if a boson moves over the lattice, the extra kinetic energy (proportional to t) has to compete with the extra potential energy. For a too small

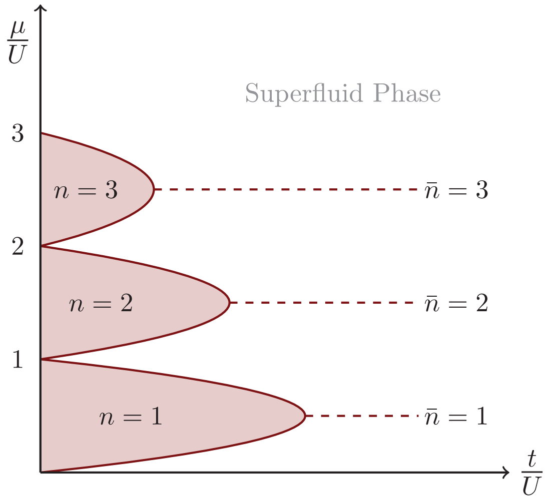

Figure 3.2: Schematic zero temperature phase diagram for the Bose-Hubbard Model (based on [FWGF89]).

value of the hopping coupling t, when U and μ are fixed, it is not convinient to leave the particles moving through the system. Indeed, the Bose-Insulating phase has to extend in the phase-space toward finite hopping rates, creating a sort of lobes. Of course, by increasing the value of the ratio t/U there will be finally, for each value of μ/U, a critical point $(t/U)_c$ above which the particles start to move over the lattice. Those critical points separate the Mott-Insulating lobes from the superfluid phase as depicted in figure 3.2.

Moreover, the analysis carried out in [FWGF89] continues by looking at the transition occurring at fixed t/U and varying the chemical potential μ. Once again, whenever the system belongs to a Mott-Insulating lobe, the extra cost one has to pay for adding an extra particle is too high with respect to the gained extra kinetic energy. Nevertheless, by increasing (or decreasing) μ, the system will finally reach a point in which the extra kinetic energy is comparable to the potential energy cost. A that point, the system will exhibits a transition to the superfluid regime.

Finally let us mention that the particular QCPs at the cusps of each Mott-Insulating lobe are multi-critical points. At those points, varying t, the transition occurs with constant local density $\bar{n}$ [FWGF89].

3.1 Superfluid to Mott insulator in experiments

As we said in the introductory part of this chapter, the generation of the first BEC with cold atoms was actually an important step to convince people to use optical lattices in order to explore the condensed-matter domain. Indeed, at the very beginning optical lattices have been essentially used to further cool down the atoms. Only from a few years, experimentalists have started to use optical lattices to obtain complex many-body states, and therefore, they began to simulate fundamental models of condensed-matter physics [Alv10]. This is exactly what Greiner *et al* did in 2002 [GME$^+$02] by exploring the Mott-Insulating to superfluid transition of ultracold atoms loaded in optical lattice.

They initially cooled ^{87}Rb atoms in order to prepare a BEC, which was then loaded onto a three-dimensional optical lattice. The system was prepared with a very low atom density

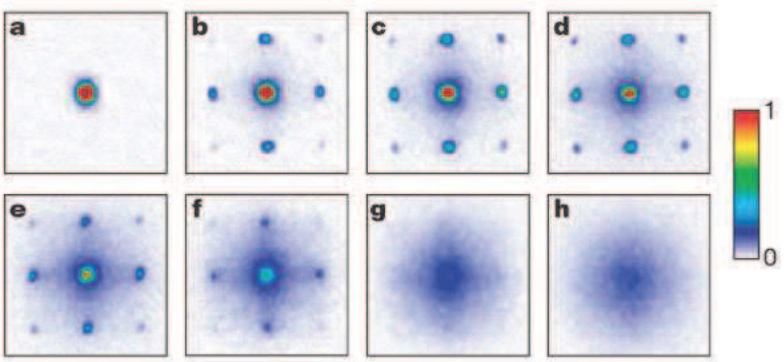

Figure 3.3: Absorption images of multiple matter wave interference patterns across the superfluid to Mott-insulator transition. From a to h the strength of the lattice potential is increased. The time of flight is fixed to $\tau = 15ms$. (Figure taken from [GME+02])

per sites in order to well reproduce the Bose-Hubbard model. Changing the experimental value of the lattice potential depth, it was possible to tune the value of the ratio t/U and, therefore, to explore different points in the phase-space of the model. The properties of the model were analyzed by looking at time-of-flight images. These images were reconstructed after removing the lattice potential and having waited for the atom cloud expansion up to a time $\tau = 15ms$.

In Figure 3.3 we reproduce the images taken from the original paper[GME+02] showing absorption images for different values of the ratio t/U. As we can see from those images, as long as the value of the ratio t/U is larger than the critical value $(t/U)_c$, the kinetic energy is dominant in the system, the atoms are in a superfluid state and a coherent momentum distribution appears during the expansion. Such a behavior is visible in Figure 3.3 as very localized absorption spots. In the opposite limit, whenever the lattice potential becomes sufficiently high to bring the system in the Mott-Insulating phase, the absorption images show an almost uniform smooth pattern. Furthermore, during the experiment the excitation spectrum was probed, confirming, as expected, that the transition from superfluid to Mott-Insulating regime is characterized by the opening of an energetic gap. Finally, the most surprising fact of this experimental study was the almost perfect overlap of the critical value $(t/U)_c$ with the theoretical prediction [FWGF89, JBC+98]. More recently, a similar behavior was reported in one- and two-dimensional systems [SMS+04, SPP07].

3.2 Bloch oscillations of atoms in an optical potential

We decided to close this chapter reporting the results of an experiment that was done some years ago by Dahan *et al.* at the *Laboratoire Kastler Brossel de l'Ecole Normale Supérieure* in Paris [DPR+96]. What has been observed in that experiment is closely related to the subject of Chapter 5. In the following we describe as faithfully as possible what reported in [DPR+96], nonetheless, for further details or references, we refer to the original work.

In that paper, they present Bloch oscillations of ultracold cesium atoms in the fundamental energy band of a periodic optical potential. They directly measure the atomic momentum distribution evolving in time under the influence of a constant inertial force for various potential depths.

They start their analysis by considering a pure one-dimensional quantum system, in the

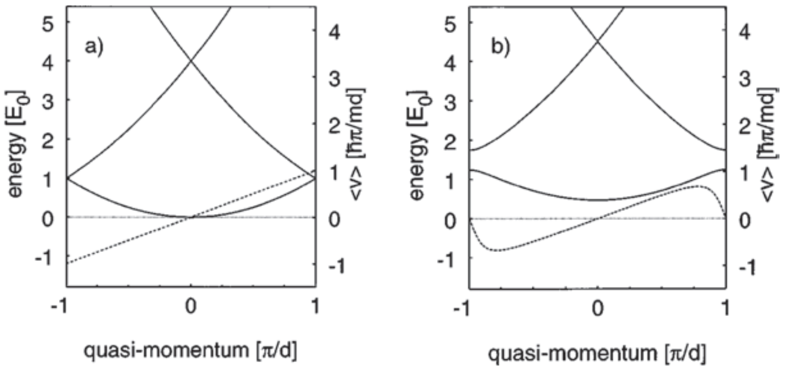

Figure 3.4: Band structure $E_n(q)$ (solid line) for a particle in aperiodic potential $U(z) = U_0 \sin^2 \pi z/d$ and mean velocity $\langle v \rangle_0(q)$ in the fundamental band (dashed line): (a) free particle case, (b) $U_0 = E_0 = \hbar^2\pi^2/2md^2$. A gap opens at $q = \pm\pi/d$. Under the influence of a weak uniform force, a particle prepared in the fundamental band remains in this band and performs a motion periodic in time called a Bloch oscillation. (Figure and caption taken from [DPR+96])

presence of a lattice potential with spacing d. This system shows a typical band structure (see Figure 3.4) and therefore, the one-particle Bloch eigenstates $|n, q\rangle$ (and eigen-energies $E_n(q)$) can be parametrized by means of the band index n ant the quasi-momentum q. Due to the lattice potential, it is possible to show that $|n, q\rangle$, and consequently $E_n(q)$, are periodic functions of q, with period $2\pi/d$ where momenta are conventionally restricted to the first Brillouin zone $[-\pi/d, \pi/d]$. Adding a constant force F, not too strong in order to prevent inter-band transitions, the one-particle initial Bloch state $|n, q_0\rangle$ evolves in time as

$$|n, q(t)\rangle, \quad \text{with} \quad q(t) = q_0 + Ft/\hbar, \tag{3.4}$$

where the evolution is periodic, with period $T = h/|F|d$, with a mean velocity given by

$$\langle v \rangle_n = \frac{1}{\hbar}\frac{dE_n(q)}{dq}. \tag{3.5}$$

As a consequence of the previous arguments, if we prepare a wave packet in the lower band, with a well-defined quasimomentum, it will oscillate in position with amplitude $\Delta_0/2|F|$, where Δ_0 is the energy width of the lower band.

In the experiment the periodic potential was generated by means of standing waves generated by a laser source which was detuned far from any atomic resonances to avoid spontaneous emission. The free atomic gas was initially prepared by using a one-dimensional Raman laser cooling method, obtaining a momentum spread of the order of $\delta p = \hbar k/4$, with $\hbar k$ the photon momentum. In this way, they obtained an atomic coherence length $h/\delta p$ that extended over several lattice periods. After that, they adiabatically switched on the optical potential, transferring the initial distribution into a mixture of Bloch states in the lower energy band. The external force F was produced by introducing a tunable frequency difference $\delta\nu(t)$ between the two counter-propagating waves. Indeed, for a linear variation of $\delta\nu(t)$ the atoms feel a constant inertial force $F = -ma = -md\frac{d\delta\nu(t)}{dt}$ in the reference frame of the optical potential. Again, the force has to be small enough to prevent inter-band transitions. Finally, after having waited a time t_a, they switched off the lattice potential and measured the momentum distribution of the atoms.

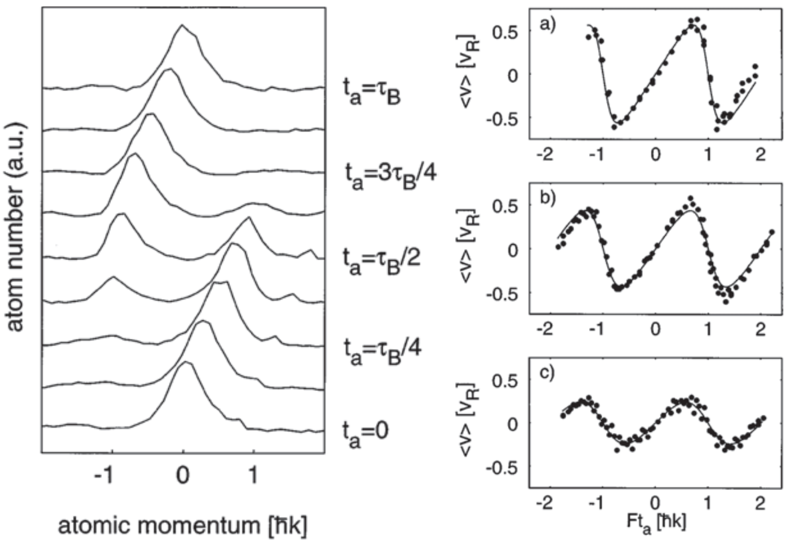

Figure 3.5: (Left figure) Bloch oscillations of atoms: momentum distributions in the accelerated frame for the equidistant values of the acceleration time t_a between $t_0 = 0$ and $t_a = T = 8.2ms$. The light potential depth is $U_0 = 2.3E_R$, where $E_R = h \cdot 2.068kHz$ is the recoil energy. The acceleration is $a = -0.85m/s^2$. The small peak in the right wing of the first five spectra is an artifact. (Right figure) Mean atomic velocity $\langle v \rangle$ as a function of the acceleration time t_a for three values of the potential depth: (a) $U_0 = 1.4E_R$, (b) $U_0 = 2.3E_R$, (c) $U_0 = 4.4E_R$. The negative values of Ft_a were measured by changing the sign of F. (Figure and caption taken from [DPR+96])

In the left side of the Figure 3.5 they plot the momentum distribution in the non-inertial frame for different waiting times t_a. The initial peak moves linearly in time while its weight decreases. As time runs on, a second peak appears at a distance $2\hbar k$; its amplitude becomes equal to the first peak amplitude when $t_a = T/2$. Then it keeps growing until $t_a = T$, the end of a full Bloch oscillation, where the initial momentum distribution is recovered.

They have also deduced from the experimental data the mean atomic velocity as a function of the waiting time for different values of the potential depth U_0 and for an acceleration $a = \pm 0.85m/s^2$. In the right side of Figure 3.5 one sees the results for the three values of U_0 considered in the experiment. Moreover, after having numerically calculated the band structure for the experimental values of U_0, they obtained the mean velocity of the Bloch states from (3.5). The agreement with the experimental data is very good. Finally, integrating $\langle v(t_a) \rangle$ they have also reconstructed the fundamental energy band.

The experiment realized by Dahan *et al* showed in a very clear way the appearance of Bloch oscillations whenever a cloud of ultracold bosonic atoms is loaded in a lattice and feels a constant force. Nevertheless, their analysis is based on the assumption of vanishing boson-boson interactions. We will se in Chapter 5 how the Bloch oscillations behave with increasing repulsive interactions, and eventually in the Hard-Core boson limit.

Part II

Quantum Quench Dynamics

The second part of the thesis contains the main results of our studies. All the performed analysis can be inscribed under the same general subject: dynamics of closed quantum systems. Indeed, both the sudden-quench dynamics and the adiabatic dynamics is investigated in details for different quantum chains in different setups. Especially with regard to the annealing process across a QCP, it turns out that inhomogeneities, like confining potentials, could really affect the defect production [DR10a, CK10, CK11]. Otherwise, the experimental advances with ultracold bosonic atoms loaded into optical lattices, led the theoretical community to be interested on simulating Bose-Hubbard type many-particles Hamiltonians in tunable setting. Recent experiments [DPR+96, WBM+96] showed the well-known Bloch Oscillations and have revitalized the theoretical research on the dynamics of bosonic models in one dimension. For example, in recent high accuracy experiments, atoms loaded in vertical lattices showed Bloch oscillations which can be used to measure gravity [CGKS+05, FPST06, PWT+11]. Finally, after freeing from the condition of zero temperature, we dedicate part of our study to understand the dynamical mechanism of thermalization, especially looking at local properties of a spatially extended quantum system.

Before introducing a sort of synopsis of each chapter, we would like to spent some word about the aims that guided us during the drawing of the chapters: in practice, the idea was to make each chapter independent, giving, each time, an introductory overview of the matter, well placed within the yet existing literature, and developing the tools (eventually referring to what has already been introduced in the first part of the thesis) which will lead to the new results.

In **Chapter 4** *we analyze the coherent quantum evolution of a many-particle system after slowly sweeping a power-law confining potential. We varied in time, along a power-law ramp, the amplitude of the confining potential in order to bring the system at the quantum critical point. Under this scheme, and using general scaling arguments, we derive the general behavior for the density of excitations and energy excess generated during the non-adiabatic sweep of the confining potential. It is found that the mean excitation density follows an algebraic law as a function of the sweeping rate with an exponent that depends on the space-time properties of the potential. We confirm our scaling laws by first order adiabatic calculation and exact results on the Ising quantum chain with a varying transverse field.*

In **Chapter 5** *we analyze the effect of a sudden quench of a linear chemical potential on a trapped one-dimensional Bose gas initially confined in a finite region of an optical lattice. In the impenetrable limit, we develop an hydrodynamical theory which provides the temporal evolution of the density profile. We found that a finite density of the particles remain confined, and another is ejected outside the initial boundaries. We found analytic expressions for the 'plateau' region and for the time-dependent shape of the ejected particles. Furthermore, using adaptive time-dependent DMRG, we investigate the same dynamics in the truly interacting Bose-Hubbard model. The resulting dynamics typically shows two different regimes. For strong repulsion the system show a principal frequency in the temporal evolution of the observables resembling the result in the impenetrable limit. Oppositely, when decreasing the coupling and the system becomes more non-integrable, its time evolution takes on a chaotic character. The features of this transition depend on the value of the constant external force.*

Finally in **Chapter 6** *we analyze the temporal evolution of an extended quantum system initially prepared in an out-of-equilibrium state. By introducing the time-dependent local density matrix we properly define a quantum temperature profile, and set a connection with the classical counterpart. In particular, we focus our attention on the dynamical scaling behaviour of the thermal equilibration mechanism for a closed quantum system initially divided in two different extended subsystems at different temperatures. After introducing the one-dimensional Hard-Core Bosons model, we perform a numerical study. We find that local observables result more robust than global ones, showing, also in the early instants of the evolution, thermal properties.*

Chapter 4

Adiabatic dynamics in confined systems

An interesting question about the behavior of a quantum system near a quantum critical point [Sac00] is how the presence of spatially varying external fields, or local modulation of the internal couplings (which may be randomly or deterministically distributed [BC04, GB97, IKR98b, IKR98a, KLR+01]), will influence the equilibrium and dynamical properties of such a system. Depending on the relevance of the perturbation generated by the field or coupling inhomogeneity, the universality class governing the behavior close to the critical point may change [IPT93]. A relevant inhomogeneity may even suppress the very existence of the critical point as, for instance, it is trivially the case on a finite-size system [Bin83]. The critical behavior will be modified locally at a boundary, as, for example, at a flat surface, at a corner, or at the tip of a parabolic-shaped system [Car83, BPP84, Car84, Pes85, AL95, KLT97, DP97, PTI91]. An extended inhomogeneity may be such that it is to weak to modify the bulk critical behavior but strong enough to change the local critical properties at a surface or at an interface [HvL81, KPT95]. One may also mention a series of works on gradient percolation, where an inhomogeneous field was introduced as a tool allowing for accurate estimates of the percolation threshold and the percolation exponents [SRG85, RGS85, RGS86, ZS86, GRS88]. The main effect of such a spatially varying field inhomogeneity is to smooth out the critical singularities. Indeed, the inhomogeneous field leads to a departure from the critical point, which introduces a finite length scale in the problem. More recently, based on the proper identification of the typical length scale, a scaling theory for the equilibrium profiles of energy and particle densities has been developed for quantum systems with power-law inhomogeneities [PKT07, ZD08, DZ09, CV09, CV10, CKT09]. Such power-law fields are particularly relevant in the context of ultracold atoms, where parabolic trapping potentials are used to confine atomic clouds.

Beautiful experiments from the ultracold-gases community have revived the theoretical studies of the nonequilibrium behavior of strongly correlated quantum systems [GME+02, LSA+07, SHL+06]. The main reason for that is that the dynamics of such atomic systems presents a very low dissipation rate and a good phase coherence over very long times [GME+02, LSA+07, SHL+06]. Consequently, the real dynamics is very well modeled by the usual quantum unitary evolution of closed systems. Among the various possible nonequilibrium situations that one may think of, a case that has received much attention is where the parameters of the quantum many-body system are varied in time such that the system reaches or crosses a quantum critical point. In this case, close to the critical point, the divergence of the intrinsic relaxation time leads to a nonadiabatic evolution of the system

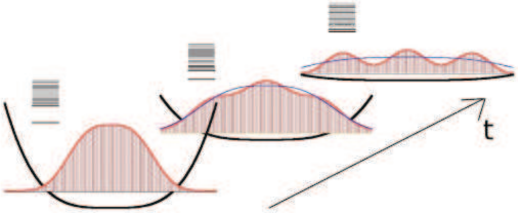

Figure 4.1: Sketch of the problem we consider in this chapter.

no matter how slow the Hamiltonian is changed. If the system is initially in its ground state, nonadiabatic transitions toward excited states lead to the generation of topological defects in the final state [ZDZ05, Dam05, DZ06, DZ07, CDDZ07, Dzi05, CL06, Pol05, GBP08, SSM08, PG08, BP08]. For example, driving a quantum system from a paramagnetic to a ferromagnetic phase through a critical point generates a final state given by a superposition over excited states carrying finite ferromagnetic domains separated by kinks or domain walls. For a slow driving rate, the density of defects is a universal scaling function of the driving rate, as in the classical Kibble-Zurek (KZ) mechanism [Kib76, Kib80, Zur85]. This may be of importance in the context of adiabatic quantum computation [FGG$^+$01], where adiabatic evolution is proposed to transfer the system from an initial state to a computational nontrivial state. If one is forced to cross a critical point in order to generate the nontrivial state, inevitably the crossing will result in the generation of excitations (defects). The optimal time ramp needed to drive the system through the critical point has to balance the unavoidable generation of defects and the time needed to cross the critical point [BP08].

Removing or loading a power-law trap smoothly in time and close to a critical point, as sketched in Figure 4.1, will lead to a final state carrying a nontrivial density of defects, which will depend on the shape of the trap [CK10, CK11]. The reason for this result is the fact that the power-law perturbation is a relevant one and modifies the universality class of the critical point, leading to an effective correlation length exponent which has to enter into the Kibble-Zurek prediction instead of the original one. In this chapter we analyze in details the coherent generation of defects during such an inhomogeneous quench [CK10, CK11]. A general scaling argument is presented from which the scaling behavior of local (such as the local energy density or order parameter) and global (such as the density of defects) quantities are derived. The minimization of defect production for a given total sweeping time is also discussed within the scaling approach. Aside from the scaling-argument approach, we also present an analytical near-adiabatic analysis and an exact numerical study of the Ising quantum chain with an inhomogeneous transverse field playing the role of the confining potential.

The chapter is organized in the following way: the next Section 4.1 is devoted to the scaling theory. The dynamical analyses is presented in Section 4.2 and the specific case of the Ising model is treated in Section 4.3. Finally we summarize our results in Section 4.4.

4.1 Scaling theory

4.1.1 Scaling arguments

The d-dimensional quantum system we consider has a quantum critical point at zero temperature governed by a scalar field h. The critical point separates a symmetric phase from a broken-symmetric one. The homogenous critical field value is h_c. We assume that close enough to the critical point the quantum control parameter h deviates in one direction from the homogeneous critical value h_c with a power law

$$\delta(x,t) \equiv h(x,t) - h_c \simeq g(t)|x|^{\omega} \tag{4.1}$$

with a positive space exponent $\omega > 0$. The amplitude $g(t)$ of the spatial deviation to the critical value (which is set fixed at $x = 0$ $\forall t$ according to (4.1)) is driven externally from a given initial value to a final one following the non-linear time ramp

$$g(t) = v|t|^{\alpha}\mathrm{sgn}(t) \tag{4.2}$$

with α a positive exponent, $\mathrm{sgn}(t)$ the sign function and where, without loss of generality, the rate amplitude v is assumed to be positive and determines the velocity of the quench. For small vs the quench is slow while it is faster at larger values. Notice that within the following parametrization, the quench dynamics connects the two distinct phases by crossing the homogeneous critical point ($h(x) = h_c$ $\forall x$) at time $t = 0$. Negative times correspond to the $\delta < 0$ phase while positive times to the $\delta > 0$ phase.

The presence of the inhomogeneous field (4.1) introduces a crossover region in space-time (x,t) around the critical locus $(0,0)$ with characteristic length-scale ℓ and time-scale τ. To see that, let us start in the far past, at $t = -T$ with $T \gg 1$, from the ground state $|GS(g(-T))\rangle$ associated to the initial amplitude value $g(-T)$. Under the unitary dynamics generated by the time-dependent hamiltonian, the system starts to evolve adiabatically, following the instantaneous ground state $|GS(g(t)\rangle$ as far as it is protected from transitions to excited states by a large energy gap $\Delta(t)$ between the ground state and the excited states. At time t, in the instantaneous state $|GS(g(t))\rangle$, the spacial power-law deviation of the control parameter δ from the critical point introduces a finite length scale $\ell(t)$ around the spatial critical locus (here at $x = 0$) [PKT07, CV09, CV10, CKT09]. The typical length can be obtained self-consistently by noting that, with this width, $\ell(t)$, is associated a given deviation $\delta(\ell) = g\ell^{\omega}$ from which a characteristic length $\delta(\ell,t)^{-\nu}$ can be constructed from the correlation length relation. From the identification $\ell(t) \sim \delta(\ell,t)^{-\nu}$ one finally finds

$$\ell(t) \sim |g(t)|^{-\nu/(1+\nu\omega)} \ . \tag{4.3}$$

The typical length scale $\ell(t)$ diverges for a vanishing deviation amplitude g, that is close to the critical point, with an effective correlation length exponent given by

$$\nu_g \equiv \frac{1}{y_g} = \frac{\nu}{1+\nu\omega} \ . \tag{4.4}$$

As time runs toward zero, the energy gap Δ of the system vanishes and correspondingly the relaxation time $\propto 1/\Delta$ gets larger and larger up to the point where the adiabatic evolution breaks down completely due to the contributions of the transitions toward instantaneous excited states. When sufficiently close to the homogeneous critical point, the response of the system to the external driving is so slow that the dynamics switches to a sudden regime. After the critical point has been crossed, for sufficiently large times, one recovers again the nearly adiabatic regime. The typical time scale τ around the critical locus, separating the nearly adiabatic dynamics from the sudden-quench regime, can be deduced from the self-consistent relation $\tau \sim \ell(\tau)^z$, where z is the dynamical exponent. This leads to

$$\tau \sim \ell^{z} \sim v^{-z/y_v} \tag{4.5}$$

where

$$\frac{1}{\nu_v} \equiv y_v = y_g + z\alpha = \frac{1+\nu(\omega+z\alpha)}{\nu} \tag{4.6}$$

is the Renormalization Group (RG) dimension of the perturbation field, such that, under rescaling by a factor b, the amplitude v transforms as $v' = b^{y_v} v$. Since ω and α are positive, the perturbation is always relevant ($y_v > 0$). Notice that within the quench, the maximal extension of the length scale ℓ scales with the rate amplitude v as $\ell \sim v^{-\nu_v}$ where ν_v plays the role of an effective correlation length exponent for the effective thermal field v. For a given value of v the typical length scale never diverges, even exactly when we cross the critical point since, before that, there is a critical slowing down which freezes completely the dynamics and avoids then the further development of correlations.

The scaling of the profile of a local quantity $\phi(x,t,v)$, like the local order parameter or the energy density, with scaling dimension x_ϕ close to the critical locus, is determined under the homogeneity hypothesis $\phi(x,t,v) = b^{-x_\phi}\phi(xb^{-1}, tb^{-z}, vb^{y_v})$. Taking the rescaling factor to be $b = v^{-1/y_v} \propto \ell \propto \tau^{1/z}$, one obtains

$$\phi(x,t,v) \quad = \quad v^{x_\phi/y_v}\Phi(xv^{1/y_v}, tv^{z/y_v}) \tag{4.7}$$

where Φ is a scaling function. As discussed previously, the prefactor exhibits the trap-size scaling $\phi \sim \ell^{-x_\varphi}$ associated to the finite-size scale $\ell \sim v^{-1/y_v}$ [PKT07, CV09, CV10, CKT09]. Notice here that the scaling form (4.7) is not expected to be valid outside the critical region, that is for $|x| \gg \ell$ since, in those regions, the field values are very far from the critical value.

In the same way, if we are interested only in the time evolution of the spatial-averaged quantity, after integration in space over the critical domain ℓ of the preceding equation, one obtains

$$\overline{\phi}(t,v) = \frac{1}{\ell}\int_\ell \mathrm{dx}\,\phi(\mathrm{x,t,v}) = \mathrm{v}^{\mathrm{x}_\phi/\mathrm{y_v}}\overline{\Phi}\left(\mathrm{tv}^{\mathrm{z/y_v}}\right) \sim \tau^{-\mathrm{x}_\phi/\mathrm{z}}\overline{\Phi}\left(\frac{\mathrm{t}}{\tau}\right) \ . \tag{4.8}$$

As an example, the averaged energy density should behave after the quench to the critical point as $e \sim v^{(d+z)/y_v}$ since its scaling dimension is $x_e = d + z$ [Her76].

4.1.2 Density of defects

The defect production generated during the quench by crossing the critical point is deduced through the identification of the typical Kibble-Zurek time-scale corresponding to the freezing of the dynamics. Equating the relaxation time $\kappa/\Delta(t)$ with the typical time-scale $\Delta(t)/|\dot{\Delta}(t)|$ at which the Hamiltonian is varied and assuming that the gap scales as $\Delta(t) \simeq \Omega_0|g(t)|^{z/y_g}$ one finds for the typical (Kibble-Zurek) time-scale

$$\tau_{KZ} \sim \left(\frac{\kappa}{\Omega_0}\frac{z\alpha}{y_g}\right)^{y_g/y_v} v^{-z/y_v} \ . \tag{4.9}$$

The defect density being proportional to the inverse of the correlation volume at the Kibble-Zurek time, one obtains from the relation $n \sim [\Delta(\tau_{KZ})]^{d/z}$ the behavior

$$n \sim \left(\frac{\kappa}{\Omega_0}\frac{z\alpha}{y_g}\right)^{d\alpha/y_v} v^{d/y_v} = (z\gamma\delta)^{\frac{d\gamma}{1+z\gamma}} \tag{4.10}$$

with $\delta = \frac{\kappa}{\Omega_0}v^{1/\alpha} \sim 1/T$ (with T defining the temporal window of the quench protocol) and $\gamma = \alpha\nu_g = \alpha/y_g$. As one would expect, the density of defects n is smaller for larger values of the protocol time window T used to reach a final value g_f from the initial g_0 value. The obvious conclusion is that, if one wants to minimize the generation of defects, the switching of the trap should be as slow as possible. However, this can lead to extremely long protocol times T and be counterproductive as, for example, in quantum computational issues where one looks for a compromise between the production of excited states and short computational times. In order to achieve this compromise one may look for the optimal power-law time-ramp protocol that minimizes the defect density n at a fixed duration T. Optimizing (4.10) with respect to $\gamma = \alpha/y_g$ for a given $\delta \sim 1/T$ one finds

$$\gamma_{opt} = \frac{1}{z}\mathcal{W}\left(\frac{1}{e\delta}\right), \tag{4.11}$$

where $\mathcal{W}(x)$ is the Lambert $\mathcal{W}$ function defined through $x = f(\mathcal{W}) = \mathcal{W}e^{\mathcal{W}}$. For a given trap shape (space exponent ω fixed) the optimum time exponent takes the value $\alpha_{opt} = \gamma_{opt}/\nu_g = \gamma_{opt}(1+\nu\omega)/\nu$. Using the asymptotic expansion of the Lambert function $\mathcal{W}(x) \simeq \ln x - \ln\ln x$ at large x, the result of [BP08] is recovered with $\omega = 0$

$$\alpha_{opt} \simeq -\frac{1}{z\nu}\ln\left(e\delta\ln\frac{1}{e\delta}\right) . \tag{4.12}$$

Loading a power-law trap potential changes significantly the value of the optimal temporal exponent α, increasing it by a factor $(1+\nu\omega)$. This means that, with a power-law trap and close to the critical point, one has to drive the system slower than without a trap in order to minimize the defect production.

In view of the scaling prediction (4.7) we expect the density of defects $n(x, v)$ produced locally within the critical region to scale as

$$n(x, v) = v^{d/y_v}\mathcal{N}(xv^{1/y_v}) = \ell^{-d}\mathcal{N}\left(\frac{x}{\ell}\right) \tag{4.13}$$

where we have set $t = \tau_{KZ} = v^{-z/y_v}$. The unknown scaling function $\mathcal{N}(u)$ should go to a constant as $u \to 0$.

4.1.3 Global shift to the critical point

A question that may naturally arise is about the validity of the present approach when the critical locus is not exactly at the expected space-time location, as it would certainly be the case in an experiment. If there is an incertitude in the locus of the critical point, following [DR10a, DR10b, Dzi10], we can distinguish several situations. First of all, if the deviation to the expected locus is due to a shift δ_g in the time ramp amplitude, such that the actual perturbation is given by

$$\delta(x, t) \simeq [g(t) - \delta_g]|x|^\omega , \tag{4.14}$$

where without loss of generality we assume $\delta_g > 0$, then the critical point is crossed (for $g(t^*) = \delta_g$) at $t^* = \left(\frac{\delta_g}{v}\right)^{1/\alpha}$. Developing $\delta(x, t)$ near t^* (and neglecting higher order contributions) we obtain

$$\delta(x, t) \simeq \left.\frac{\partial\delta(x, t)}{\partial t}\right|_{t^*}(t - t^*) = \hat{v}_g(t - t^*)|x|^\omega, \tag{4.15}$$

where we have identified a new rate $\hat{v}_g = \alpha v^{1/\alpha}\delta_g^{1-1/\alpha}$. The effect of a finite δ_g leads then to an effective linear time ramp without changing the spatial behavior. Our scaling predictions hold then with the time exponent α replaced by the new time exponent $\hat{\alpha} = 1$ and the rate v by the effective rate $\hat{v}_g$.

If the deviation to the critical point is due to a global residual shift δ_h such that the actual trap has the form $\delta(x,t) = g(t)|x|^{\omega} - \delta_h$, one has to distinguish between a small shift and a relatively large one. Consider first the case of a small global shift δ_h, such that we are still in a scaling regime. The scaling dimension associated to the global shift is that of the unperturbed system $1/\nu$. Under rescaling by a factor b, the length scale and time scale changes according to

$$b^{-1}\ell(v,\delta_h) = \ell(vb^{y_v}, \delta_h b^{1/\nu}), \quad b^{-z}\tau = \tau(vb^{y_v}, \delta_h b^{1/\nu}) \tag{4.16}$$

which leads taking $vb^{y_v} = 1$ to

$$\ell = v^{-1/y_v}\tilde{\ell}(\delta_h v^{-1/\nu y_v}), \quad \tau = v^{-z/y_v}\tilde{\tau}(\delta_h v^{-1/\nu y_v}) \ . \tag{4.17}$$

The scaling functions $\tilde{\ell}(u)$ and $\tilde{\tau}(u)$ have to satisfy the limiting behavior $\tilde{\ell}(0) = \ell_0$, $\tilde{\tau}(0) = \tau_0$ and for $u \gg 1$

$$\tilde{\ell}(u) \sim u^{-\nu}, \quad \tilde{\tau}(u) \sim u^{-z\nu}$$

in order to match the usual scaling in absence of the trap. Physically, these assumptions mean that the shortest length between $\xi_h \sim \delta_h^{-\nu}$ and $\ell_v \sim v^{-1/y_v}$ dominates the behavior near the critical locus. The trap size scaling (4.7) is expected to hold when $1 \ll \ell_v \ll \xi_h$, that is when the system is critical enough in the absence of the trapping potential. The general scaling for a local field is given by

$$\phi(x,t,v,\delta_h) = b^{-x_\phi}\Phi(xb^{-1}, tb^{-z}, vb^{y_v}, \delta_h b^{1/\nu}) \ , \tag{4.18}$$

and again with $vb^{y_v} = 1$ we have the following trap-size scaling

$$\phi(x,t,v,\delta_h) = v^{x_\phi/y_v}\Phi(xv^{1/y_v}, tv^{z/y_v}, \delta_h v^{-1/\nu y_v}) \ , \tag{4.19}$$

which is nothing but the scaling

$$\phi(x,t,v,\delta_h) = \ell_v^{-x_\phi}\tilde{\Phi}\left(\frac{x}{\ell_v}, \frac{t}{\ell_v^z}, \frac{\xi_h}{\ell_v}\right) \ . \tag{4.20}$$

Under this new scaling assumption we have in particular for the energy gap

$$\Delta(v,\delta_h) \simeq v^{z/y_v}\Omega(\delta_h v^{-1/\nu y_v}) \ . \tag{4.21}$$

For $\delta_h \ll 1$ and $v \to 0$ we have to recover the homogeneous behavior $\Delta \sim \delta_h^{z\nu}$ which imposes $\Omega(u) \sim u^{z\nu}$ for $u \gg 1$. For $\delta_h v^{-1/\nu y_v} \to 0$ developing the function Ω_0 close to zero we obtain

$$\Delta(v) \simeq \Omega_0 v^{z/y_v} + \Omega_0' v^{(z\nu-1)/\nu y_v}\delta_h + o(\delta_h) \ . \tag{4.22}$$

For the defect density, from the Kibble-Zurek prediction $n \sim \Delta^{d/z}$ one obtains the behavior

$$\begin{aligned} n &\sim \Omega_0 v^{d/y_v}\left(1 + \frac{\Omega_0'}{\Omega_0}v^{-1/\nu y_v}\delta_h + o(\delta_h)\right)^{d/z} \\ &\simeq \Omega_0 v^{d/y_v} + \frac{d}{z}\Omega_0' v^{d/y_v - 1/\nu y_v}\delta_h + o(\delta_h) \ . \end{aligned} \tag{4.23}$$

For the special case of the Ising quantum chain that we consider in the following, we have $d = 1$, $\nu = 1$ and $z = 1$, then to the first order in δ_h the corrections are independent on v:

$$n_{Ising} \sim \Omega_0 v^{1/(1+\omega+\alpha)} + \Omega_0'\delta_h + o(\delta_h) \ , \tag{4.24}$$

generating a constant shift to the original behavior.

For a large constant shift δ_h taking the system out of the previous scaling regime, we have to distinguish between negative and positive global shifts. In order to fix the ideas for the discussion, let us set $g(t) = -v|t|^\alpha \mathrm{sgn}(t)$ and drive the system from an initial negative time $t_i = -t_0$ to $t = 0$ where the coupling profile is completely flat: $\delta(x, 0) = -\delta_h$. If δ_h is negative, then since $\delta(x,t) \geq |\delta_h| \ \forall x$, the system stays in his disordered phase during the full evolution. Its dynamics is always nearly adiabatic since at any time $t \in [-t_0, 0]$ the gap keeps large values enough for $|\delta_h| = \mathcal{O}(1)$. One expects in this case an exponentially small defect generation. On the contrary, for a positive global shift δ_h, at each time, there is a region around $x = 0$ which is already in the symmetry-broken phase (negative $\delta(x,t)$ values). During the time evolution, from $t = -t_0$ to $t = 0$, this area around the origin $x = 0$ will grow, propagating the symmetry-broken phase into the symmetric one [DR10b, DR10a, Dzi10]. The temporal dependence of the critical front $x^*(t)$, separating both phases, determined from the critical locus condition $\delta(x^*, t) = 0$ is given by

$$|x^*(t)| = \left(\frac{\delta_h}{v}\right)^{1/\omega} (-t)^{-\alpha/\omega}, \quad \text{with } t \in [-t_0, 0] \ . \tag{4.25}$$

Since α and ω are both positive, the critical locus $x^*(t)$ is expelled to infinity as we approach $t = 0$. At the beginning of the quench the critical locus front propagates slowly enough such that the ordered phase extends into the disordered one with a very low rate of defects generation. However, as time runs toward zero, the velocity of the front becomes very large such that there is no more causal connection with the already nucleated ordered phase and the disordered one. This leads to an effective sudden quench regime for the part of the system which is outside the causal region. In order to obtain the dependence of the threshold point x_0 after which the causality is lost, we develop $\delta(x,t)$ near, lets say, the positive critical front $x^*(t) > 0$. One has close to x^* a linear front

$$\begin{aligned} \delta(x,t) &\simeq \left.\frac{\partial \delta(x,t)}{\partial x}\right|_{x^*(t)} (x - x^*(t)) \\ &= \hat{v}_h (-t)^{\alpha/\omega} (x - x^*(t)) \end{aligned} \tag{4.26}$$

with a local slope $\hat{v}_h(-t)^{\alpha/\omega}$ where the rate $\hat{v}_h = \omega v^{1/\omega} \delta_h^{1-1/\omega}$. Notice here that the slope of the linear front is decaying as $t \to 0$ as $|t|^{\alpha/\omega}$, that is as the trap is opening. This front drives locally the system from one phase to the other with a time dependent velocity $c^*(t) \equiv dx^*/dt \sim x^{*1+\omega/\alpha}(v/\delta_h)^{1/\alpha} \sim x^*(t)/t$. As was pointed out in [DR10b, DR10a, Dzi10], the propagation of the front turns out to suppress the Kibble-Zurek excitations in a region around the origin and rejects the defects production outside this region. At the critical locus x^*, the linearized perturbation introduces a local length scale $\ell^*(t) = \ell(x^*(t)) \sim (\delta_h/x^*(t))^{-\nu/(1+\nu)}$ and time scale $\tau^*(t) \sim \ell^*(t)^z$ according to the scaling argument (4.3) developed in the introduction (see [PKT07, CKT09]). To get an idea of the extension of that region, we compare the velocity $c^*(t)$ of the front with the typical velocity, close to x^*, $\ell^*(t)/\tau^*(t) \sim \ell^*(t)^{1-z}$. From that, one may extract a time τ_0, where both velocities become of the same order, and then deduce the threshold locus $x_0 \equiv x^*(\tau_0)$. In the case of the Ising chain treated below, since the critical exponents $z = \nu = 1$, the system enters into the sudden regime as soon as the front velocity $c^*(t)$ is larger than the sound velocity (hereafter set to one). One obtains from the equation $c^*(\tau_0) = 1$

$$x_0 = x^*(\tau_0) \sim \tau_0 \sim \left(\frac{\delta_h}{v}\right)^{1/(\alpha+\omega)} \ . \tag{4.27}$$

Around the point x_0 one expects a critical region with typical fluctuations of order

$$\left(\frac{x_0}{\delta_h}\right)^{\nu/(1+\nu)} = \sqrt{\frac{x_0}{\delta_h}} \tag{4.28}$$

since for the Ising chain $\nu = 1$ and $\omega = 1$ in a linearized profile. For more details about the calculation of the scaling of the front propagation in the example case of the Ising model with $\omega = 1$ and $\alpha = 2$ see Appendix B.

4.2 Dynamical analysis

If the time-variation of the Hamiltonian is slow enough one can use a nearly adiabatic approximation (see Chapter 1 and Appendix A) in order to describe the actual state $|\Psi(t)\rangle = \mathcal{U}(t,t_0)|0(t_0)\rangle$ obtained from the initial ground state $|GS\rangle = |0(t_0)\rangle$ of the initial hamiltonian $\mathcal{H}(t_0)$. Introducing the instantaneous eigenbasis $\{|k(t)\rangle\}$ (which is assumed to be discret for simplicity) $\mathcal{H}(t)|k(t)\rangle = E_k(t)|k(t)\rangle$ one obtains from standard perturbation theory the "one-jump" expansion

$$|\Psi(t)\rangle \approx \mathrm{e}^{-i\int_{t_0}^{t} dsE_0(s)}\left[|0(t)\rangle + \sum_{k\neq 0}|k(t)\rangle\int_{t_0}^{t} dt'\langle\dot{k}(t')|0(t')\rangle \mathrm{e}^{-i\vartheta_k(t',t)}\right], \tag{4.29}$$

where $\vartheta_k(t',t) = \int_{t'}^{t} ds\delta\omega_{k0}(s)$ with Bohr frequency $\delta\omega_{k0}(t) \equiv E_k(t) - E_0(t)$. Notice that this expansion is valid only if the eigenvectors are changing continuously with time. The first term in the right hand-side is the usual adiabatic result: the state is in the instantaneous eigenstate $|0(t)\rangle$ (here the ground state) of the Hamiltonian $\mathcal{H}(t)$, multiplied by a dynamical phase factor. It corresponds to no jump at all. The second term is the "one-jump" contribution. It represents an adiabatic evolution from the initial state up to a time t', a sudden transition at t' toward an excited state $|k(t')\rangle$, followed by an adiabatic evolution from $|k(t')\rangle$ to $|k(t)\rangle$. The total contribution results from the integration over all times $t' \in [t_0, t]$ at which the transition could take place, and then summed over all transition states. Higher order terms are build by taking into account more than one single jump between the instantaneous states and are neglected here. Using the identity $\langle\dot{k}(t)|q(t)\rangle = \langle k(t)|\partial_t\mathcal{H}(t)|q(t)\rangle/\delta\omega_{kq}$ for $k \neq q$, the transition amplitudes $a_k(t_0,t) = \langle k(t)|\Psi(t)\rangle$ (up to a global phase factor) are given by

$$a_k(t_0,t) = \int_{g(t_0)}^{g(t)} dg\frac{\langle k(g)|\partial_g\mathcal{H}(g)|0(g)\rangle}{\delta\omega_{k0}(g)}\mathrm{e}^{-i\vartheta_k(g,g(t))} \tag{4.30}$$

where the phase factor is given by

$$\vartheta_k(x,y) = \frac{v^{-1/\alpha}}{\alpha}\int_x^y dg\,|g|^{1/\alpha-1}\delta\omega_{k0}(g)\,. \tag{4.31}$$

In the scaling limit, following the same lines proposed in Chapter 1, the lowest energy levels behave as $\delta\omega_k = g^{z/y_g}\Omega_k$ with Ω_k some not yet specified dispersion law. Then,

$$\begin{aligned}\vartheta_k(x,y) &= \frac{v^{-1/\alpha}}{\alpha}\int_x^y dg\,g^{1/\alpha+z/y_g-1}\Omega_k \\ &= \frac{\Omega_k v^{-1/\alpha}}{y_v/y_g}g^{y_v/\alpha y_g}\Big|_x^y\,.\end{aligned} \tag{4.32}$$

Notice the dependence of the phase factor $\vartheta_k(x, y)$ from the rate amplitude v. For $v \ll 1$ the oscillations frequency of the exponential becomes higher and higher leading to vanishing amplitudes. Otherwise, for $v \gg 1$, $\exp(-i\vartheta_k) \sim 1$ and the evolution becomes a sudden quench.

Using the result (4.32) in (4.30) and assuming the scaling relation $\langle k(g)|\partial_g \mathcal{H}(g)|0(g)\rangle = g^{x_\partial / y_g} G_k$, after changing to the integration variable $l = v^{-1/\alpha} g^{y_v/\alpha y_g}$, we have

$$a_k(t_0, t) = v^{\frac{y_g + x_\partial - z}{y_v}} \mathrm{e}^{-i \frac{\Omega_k}{y_v/y_g} u^{\frac{y_v}{y_g}}} \frac{\Delta_k}{\Omega_k} \int_{u_0^{\frac{y_v}{y_g}}}^{u^{\frac{y_v}{y_g}}} dl\, \tilde{F}(l) \tag{4.33}$$

where $\tilde{F}(l)$ is some complicated function that does not depend on v and t (at least in the scaling limit) and with the scaling variable $u = tv^{z/y_v}$ $(u_0 = t_0 v^{z/y_v})$ in agreement with the general time-dependent scaling arguments in (4.7, 4.8). The prefactor show the scaling relation between the RG dimension x_a of the transition amplitude and the RG dimension x_∂ of the derivative of the Hamiltonian with respect to the coupling . In order to obtain the expected scaling dimension of the amplitude ($x_a = 0$) one should have $x_\partial = z - y_g$ that is the expected scaling dimension for $\partial_g \mathcal{H}$. Again, we want to stress that the argument adopted before is correct up to the leading-order scaling corrections and it is useful for showing the agreement between the adiabatic calculation and the time-dependent scaling arguments near a critical point. Otherwise, if we want to calculate the excitation density $n = \sum_{k \neq 0} |a_k(t \to \infty)|^2 \sim \int dk |a(k, t \to \infty)|^2$ when the system, starting from $t_0 = -\infty$, cross the critical point at $t = 0$, one should be careful about the momentum dependence of Ω_k and G_k due to the next-to-leading order scaling corrections, and to the possibility to extend the momentum integral to infinity.

The density of defects generated with the nonlinear ramp $g(t)$ is given by summing the transition probabilities $|a_k|^2$ over all the excited states $|k(g)\rangle$:

$$n \simeq \int \frac{d^d k}{(2\pi)^d} \left| \int_{-\infty}^{\infty} dg \frac{\langle k(g)|\partial_g \mathcal{H}(g)|0(g)\rangle}{\delta\omega_{k0}(g)} \mathrm{e}^{-i\vartheta_k(g, vt^\alpha)} \right|^2. \tag{4.34}$$

Taking in mind the previous remarks, to analyze the behavior of the transition amplitude we need to know the behavior of the energy spectrum $\delta\omega_{k0}(g)$ and of the perturbation matrix elements $\langle k(t)|\partial_t \mathcal{H}(t)|q(t)\rangle$ which will depend on the precise space- and time-dependence of the perturbation field. On the basis of general scaling arguments one expects

$$\begin{aligned} \delta\omega_{k0}(g) \quad &\sim \quad \ell^{-z} \Omega(\ell^{-z}/k^z), \\ \langle k(g)|\partial_g \mathcal{H}(g)|0(g)\rangle \quad &= \quad \ell^{-z+y_g} G(\ell^{-z}/k^z), \end{aligned} \tag{4.35}$$

with $\ell \sim g^{-1/y_g}$ the typical length introduced by the spatial perturbation at time t. Ω and G are some unspecified scaling functions satisfying the condition (1.30). Now, using the scaling relations in the excitation density formula and performing the substitutions $g = k^{y_g} l$ we obtain

$$n \simeq \int \frac{d^d k}{(2\pi)^d} \left| \int_{-\infty}^{\infty} dl\, l^{-1} F(l) \mathrm{e}^{-i \frac{1}{\alpha} v^{-1/\alpha} k^{y_g/\alpha + z} \int^l dl' \tilde{\Omega}(l')} \right|^2, \tag{4.36}$$

where $F(l) = G(l^{z/y_g})/\Omega(l^{z/y_g})$ and $\tilde{\Omega}(l) = l^{1/\alpha + z/y_g - 1} \Omega(l^{z/y_g})$. Now, changing the momentum integration variable to[1] $\eta = v^{-1/(y_g + z\alpha)} k$, we finally find

$$n \simeq C v^{d/(z\alpha + y_g)} = C v^{d/y_v} \tag{4.37}$$

---

[1] Notice that this substitution follows from the exponent in (4.36) by fixing $v^{-1/\alpha} k^{y_g/\alpha + z} = \eta^{y_g/\alpha + z}$.

where C is a non-universal constant independent of v but which depends on the details of the transition.

For the integral (4.36) to converge at $g = 0$, that is for a quench crossing the critical point, the scaling function $F(u) = G(u)/\Omega(u)$ has to decay to zero at least linearly at small u , which is the case for the spatially homogeneous quench [Sac00, Pol05]. In the spatially inhomogeneous situation the convergence close to the critical point is not guaranteed, see below the analytical example of the Ising chain with $\omega = 1$. Consequently one cannot use in general the first order perturbation expansion (4.30) for a quench crossing the critical point. Nevertheless, the adiabatic approximation can be used for quenches that take the system close to the critical point without crossing it. Getting closer and closer to the critical point the transition amplitudes will display a scaling signature.

4.3 Ising quantum chain

4.3.1 Diagonalization and nearly adiabatic dynamics

Let us consider the specific case of the Ising quantum hamiltonian in a time-dependent inhomogeneous transverse field:

$$\mathcal{H}(t) = -\frac{1}{2}\sum_{n=1}^{L-1} \sigma^x_n \sigma^x_{n+1} - \frac{1}{2}\sum_{n=1}^{L} h_n(g)\sigma^z_n, \tag{4.38}$$

where $h_n(g) = 1 + g(t)n^\omega$, with $g(t) = v|t|^\alpha \mathrm{sgn}(t)$. Because it is integrable, this model has been used extensively as a standard theoretical laboratory for issues related to quantum phase transitions [Sac00]. Let us recall that, in the unperturbed case ($h_n = h, \forall n$) the system present a critical point at $h = 1$ separating a disordered phase (for $h > 1$) from a symmetry-broken ordered phase at $h < 1$. The dynamical exponent $z = 1$ and the (thermal) correlation length exponent $\nu = 1$. More recently, it became a favorite test model in various out-of-equilibrium situations such as those generated by suddenly quenching its transverse field from a given initial value to a new one [IR00, Kar02, ST99, DPK08, PK07, EKPP08]. In this study, the inhomogeneous time-dependent field plays a role similar to a trapping potential. The spatial critical locus has been set at the left boundary of the chain (one could have also considered the case of a centered critical locus without real differences from what follows).

In order to diagonalize (4.38), one may perform a Jordan-Wigner transformation mapping the Pauli matrices into fermionic operators. In term of Clifford's operators (Majorana fermions)

$$\Gamma^1_n = \prod_{j=1}^{n-1}(-\sigma^z_j)\sigma^x_n, \quad \Gamma^2_n = -\prod_{j=1}^{n-1}(-\sigma^z_j)\sigma^y_n \tag{4.39}$$

with $\Gamma^{i\dagger}_n = \Gamma^i_n$ satisfying the anti-commutation rules $\{\Gamma^i_n, \Gamma^j_m\} = 2\delta_{ij}\delta_{nm}$, the Hamiltonian (4.38) takes the quadratic form

$$\mathcal{H}(t) = \frac{1}{4}\mathbf{\Gamma}^\dagger \mathbf{T}(g)\mathbf{\Gamma}, \tag{4.40}$$

where $\mathbf{\Gamma}^\dagger = \left(\begin{array}{cc} \mathbf{\Gamma}^{1\dagger}, & \mathbf{\Gamma}^{2\dagger} \end{array}\right)$ is the $2L$-component row vector with $\mathbf{\Gamma}^{i\dagger} = \left(\begin{array}{cc} \Gamma^{i\dagger}_1, & \cdots, \Gamma^{i\dagger}_L \end{array}\right)$ for $i = 1, 2$. The $2L \times 2L$ hermitian matrix $\mathbf{T}(g)$ is given by

$$\mathbf{T}(g) = \left(\begin{array}{cc} \emptyset & \mathbf{C}(g) \\ \mathbf{C}^\dagger(g) & \emptyset \end{array}\right) \tag{4.41}$$

where $\mathbf{C}(g)$ is the interaction matrix with elements

$$C_{m\,n}(g) = -i\left[h_n(g)\,\delta_{m\,n} + \delta_{m\,n+1}\right] \ . \tag{4.42}$$

Introducing, at each value of g (i.e., at each time), the (instantaneous) eigenvectors

$$V_p(g) = \frac{1}{\sqrt{2}}\begin{pmatrix} \phi_p(g) \\ -i\psi_p(g) \end{pmatrix} \tag{4.43}$$

of the eigenvalue problem $\mathbf{T}(g)V_p(g) = \epsilon_p(g)V_p(g)$ one can map the Clifford operators onto a set of diagonal Fermi operators:

$$\eta_p(g) = \frac{1}{2}\sum_{n=1}^{L}\left\{\phi_p(n,g)\Gamma^1_n + i\psi_p(n,g)\Gamma^2_n\right\}, \tag{4.44}$$

$$\eta^\dagger_p(g) = \frac{1}{2}\sum_{n=1}^{L}\left\{\phi_p(n,g)\Gamma^1_n - i\psi_p(n,g)\Gamma^2_n\right\}, \tag{4.45}$$

where the fermionic creation and annihilation operators $\eta^\dagger_p(g)$, $\eta_p(g)$ satisfy the canonical Fermi-Dirac anticommutation rules $\{\eta^\dagger_p(g), \eta_q(g)\} = \delta_{pq}$ for the same value of g. In terms of this new set of operators, the Hamiltonian takes the diagonal form

$$\mathcal{H}(t) = \sum_{p=1}^{L}\epsilon_p(g)\left[\eta^\dagger_p(g)\eta_p(g) - 1/2\right] \tag{4.46}$$

where $\epsilon_p(g)$ are the positive eigenvalues of $\mathbf{T}(g)$. Consequently the instantaneous ground state $|GS(g(t))\rangle$ is the instantaneous vacuum state $|0(g)\rangle$ destroyed by all the $\eta(g)$'s:

$$\eta_q(g)|0(g)\rangle = 0 \ \forall q. \tag{4.47}$$

As shown in [CKT09], in the scaling limit $g \to 0$, $L \to \infty$ while keeping gL^ω constant[2], under the rescaling

$$\begin{aligned} x &= |g|^{-1/y_g}u, & \epsilon_k &= |g|^{1/y_g}\Omega_k, \\ \phi_k &= |g|^{1/2y_g}\tilde{\phi}_k, & \psi_k &= |g|^{1/2y_g}\tilde{\psi}_k, \end{aligned} \tag{4.48}$$

with $1/y_g = 1/(1+\omega)$, one obtains from the eigenvalue problem the following differential equations:

$$\begin{aligned} \left[\frac{d^2}{du^2} + \Omega_k^2 - \mathrm{sign}(g)\omega u^{\omega-1} - u^{2\omega}\right]\tilde{\phi}_k(u) &= 0, \\ \left[\frac{d^2}{du^2} + \Omega_k^2 + \mathrm{sign}(g)\omega u^{\omega-1} - u^{2\omega}\right]\tilde{\psi}_k(u) &= 0, \end{aligned} \tag{4.49}$$

with boundary conditions $\partial_u\tilde{\phi}|_0 = 0$, $\tilde{\phi}(\infty) = 0$ and $\tilde{\psi}(0) = 0$, $\partial_u\tilde{\psi}|_\infty = 0$. When g changes its sign the two equations are exchanged but the boundary conditions remain the same. The scaling relations (4.48) with the normalization condition of the solution $(\tilde{\phi}_k, \tilde{\psi}_k)$ assure the correct normalization of the eigenvectors (ϕ_k, ψ_k).

---

[2] The scaling prescription $gL^\omega =$ const. insures that we are describing the system in the vicinity of the critical region only.

In terms of the diagonal Fermi operators, the perturbation $\partial_g \mathcal{H}(g)$ takes the form

$$\partial_g \mathcal{H}(g) = \frac{1}{2} \sum_{p,q} X^{\omega}_{pq}(g) [\eta^{\dagger}_p(g) + \eta_p(g)][\eta^{\dagger}_q(g) - \eta_q(g)], \tag{4.50}$$

with $X^{\omega}_{pq}(g) = \sum_n \phi_p(n,g) n^{\omega} \psi_q(n,g)$ expressed in terms of the Bogoliubov coefficients ϕ and ψ. Consequently, the time-dependent part of the Ising Hamiltonian induces transitions from the ground state to the two-particles states $|pq(g)\rangle = \eta^{\dagger}_q(g)\eta^{\dagger}_p(g)|0(g)\rangle$ only. The non-vanishing perturbation matrix elements are given by

$$\langle pq(g)|\partial_g \mathcal{H}(g)|0(g)\rangle = \frac{1}{2} \Delta_{pq}(g), \tag{4.51}$$

with $\Delta_{pq}(g) = F_{qp}(g) - F_{pq}(g)$. In the continuum limit, using the scaling variables (4.48), we can write $F_{pq}(g)$ as an integral over the u variable:

$$F_{pq}(g) = |g|^{-\omega/(1+\omega)} \int_0^{\infty} du \, \tilde{\phi}_p(u) u^{\omega} \tilde{\psi}_q(u). \tag{4.52}$$

which exhibits a $|g|^{-\omega/(1+\omega)}$ scaling dependency. In Figure 4.2 we have plotted the one-particle energy levels for $\omega = 1, 2, 3$ showing the agreement with the scaling form (4.48). In Figure 4.3 we present the scaling properties of the matrix elements (4.51), as deduced from (4.52), for different values of the exponent ω. Again, the agreement with the expected scaling is very good for large system sizes and small g values.

During the quench, the departure from the adiabatic ground state can be deduced from the instantaneous occupation number $n_q(t) = \langle \varphi(t)|\eta^{\dagger}_q(g(t))\eta_q(g(t))|\varphi(t)\rangle$ of mode q. Inserting the lowest-order expansion $|\varphi(t)\rangle \simeq |0(t)\rangle + \sum_{p,q} a_{pq}(t_0,t)|pq(g(t))\rangle$ one has for the density of q excitations

$$n_q(t) \simeq 4 \sum_p |a_{pq}(t_0,t)|^2 \; . \tag{4.53}$$

The total defect density is given by summing up all the contributions coming from each q level:

$$n(t) = \sum_q n_q(t) \; . \tag{4.54}$$

To see this explicitly, let us recall that, at any time t, the Ising quantum chain is diagonalized in terms of noninteracting fermionic particles. The adiabatic ground state is the vacuum state with respect to these fermions ($\eta_q(g)|0(g)\rangle = 0 \; \forall q$). Consequently, the number of fermions on the top of the instantaneous vacuum gives the number of defects. For example, if one quenches the Ising chain toward its deep ferromagnetic phase ($h_n \simeq 0, \; \forall n$), then the two ground states are the ferromagnetic states in the x-direction $|\ldots \uparrow\uparrow\uparrow\uparrow\uparrow\uparrow\uparrow \ldots\rangle$ and $|\ldots \downarrow\downarrow\downarrow\downarrow\downarrow\downarrow \ldots\rangle$. The final state of the chain after the quench is a superposition of states like $|\ldots \uparrow\uparrow\uparrow\downarrow\downarrow\downarrow\downarrow\uparrow\uparrow\uparrow\downarrow \ldots\rangle$ with finite domains separated by kinks. The number of such kinks is given by the operator $N = 1/2 \sum_n (1 - \sigma^x_n \sigma^x_{n+1})$ and it is easy to show that it is given by $\sum_q \eta^+_q \eta_q$ where the ηs are the corresponding creation and annihilation operators diagonalizing the chain at $h_n \simeq 0, \forall n$. This will remain true at all finite values of the transverse field, the only difference being that the number of defects is still given by $\sum_q \eta^+_q(h)\eta_q(h)$ but no more by the kink number operator $N = 1/2 \sum_n (1 - \sigma^x_n \sigma^x_{n+1})$, since, at $h \neq 0$, the basic excitations over the ground state are no longer kinks (even if they will be close to kinks as soon as we entered into the ferromagnetic regime).

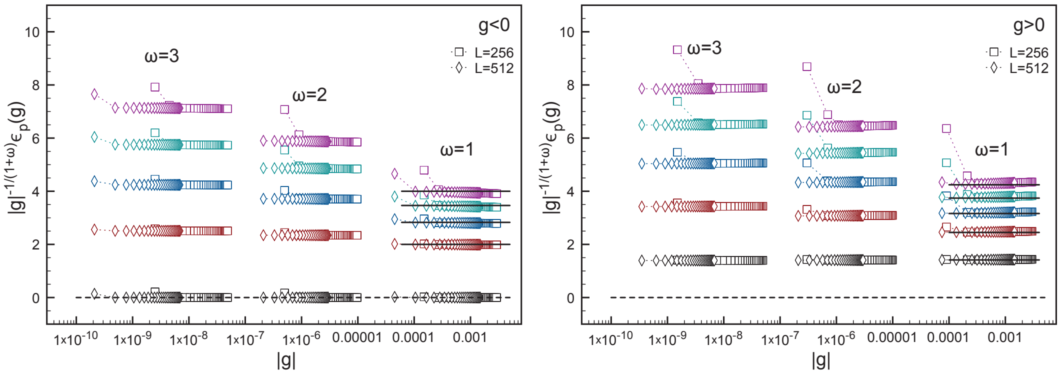

Figure 4.2: The first five Ising one-particle energy levels for different values of the exponent ω, in the ordered phase ($g < 0$) and in the disordered phase ($g > 0$). The value of the gradient g varies in order to keep gL^ω sufficiently small (we have used $L = 256$ (square) and $L = 512$ (diamonds) for the numerical diagonalization) and to fulfill the scaling hypothesis $gL^\omega \ll 1$. The *plateau* region shows the range of validity of the scaling relation $\epsilon_k = |g|^{1/(1+\omega)}\Omega_k$ in the sense that, in the scaling limit $g \to 0, L \to \infty$, all the dependence on the gradient g is encoded in the power-law factor $|g|^{1/(1+\omega)}$. In other words, in the range of validity of the scaling hypothesis, $\partial_g \Omega_k = 0$. Otherwise, for different shape of the spatial potential (different ω) we have, in the scaling limit, different differential equation and thus different eigenvalues and eigenvectors. Summarizing, the dispersion law $\Omega_k(\omega)$ depends on ω. This is the reason why the *plateau* are shifted for different values of ω. In particular, for $\omega = 1$, the straight lines show the analytical dispersion law in Eq. (4.62). The deviation for small values of the gradient is a finite-size effect which is getting smaller and smaller as the system size is increased. The dashed line indicates the zero energy, showing the existence of a vanishing excitation in the ordered phase.

The density of defects at a given lattice site can be deduced from the total defect density operator $\hat{n}(g) \equiv \sum_q \eta_q^\dagger(g)\eta_q(g) \equiv \sum_i \hat{n}_i(g)$, where the second sum runs over the space variable. Using the representations (4.44) of the Fermi operators, one has

$$\hat{n}(g) = \sum_q \sum_{i,j} \frac{1}{4} \left[\phi_q(i,g)\Gamma_j^1 - i\psi_q(i,g)\Gamma_j^2\right] \left[\phi_q(j,g)\Gamma_j^1 + i\psi_q(j,g)\Gamma_j^2\right]. \tag{4.55}$$

Using the ortonormalization relations $\sum_q \phi_q(i,g)\phi_q(j,g) = \sum_q \psi_q(i,g)\psi_q(j,g) = \delta_{ij}$ one obtains:

$$\begin{aligned} \hat{n}(g) &= \frac{1}{4}\sum_i \left(\Gamma_i^1\Gamma_i^1 + \Gamma_i^2\Gamma_i^2\right) + \\ &+ \frac{i}{4}\sum_{i,j}\left\{\left(\sum_q \phi_q(i,g)\psi_q(j,g)\right)\Gamma_i^1\Gamma_j^2 - \left(\sum_q \phi_q(j,g)\psi_q(i,g)\right)\Gamma_i^2\Gamma_j^1\right\}, \end{aligned}$$

and exploiting the anticommutation relations $\{\Gamma_i^\alpha, \Gamma_j^\beta\} = 2\delta_{\alpha\beta}\delta_{ij}$ one finally obtains

$$\hat{n}(g) = \sum_i \frac{1}{2}\left\{1 - i\sum_{j,q}\phi_q(i,g)\psi_q(j,g)\Gamma_j^2\Gamma_i^1\right\}, \tag{4.56}$$

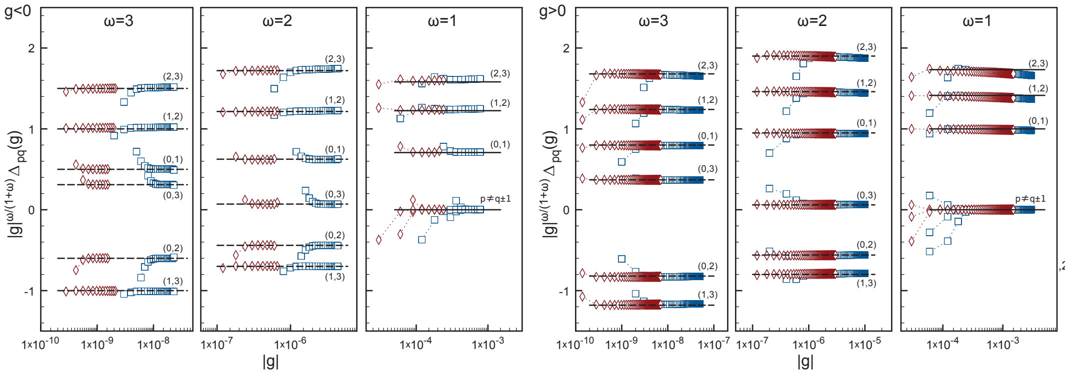

Figure 4.3: Scaling property in the ordered phase ($g < 0$) and in the disordered phase ($g > 0$) of the matrix elements (4.51) for different values of the exponent ω. Different colors are used for distinguishing different sizes (blue squares for $L = 256$, red diamonds for $L = 512$). Also in this case, the *plateau* region shows the range of validity of the scaling relation (4.52). For $\omega = 2, 3$ the dashed lines are guides for the eyes. For $\omega = 1$, the straight lines show the dependence on pq as in (4.64) and one can notice the vanishing amplitude for $p \neq q \pm 1$.

from which one can identify the local defect operator

$$\hat{n}_i(g) \equiv \frac{1}{2}\left\{1 - i\sum_{j,q}\phi_q(i,g)\psi_q(j,g)\Gamma_j^2\Gamma_i^1\right\} . \tag{4.57}$$

The local density of defects generated at site i and at time t is then simply given by

$$n_i(t) \equiv n(i,t) \equiv \langle\varphi(t)|\hat{n}_i(g(t))|\varphi(t)\rangle . \tag{4.58}$$

As we saw in the Chapter 1, another quantity much used in order to quantify the deviation from adiabaticity is the so called fidelity, $\mathcal{F}(t) \equiv |\langle 0(t)|\varphi(t)\rangle|^2$. In our approximation it is given by

$$\mathcal{F}(t) \simeq 1 - \sum_{p,q}|a_{pq}(t)|^2 = 1 - \frac{1}{4}\sum_q n_q(t) \tag{4.59}$$

and then trivially deduced from the knowledge of the populations n_q. One can also consider the excess energy with respect to the instantaneous adiabatic ground state

$$e(t) = \langle\mathcal{H}(t)\rangle_t - E_0(g) = \sum_q \epsilon_q(g)n_q(t), \tag{4.60}$$

which, in the first order adiabatic approximation, becomes

$$e(t) = \langle\mathcal{H}(t)\rangle_t - E_0(g) \approx 4\sum_{p,q}\epsilon_p(g)|a_{pq}(t)|^2. \tag{4.61}$$

4.3.2 Exact solution for the linear spatial perturbation

For a linear spatial modulation (i.e., at $\omega = 1$), the differential equations (4.49) can be explicitly solved in the thermodynamical limit $L \to \infty$ since the problem reduces to a

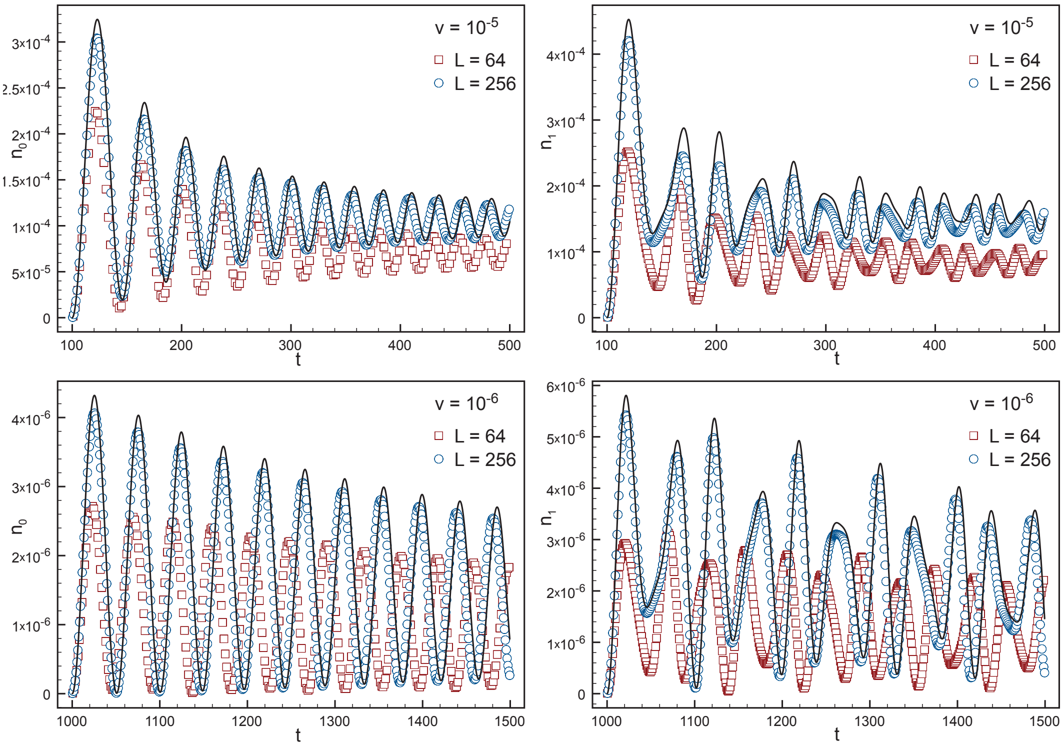

Figure 4.4: Evolution of the occupation number of the first (left figures) and the second (right figures) adiabatic energy level for two different values of the quench parameter v and for $\omega = 1$, $\alpha = 1$. We load the trapping potential by varying the gradient in a suitable interval in order to assure, for the bigger size $L = 256$, the validity of the scaling limit. The full lines are the analytical predictions valid in the adiabatic limit $v \to 0$.

quantum one-dimensional harmonic oscillator. The Bogoliubov coefficients are given by the wave functions χ_p (up to normalization) of the harmonic oscillator [CKT09]:

$$\begin{aligned} \phi_p(x) &= |g|^{1/4}\sqrt{2}\chi_{2p}(u), \\ \psi_p(x) &= \mathrm{sign}(g)|g|^{1/4}\sqrt{2}\chi_{2p+\mathrm{sign}(g)}(u), \\ \epsilon_p &= |g|^{1/2}\sqrt{4p+1+\mathrm{sign}(g)}, \end{aligned} \tag{4.62}$$

The functions χ_n are normalizied in $[-\infty, \infty]$, so that $\sqrt{2}\chi_n$ are correctly normalized in $[0, \infty]$ and we have assumed $\chi_{-1}(u) \equiv 0$. The matrix elements $\langle pq(g)|\partial_g \mathcal{H}(g)|0(g)\rangle$ in (4.30) are then proportional to the position matrix elements of the harmonic oscillator $(\chi_p, u\chi_q)$, such that the only non vanishing transition amplitudes $a_{pq}(t_0, t)$ are those with $p = q \pm 1$.

Plugging the exact solution into (4.30) one obtains a closed expression for the amplitudes a_{pq}. However, contrary to the spatial homogeneous case ($\omega = 0$) where the integral (4.30) converges at the critical value $g = 0$, here the linear spatial inhomogeneity modifies the dependence on g of the integrant to a g^{-1} behavior, leading to a logarithmic divergence at $g = 0$. This divergence is caused by the square root dependence on $|g|$ of the excitation spectrum $\epsilon_p = |g|^{1/2}\sqrt{4p+1+\mathrm{sign}(g)}$ with $p = 0, 1, 2, ...$ [CKT09]. Consequently, the first order adiabatic expansion (4.29) breaks down at the critical point $g = 0$ (i. e., at time $t = 0$). Nevertheless, for quenches that do not cross the critical point (the starting and the ending point of g are on the same side of the critical locus), one can still use (4.30) and one has explicitly [CK10, CK11]

$$|a_{pq}(t_0, t)|^2 = \left| \frac{\Delta_{pq}}{2\Omega_{pq}} A_{\rho_{pq}}\left(|g_0|, |g(t)|\right) \right|^2 \tag{4.63}$$

with

$$\Delta_{pq}(g) = \sqrt{\frac{p+q}{2} + \frac{1+\mathrm{sgn}(g)}{4}}\left[\delta_{p\,q-1} - \delta_{p\,q+1}\right] \,, \tag{4.64}$$

$\Omega_{pq}(g) = |g|^{-1/2}\delta\omega_{pq,0}(g) = |g|^{-1/2}(\epsilon_p(g) + \epsilon_q(g))$ and $\rho_{pq} = -2\Omega_{pq}\frac{v^{-1/\alpha}}{\alpha+2}\mathrm{sgn}(g)$. The function

$$A_\rho(x, y) = \frac{2\alpha}{2+\alpha}\left[\mathrm{E}_1\left(i\rho x^{\frac{2+\alpha}{2\alpha}}\right) - \mathrm{E}_1\left(i\rho y^{\frac{2+\alpha}{2\alpha}}\right)\right] \tag{4.65}$$

is expressed in terms of the exponential integral $\mathrm{E}_1(z) = \int_z^\infty dt\, t^{-1}\mathrm{e}^{-t}$ for $|\mathrm{Arg}(z)| < \pi$.

Let us discuss this analytical result. Consider first the case where the quench starts far away from the critical point, $|g_0| \gg 1$; that is, in an almost uncorrelated initial state. In that case, since $|g_0| \gg 1$ we have $\mathrm{E}_1\left(i\rho|g_0|^{\frac{2+\alpha}{2\alpha}}\right) \simeq 0$ and the function $A(x, y)$ entering into (4.63) is dominated by the contribution of its second argument:

$$A_\rho(|g_0|, |g(t)|) \simeq -\frac{2\alpha}{2+\alpha}\mathrm{E}_1\left(i\rho|g(t)|^{\frac{2+\alpha}{2\alpha}}\right) \,. \tag{4.66}$$

Recalling that $\rho \propto v^{-1/\alpha}$ and $|g(t)| = v|t|^\alpha$ one recovers precisely the expected scaling behavior $n_q(g_0; t, v) = f(v|t|^{2+\alpha})$ with $y_v = 2+\alpha$, which corresponds to the prediction (4.8) with $\nu = z = 1$ for the critical Ising chain and $\omega = 1$ for a spacial linear perturbation.

If the initial gradient g_0 is not sufficiently large, one cannot anymore neglect the contribution to $A_\rho(|g_0|, |g(t)|)$ of its first argument. Consequently, after the quench one observes the non-homogeneous behavior $n_q(g_0; t, v) \sim f_0(g_0) + f_1(|t|v^{1/y_v})$. The expected scaling behavior (4.8) is broken by the presence of the boundary term $f_0(g_0)$, which accounts for the high correlations in the initial ground state $|0(g_0)\rangle$ (since g_0 is not far from the critical point). In Figure 4.4 we see that, for small enough values of v and sufficiently large systems, the exact numerical derivation of $n_0(t)$ and $n_1(t)$ perfectly fits the analytical result obtained from (4.63).

For a quench at or crossing the critical point the situation is more complicated since, as stated before, the (un-normalized) perturbation formula (4.30) leads to a divergence at $t = 0$. However, for a finite-size chain, the energy gap $\delta\omega_{k0}$ stays finite at the critical point which wash out the critical divergences, and one can perform a finite-size scaling study.

4.3.3 Finite size scaling analysis for general ω

For the general ω case, we have performed a numerical study with the following protocol: we start far away in the disordered phase with a fixed initial value $g = 1$ and drive the system to the critical point $g = 0$. The density of defects $n = \sum_q n_q$ and energy excess $e = \langle\mathcal{H}(t)\rangle_t - E_0(g)$ are calculated from (4.54) and (4.60) respectively. The numerical results are obtained by exact diagonalization of finite chains with up to 256 spins and the finite-size data are then extrapolated to the infinite-size limit.

For a given set of ω and α values, we have done numerical diagonalization on systems with sizes from $L = 16$ to $L = 256$ sites, by steps of $\Delta L = 16$ obtaining 16 data sets. For

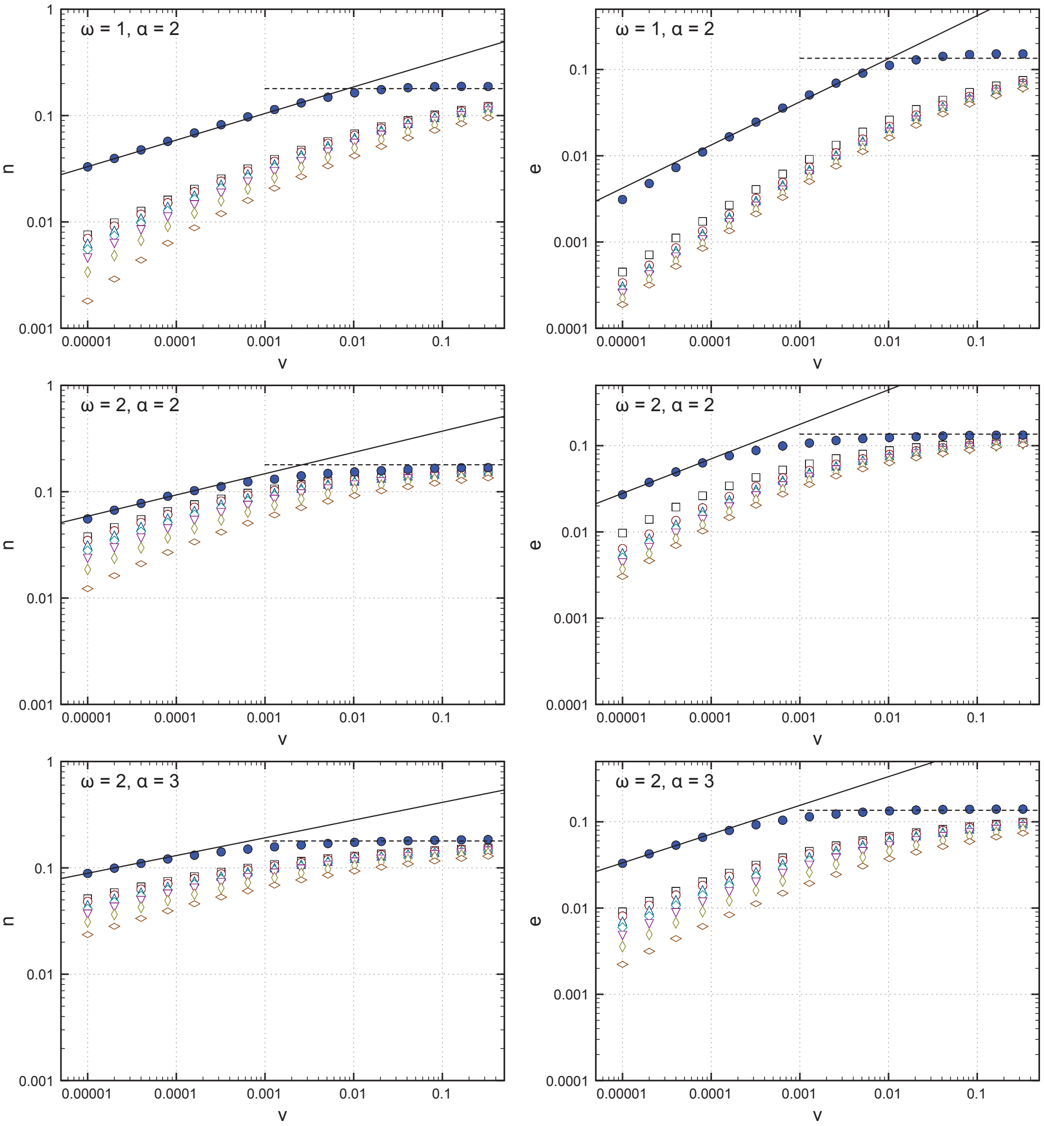

Figure 4.5: Density of defects n (left) and Energy density e (right) versus the quench parameter v for a critical quench. The amplitude changes from $g = 1$ to $g = 0$. Empty symbols correspond to different system sizes ($L = 96$ to $L = 256$ from bottom to top). The extrapolated data (filled circles) show, in the adiabatic limit $v \ll 1$, a perfect agreement with the scaling prediction: $n \sim v^{1/4}$, $e \sim v^{1/2}$ for $\omega = 1$, $\alpha = 2$; $n \sim v^{1/5}$, $e \sim v^{2/5}$ for $\omega = 2$, $\alpha = 2$; $n \sim v^{1/6}$, $e \sim v^{1/3}$ for $\omega = 2$, $\alpha = 3$ (straight lines). The dashed lines give the sudden-quench value $n_{sq} \approx 0.179$, $e_{sq} \approx 0.136$ evaluated on a system with $L = 1024$ spins.

each system size we have varied the amplitude v from a very small value, $v = 10^{-5}$, up to the relatively large value $v = 0.5$. In order to extract the asymptotic infinite-size behavior we have assumed, for any v, the finite-size scaling of the defect density

$$n(v,L) = n(v) + f_1(v)L^{-\lambda_c} + f_2(v)L^{-2\lambda_c} + \dots \tag{4.67}$$

where λ_c is an unknown correction to scaling exponent (the same procedure was used for the energy density). The second-order correction to scaling was kept in order to describe correctly the behavior at small v. The fit was done by looking for a global value of the scaling exponent λ_c independently on v. Defining the fitting function $F(v,x,\lambda) = A(v) + B(v)x^{\lambda} + C(v)x^{2\lambda}$, we have performed, for each values of v, a linear fit of the data varying the fit exponent λ in a reasonable range $[\lambda^{min}, \lambda^{max}]$. For a given v and λ we have then obtained the best parameters $\{A^*(v,\lambda), B^*(v,\lambda), C^*(v,\lambda)\}$. Looking for the minimum of the global least square function $\chi^2(\lambda) = \frac{1}{N-3}\sum_v \sum_x [n(v,x) - F^*(v,x,\lambda)]^2$, with $F^* = A^* + B^* x^{\lambda} + C^* x^{2\lambda}$, we have obtained the best global correction to scaling exponent λ^* and identified the infinite size value $n(v)$ with the coefficient $A^*(v,\lambda^*)$. We have also checked the stability of the fit under the variation of the number N of data sets used in the fitting procedure.

The results are reported in Figure 4.5 for the total defect density and for the energy excess for different spatial and temporal exponents ω and α. First of all, we observe that the finite-size values are always smaller than the extrapolated ones. Indeed, on the finite system the gap does not vanish even close to the critical locus and, consequently, the generation of defects is smaller than the expected one in the thermodynamical limit. At small v the extrapolated data are in perfect agreement with the scaling predictions $n \sim v^{d/y_v}$ and $e \sim v^{(d+z)/y_v}$ with $d = z = 1$, which are represented by the full lines. As the quench amplitude v is getting larger, we observe a crossover from the inhomogeneous Kibble-Zurek scaling scenario predictions toward a regime which is independent of the quench protocol (α and ω values) at large v. The observed saturation at large v of the defects production and of the energy excess is due to the fact that, for very fast quenches, the only relevant parameters are the initial and final amplitudes g. Indeed, if the initial amplitude is very high in modulus, the correlation length is very small (of the order of the lattice spacing) and the initial state is very close to the completely disordered state. Consequently, there is almost no differences for different values of ω. One expects the same defect production (and same energy excess) as in the case of a sudden quench of a completely disordered initial state toward the critical point. This is shown in Figure 4.5 by the horizontal dashed lines which mach perfectly the actual extrapolated numerical datas. A similar behavior is reported in [KV97, DLZ99, Zur09], where for sufficiently fast inhomogeneous quenches, one recovers the homogeneous defect production (corresponding here to the homogeneous sudden-quench saturation at large v), while for sufficiently slow inhomogeneous quenches (here small v) the defect production is significantly lowered. The reason for this is that, when the inhomogeneity is switched off sufficiently fast, there is no causal connection between different space points and the new phase starts to grow independently from every space point, which is exactly what happens in an homogeneous quench. On the contrary, if the unloading of the inhomogeneous perturbation is slow enough, the new phase nucleates from a single initial point (the critical locus) and communicates its phase through the whole system. Consequently, the defect production is lowered. Another way of understanding the crossover is by taking into account that, for a given v, the quench is done within a time $t_q = g^{1/\alpha} v^{-1/\alpha}$. The typical Kibble-Zurek time scale is given by $\tau_{KZ} = \tau_0 v^{-1/y_v}$. If the quench protocol time t_q is smaller than the Kibble-Zurek time τ_{KZ}, which happens at $v > v^*$ where v^* is deduced from $t_q|_v^* = \tau_{KZ}|_v^*$, then the dynamics starts already from the very beginning in the sudden quench regime and there is no near-adiabatic evolution and one expects the same defect production as in a real sudden quench. On the other hand, for a larger value of t_q (i. e., a smaller value of v), the dynamics starts first in a near-adiabatic regime, leading finally to a lower defect production.

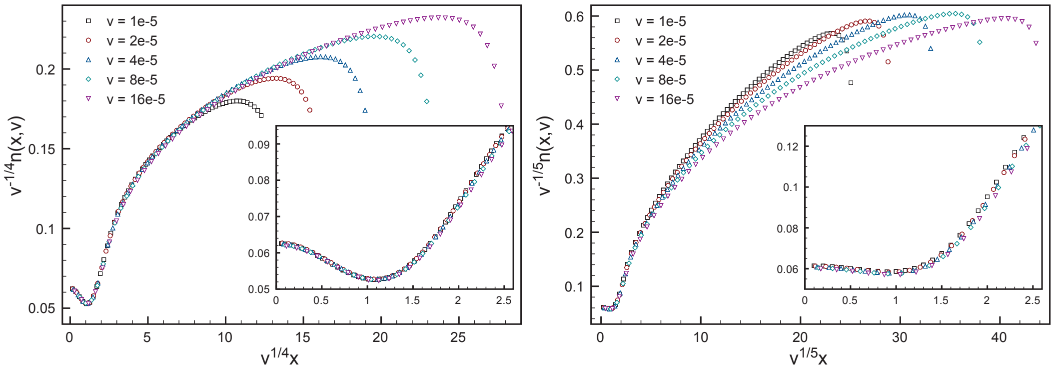

Figure 4.6: Rescaled local defect density as predicted by (4.13) for the Ising chain with $L = 256$, $\omega = 1$, $\alpha = 2$ (left) and $\omega = 2$, $\alpha = 2$ (right). The quench is done from $g = 1$ to the critical point $g = 0$. The different lines correspond to different rates v. The scaling is expected to be valid for $v^{1/4}x$(left) and $v^{1/5}x$(right) small enough. The deviations on the right side at large arguments are finite size effects. Inset: Same as main but zoomed close to the origin.

4.3.4 Local density and global shift of the critical locus

In order to characterize the space dependence of the defects production we have also computed the local defect density from the definition (4.57) and (4.58). The local density is expected to scale according to (4.13) where the appropriate scaling variable is $xv^{1/y_v} = x/\ell$. In Figure 4.6 we have plotted the rescaled defect density $v^{-1/y_v}n(x, v)$ versus the scaling variable xv^{1/y_v} for a chain of size $L = 256$ and for a quench starting at $g = 1$ and ending at $g = 0$ with space exponent $\omega = 1$ (linear profile), $\omega = 2$ (parabolic profile) and temporal ramp exponent $\alpha = 2$ for various values of v. The scaling is expected at small values of the scaling argument (which is shown in the inset of (4.6)) and as seen in the figure it is obviously satisfied. At large values of the scaling variable we observe a systematic finite-size deviation which appears earlier for smaller values of v (larger values of the length scale $\ell = v^{-1/y_v}$). We see clearly on this plot that the effect of the linear varying field is to reduce the defect production in the vicinity of the critical region, expelling out of it the generation of defects. Close to $xv^{1/y_v} = 0$, the non-monotonous behavior is probably generated by the presence of the left boundary of the chain which effectively lowers the local spin-spin couplings, facilitating then the generation of defects. The competition between this facilitation and the lowering of the defect production by the inhomogeneity close to the critical locus leads to the appearance of a locus of minimum defect generation, which from the inset of Figure 4.6 is found around $xv^{1/y_v} = 1.1$.

When a small global shift δ_h is added to the system, one expects the modified scaling (4.23) for the defect density, which reduces to the linear shift (4.24) in the Ising chain case, since $\nu = z = d = 1$. In Figure 4.7 we have plotted the total density of defect in order to check the scaling prediction (4.24). The expected deviation to the zero shift case is supposed to be linear but nevertheless we have represented the graph in a log-log scale in order to amplify the scaling region. One sees clearly on the figure that there is a perfect agreement between the numerical results and the scaling prediction over almost four decades. At large negative shifts δ_h, the expected scenario developed in the preceding section is that of a complete fall down of the excitations in a causal region around the origin, where the ordered phase propagates through the disordered one coherently (without generating any defect), followed

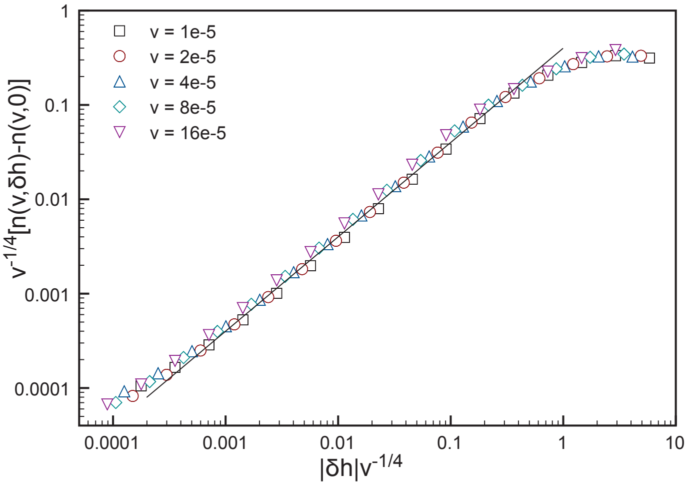

Figure 4.7: Rescaled defect density in the case of a finite global shift to the critical point as predicted by (4.24) for the Ising chain with $L = 256$, $\omega = 1$ and $\alpha = 2$. The quench is done from $g = 1$ to $g = 0$ at different rates v. The straight line represent the expected linear deviation to the $\delta_h = 0$ case.

at large distances with a sudden increase of the defect production. This increase is due to the fact that the critical front propagates too fast through the disordered phase to permit a local relaxation of the phase to the new field parameters. We illustrate that on Figure 4.8 where we have plotted the local density of defects for different shift values δ_h and rates v obtained numerically on a chain of size $L = 256$, with a linear perturbation ($\omega = 1$) and time ramp exponent $\alpha = 2$. We observe that for large values of $|\delta_h|$, there is indeed a drastic decay of the defect density that extends from the origin up to a threshold locus $x_0(\delta_h, v)$ after which the density suddenly grows up. The pattern of the local density $n(x, \delta_h, v)$ at $x > x_0$ is much more complicated where secondary peaks appear and consequently it is hard to interpret this behavior. Nevertheless, the abrupt increase of the excitation density after a threshold locus validates the proposed scenario (see [DR10b, DR10a, Dzi10] where this scenario was developed for a critical front moving at constant velocity). In the inset of figure (4.8) we have drawn the dependence of the threshold locus x_0, extracted from the maximum of the space derivative of the density, versus the variable $(\delta_h/v)^{1/3}$ which corresponds for $\omega = 1$ and $\alpha = 2$ to the prediction (4.27) derived from the local scaling assumptions developed in section 4.1.3. The agreement with (4.27) seen from the inset of Figure 4.8 is very good. One may have also extracted the $(\delta_h/v)^{1/3}$ behavior from the maximum of the first peak. However doing so is a bit less convincing since broad secondary peaks have an influence on the position of the first maximum. Notice also that very close to the origin, there is a density peak which falls off as $e^{-x/q(\delta_h)}$ on a v-independent length scale $q(\delta_h)$. Somehow a small finite density of excitations is trapped at the left boundary, while the remaining excitation density is rejected on the right of x_0.

4.4 Discussion and Summary

In summary, we have developed a scaling theory which predicts the behavior of the non-linear quench of a power-law perturbation close to a critical point. Such a power-law potential

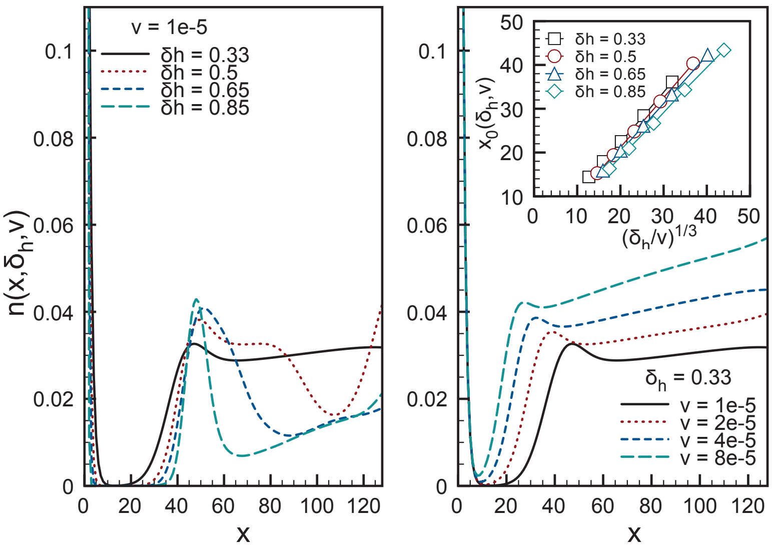

Figure 4.8: Local defect density in the case of a finite global shift to the critical point for the Ising chain with $L = 256$, $\omega = 1$ and $\alpha = 2$. The quench is done from $g = 1$ to $g = 0$. The left figure gives the behavior at fixed rate v for different values of the shift δ_h. The right figure shows the behavior at constant shift δ_h for different values of v. The inset gives the locus x_0 of the fast increase of the defect density, as a function of the expected leading scaling behavior $(\delta_h/v)^{1/3}$.

is relevant especially in the context of confined ultra-cold systems, where the dynamics is well described by the unitary evolution of closed systems. Within our scaling approach, we have derived the scaling properties of physical quantities like the density of defects or the energy excess generated during the loading or unloading of the power-law trap. The basic ingredient behind the scaling analysis is the identification of a so-called Kibble-Zurek time scale, separating between a nearly-adiabatic regime and a sudden one. This (Kibble-Zurek) time scale depends on the universal properties of the critical point as well as on the exponents characterizing the temporal ramp and the shape of the spatial trap. One of the main message of this study is in particular that the optimal nonlinear way of crossing the critical point is strongly affected by the presence and the shape of the trapping potential. As a theoretical test of the scaling theory we have used the exactly solvable Ising model in a transverse field. The analyses revealed quite strong finite size corrections, as seen on Figure 4.5, to the expected scaling predictions for the density of defects and the energy excess. Nevertheless, the datas extrapolated to the infinite size limit fulfill very well the scaling predictions.

One of the main limitation of the present study with respect to a real experiment is that the dynamics driving the system is supposed to be unitary with no parasite interactions at all with the environment, no extra dissipation and no loss of quantum coherence. This of course is a serious limitation if one considers long protocol times. A relevant extension of the present work would be to take into account such extra interactions. The influence of temperature on the scaling predictions, as for example in [PSA+08, PA09], is also one of the more relevant extensions of this work that have to be done.

Chapter 5

Self-trapping bosons in tilted optical lattice

Recently, the study of Bose-Hubbard type many-particle Hamiltonians has been revitalized mainly thanks to the experimental advances in the domains of condensed-matter physics and quantum optics. For example, major improvements have been made in the realization of optical lattices [BDZ08, PSSV11]. New techniques allowed to control the boson-boson interaction in a particularly fine way; similarly, it is possible to locally modify the chemical potential by means of a fictitious magnetic field. All these advances have made it possible the exploration of new phenomena [JBC+98, SMS+04, SPP07, DPR+96, WBM+96, CGKS+05, FPST06, PWT+11]. The main peculiarities of the dynamics of such a systems are low dissipation rate and phase coherence over very long times. Among the motivations for investigating such a wide subject are the demonstration of purely quantum effects, the role of integrability on the thermalization process, and the possibility to manipulate desired states in a controlled way.

Two examples are particularly relevant for the topic of this chapter: Bloch oscillations [Blo28, Zen32] and how atoms are released from a confined region. Bloch oscillations, a typical quantum phenomenon, emerge when a single-particle travels on a lattice experiencing a constant external force F (potential ramp). Recent experiments showing Bloch oscillations of ultracold bosons in tilted optical lattice confirm the quantum mechanical prediction easily explained for non-interacting one-dimensional models [DPR+96, GHM+08]. They can survive to the many-body regime, with a damping possibly related to integrability and chaoticity of the Hamiltonian [Kol03]. On the other side, the trap release of atoms is a standard protocol with cold atoms, but keeping the optical lattice on during the expansion could allow one to handle metastable states [HMMR+09] and study transport phenomena such as the absence of diffusion in disordered potentials [BJZ+08, RDF+08].

In this chapter, we propose an experimentally "realistic" setup which ejects interacting bosons leaving on an optical lattice using a linear ramp potential. This "Galileo ramp" experiment displays remarkable features that are understood with analytical and numerical calculations. Only part of the particles are ejected and form a wave-packet which shape and number of particles are determined. Thanks to the initial preparation and correlations, these traveling particles remain strongly entangled with the ones self-trapped in the confining region, hence creating two spatially separated, entangled, many-body condensates. Lastly, the self-trapped particles show a very rich dynamics reminiscent of Bloch oscillations, with a plateau in the density profile due to many-body interferences and damping related to the integrability of the model.

In the Hard-Core boson limit, we develop an hydrodynamical theory that perfectly catch the behavior of the boson density and current profile. Furthermore, using numerical technics, we analyze how the local interaction strength U of the Bose-Hubbard Hamiltonian drives the system from integrable to non-integrable regimes.

The chapter is organized in the following way: the next Section 5.1 gives a brief introduction to the Bose-Hubbard model and its limiting cases. After setting the dynamical protocol (Section 5.2) and showing some introductory results (Section 5.3), we formulate the hydrodynamical theory in Section 5.4. There we specialize our analysis for the Hard-Core bosons. Afterward we consider some properties of noninteracting bosons in Section 5.5. In Section 5.6 we come back to the real boson dynamics showing the t-DMRG and Lanczos simulations. Finally we summarize our results in Section 5.7.

5.1 Bose-Hubbard model redux

Considering a one dimensional lattice of length L where, for each site, we put some bosons particles; we describe the model by using the Bose-Hubbard (BH) Hamiltonian with open boundary conditions

$$H_{BH} = -\sum_{i=1}^{L-1} t_i \left(b_i^\dagger b_{i+1} + h.c. \right) + \frac{1}{2} \sum_{i=1}^{L} U_i n_i \left(n_i - 1 \right) + \sum_{i=1}^{L} V_i n_i - \mu \sum_{i=1}^{L} n_i, \tag{5.1}$$

where, for each site, b_i and $b_i^\dagger$ are the annihilation and creation bosons operators respectively and $n_i = b_i^\dagger b_i$ is the number operator. In general the hopping term t_i, the local boson interaction U_i and the external potential V_i can be inhomogeneous over the lattice.[1]

The firs therm of the Hamiltonian describes the kinetic energy of the particles: a boson may be destroyed (created) on the lattice site i and created (destroyed) on $i+1$. The coupling t_i gives the measure of the energy cost of a particle-jump between two neighboring sites. The second term takes into account the energy that one has to spent for putting a boson in a specific lattice site. Despite the nature of bosons to condensate in space, this term introduce a local pair repulsion (normally $U_i \geq 0$) if the number of particles in a site is greater than one. The third term introduces an inhomogeneous external potential that allows to have a different particle density for each site over the lattice. By tuning this parameter it is possible to localize the bosons wherever in the lattice. Finally the last term is the usual chemical potential term.

Henceforth, we fix for all the lattice sites the homogeneous value of the hopping coupling $t = 1/2$ and the homogeneous value of the chemical potential $\mu = 0$, and we relax the inhomogeneous condition of local boson interaction by choosing the same value U at all lattice sites. Otherwise, the potential V_i is still inhomogeneous.

The phase diagram of the homogeneous Bose-Hubbard model shows two different phases (see Chapter 3 and Figure 3.1): a Mott-Insulator phase (MI) when the kinetic energy is much smaller than the potential energy and a Superfluid phase (SF) otherwise. The incompressible MI phase has an excitation gap so that the bosons are localized: a slight change in the chemical potential does not change the number of bosons. Particle density is quantized at integer values $n_0(V/U) = 0, 1, 2, \ldots$. Otherwise, the compressible SF phase is gapless and the bosons are delocalized over the entire lattice.

---

[1] Throughout this chapter we chose the sign plus for the external potential term in the Hamiltonian.

Despite its simplicity, the Bose-Hubbard model is not exactly solvable even in one dimension. Therefore, it is necessary either to simplify the model in order to have a new analytically solvable model which exhibits all the salient properties of the Bose-Hubbard model, or to analyze the model by using numerical methods.

5.1.1 Hard-Core boson limit

When the particle density $n = N/L = \sum_i n_i/L$ is very small and the boson-boson local interaction sufficiently strong, the system lives in the superfluid phase with $0 < n < 1$. In this case, we can send the local repulsion U to infinity only allowing 0 or 1 particle for each site. From the viewpoint of the phase diagram shown in Figure 3.1, this approximation corresponds to send the system into the origin of the axis. Such a model is named Hard-Core bosons model and it is analytically solvable by performing a mapping to noninteracting fermions. This mapping is established using the following transformation from the bosonic creation and annihilation operators to the spin ladder operators:

$$\begin{aligned} b_i^\dagger &\equiv \sigma_i^+ = \frac{\sigma_i^x + i\sigma_i^y}{2}, \\ b_i &\equiv \sigma_i^- = \frac{\sigma_i^x - i\sigma_i^y}{2}, \\ n_i &= b_i^\dagger b_i = \frac{1+\sigma_i^z}{2}, \end{aligned} \tag{5.2}$$

which, after inserting into the Hamiltonian (5.1) with $t = 1/2$, yields

$$H_{HC} - \frac{1}{2}\sum_{i=1}^{L} V_i = -\frac{1}{4}\sum_{i=1}^{L-1}\left(\sigma_i^x\sigma_{i+1}^x + \sigma_i^y\sigma_{i+1}^y\right) + \frac{1}{2}\sum_{i=1}^{L} V_i\sigma_i^z. \tag{5.3}$$

After the Jordan-Wigner transformation

$$c_i = \prod_{j<i}(-\sigma_j^z)\sigma_i^-, \quad c_i^\dagger = \sigma_i^+\prod_{j<i}(-\sigma_j^z) \tag{5.4}$$

the Hard-Core boson Hamiltonian is mapped into

$$H_{HC} = \sum_{i,j} c_i^\dagger T_{ij} c_j, \quad T_{ij} = V_i\delta_{ij} - \frac{1}{2}[\delta_{i\,j-1} + \delta_{i-1\,j}], \tag{5.5}$$

where the nonlocal operators c_i and $c_i^\dagger$ satisfy the Fermi algebra $\{c_i^\dagger, c_j\} = \delta_{ij}$. We can diagonalize H_{HC} by using a Bogoliubov transformation that maps the lattice fermionic operators c_i ($c_i^\dagger$) to diagonal ones η_i ($\eta_i^\dagger$)

$$\eta_q = \sum_i \phi_q(i)c_i, \quad \eta_q^\dagger = \sum_i \phi_q(i)c_i^\dagger \tag{5.6}$$

obtaining

$$H_{HC} = \sum_q \epsilon_q \eta_q^\dagger \eta_q, \tag{5.7}$$

where ϵ_q are the one-particle energy levels.

In the homogeneous case (at zero gradient) the one particle energies ϵ_q are given by

$$\epsilon_q = V - \cos q, \tag{5.8}$$

and the Bogoliubov coefficients are

$$\phi_q(i) = \sqrt{\frac{2}{L+1}}\sin(qi) \tag{5.9}$$

with $q_k = k\pi/(L+1) \in [0,\pi]$ and they build in the thermodynamical limit a single energy band of width $\Delta = 2$. For $V > 1$, all excitation energies ϵ_q are positive and the ground state $|GS\rangle$ is the bare vacuum $|0\rangle$. For $|V| < 1$,

$$|GS\rangle = \prod_{q \leq q_F} \eta_q^\dagger |0\rangle, \tag{5.10}$$

with $q_F = \arccos V$ leading to a bosonic density

$$\rho_0 = \langle GS|n_i|GS\rangle \simeq \frac{q_F}{\pi}, \tag{5.11}$$

apart from small finite-size oscillations. For $V \leq -1$, $\rho_0 = 1$ corresponding to the $n = 1$ Mott phase.

5.1.2 Noninteracting bosons

In the opposite limit, when the local interaction term disappears ($U = 0$), the Bose-Hubbard Hamiltonian is still exactly diagonalizable. Indeed, the Hamiltonian (5.1), with homogeneous hopping term $t = 1/2$, becomes

$$\begin{aligned} H_{U=0} &= -\frac{1}{2}\sum_{i=1}^{L-1}\left(b_i^\dagger b_{i+1} + h.c.\right) + \sum_{i=1}^{L} V_i n_i \\ &= \sum_{i,j} b_i^\dagger T_{ij} b_j, \end{aligned} \tag{5.12}$$

that is yet quadratic in the bosonic operators. The matrix elements T_{ij} are the same as in (5.5). The only difference between $H_{U=0}$ and H_{HC} stays in the different algebra $[b_i, b_j^\dagger] = \delta_{ij}$. Now, following the same lines, we can introduce the diagonal boson operators

$$\xi_q = \sum_i \phi_q(i) b_i, \quad \xi_q^\dagger = \sum_i \phi_q(i) b_i^\dagger \tag{5.13}$$

obtaining the set of non-interacting bosonic oscillators:

$$H_{U=0} = \sum_q \epsilon_q \xi_q^\dagger \xi_q. \tag{5.14}$$

Therefore, in the homogeneous case, we obtain the same one-particle energies and Bogoliubov coefficients as in the Hard-Core boson limit. For $V > 1$ the ground state is still the bare vacuum. Otherwise, for $V < 1$ the lower energy level $\epsilon_0 < 0$ is fully occupied by all the bosons we have put into the system, let's say N, in such a way that one has

$$|GS_N\rangle = \left(\xi_0^\dagger\right)^N |0\rangle. \tag{5.15}$$

In other words, all particles condense in the one-particle state associated to the lower negative one-particle energy. The bosonic density in that case is

$$\rho_0 = \langle GS_N|n_i|GS_N\rangle = N|\phi_0(i)|^2. \tag{5.16}$$

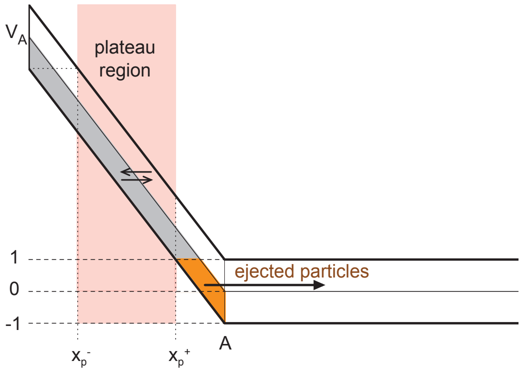

Figure 5.1: Sketch of the the dynamical protocol. The light red region represents the *plateau* region. Gray stripe indicates the trapped bosons, on the contrary, particles over the orange region are ejected.

Finally, when we are working with a finite nonzero interaction, so that neither the Hard-Core boson approximation nor the noninteracting approximation can be applied, a way to analyze the static and dynamical properties of the Bose-Hubbard model is by performing numerical simulation using the time-dependent density-matrix renormalization-group (t-DMRG). This numerical method allows us to simulate the time evolution of a one-dimensional quantum system reducing the dimension of the Hilbert space in which the system lives. For an introductory presentation of the method we remand to the Appendix C.

5.2 Tilted optical lattice

In our protocol, to load N bosons in region $\mathcal{A} = [0, A]$ we prepare the initial state by selecting the ground state of the Hamiltonian with a potential $V_0(x) = V_0$, $\forall x \in [0, A]$ and $V \gg 1$ for $x > A$ in such a way to have exactly N bosons. In particular, in the Hard-Core boson limit it leads to $V_0 = \cos(\pi N/A) \equiv \cos(\pi\rho_0)$ where ρ_0 is the initial density in region $\mathcal{A}$.

The initial state is then approximately characterized by a non-vanishing density $\rho(x) \simeq \arccos(V_0)/\pi$ for $x \in [0, A]$ and zero density elsewhere. Starting from this state, the system is evolving in time with the zero-temperature unitary dynamics generated by the Hamiltonian with the new potential

$$V(x) = \left\{ \begin{array}{ccc} V_A - px & \text{for} & x \in [0, A] \\ 0 & \text{for} & x > A \end{array} \right. , \tag{5.17}$$

where $p = V_A/A$ in order to have $V(x)$ continuous in $x = A$. In Figure 5.1 we draw the potential $V(x)$ that governs the dynamics. For more detailed explanations about the different regions plotted in the figure we remand to the following sections.

Of course, for the numerical simulation, both exact numerical diagonalization and t-DMRG method, we have to work with a finite chain with length L. Moreover, it is also possible to relax the condition over N and to work by fixing U and V_0. Since the Bose-Hubbard Hamiltonian conserves the total number of particles, N is left unchanged during the temporal evolution.

For having more numerical data to compare between the Hard-Core limit results and t-DMRG simulations, especially with respect to the period of the oscillations in density

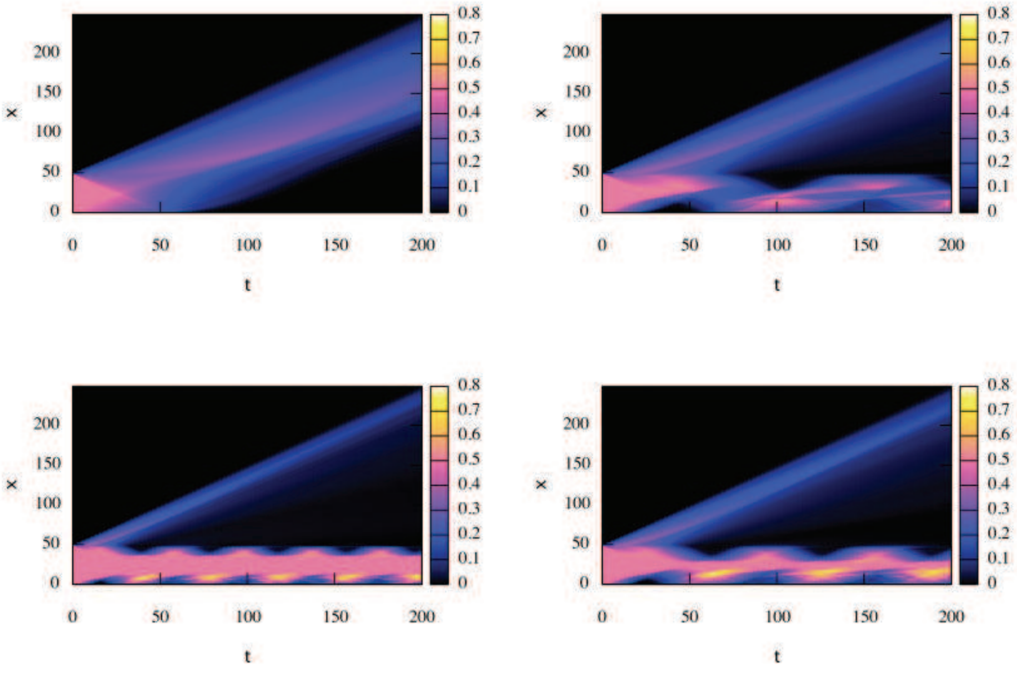

Figure 5.2: Maps of particle densities for the HC boson model in a system with $A = 50$. Initial filling is $\rho_0 = 1/2$. Starting from the top left figure and going clockwise, one has $V_A = 1$, 3, 5 and 8. Notice that trapped particles yet appear for $V_A = 3$ without the presence of a plateau. At $V_A = 5$ plateau region appears and becomes larger for $V_A = 8$. Blue stripe represents particles leaving the ramp.

particle profile and particle density current (see next sections), we use also another quench protocol by defining the Hamiltonian that control the evolution with the potential profile

$$V(x) = V_A - px, \quad x \in [0, L], \quad p = V_A/L, \tag{5.18}$$

enlarging the ramp over the whole lattice. In this case, the initial state is characterize by N bosons spread out over the whole chain.

Finally, we want to remark that our protocol is compatible with the one-band approximation of the Bose-Hubbard Hamiltonian whenever we can neglect inter-band transitions. Indeed, lattices introduce a band structure and, in general, if these bands are close enough, particles can jump from one band to another band. Thus, at the boundaries of the Brillouin zone (see Figure 3.4), where the energetic gap gets the minimum value δ, particles filling the constant force p could escape toward the upper band with a probability given by the Landau-Zener formula $\exp -c\delta^2/p$ [DPR+96], where c is a constant. To avoid transitions the condition $p \ll c\delta^2$ should be fulfilled.

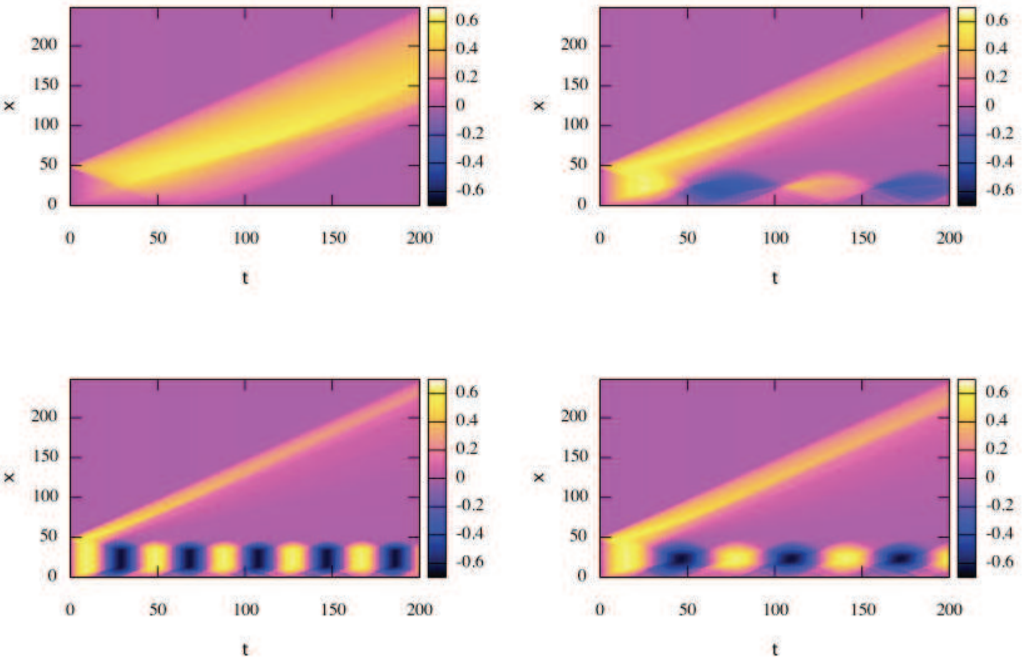

Figure 5.3: Maps of current densities for the HC boson model. System parameters are the same as in Figure 5.2. Notice perfect oscillations for $V_A = 5, 8$, i.e. when a plateau occurs in the particle density. Yellow stripe is the current associated to the ejected particles.

5.3 Hard-Core boson dynamics: overview

Before introducing the hydrodynamical theory as a powerful method to explain the behavior of the Hard-Core bosons, we just summarize the results we have observed in the dynamics of such a model. From Figure 5.2 and Figure 5.3 one may extract some original results. In these overview simulations we consider a system of total length $L = 250$ with $N = 25$ Hard-Core bosons loaded in the region $\mathcal{A} = [0, 50]$, i.e. with half filling initial condition. After loading the ramp we observe, for different slopes ($V_A = 1,\ 3,\ 5,\ 8$), the evolution of particle density and current profiles. In Figure 5.5 we show the same quantities for different initial filling $\rho_0 = 0.2,\ 1$.

1. At small values of the potential at the leftmost site V_A, almost all particles leave the ramp. By increasing the slope p we observe that part of the original particles are trapped. This trapped particles oscillate along the ramp whenever the system is initially prepared in a superfluid phase, otherwise, for $\rho_0 = 1$ we do not observe any oscillation (See Figure 5.5). Moreover, when V_A overcome a 'critical' value V_A^*, a 'plateau' zone Ω, i.e. a zone with a constant density of particles, appears in the middle of the ramp.

2. The 'plateau' region in the middle of the ramp becomes larger and larger by increasing

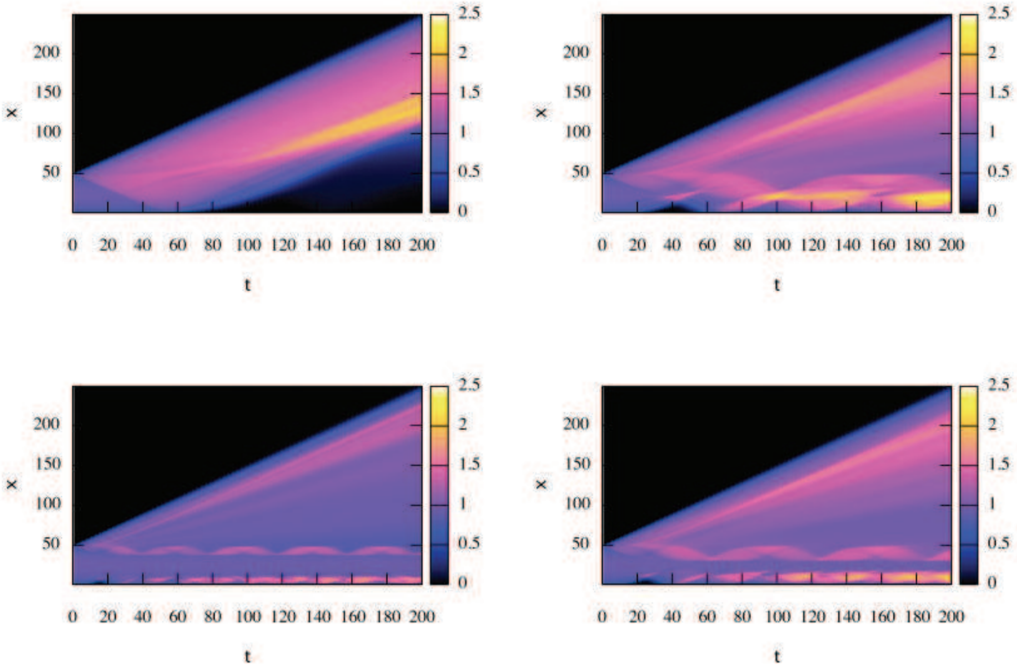

Figure 5.4: Maps of entropy densities for the HC boson model. System parameters are the same as in Figure 5.2. Notice the entanglement growing between the ejected particles and the trapped ones.

the value of the potential slope

$$L_{plat} \simeq A\left(1-\frac{4}{V_A}\right), \quad \text{for} \quad \mathrm{V_A} \gtrsim 4. \tag{5.19}$$

3. The period of the density profile oscillations is given by

$$T = 2\pi\frac{A}{V_A} = \frac{2\pi}{p}. \tag{5.20}$$

4. In the plateau region, current of particles is uniform and shows a perfect sinusoidal behavior in time

$$j(x,t) \propto \sin(2\pi t/T), \quad x \in \Omega. \tag{5.21}$$

   As expected, in the 'plateau' region $\partial_x J(x,t) = 0$, implying a stationary density through $\partial_t \rho(x,t) = 0$.

5. Finally, in Figure 5.4 we plot the entanglement entropy $S(x,t)$ between the leftmost x sites of the system and the rest. The entropy gives a signature of the entanglement between the trapped particles and the ejected particles. In other words, the ramp protocol comes out to be a good method to create an entangled pair made of two macroscopic packets of bosons.

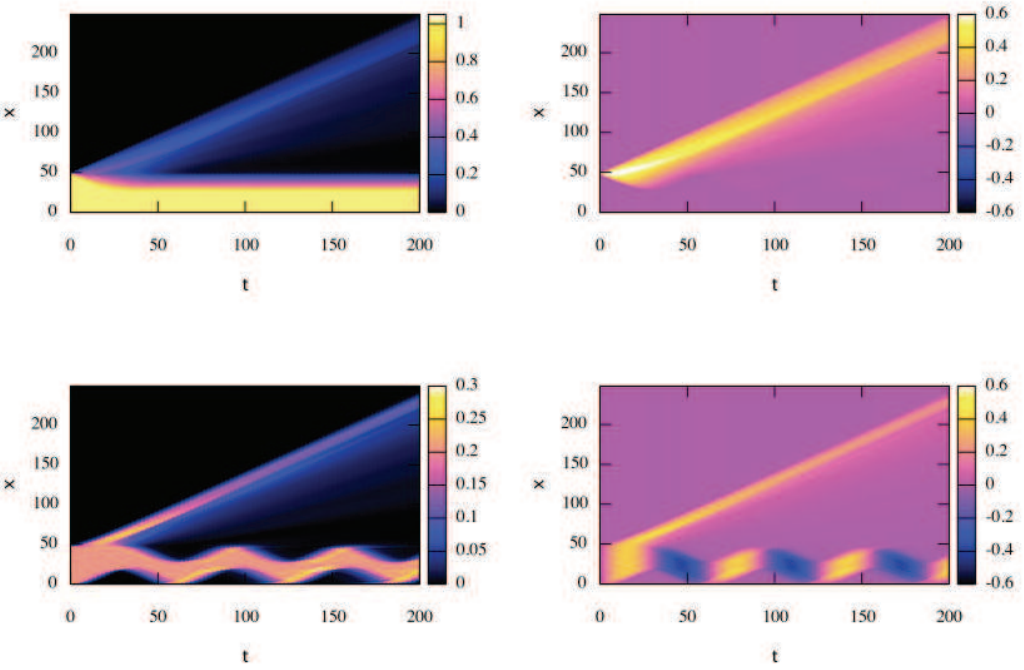

Figure 5.5: Maps of the density of particles (left figures) and current (right figures) for the HC boson model. Here we fixed the potential to $V_A = 5$ and the slope length to $A = 50$. We analyze the evolution for different initial occupancy. Top figures show the evolution for a system initially prepared in the Mott phase ($\rho_0 = 1$). In the bottom figures the system is prepared with $\rho_0 = 0.2$.

5.4 Hard-Core boson dynamics: hydrodynamical theory

The main features of the behavior that we observed in the Hard-Core boson simulations can be simply understood in the hydrodynamical limit $N \gg 1$, $A \gg 1$ while keeping the density $\rho_0 = N/A$ constant. The fundamental idea is that, for a sufficiently large size ($A \to \infty$) and a sufficiently small gradient ($p \ll 1$) we can describe the system by supposing a local equilibrium. In other words, inside each interval $[x - dx/2, x + dx/2]$, we suppose the infinitesimal system locally at equilibrium with potential $V(x)$, thus having locally the same properties like an homogeneous system.

Local equilibrium approximation We briefly sketch the demonstration of the local equilibrium approximation in presence of an "arbitrary" potential.

i. Let us consider an infinite one-dimensional system in a lattice; only for this purpose we introduce the lattice spacing $a \in \mathbb{R}^+$ with $a \ll 1$. Let $V(x)$ a continuous and smooth potential (let us say $V \in C^1$), defined in $\mathbb{R}$. After introducing the spatial interval

$[x, x+\Delta x]$, we suppose that the condition

$$\begin{aligned}&\forall\, M \in \mathbb{N}, \delta > 0,\ \exists\, a > 0, \Delta x > 0\ :\\ &\Delta x/a = M, \quad |\max V(y) - \min V(y)|/\Delta x < \delta\ \forall y \in [x, x+\Delta x]\end{aligned} \tag{5.22}$$

is fulfilled. In other words, the condition (5.22) means that, for an infinite system and a non-pathological function $V(x)$, we can found a sufficiently small interval Δx and lattice spacing a in order to have a great number of sites M in Δx with the supplementary condition that the potential is almost constant over the interval. Roughly speaking, for each lattice sites in the considered interval, the potential keeps the same value

$$\forall\, j \in \mathbb{N}\ :\ ja \in [x, x+\Delta x] \Rightarrow V(ja) = V(x). \tag{5.23}$$

ii. Let us consider the quadratic fermionic Hamiltonian

$$H = -\frac{1}{2}\sum_j [c^\dagger_{ja} c_{(j-1)a} + h.c.] + \sum_j V(ja) c^\dagger_{ja} c_{ja}. \tag{5.24}$$

Now, splitting the real axis in intervals $[n\Delta x, (n+1)\Delta x]$ with $n \in \mathbb{N}$, we can recast H in the following form

$$H = \sum_n \Big\{ H_{\Delta x}[n] + H_{int}[n, n+1] \Big\} \tag{5.25}$$

where the local Hamiltonian is

$$\begin{aligned} H_{\Delta x}[n] = & - \frac{1}{2}\sum_{j=1}^{M-1} [c^\dagger_{n\Delta x + ja} c_{n\Delta x + (j-1)a} + h.c.] \\ & + \sum_{j=1}^{M} V(n\Delta x + ja) c^\dagger_{n\Delta x + ja} c_{n\Delta x + ja}\,, \end{aligned} \tag{5.26}$$

and

$$H_{int}[n, n+1] = -\frac{1}{2}\left[c^\dagger_{(n+1)\Delta x} c_{n\Delta x} + h.c. \right] \tag{5.27}$$

takes into account the local coupling between neighboring intervals.

iii. Now, taking the continuum limit $a \to 0$, $\Delta x \to 0$ by keeping $\Delta x/a = M \gg 1$ (and eventually considering $M \to \infty$), we can introduce the continuous variables

$$\begin{aligned} x &= n\Delta x, \qquad & x &\in]-\infty, +\infty[\\ y &= ja, \qquad & y &\in [0, \Delta x], \end{aligned} \tag{5.28}$$

and the continuous creation and annihilation field operators

$$c_{ja} \to \hat{\Psi}(y), \quad c^\dagger_{ja} \to \hat{\Psi}^\dagger(y). \tag{5.29}$$

In the limit $M \to \infty$ we can discharge the H_{int} contribution in the Hamiltonian, since

$$\frac{\langle H_{int} \rangle}{\langle H_{\Delta x} \rangle} \sim \frac{1}{M} \to 0, \tag{5.30}$$

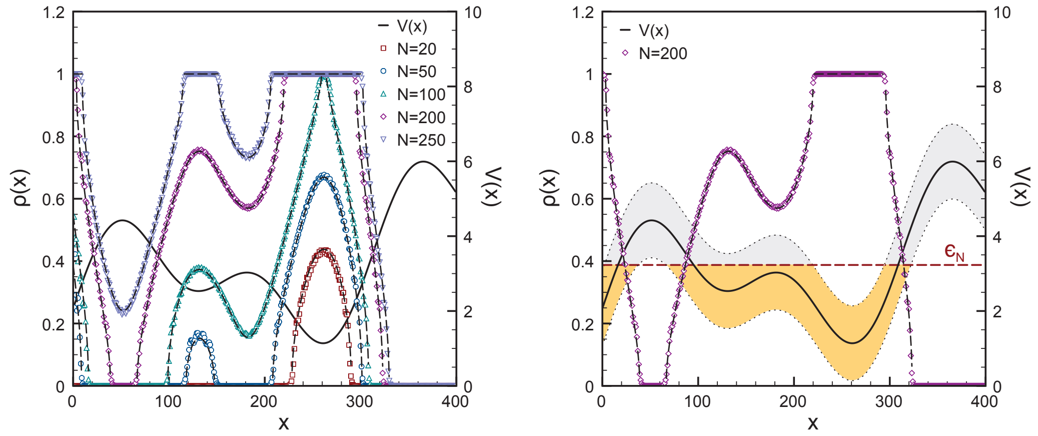

Figure 5.6: Density profile for the XX Hamiltonian with potential $V(x) = 2x/L + 1.5\sin(8x/L) + \sin(16x/L)$, with system size $L = 400$. In to the left, different symbols represent the numerical diagonalization of the Hamiltonian for different filling N. The black dashed lines are the local equilibrium prediction (5.36). In to the right, we focus our attention on $N = 200$ filling. The gray stripe represents the allowed energy-band $[V(x)-1, V(x)+1]$. The yellow region represents the occupied levels up to the Fermi energy (red dashed line). Notice how the local density depends, through the (5.36), on the thickness of the occupied bandwidth.

and the Hamiltonian takes the form

$$H = \frac{1}{\Delta x}\int_{-\infty}^{+\infty} dx\, \mathcal{H}[x], \tag{5.31}$$

where

$$\mathcal{H}[x] = \frac{1}{a}\int_0^{\Delta x} dy \Big\{ -\frac{1}{2}\hat{\Psi}^\dagger(x+y)\hat{\Psi}(x+y-a) + h.c. + V(x)\hat{\Psi}^\dagger(x+y)\hat{\Psi}(x+y) \Big\}, \tag{5.32}$$

since, by hypothesis, $V(x+y) = V(x)$, $\forall y \in [x, x+\Delta x]$. The local Hamiltonian $\mathcal{H}[x]$ is simply the continuous XX Hamiltonian, translated by x with an homogeneous potential $V(x)$, and it can be easily diagonalized through the canonical mapping

$$\hat{\Psi}(x+y) = \int_0^{\pi} dq\, \phi_q(x+y)\eta(q,x), \quad \hat{\Psi}^\dagger(x+y) = \int_0^{\pi} dq\, \phi_q^*(x+y)\eta^\dagger(q,x), \tag{5.33}$$

where the field $\eta(q,x)$ ($\eta^\dagger(q,x)$) annihilates (constructs) a particle with momentum q in the region $[x, x+\Delta x]$. The exact form of the functions $\phi_q(u)$ essentially depends on the boundary conditions. In particular, they are different from zero only in the interval $[0, \Delta x]$[2]. These fields satisfy the anti-commutation rules $\{\eta(q,x), \eta^\dagger(p,y)\} = \delta(x-y)\delta(q-p)$. The delta function for different modes is a consequence of the local diagonalization procedure that preserves the anti-commutation rules; otherwise, the anti-commutation at different spatial points is essentially due to having dropped out H_{int} in the total Hamiltonian. By using these new fields, the Hamiltonian takes the

---

[2] Notice that the functions $\phi_q(u)$ are the Bogolyubov coefficients which diagonalize $\mathcal{H}[0]$.

diagonal form

$$H = \int_{-\infty}^{+\infty} dx \int_{0}^{\pi} dq \, [-\cos q + V(x)] \eta^{\dagger}(q,x) \eta(q,x). \tag{5.34}$$

Therefore, the N-particles ground state is constructed by adding to the vacuum state each particle in the proper phase-space point (q, x) starting from the lower energy of $\epsilon(x, q) = -\cos q + V(x)$ up to the Fermi level ϵ_N:

$$|\Psi_N\rangle = \prod_{q,x}^{\epsilon_N} \eta^{\dagger}(q,x)|0\rangle. \tag{5.35}$$

For $N \gg 1$, this implies for the ground-state density profile

$$\rho(x) = \begin{cases} 0 & V(x) - 1 > \epsilon_N \\ \arccos(V(x) - \epsilon_N)/\pi & |V(x) - \epsilon_N| < 1 \\ 1 & V(x) + 1 < \epsilon_N \end{cases}, \tag{5.36}$$

where the Fermi energy is found by imposing the constraint on the total number of particles

$$\int \rho(x) \, dx = N. \tag{5.37}$$

In Figure 5.6 we compare the exact numerical diagonalization with the local equilibrium prediction in a system with $L = 400$ and potential $V(x) = 2x/L + 1.5 \sin(8x/L) + \sin(16x/L)$. Notice the good matching between the equation (5.36) and the numerical data. The local equilibrium approximation breaks down whenever the local number of particle is small and the potential varies sharply ($\partial_x V(x) \gg 1$). In particular, in the right figure, we graphically reproduce the occupied energy levels (yellow region) for the $N = 200$ filling. In practice, since $\cos q \in [-1, 1]$, the energies $\epsilon(q, x)$ fall in the gray strip which follows the shape of the potential. Finally, the Fermi energy ϵ_N determines which levels are filled in order to have exactly a total of N particles.

Putting forward this considerations, we look at the phase-space of the system and, for each point (x, q) we define an infinitesimal region $\Delta x \Delta q$ surrounding such a point. We can introduce the coarse-grained particle density

$$\rho_0(x,q) = \frac{1}{\Delta x \Delta q} \int_{x-\Delta x/2}^{x+\Delta x/2} \int_{q-\Delta q/2}^{q+\Delta q/2} |\phi_p(y)|^2 dp dy, \tag{5.38}$$

stating that the initial coarse-grained phase-space density is almost uniformly distributed over the occupied region:

$$\rho_0(x,q) = \frac{1}{\pi} \theta(q) \theta(q_F - q) \theta(x) \theta(A - x), \tag{5.39}$$

in such a way that, integrating over the momenta we recover the initial spatial density

$$\rho_0(x) = \int \rho_0(x,q) dq = \frac{q_F}{\pi} \theta(x) \theta(A - x). \tag{5.40}$$

Just after the sudden quench to the new potential, the kinetic energy is locally left unchanged, therefore the distribution of bosons over the region $\mathcal{A}$ with a given momentum

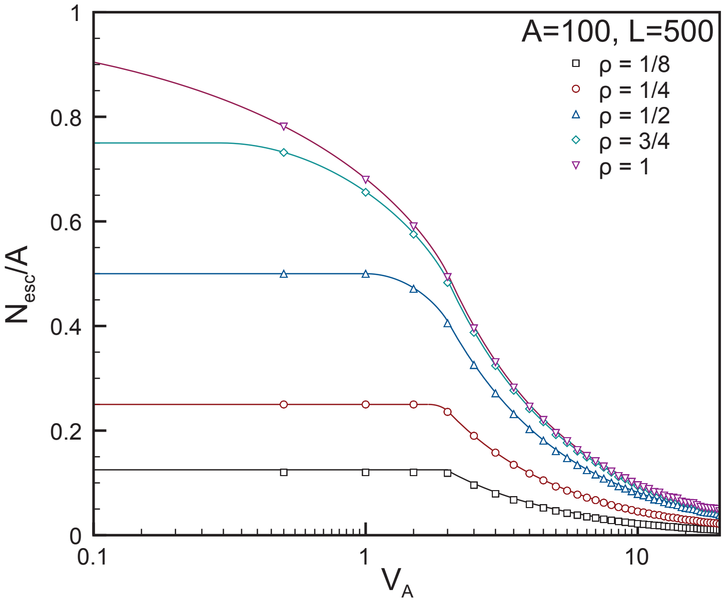

Figure 5.7: Particle density departing from the left zone as a function of the potential V_A. The different symbols represent simulations for different initial filling densities. We used $L = 500$, $A = 100$. The straight lines are the theoretical predictions reported in Table 5.1.

q (kinetic energy $-\cos q$) is shifted in energy by the additional potential energy $V(x)$. One has, for a given energy E, the space distribution

$$\begin{aligned} \rho_0(E,x) &= \int dq \rho_0(x,q)\delta(E - V(x) + \cos q) \\ &= \begin{cases} \frac{1}{\pi}\int_0^{q_F} dq\delta(E - V(x) + \cos q) & \text{for} \quad x \in [0, A] \\ 0 & \text{for} \quad x > A \end{cases} \end{aligned} \tag{5.41}$$

The new energy band, with the same width $\Delta = 2$ as the initial one, is deformed in space, following the potential $V(x)$ as sketched on Figure 5.1. During the time evolution the dynamics is unitary and, since the Fermi quasi-particles are noninteracting, the energy is conserved for each of them. In region $\mathcal{A}$ only those initial particles with energy E within the range $[-1, 1]$ (we have chosen the new zero of energy to be 0) are connected to the propagating states of the band at $x > A$. These particles will escape from the region $\mathcal{A}$ and propagate to $+\infty$ as time runs on.

5.4.1 Ejected particles

The total number of bosons N_{esc} leaving the region $\mathcal{A}$ is just given by integrating equation (5.41) over the connected domain. Using energy variable, it corresponds to the range $[-1, 1]$. In particular, one obtains for $V_A = pA \leq 1 + \cos(\pi\rho_0)$, $N_{esc} = N$, that is all the particles leave the initial region. On the contrary, for a given length A, if we increase the slope p, part of the particles is trapped in region $\mathcal{A}$. As an example, for $V_A \geq 2$, the number of bosons

V_A	N_{esc}
$[0, 1 + V_0]$	N
$[1 + V_0, 2]$	$\frac{1}{p}\left(\rho_0 + \frac{\sin \pi\rho_0}{\pi}\right) - g(V_A)$
$[2, \infty]$	$\frac{1}{p}\left(\rho_0 + \frac{\sin \pi\rho_0}{\pi}\right)$

Table 5.1: . Ejected HC bosons for different value of the slope. See the text for the definition of the function $g(V_A)$.

leaving $\mathcal{A}$ is

$$\begin{aligned} N_{esc} &= \frac{1}{\pi}\int_{x_p^+}^{A} dx \int_0^{\hat{q}(x)} dq \\ &= \frac{1}{\pi p}\int_{-1}^{1} dE \int_0^{\hat{q}(E)} dq, \end{aligned} \tag{5.42}$$

and using

$$\hat{q}(E) = \begin{cases} q_F & \text{for} \quad -\cos q_F \le E \le 1 \\ \arccos(-E) & \text{for} \quad -1 \le E \le -\cos q_F \end{cases} \tag{5.43}$$

one obtains

$$\begin{aligned} N_{esc} &= \frac{1}{\pi}\left\{ q_F(1+\cos q_F) - \int_1^{\cos q_F} \arccos(y)dy \right\} \\ &= \frac{1}{p}\left(\rho_0 + \frac{\sin \pi\rho_0}{\pi}\right), \quad V_A \ge 2. \end{aligned} \tag{5.44}$$

In Tables 5.1 we summarize the results for N_{esc} for different values of V_A, where the function $g(V_A)$ is given by

$$g(V_A) = \frac{1}{p\pi}\left[(1-V_A)\arccos(V_A-1) + \sqrt{V_A(2-V_A)}\right]. \tag{5.45}$$

Finally, in Figure 5.7 we compare the theoretical curves with the exact numerical diagonalization.

Since there are no accessible states to the right of the tilded band edge, the particles with energy E within $[1, V_A + 1]$ are trapped within the region $[x_{min}(E), x_{max}(E)]$, where the boundary values $x_{min}(E)$ and $x_{max}(E)$ are solutions respectively of

$$V(x_{min}) - 1 = E \quad \text{and} \quad V(x_{max}) + 1 = E, \tag{5.46}$$

if we neglect small tunneling escapes at the band edges.

5.4.2 Hydrodynamical equation of motion

The motion of the elementary particles is ballistic with velocities depending only on there kinetic part $E - V(x) = -\cos q$. At each initial position x and momentum q (or for a given energy E), half of the local density in (5.41) is emitted to the right with velocity $v^+(q)$ and half to the left with the opposite velocity $v^-(q)$. The modulus of the velocities is given simply by considering the dispersion relation

$$v^{\pm}(q) = \pm \left| \frac{\partial E}{\partial q} \right| = \pm \sin q. \tag{5.47}$$

At the band edges the particles are reflected and they start to travel on the opposite side. Using the fact that the energy is conserved during the unitary dynamics, together with the definition of the velocity, one obtains the equation of motion

$$\begin{aligned} \frac{dx}{dt} &= \pm \sin q, \\ p\frac{dx}{dt} &= \sin q \frac{dq}{dt}, \end{aligned} \tag{5.48}$$

which, for an initial particle located in (x_0, q_0), yields

$$\begin{cases} E - V(x^{\pm}(t)) &= -\cos(q_0 \pm pt) \\ E - V(x_0) &= -\cos(q_0) \end{cases}, \tag{5.49}$$

$x^{\pm}(t)$ giving the evolution of the particles with the sign $+$ standing for an initial right mover and the sign $-$ for a left mover.

Once we have the equation of motion of a single particle starting in (x_0, q_0), the right and left densities at time t are given by

$$\rho^{\pm}(x, q, t) = \frac{1}{2} \iint dq_0 dx_0 \mathcal{G}^{\pm}(x, q, t; x_0, q_0) \rho_0(x_0, q_0), \tag{5.50}$$

with total density $\rho(x, q, t) = \rho^+(x, q, t) + \rho^-(x, q, t)$. The right and left propagators $\mathcal{G}^{\pm}$ are simply given by

$$\mathcal{G}^{\pm}(x, q, t; x_0, q_0) = \delta(x - x^{\pm}(x_0, q_0, t)) \delta(q - q^{\pm}(x_0, q_0, t)), \tag{5.51}$$

where we have reported the explicit dependence of the solution $x^{\pm}$ and $q^{\pm}$ on the initial conditions (x_0, q_0). The meaning of the equation (5.50) together with the equation (5.51) is actually easy to understand: we are looking for the particles that at time t are exactly in the infinitesimal region $dxdq$ around (x, q); these particles are given by the subdomain $\mathcal{D}_{(x,q)} \subset \mathcal{D}_0$ (where $\mathcal{D}_0$ represents the phase-space domain occupied by the initial phase-space density ρ_0) connected to the region $dxdq$ through the delta functions $\delta(x - x^{\pm})\delta(q - q^{\pm})$ (See Figure 5.8).

Moreover, if we are only interested in the spatial density, we can integrate over the momentum q and, using the normalization of the delta function and the initial uniform phase-space density (5.39), one has

$$\rho^{\pm}(x, t) = \frac{1}{2\pi} \int_0^{q_F} dq_0 \int_{\mathcal{D}} dx_0 \delta(x - x^{\pm}(x_0, q_0, t)), \tag{5.52}$$

where $\mathcal{D}$ is the specific spatial (or energetic) domain we are working with.

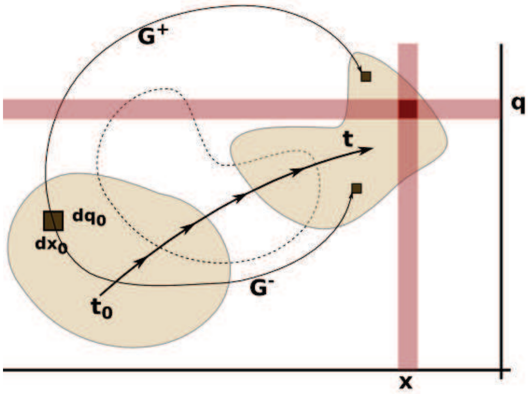

Figure 5.8: Pictorial representation of the dynamics in the phase space. Each infinitesimal volume $dx_0 dq_0$ of the initial distribution moves along the propagator $G^{\pm}$ and, at time t, a new distribution is produced.

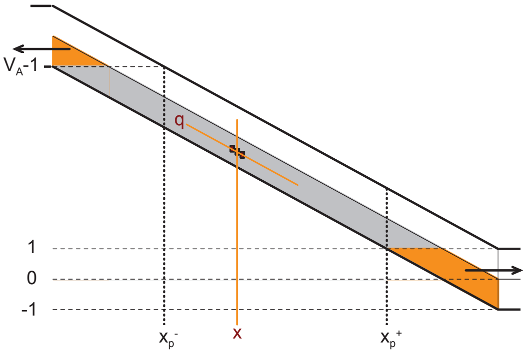

Figure 5.9: After connecting also the higher energy states to a propagating band, the only particles that stay trapped are those on the gray stripe and they show a periodic motion.

5.4.3 Trapped particle dynamics

We begin our studies by looking at the temporal evolution of the density profile of particles initially located in the energy band $[1, V_A - 1]$. In this case, instead of (5.52), it is better to change the integration variable x_0 to the energy variable E. By using the equivalence

$$dx_0 \delta(x - x^{\pm}(x_0, q_0, t)) = dE \delta(E - V(x) + \cos(q_0 \pm pt)), \tag{5.53}$$

we obtain

$$\rho^{\pm}(x,t) = \frac{1}{2\pi} \int_0^{q_F} dq_0 \int_1^{V_A - 1} dE \delta(E - V(x) + \cos(q_0 \pm pt)). \tag{5.54}$$

At higher energies, for $E \in [V_A - 1, V_A + 1]$, the presence of the free boundary at $x = 0$ breaks this very simple harmonic motion. Indeed, particles sharing initially the same momentum q are not reflected at the left wall ($x = 0$) at the same time and a dephasing appears between them. Consequently, the contribution of these particles to the total spatial density is somehow incoherent. A simply way to avoid this incoherent contribution is to connect the system on the left with a left propagating band, by taking $V(x < 0) = V_A$, such that

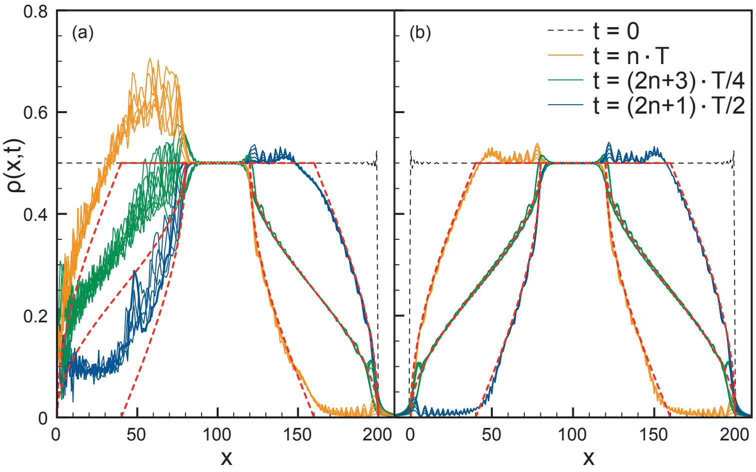

Figure 5.10: Trapped boson space density at different times. Black dashed curve is the initial density profile at time $t = 0$. Red dashed curves represent the temporal evolution of the profile as predicted by the hydrodynamical theory. In (a) the free boundary condition in $x = 0$ is still present. In (b) we have left the higher energy modes to escape to the far left. System parameters are $\rho_0 = 1/2$, $V_A = 5$, $L = 1000$, $A = 200$.

these high energy particles leave the region $\mathcal{A}$ to the far left as those low energy particles have done to the far right (see Figure 5.9). Notice that V_A has to be larger than the band width $\Delta = 2$ in order to have self-trapped particles. In the following we pursue our analysis with $V_A > \Delta$. The trapped bosons space density $\rho(x,t) = \rho^+(x,t) + \rho^-(x,t)$ is obtained by integrating (5.54) over the energy range. After the change of variables $z = q_0 \pm pt$ one has

$$\rho^{\pm}(x,t) = \frac{1}{2\pi}\int_{\pm pt}^{q_F \pm pt} dz\theta(V_A - 1 - px - \cos z)\theta(px - 1 + \cos z), \tag{5.55}$$

thus, thanks to the symmetries of the integral,

$$\rho(x,t) = \frac{1}{2\pi}\int_{pt-q_F}^{pt+q_F} dz\theta(V_A - 1 - px - \cos z)\theta(px - 1 + \cos z). \tag{5.56}$$

The lower bound of the integrand is given by the locus of the point where the one-particle energy $V(x) - \cos z$ reaches the upper trapping value $V_A - 1$:

$$x_{inf}(z) = \frac{1 - \cos z}{p}. \tag{5.57}$$

The upper spatial bound is fixed by the lower self-trapping energy $V(x) - \cos z = 1$ and leads to

$$x_{sup}(z) = x_{inf}(z) + \frac{V_A - 2}{p}. \tag{5.58}$$

These left and right boundaries are 2π-periodic functions of z. At partial filling, for $\rho_0 < 1$, it implies a periodic motion of the self-trapped density (5.56) with oscillation period $T = 2\pi/p$. On the contrary, at complete filling (Mott initial state with $\rho_0 = 1$), $q_F = \pi$ and the integration range in (5.56) is over a full period of the theta functions and leads to a static density profile (after the escaping particles have left the region $\mathcal{A}$). The self-trapped density oscillates in time only if the system has been prepared initially in the superfluid phase $\rho < 1$. Another very interesting feature of the self-trapped density at large enough gradients, $p > 4/A$, is the appearance of a stationary plateau with $\rho(x,t) = \rho_0$ for $x \in \Omega = [x_p^-, x_p^+]$ with

$$x_p^{\pm} = \frac{A}{2} \pm \left(\frac{A}{2} - \frac{2}{p}\right) = \frac{A}{2}\left[1 \pm \left(1 - \frac{4}{V_A}\right)\right]. \tag{5.59}$$

As a function of time, the remaining bosonic density oscillates between a macroscopic left state, where the density is enhanced in the region $[0, x_p^-]$, and a right state with enhanced density in $[x_p^+, A]$. The explicit density profile is easily computed at any time t from (5.56). For example, at integer multiplies n of the period $T = 2\pi/p$, the distribution of the trapped bosons is shifted maximally to the left and it is given by

$$\rho(x, nT) = \begin{cases} \arccos[V(x) - V_A + 1]/\pi & 0 \le x \le x_{inf}(q_F) \\ \rho_0 & x_{inf}(q_F) \le x \le x_p^+ \\ \rho_0 - \arccos[V(x) - 1]/\pi & x_p^+ \le x \le x_{sup}(q_F) \\ 0 & x_{sup}(q_F) \le x \le A \end{cases}. \tag{5.60}$$

Notice that the plateau extends to the left up to the value $x_{inf}(q_F)$. The distribution then propagates from this macroscopic left state to the macroscopic right one (reached at odd multiplies of the half period $t = (2n+1)T/2$). The spatial profile of the right state is simply deduced from the left one by the transformation $x \to A - x$, using the mirror symmetry at $A/2$. In Figure 5.10 we have plotted the density profile at different times, both for high energy states non-connected (a) and connected (b) with a left propagating band. Notice how the incoherent contribution of the high energy modes in (a) increases both the average value and the fluctuations of the particle density near the left boundary.

So far, we have seen the oscillation of a macroscopic state of particles from the left to the right of the trapping-zone. Thus, we expect a current of particles that flows through the plateau region. This current should be spatially constant within the plateau region and it should be periodic with period T. Indeed, proceeding on the same lines, one can compute the bosonic current density $j(x,t)$. The local current across two neighboring sites $l-1$ and l is defined via the Heisenberg continuity equation

$$\frac{dn_l}{dt} = i[H, n_l] \equiv -\nabla j_l = j_{l-1} - j_l, \tag{5.61}$$

that leads to

$$j_l = -\mathrm{Im}(b_l b_{l+1}^\dagger) = \frac{i}{2}(b_l b_{l+1}^\dagger - b_{l+1} b_l^\dagger). \tag{5.62}$$

In the hydrodynamical limit considered here, the current is simply $j = \rho v$, and it leads to the sum over all momenta of $[\rho^+(q) - \rho^-(q)] \sin q$, which basically adds a $\sin z$ factor inside the integral (5.56):

$$j(x,t) = \frac{1}{2\pi}\int_{pt-q_F}^{pt+q_F} dz \sin z\, \theta(V_A - 1 - px - \cos z)\theta(px - 1 + \cos z). \tag{5.63}$$

It is easily shown that the current (5.63) and the density (5.56) verify the continuity equation $\partial_t \rho(x,t) = -\partial_x j(x,t)$. Moreover, in the plateau region $\Omega = [2/p, A - 2/p]$ the conditions imposed by the theta functions are always fulfilled and one has simply

$$j(x,t) = \frac{1}{\pi}\sin(q_F)\sin(pt), \quad \forall x \in \Omega. \tag{5.64}$$

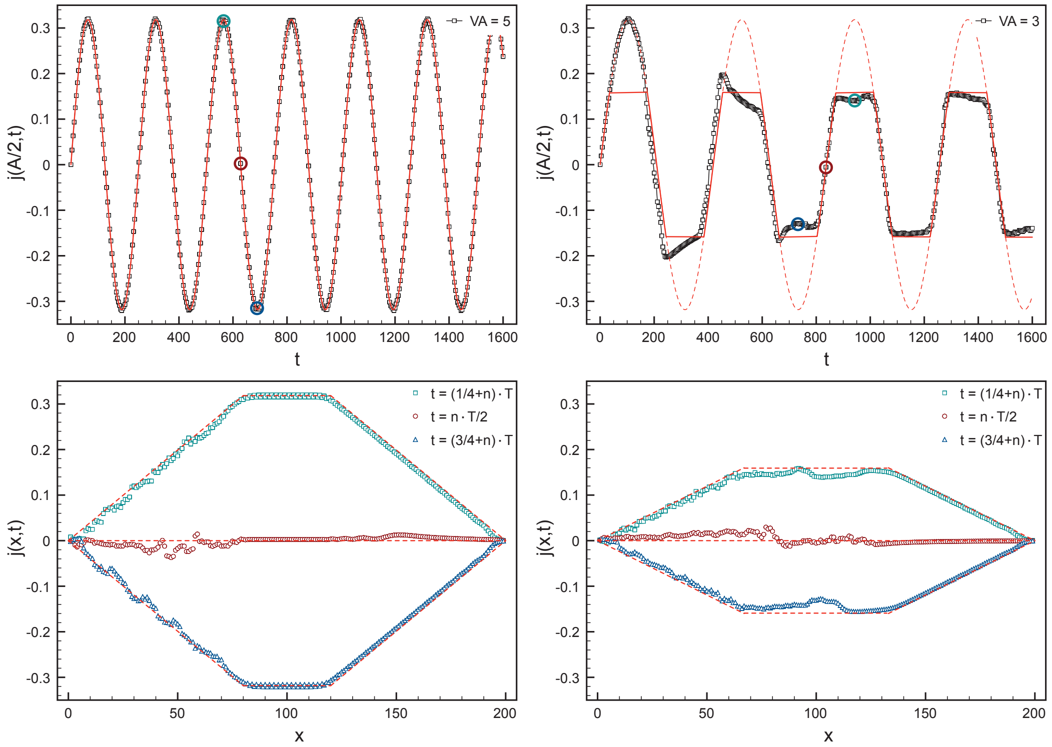

Figure 5.11: (top) Time evolution of the current in the middle of the ramp $x = A/2$ for different values of V_A. The straight red lines are the hydrodynamical predictions as reported in the text. The small colored circle indicate the temporal instants at which the spatial profile of the current are plotted (bottom). Here, the dashed red lines are the hydrodynamical predictions. The irregular fluctuations in the left part of the spatial profiles are essentially due to the incoherent motion of the high energy particles. Indeed, numerical simulations are done with free boundary condition in $x = 0$. System parameters are $\rho_0 = 1/2$, $L = 1000$, $A = 200$.

Notice that there is a maximum particles exchange at half filling ($q_F = \pi/2$), while obviously there is no more particle exchange in the Mott phase (complete filling $q_F = \pi$) which reflects the fact that the trapped density profile remains stationary in time.

We can also calculate the temporal evolution of the current at $x = A/2$ for $2 < V_A < 4$ (no plateau region but still trapped particles). Specializing the calculation for the parameters in Figure 5.11, i.e. $q_F = \pi/2$ and $V_A = 3$, and changing the integration variable to $y = \cos z$, one has

$$j(A/2,t)_{\{V_A=3,q_F=\pi/2\}} = \frac{1}{2\pi}\int_{-\sin(pt)}^{\sin(pt)} dy\,\theta(1/2-y)\theta(1/2+y), \tag{5.65}$$

that yields

$$j(A/2,t)_{\{V_A=3,q_F=\pi/2\}} = \begin{cases} \sin(pt)/\pi & |\sin(pt)| \leq 1/2 \\ 1/2\pi & |\sin(pt)| \geq 1/2 \end{cases} . \tag{5.66}$$

The cut for $|\sin(pt)| > 1/2$ is essentially due to the escaping particles which initially are located at $x = A/2$. Indeed, for $V_A < 4$ the lower propagating zones extend over the middle of the condensate, i.e. $x_p^+ < A/2$ (see Figure 5.9), producing a lowering of the current intensity after the escaping particles are ejected. As a support of this, notice how during the first half period, as all the particles are moving from the left to the right and have not yet abandoned the condensate, the current shows a perfect sinusoidal signal. If we generalize these arguments, it is possible to catch some properties of $j(x,t)$ for every value of $V_A > 2$ and q_F. Indeed, by comparing the length $2|\sin(pt)||\sin(q_F)|$ of the integration interval $[\cos(pt-q_F), \cos(pt+q_F)]$, with the length $V_A - 2$ of the definition interval of the theta functions, we argue that for

$$V_A - 2 \geq 2|\sin(q_F)|, \tag{5.67}$$

there will be a spatial interval (the plateau region $\Omega \in \mathcal{A}$) in which the current will show a complete sinusoidal behavior. Otherwise, whenever the condition (5.67) is violated, the current will exhibit cuts in its temporal evolution $\forall x \in \mathcal{A}$.

Furthermore, starting from equation (5.63), and still considering the high energy particles connected to a propagating band which extends to the far left, we can straightforwardly calculate the current profile in space for time multiple of $T/4$. Changing the integration variables to $y = \cos z$ one has

$$j(x, T/4 + nT) = \frac{1}{2\pi}\int_{-\sin q_F}^{\sin q_F} dy\, \theta(V_A - 1 - px - y)\theta(px - 1 + y). \tag{5.68}$$

Now we specialize the integral for the parameters in Figure 5.11: $q_F = \pi/2$ and $V_A = 5$ and 3. In the case with a plateau region ($V_A = 5$), the theta functions impose the conditions $y > 1 - px \in [-4, 1]$ and $y < 4 - px \in [-1, 4]$. By comparing this boundary with the extremes of integration $[-1, 1]$ one has:

$$j(x, T/4 + nT)_{\{V_A=5, q_F=\pi/2\}} = \begin{cases} px/2\pi & 0 \leq x \leq 2/p \\ 1/\pi & 2/p \leq x \leq 3/p \\ V_A/2\pi - px/2\pi & 3/p \leq x \leq A \end{cases}. \tag{5.69}$$

In the other case, for $V_A = 3$, we have the conditions $y > 1 - px \in [-2, 1]$ and $y < 2 - px \in [-1, 2]$. Again, comparing with the extremes of integration, we get the result:

$$j(x, T/4 + nT)_{\{V_A=3, q_F=\pi/2\}} = \begin{cases} px/2\pi & 0 \leq x \leq 1/p \\ 1/2\pi & 1/p \leq x \leq 2/p \\ V_A/2\pi - px/2\pi & 2/p \leq x \leq A \end{cases}. \tag{5.70}$$

All these results are compared in Figure 5.11 with the numerical data we have obtained on finite Hard-Core boson systems. For sufficiently high potential such that there are still trapped particles but no more a plateau (for $V_A = 3$ in Figure 5.11), the current is initially coherent, then, due to the escaping particle dynamics, it loses the complete sinusoidal shape, as explained before, nevertheless retaining its periodic behavior.

5.4.4 Escaping particle profile

One can use the same hydrodynamical description in order to predict also the time-evolution of the profile of the escaping particles. With respect to the Figure 5.12, the particles leaving the initial region $\mathcal{A}$ are those in the spatial interval $[x_p^+, A]$ (i.e. with energies within $[-1, 1]$), and with momenta up to the Fermi-level q_F imposed by the initial condition. Considering a local phase-space infinitesimal volume $dx_0 dq_0$ around an allowed (x_0, q_0), it corresponds to $dE dq_0/p$ around an allowed (E, q_0). This local density evolves, under the influence of the

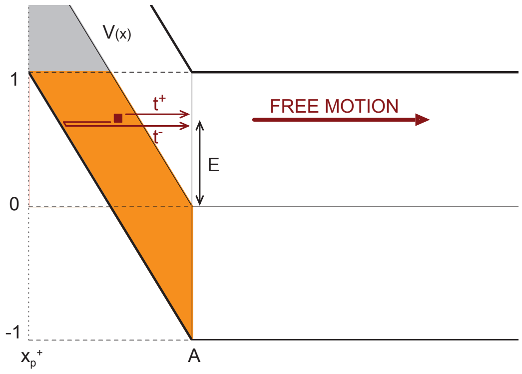

Figure 5.12: Sketch of the area in the phase-space of the particles energetically connected to the propagating band. Here the Fermi-level was fixed to $q_F = \pi/2$, corresponding to half-filling initial condition. See the text for more explanations.

linear potential, up to a time $t^{\pm}$ (respectively for right$(+)$ and left$(-)$ modes). After that time, the evolution continues with constant velocity $\sqrt{1-E^2}$ through the right band. By imposing that particles arrive at $t = t^{\pm}$ at position A one has:

$$t^{\pm} = \frac{1}{p}\arccos(-E) \mp \frac{q_0}{p}. \tag{5.71}$$

Notice that, at least in the worst case (Mott initial state), all particles leave the ramp for $t \geq T$. Thus, we have

$$x^{\pm}(E, q_0, t) = \sqrt{1-E^2}(t - t^{\pm}) + A. \tag{5.72}$$

The evolution of the density profile of the ejected particles ($x > A$) is then given by the sum of the evolved densities

$$\rho^{\pm}_{esc}(x,t) = \frac{1}{2\pi p}\int_{-1}^{1} dE \int_{0}^{\hat{q}(E)} dq_0\, \delta(x - x^{\pm}(E, q_0, t)), \tag{5.73}$$

where $\hat{q}(E)$ is the same function introduced in (5.43). Now using the property of the delta function $\delta(f(z)) = \delta(z - z_0)/|f'(z_0)|$ where $f(z_0) = 0$, we can rearrange the integral as

$$\begin{aligned} \rho^{\pm}_{esc}(x,t) &= \frac{1}{2\pi}\int_{-1}^{1} \frac{dE}{\sqrt{1-E^2}} \int_{0}^{\hat{q}(E)} dq_0\, \delta(q_0 - q^{\pm}(E,x,t)) \qquad (5.74)\\ &= \frac{1}{2\pi}\int_{-1}^{1} dE \frac{\theta(q^{\pm}(E,x,t))\theta(\hat{q}(E) - q^{\pm}(E,x,t))}{\sqrt{1-E^2}}, \end{aligned}$$

where

$$q^{\pm}(E,x,t) = \pm\left[\frac{p(x-A)}{\sqrt{1-E^2}} + \arccos(-E) - pt\right]. \tag{5.75}$$

Also for the ejected particles, exploiting the hydrodynamical relation $\partial_t \rho(x,t) = -\partial_x j(x,t)$, starting from equation (5.74), since, for $t > t^{\pm}$, each mode propagates with constant velocity $v(E) = \sqrt{1-E^2}$, we basically obtain

$$j^{\pm}_{esc}(x,t) = \frac{1}{2\pi}\int_{-1}^{1} dE\, \theta(q^{\pm}(E,x,t))\theta(\hat{q}(E) - q^{\pm}(E,x,t)), \tag{5.76}$$

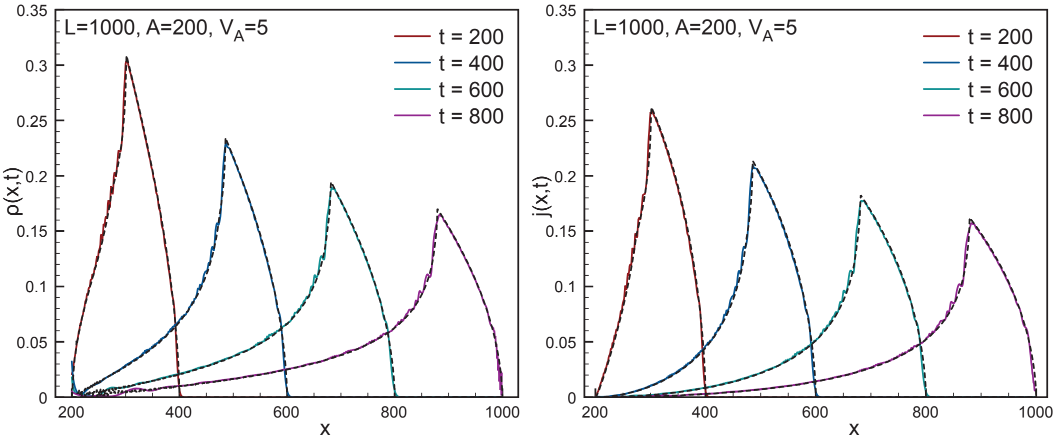

Figure 5.13: Density (left) and current (right) profiles of the ejected particles at different times for the HC boson model. The dashed black lines represent the hydrodynamical prediction (5.74) and (5.76), perfectly in agreement with the numerical simulations (colored full lines).

for the ejected current. In Figure 5.13 we see the very good agreement, up to small quantum interference effects, between the actual data obtained numerically by exact diagonalization and the hydrodynamical prediction.

5.5 Noninteracting boson dynamics

Before introducing the simulations for the real boson dynamics, it would be better to compare the results we have got in the Hard-Core boson limit with the dynamics of noninteracting bosons. As we previously said, the value $U = 0$ in the Bose-Hubbard Hamiltonian corresponds to another integrable point in the parameter space. The dynamics is the same as in the Hard-Core boson limit, but now, the initial particle density in space is given by

$$\rho_0 \simeq \frac{2N}{A} \sin^2\left(\frac{\pi x}{A}\right), \tag{5.77}$$

where N is the total number of particles we have put into the system. In Figure 5.14 and 5.15 we plot the particle density profile and the current profile for noninteracting bosons. In that case the dynamics does not depend on the initial particle density since particles occupy the lower one-particle energy level and the dynamics is finally governed by the lower momentum q_0 associated to that state.

Ejected particles Also in this case we can use energetic considerations to describe how the total number of ejected particles N_{esc} varies as a function of the gradient $p = V_A/A$. The initial density (5.77) describes N bosons in the lower energy level, i.e. with momentum $q_0 \simeq \pi/A$. After the sudden quench, referring to the Figure 5.1, all particles should stay in the line corresponding to the lower boundary of the energy band, $V_A - px - 1$. Also in this case, the particles leaving the ramp are those with energy $E \in [-1, 1]$, i.e. confined in the

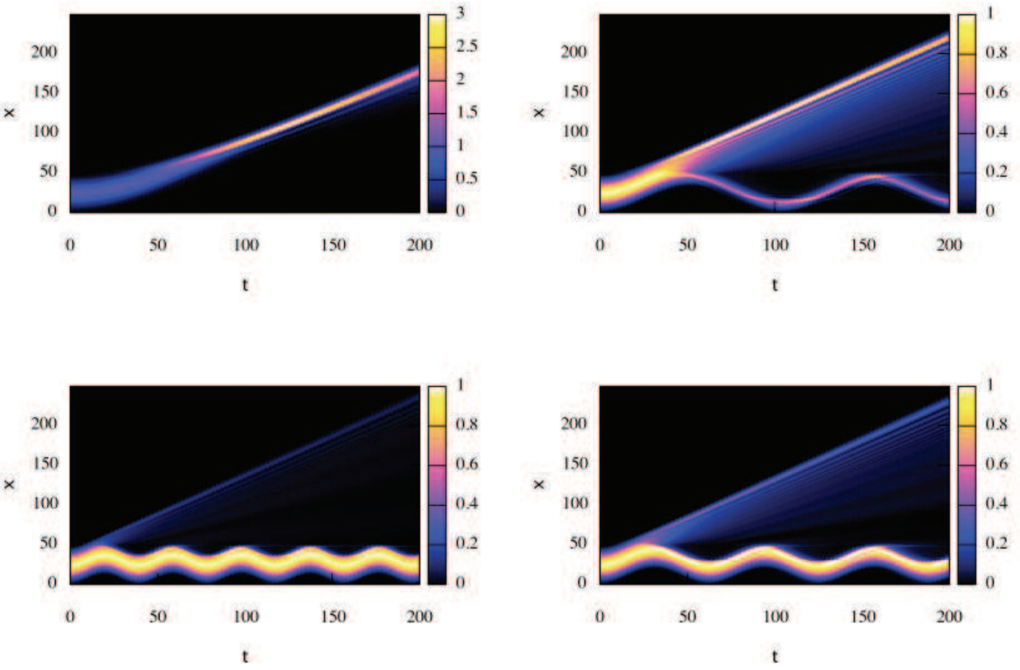

Figure 5.14: Maps of particle densities for noninteracting bosons in a system with $A = 50$ and $N = 25$. Starting from the top left figure and going clockwise, one has $V_A = 1$, 3, 5 and 8. Notice that trapped particles appear for $V_A = 3, 5, 8$ without the presence of a plateau. Otherwise, particles still oscillate along the ramp. Diagonal stripe represents particles leaving the ramp.

spatial interval $[x_p^+, A]$. Thus, one has

$$\begin{aligned} N_{esc}^{U=0} &= \frac{2N}{A}\int_{x_p^+}^{A} dx \sin^2\left(\frac{\pi x}{A}\right) \\ &= \begin{cases} N & \text{for} \quad V_A \in [0,2] \\ N\left[\frac{2}{V_A} - \frac{1}{2\pi}\sin\left(\frac{4\pi}{V_A}\right)\right] & \text{for} \quad V_A \geq 2 \end{cases} . \end{aligned} \tag{5.78}$$

By comparing the formula (5.78) with the similar hydrodynamical result for the Hard-Core boson reported in Table 5.1 one can notice that, for noninteracting bosons, $N_{esc}^{U=0}$ does not depend on V_0. This is obviously due to the properties of the bosons which, whatever the initial number of particles is, condensate in the lower one-particle energy level E_0. Notice that a fraction of noninteracting bosons starts to be trapped when V_A becomes greater than 2, and this ‘transition’ is somehow more abrupt with respect to the Hard-Core boson behavior. Indeed, in the high slope limit, we obtain

$$N_{esc}^{HC} \sim V_A^{-1}, \quad N_{esc}^{U=0} \sim V_A^{-3}, \quad V_A \to \infty. \tag{5.79}$$

In Figure 5.16 we compare the noninteracting boson with the Hard-Core boson. As we expect, for sufficiently high gradient, the ejected noninteracting boson are less than the

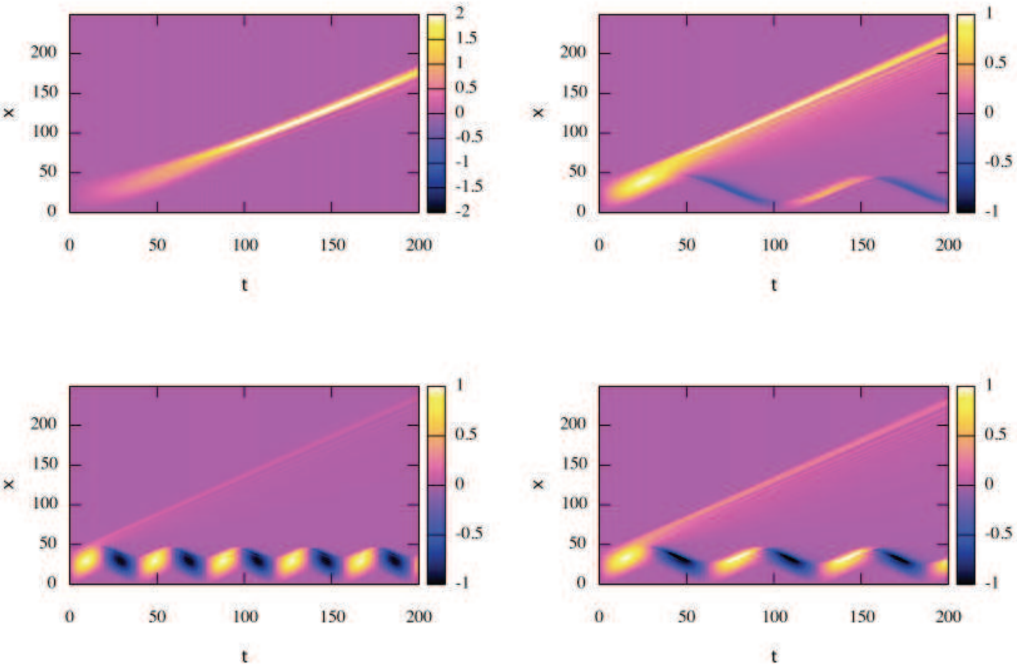

Figure 5.15: Maps of current densities for noninteracting bosons. System parameters are the same as in Figure 5.14. Again, notice the oscillations of the trapped particles for $V_A = 3, 5, 8$. Yellow diagonal stripe is the current associated to the ejected particles.

Hard-Core ones. This is because there are less accessible sites in the region $\mathcal{A}$ for the HC bosons with respect to the noninteracting bosons. The opposite behavior, for small gradient, is essentially due to the uniform distribution of the initial density, up to the Fermi level q_F, for the HC bosons. Indeed, starting with no gradient ($V_A = 0$), Hard-Core bosons start to be trapped in the ramp at $V_A = 1 + V_0$, earlier than noninteracting bosons do. Then, due to the stronger decay of $N_{esc}^{U=0}$ with respect to N_{esc}^{HC}, for sufficiently high value of V_A we obtain the condition $N_{esc}^{HC} > N_{esc}^{U=0}$. The gray region in the Figure 5.16 represents the area where we expect to find the function describing the number of particles ejected in the case of real bosons, i.e. when the dynamics is governed by the Bose-Hubbard Hamiltonian. In other words, the behavior of real bosons should be confined by the two limiting cases.

What we said before is correct in the thermodynamical limit, that is when the system size becomes infinite. Indeed, in such a case, we should have $A \to \infty$, $V_A \to \infty$ with $p = V_A/A < 1$. Otherwise, if one considers small systems, whenever the value of the potential V_A overcomes the length of the region $\mathcal{A}$, and thus the slope p becomes higher then 1, each site of the chain will be energetically unconnected from its neighboring sites. It means that only the rightmost site of the ramp will be connected to the propagative band, therefore at most one particle may be ejected and the behavior of the Hard-Core bosons is reduced to that of noninteracting bosons (see Figure 5.17).

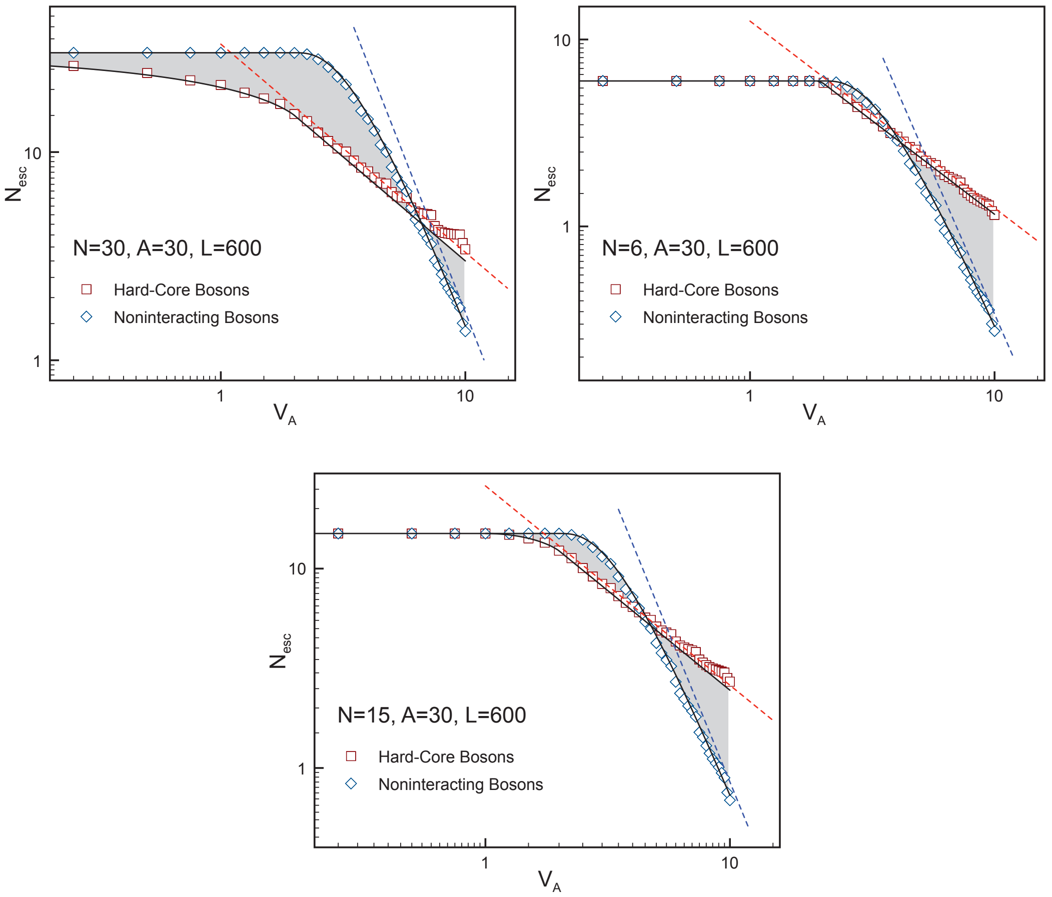

Figure 5.16: Log-Log plot of the total number of particles leaving the ramp as a function of V_A, for different initial filling. We compare the Hard-Core boson result (squares) with the noninteracting boson case (diamonds). Black lines represent the hydrodynamical prediction in both cases. Dashed lines are the power-law behavior in the high slope limit.

5.6 Bose-Hubbard dynamics

Now, we finally turn our attention to the real boson dynamics. As we said before, the Bose-Hubbard Hamiltonian is not analytically tractable, thus we have to resolve the dynamics via numerical approximative methods. Indeed, for simulating the Bose-Hubbard Hamiltonian we have used both the t-DMRG method and the Lanczos diagonalization method. Regarding the t-DMRG method, at the beginning we fix the Hamiltonian equal to H_0, in order to load N bosons in the region $\mathcal{A}$ of the chain, then we look for the ground state using the static DMRG algorithm. In particular, we set the accuracy of the algorithm requiring a precision of 10^{-6} on the ground state energy value. Otherwise, we do not fix limitations on the number of states M describing a block. We increase such a number at each sweep until a satisfactory convergence is reached.

After we have prepared an approximate ground states $|\Psi_0\rangle$, we suddenly change the Hamiltonian introducing a linear potential as mentioned before and we start the simulation with the t-DMRG algorithm. We perform the temporal evolution using a temporal step

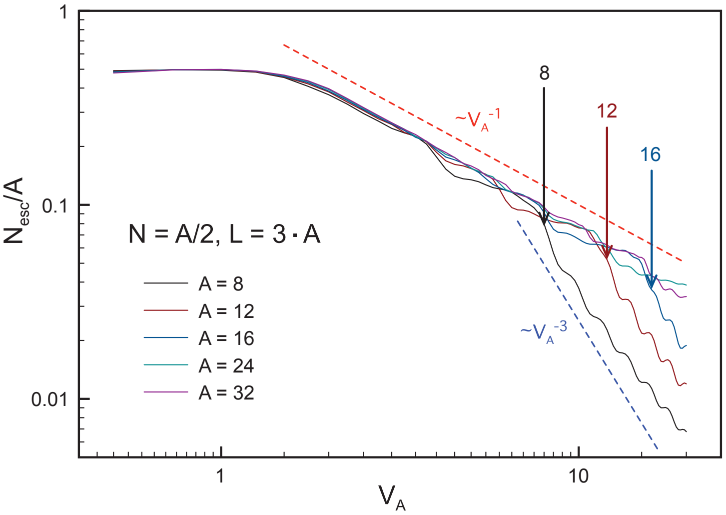

Figure 5.17: Log-Log plot of the total number of Hard-Core bosons leaving the ramp as a function of V_A, for small system sizes. Notice how the behavior follows the hydrodynamical prediction V_A^{-1} up to a 'critical' value $V_A^* \sim A$. For $V_A > V_A^*$, $N_{esc}^{HC}(V_A)$ shows the same scaling behavior of the noninteracting bosons.

$dt = 0.05$ from $t = 0$ to $t = t_{end}$. For each temporal step we perform two t-DMRG sweeps to properly evolve the system from t to $t + dt$. Then, we use another sweep to better adjust the Hilbert space, eventually enlarging the number of states M. This is done by looking at the growing of the entanglement entropy. Finally, we use a sweep for measuring the observables. This algorithm is repeated until the final time is reached. For details on the tDMRG implementation see Appendix C.

5.6.1 Linear ramp and departing particles

According to the quench protocol, we perform t-DMRG simulations on a lattice with length L. We use a local Hilbert space of dimension $D = 3$, i.e. 0, 1 or 2 particles for each site. The evolution ends at time $t_{end} = L - A$ according to the fact that the maximum speed of the quasi-particles in such a system is approximatively equal to 1 and then, we stop the simulation before the faster particles reach the right boundary of the chain.

In Figure 5.18 we plot the temporal evolution of the boson density profile $n(i, t)$, current profile $j(i, t)$ and entanglement entropy $S(i, t)$ for a system with length $L = 64$. The initial state is prepared by fixing $A = 16$ and $U = 10, 5$; V_0 was fixed in order to have $N = 8$ particles. At $t = 0$ we modify the chemical potential as prescribed in the previous sections, fixing $V_A = 8$. As predicted by the local equilibrium theory, it is possible to observe a 'plateau' region in the density profile. Apart from a small fraction of ejected particles, the bigger part of bosons rests trapped in region $\mathcal{A}$. Also the current manifests a regular behavior oscillating with main period $T \sim 2\pi/p$. Nonetheless, the effect of a finite value of U is evident: the amplitude of the oscillations become smaller and smaller with time; somehow, due to the non-integrability of the model, a sort of decoherence appears. Finally, observing the entanglement entropy profile, it is obvious that, despite the small part of ejected particles, after connecting the left part of the system with the right part, the entanglement between the first A sites and the last $L - A$ sites increase in time, giving a signature of the propagation

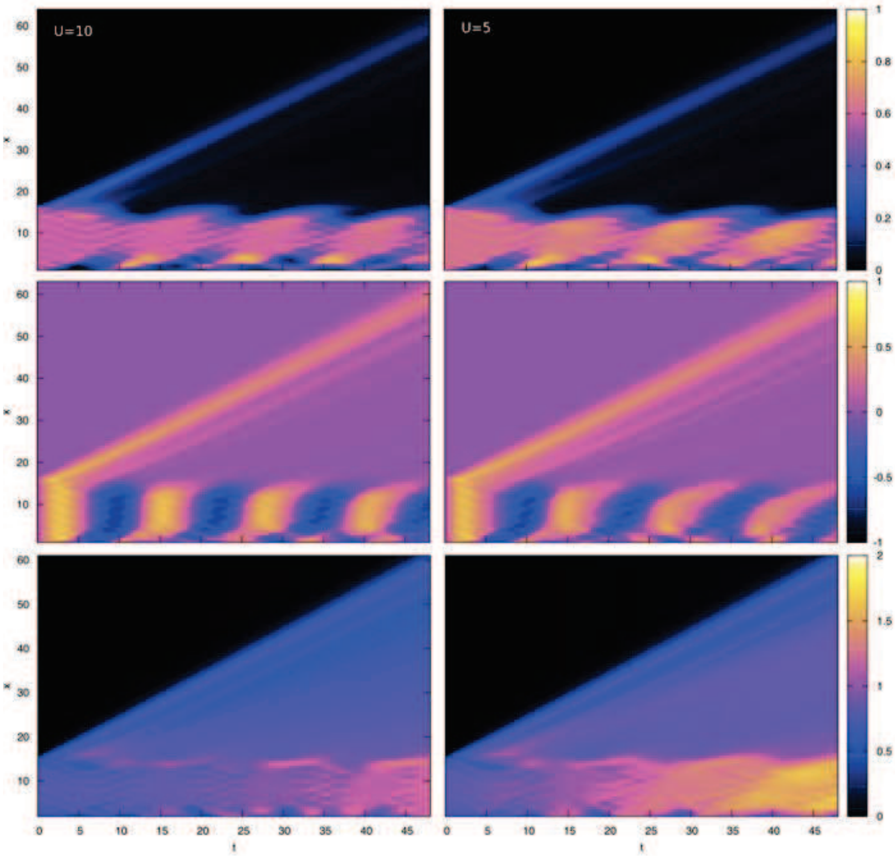

Figure 5.18: From top to bottom, density of particles, current and entropy profiles. The t-DMRG simulations has been done in a system of dimension $L = 64$, with $A = 16$ and $V_A = 8$. Two different values of the local interaction are plotted: $U = 10$ (left) and $U = 5$ (right).

of the escaping particles. To have a better understanding of the effects of a small value of the one-site boson-boson repulsion, we compare, in Figure 5.19, the evolution of systems with length $L = 32$ and $A = 8$, for $U = 10$ and $U = 1$. Now, for $U = 1$, the 'decoherence' effect is definitely stronger than before: the non-integrability of the model results in a strong growing of the entropy inside the region $\mathcal{A}$. In this latter case, a 'plateau' region still survives but the density oscillations are strongly damped while one still observes a small signature on the current density profile.

Ejected particles for real bosons — As we said before, it should be interesting to compare the number of ejected particles in the case of real boson dynamics with respect to the results we already obtained for Hard-Core bosons and Noninteracting bosons. Indeed, for a sufficiently small system, it is possible to simulate the dynamics of the Bose-Hubbard model using the Lanczos algorithm to obtain the initial ground-state $|\Psi(0)\rangle$. Then, the evolution is performed by reiterating the Schrödinger equation $|\Psi(t + dt)\rangle = \exp(-iHdt)|\Psi(t)\rangle$ with

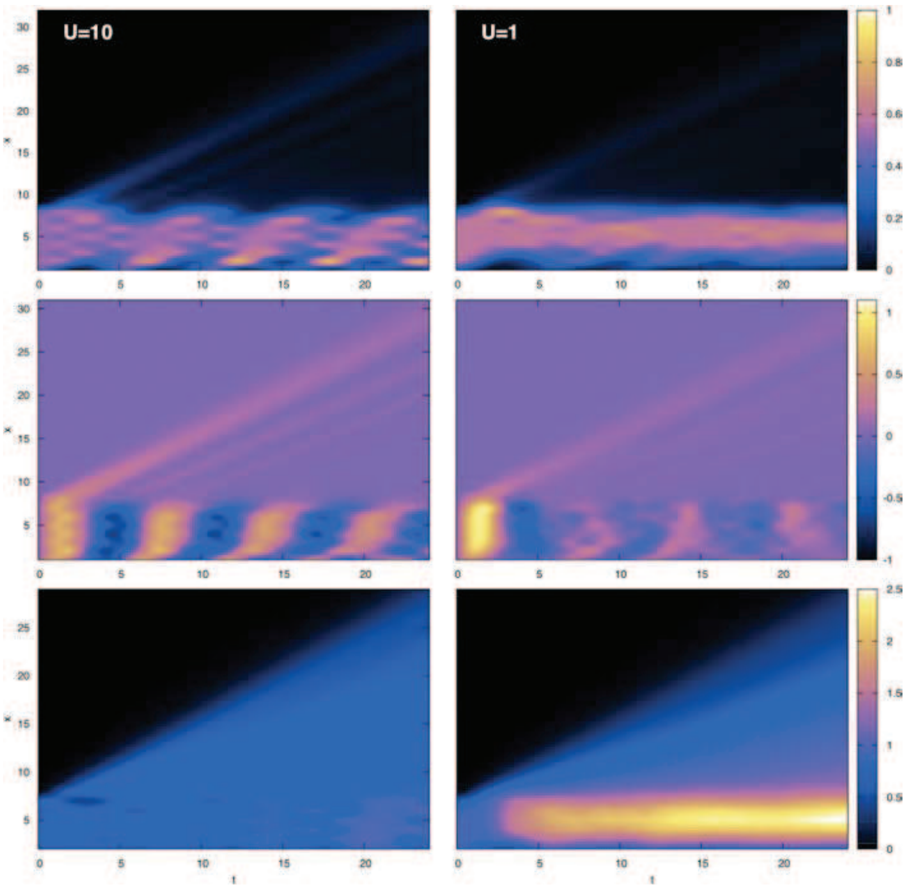

Figure 5.19: From top to bottom, density of particles, current and entropy profiles. The t-DMRG simulations has been done in a system of dimension $L = 32$, with $A = 8$ and $V_A = 8$. Two different values of the local interaction are plotted: $U = 10$ (left) and $U = 1$ (right).

the approximation

$$\exp(-iHdt) \sim \sum_{n=0}^{n_{max}} \frac{(-idt)^n}{n!} H^n. \tag{5.80}$$

The method has basically two sources of errors: the Lanczos precision on the initial state, and the truncation error due to n_{max}. In particular, the convergence criterion in the temporal evolution is fixed by imposing the unitary condition $\langle\Psi(t+dt)|\Psi(t+dt)\rangle = 1$ up to the machine precision. Basically, the evolution in the interval $[t, t+dt]$ is reiterated for different values of n_{max} up to convergence is achieved. Finally, we have to fix also the maximum number of bosons N_{max} for each site. If we are working with a system with a total number of particles $N < N_{max}$ the evolution is exact. Otherwise, for $N > N_{max}$, one introduces another source of error which is smaller the larger the interaction U between the particles is. Thus, we initially prepared a system of total length $L = 32$ with $N = 4$ bosons in the first $A = 8$ leftmost sites. Then, for each value of V_A, we have left the system to evolve up to time $t = 24$. Here, we have chosen N_{esc} in two different way: the maximum value it acquired during the whole temporal evolution, and the value at $t = 24$. In Figure 5.20 we show the

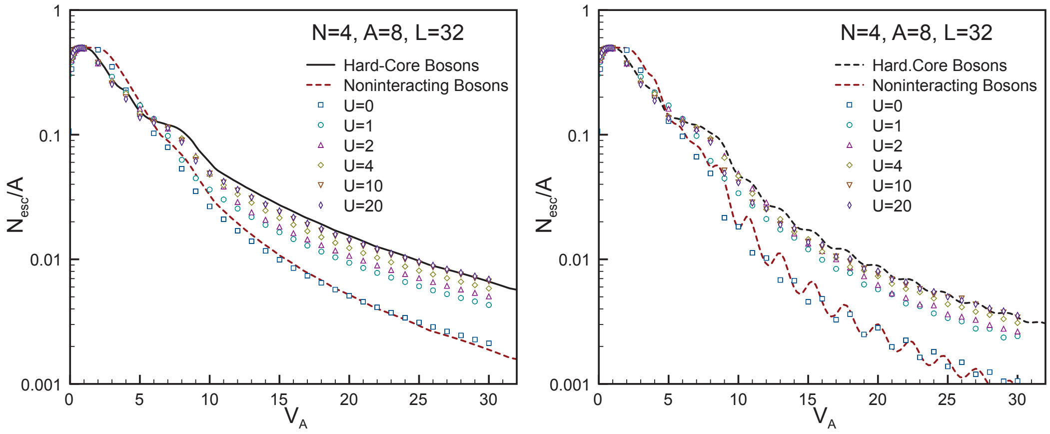

Figure 5.20: Plot of the particles leaving the ramp as a function of V_A. We compare the Hard-Core boson result (black solid line) and the noninteracting boson case (red dashed line) with the Lanczos simulations for real boson dynamics (symbols). In the left figure, N_{esc} is given by the maximum number of ejected particles during the temporal evolution up to the time $t = 24$. In the right figure we keep the values at $t = 24$. These data have been obtained in collaboration with G. Roux (LPTMS, Paris).

results. As predicted before, the real boson data fall between the two limiting cases. The deviation for smaller values of the potential V_A is essentially due to $N_{max} = 3$. Notice how such a deviation is stronger for smaller value of U. Indeed, for small values of U the bosons should behave similarly to noninteracting bosons, however, a finite N_{max} introduces a cutoff in the single-site repulsion in such a way that one has an effective interaction

$$U_{eff} = \begin{cases} U & n \le N_{max} \\ \infty & n > N_{max} \end{cases} , \tag{5.81}$$

where n is the average value of bosons per site. Finally, for V_A close to zero, the lowering of the values of $N_{esc}(V_A)$ is essentially a dynamical effect. In practice, data in Figure 5.20, extrapolated from the time window $t \in [0, 24]$, are quite far from its infinite limit.

Entanglement entropy for real bosons — After the quench, the condensate is split into two entangled pieces moving apart: the escaping particles on one hand and the self-trapped ones on the other hand. Moreover, the tDMRG comes out to be naturally well suited for calculating the entanglement between particles on both sides of position x. Indeed, at each step, the algorithm determines the reduced density matrices of the left $[0, x]$ and right $[x, L]$ subsystems. From the eigenvalues of these matrices is straightforward to calculate the von Neumann entropy $S(x, t) = -Tr\{\rho(x, t) \ln \rho(x, t)\}$, with $\rho(x, t) \equiv Tr_{>x}\{|\Psi(t)\rangle\langle\Psi(t)|\}$.

The surface plots at bottom of Figure 5.19 represent the space-time behavior of the entanglement entropy $S(x, t)$ for the Bose-Hubbard model with $L = 32$ sites, initially prepared with $A = 8$ and $N = 4$. In that case, the evolution is done with a linear potential in region $\mathcal{A}$ with slope $p = 1$. As the particles are ejected in the empty region, the entropy grows, indicating, for each x and t, the entanglement between the region $[0, x]$ and the region $[x, L]$. In the self-trapping region, we observe a strong enhancement of the entanglement at $U = 1$ which has to be compared to the almost constant behavior close to the integarble point $U = \infty$.

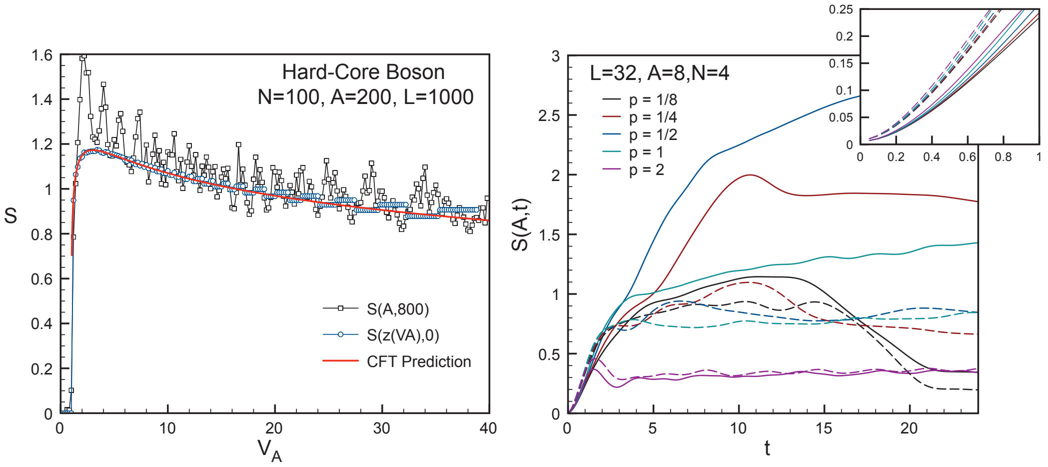

Figure 5.21: (Left) Asymptotic value of the entanglement entropy in the HC boson model for different values of the potential V_A. The evolved entropy $S(A, t = 800)$ (black squares) is compared with the initial entropy $S_0(z(V_A))$ (blue circles) between $[0, z(V_A)]$ and $[z(V_A), A]$, where $z(V_A) \equiv x_p^+$ approximately separates the trapped density from the ejected one. The full red line is the CFT prediction for $S_0(z(V_A))$. (Right) Evolution of the entanglement entropy between regions $[0, A]$ and $[A, L]$ in the Bose-Hubbard model with $U = 1$ (full lines) and $U = 10$ (dashed lines). We have used different colors for different slopes $p = V_A/A$.

In particular, on the right of Figure 5.21, we show the behavior of $S(A, t)$, i.e. the entanglement entropy between the confined-boson packet and the escaping particles. We make this analysis for different values of the slope p and for two different one-site interaction strengths $U = 1$ and $U = 10$. As expected, the entropy grows as the time runs on, up to an asymptotic value that essentially depends on N, U and p. The asymptotic value is reached only if the escaping particles can move far away from the initial region. Of course, as we are working with a finite system, for some values of the couplings, the asymptotic value is not still reached. Notice how, at very low p ($p = 1/8$ in Figure 5.21), when all initial particles are energetically connected to the propagative band, after an initial increase due to the crossing of the position $x = A$ by the particle wave-packet, we observe a fall down of the entanglement related to the (almost-)complete escape of the initial cloud from region $\mathcal{A}$. This behavior is almost independent on the boson interaction value of U. Fixing the value of U, by increasing the slope p, we see a growing of the $S(A, \infty)$. The asymptotic value of the entropy essentially depends on the value of U as well as on the number of the ejected particles: it reaches its maximum when approximately one half of the initial condensate is emitted. The entanglement starts then to decrease at higher slopes since the number of ejected particle fall down (see the case $p = 2$ in Figure 5.21). Moreover, when the system is far away from the integrability points, e.g. for $U = 1$, its initial many-body wave function is already quite entangled. As a consequence, we can see an enhancement of the entanglement entropy. In other words, the asymptotic entanglement basically depends into two factors: the “one-particle entangled” between an emitted particle and the original many-body wave function, and the number of such emitted particles. The “one-particle entangled” essentially depends on U: it is enhanced as the system moves far away from $U = 0$ or $U = \infty$. Otherwise, the dominant behavior of the number of emitted particles depends on the value of the slope p (with a residual weak dependence on U see Figure 5.20).

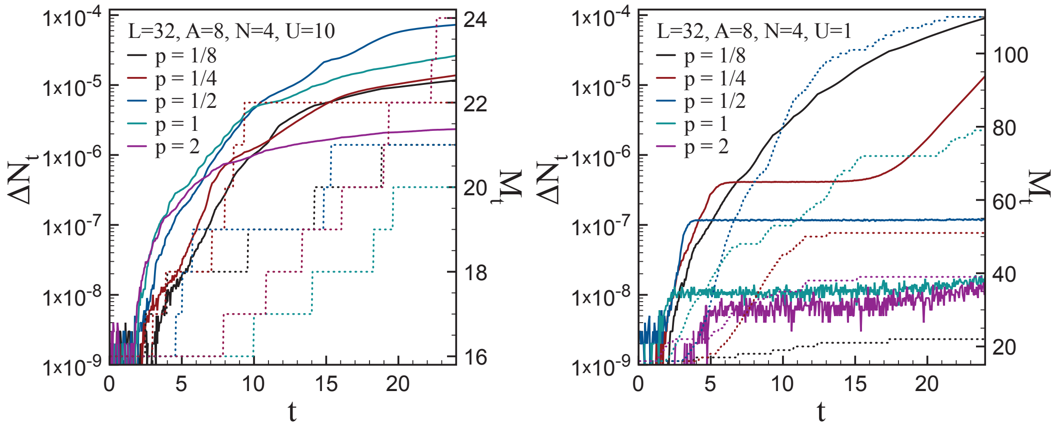

Figure 5.22: The "defect of particles" ΔN_t (full lines) an the adapted Hilbert space dimension $M(t)$ (dashed lines) for the tDMRG simulations and for strong (on the left) and weak (on the right) local interactions U. Different colors represent different potential slope p. Notice how away from the integrability point ($U = 1$) the tDMRG needs much more states to give almost the same accuracy as that obtained when the system is close to the integrability ($U = 10$).

We give a numerical evidence of such an argument by confronting (see on the left of Figure 5.21), in the Hard-Core boson limit, the asymptotic entanglement entropy $S(A, \infty)$ as a function of V_A with the initial bipartite entanglement entropy $S_0(x_p^+)$ evaluated at the point $x_p^+ = A - 2A/V_A$ which approximately separates the trapped particles from those connected to the propagative band. In particular, the initial bipartite entropy is predicted by Conformal Field Theory (CFT) arguments to be

$$S_0(x) = \frac{1}{6} \ln \left(\frac{4A \sin \pi \rho_0}{\pi} \sin \frac{\pi x}{A} \right) + c', \tag{5.82}$$

where $c' \simeq 0.25$ is a non-universal constant [ABS11, CMV11, CMV]. We see that the asymptotic value is nothing but the total initial entanglement between the density that will remain trapped and the escaping one.

Finally, in the inset of Figure 5.21 we show the early instants evolution of $S(A, t)$: the initial growing of the entropy is strongly affected by the rate at which the particles are emitted. This initial emitting rate depends on the one-site repulsion strength U as well as on the slope p. The particles are initially emitted at a rate faster the higher is the slope and the stronger is the one-site repulsion.

Adaptive t-DMRG: technical details and error analysis — To study the the time-evolution of the Bose-Hubbard model we have implemented an adaptive t-DMRG algorithm[Vid03, Vid04, DKSV04, WF04]. In all tDMRG simulations we have fixed $J = 1/2$ and the local Hilbert space dimension $D = 3$ (0,1 or 2 bosons per sites). With reference to the previous entanglement entropy analysis, the system, with total site number $L = 32$, has been initially prepared in the ground state of the initial Bose-Hubbard Hamiltonian H_0 characterized by a given value of the repulsion strength U and an initial potential V_i. The initial potential is fixed to $V_i = V_0$ in the region $[0, A = 8]$ and to a large value $V_i = 10$ outside (such that no particles are present for $i > A$). The value V_0 (depending on U) is

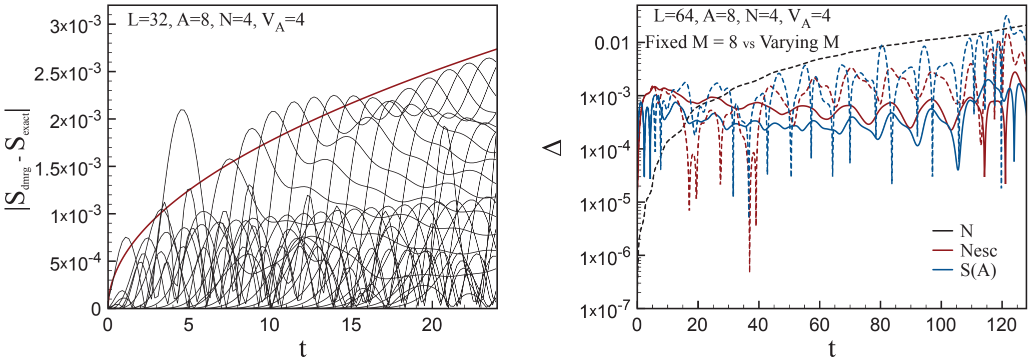

Figure 5.23: [On the left]: Difference between the entanglement entropy calculated via the adaptive t-DMRG $S_{dmrg}(x,t)$ and the exact entropy $S_{exact}(x,t)$ for the Hard-Core boson limit. Each black line represents the entanglement entropy error for different sizes of the subsystem. The red curve is the random-walk error accumulation as predicted on the text. The total error is essentially due to the Trotter decomposition. [On the right]: Deviation of the total number of particles ΔN_t, of the escaping particles $\Delta N_{esc}(t)$ and of the entropy $\Delta S_A(t)$. In this case we have simulated a larger system ($L = 64$) for a long time ($T = 128$). We compare two types of algorithm: the tDMRG with varying M (full lines) and the tDMRG with fixed $M = 8$ (dashed lines). In the first case the "defect of particle" is vanishing, thus it is not traced.

chosen such that the density $\rho = N/A \simeq 1/2$ in the region $[0, A]$. The ground state of the initial Hamiltonian is obtained by a standard static DMRG simulation, by growing first the system with an infinite-system algorithm followed then by a finite-system procedure [Whi92, Whi93, Sch05, CRRM08]. The simulation is started with 4-sites and goes on up to the desired 32 sites system with the infinite-system algorithm. During this infinite-system part, the maximal dimension of the block Hilbert space is fixed to $M = A = 8$. Then the finite-system procedure is implemented where at the end of each sweep the value of M is upgraded looking for the energy convergence. It turned out that after ~ 4 sweeps and with a maximal number of states kept $M \in [16, 24]$ the energy converges up to a precision of $\sim 10^{-8}$. Of course, the precise value of M and the number of sweeps depend on U.

Once the initial ground state has been obtained, we suddenly change the Hamiltonian to H_1 by quenching the potential to the new values $V_i = V_A - pi$ in the region $[0, A]$ and zero elsewhere. We perform adaptive t-DMRG simulations using a second order Suzuki-Trotter decomposition of the evolution operator [WF04]. Explicitly, for a single time step, we have used the approximation

$$\mathcal{U}(t, t+dt) = \mathrm{e}^{-iH_1 dt} \approx \mathrm{e}^{-iH_1(1)dt/2} \cdots \mathrm{e}^{-iH_1(L-1)dt/2} \mathrm{e}^{-iH_1(L-1)dt/2} \cdots \mathrm{e}^{-iH_1(1)dt/2}, \quad (5.83)$$

with time step $dt = 0.05$ up to the final time $T = 24$. Here, $H_1(\ell)$ is the local Hamiltonian acting on the two central free sites at the ℓth DMRG step. With this decomposition one needs a complete left-to-right plus right-to-left sweep to evolve the system from t to $t + dt$. After that, we perform another half sweep without temporal evolution but just targeting the already evolved state in order to improve the truncated Hilbert space description. Then the following half sweep is used for measurement purposes. At this point, we take trace of the maximal value of the block entanglement entropy and we upgrade the value of the block number of states kept at time $t+dt$ to $M(t+dt) = \mathrm{int}[M(t) \times \exp \Delta S_{max}(t)]$ in order to take into account the eventual growth of correlations. Starting the evolution with $M(0) \in [16, 24]$ we finish with $M(T) \in [24, 110]$ depending on the value of U and F.

The t-DMRG algorithm describes the system evolution using a truncated Hilbert space and therefore introduces systematic errors in the dynamical description of the observables. An estimate of the incertitude describing the evolved state can be obtained in the following way: the exact dynamics has to conserve the total number of particles ($[\hat{N}, H_{BH}] = 0$ where $\hat{N} = \sum_i \hat{n}_i$), while in the t-DMRG evolution one has a loss of particles due to the Hilbert space truncation and this "defect of particles", $\Delta N_t \equiv |N(t) - N(0)|$, which is an increasing function of time can be used as a measure of the error introduced by the Hilbert-space truncation procedure during the evolution [DKSV04, GKSS05]. Depending on the parameters of the simulation we obtained $\Delta N_T \in [10^{-8}, 10^{-4}]$ (see Fig. 5.22). We want to remark that the Trotter decomposition should not have effects on ΔN_t, indeed, even approximating the evolution operator as in (5.83) the conservation of particles is locally fulfilled $[\hat{N}, \mathrm{e}^{-iH_1(\ell)dt/2}]$ at each step of the algorithm. In other words, to apply the local evolution operator does not change the number of particles carried by the state, the only change of N occurs at the renormalization step.

Truncation error on other observables can be deduced from this quantity. For example, if we consider the entanglement entropy, assuming that $S(t) \sim \ln N_{esc}(t)$ [ABS11, CMV11, CMV], and since the error on the escaping particles should be somehow proportional to the "defect of particles" $\Delta N_{esc}(t) \propto \Delta N_t$, the maximal error on the entropy should be of the order of $\Delta S \sim \Delta N_T / N_T$. We want to make clear that this error analysis is based on the assumption that the approximations introduced by the truncation procedure have an effect on a generic observable proportional to the effect on the dynamics of the total number of particles. In principle the total number of particles should be conserved and ΔN_T should vanish. It does not mean that if $\Delta N_t = 0$ then the related observables have no errors but rather that whenever $\Delta N_t \neq 0$ one may use it as a rough estimate of the algorithm precision.

The other source of error in the t-DMRG algorithm is linked to the Suzuki-Trotter decomposition. Whenever one considers a non-conserved observable, for each time step dt, the second-order approximation of the evolution operator introduces an error proportional to dt^3. For evolving the state up to time t we need t/dt steps. Supposing a random-walk error accumulation we finally obtain a global Trotter error of the order of $\sim dt^{5/2}\sqrt{t}$.

To confirm what we said, we performed further analysis in the Hard-Core Boson limit. Indeed, in such a limit we can check the t-DMRG dynamics by comparing with the exact one. For this purpose on the left Figure in 5.23 we compare the t-DMRG calculation of the entanglement entropy with the exact evolution in the case of a potential slope $p = 1/2$. One can see that the error is essentially due to the time-step error introduced by the Suzuki-Trotter decomposition $\sim 10^{-4}\sqrt{t}$ (full red line). Moreover, in this case we found $N(t) = N(0) = 4$ confirming the fact that the only source of error in such simulation is the Trotter error.

A further analysis is presented on the right in Figure 5.23. In this case, in a larger system ($L = 64$) and for a longer time evolution ($T = 128$) we explore the behavior of the "defect of particles" ΔN_t, the escaping particle error $\Delta N_{esc}(t)$ and the entanglement entropy error $\Delta S_A(t)$ in two different setup: M-fixed t-DMRG vs M-varying t-DMRG. The "defect of particle" is vanishing in the M-varying case. One can clearly see that for times less than ~ 20 (runaway time) the two protocol give almost the same results. After that time, in the M-varying protocol the error is kept approximatively equal to the Trotter error $\sim 3 \cdot 10^{-4}$, otherwise in the M-fixed protocol, for times longer than the runaway time, the accumulated truncation error becomes larger and larger breaking down the accuracy of the algorithm. One final remark: whenever the truncation error is dominating, i.e. one may neglect the

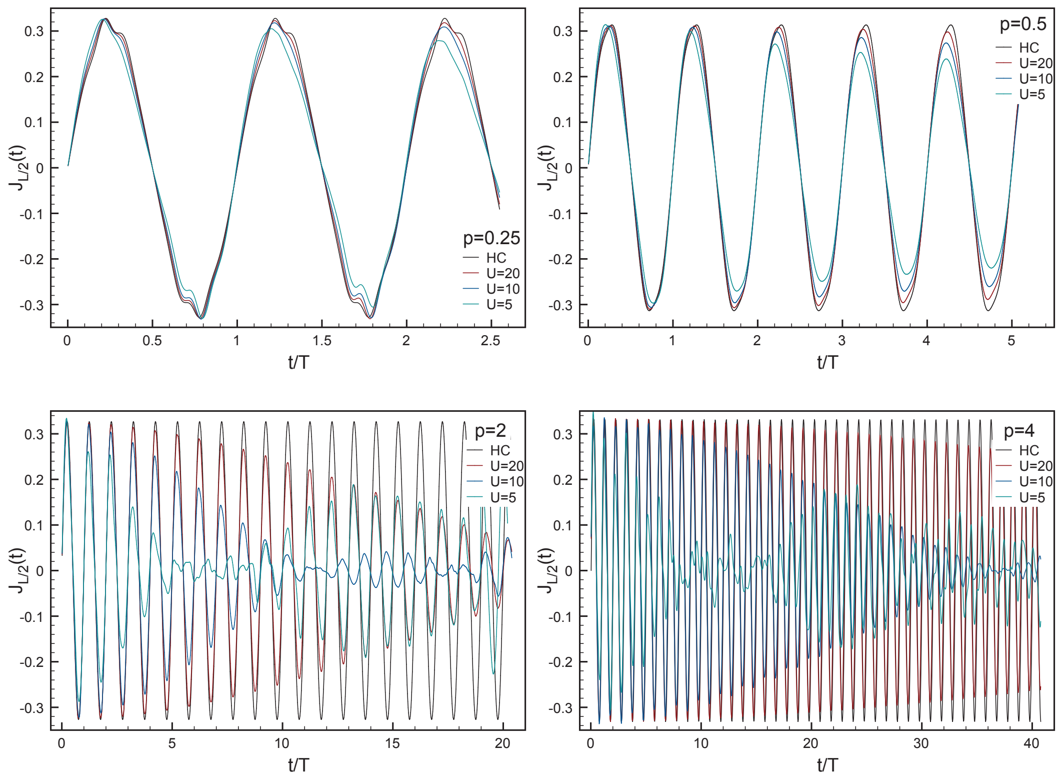

Figure 5.24: t-DMRG simulations of the current in the middle of a system of dimension $L = 32$ with $N = 16$ particles. We initially prepare the system with a flat potential, then we suddenly switch on a linear ramp with slope p. Different colors represent different values of U. Times are rescaled with respect to the Bloch period $T = 2\pi/p$.

Trotter error, we have $\Delta S_A(t) \sim \Delta N_{esc}(t) \sim \Delta N_t$.

Finally, what has been said is restricted to a fixed dimension D of the local Hilbert space and it does not give an estimate of how the observables change varying D. The convergence of observables with D has been simply checked on smaller system sizes.

5.6.2 Quench in a box

To better understand how the properties of the 'plateau' region change when one considers a non-integrable model, we performed simulation in a system initially prepared with N particles spreaded over the whole lattice of length L. The evolution is performed switching on a linear ramp over the whole lattice. In particular, for different values of the gradient p and for different values of the boson-boson interaction U, keeping $N = L/2$ (half filling), we have done t-DMRG simulations on a lattice with length $L = 32$, fixing the local Hilbert space dimension to $D = 3$. Analyzing the current in the middle of the box (where the 'plateau' region appears) we confirm the theoretically predicted oscillations for sufficiently large values of U. On the contrary, when U becomes smaller, the potential term on the Bose-Hubbard Hamiltonian modifies the free-fermion behavior introducing an interaction between the quasi-particles and modifying the shape of the current. In Figure 5.24 we compare the t-DMRG simulations for the current in the middle of the box with the Hard-Core boson

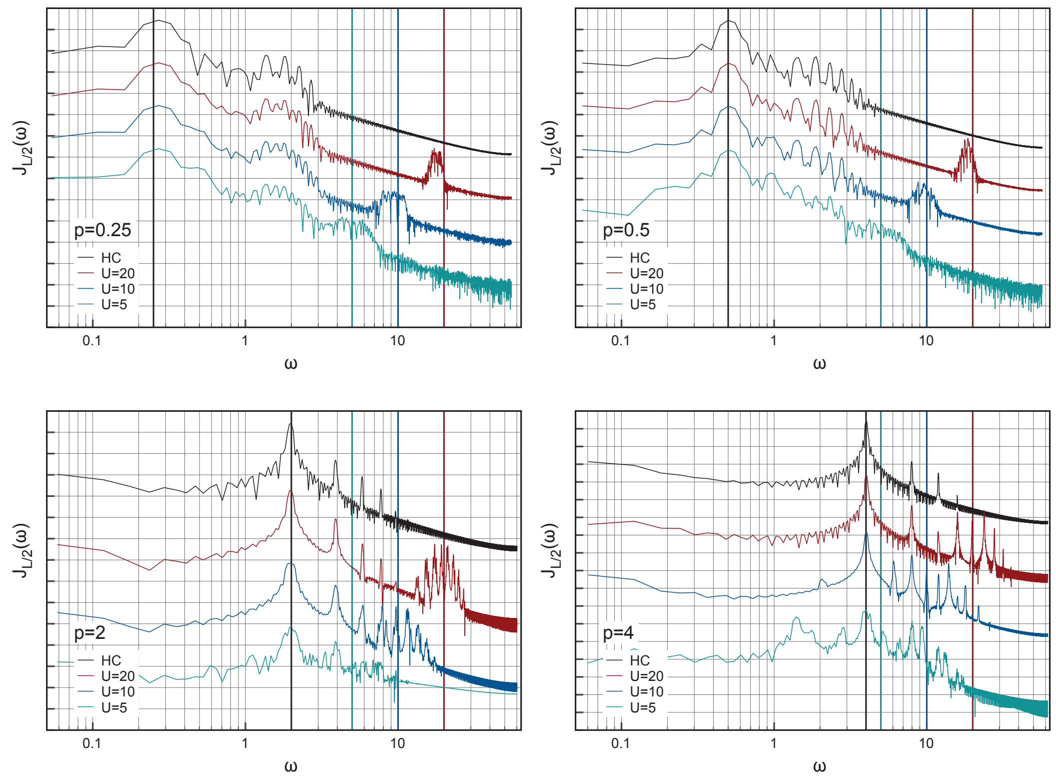

Figure 5.25: Spectral analysis for the signals reported in Figure 5.24. For clarity data are vertically shifted. Vertical lines indicate the frequencies ω^* (black line) and $\tilde{\omega}$ (colored lines).

behavior for different values of U and p. The presence of different peaks in the spectrum is perfectly showed in Figure 5.25. Indeed, we compare the Fast Fourier Transform of $J_{L/2}(t)$ for $U = 20$, 10, 5 and $p = 0.25$, 0.5, 2, 4 with the spectrum we obtained for the Hard-Core bosons. The spectrum has a bandwidth around $\omega^* = 2\pi/T = p$ because we perform the numerical spectral analysis in a finite temporal window $t \in [0, 32]$. Notice that for $p = 4$, the main characteristics of the spectra corresponding to $U = 20, 10$ are quite similar, on the contrary for $U = 5$ a new high peaks appear at a lower frequency than ω^*. Furthermore, in the case of smaller gradient $p = 0.25$, 0.5, 2 a new small broad peak appears at frequencies $\tilde{\omega} \simeq U$. For $p = 4$ this new broad peak is no more visible, nevertheless its effects are still visible: indeed, the underlying presence of such broad peak amplifies the high-frequency harmonics of the principal peak.

The analysis of these spectra is an hard task, specially because of the overlapping of many different effects. Actually, the only effect that it is clear from the analysis of Figure 5.25 is just the appearance of the peak at $\tilde{\omega} \simeq U$. Such a semicircular peak was already predicted in the dynamic structure factor $S(q, \omega)$ of a boson gas in an optical lattice [GMG09].

From the equation of motion for the particle density n_i, we have implicitly defined its conjugate operator $-\nabla J_i = J_{i-1} - J_i$. In particular, selecting the site in the middle of the ‘plateau’, we plot in Figure 5.26 the trajectories of the site $L/2$ in the phase space. We expect that for the Hard-Core bosons model, in the thermodynamical limit, the path reduces

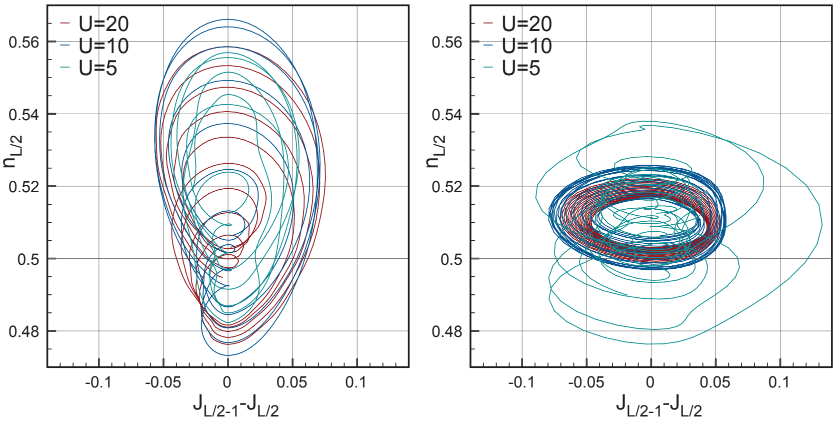

Figure 5.26: Phase space trajectories for the same systems as in Figure 5.24: $p = 1$ (left), $p = 4$ (right).

to the point $(0, 1/2)$. For a finite system there are always oscillations in the observables due to the finite size. On the other hand, the shape of the path also depends on the value of the couplings. In particular, for $p = 4$, by decreasing the value of U we observe an increasing of the fluctuations on the value of the density and the current: paths for $U = 20, 10$ are quite regular showing only one principal frequency, otherwise, for $U = 5$ a more complicated trajectory appears. This completely different behavior is related to the complexity of the frequency spectrum as shown in Figure 5.25. Moreover, analyzing the Figure for $p = 1$, it seems that for smaller value of the slope, the variations in the value of the boson-boson local interaction U have less influence on the shape of the phase-space trajectories. However, such trajectories yet show a different shape with respect to the $p = 4$ cases: major fluctuations are present in the particle density value, showing that a greater number of particles moves along the ramp, in accord to the local equilibrium theory.

Lanczos method in a box We perform further numerical investigations by using the Lanczos algorithm. In this case the lattice length is varied from $L = 12$ to $L = 18$. The system is prepared in the ground-state of a box without the linear potential which is suddenly turned on at $t = 0$. The simulation is performed by taking $N_{max} = N$ (half-filling initial condition). It is interesting to investigate whether the non-integrable nature of the Bose-Hubbard Hamiltonian has consequences on experimentally accessible observables. One of them is the momentum distribution $n_k(t) = \langle \hat{n}_k \rangle(t)$, with

$$\hat{n}_k = \frac{1}{L} \sum_{n,m} \mathrm{e}^{ik(m-n)} b_m^\dagger b_n, \tag{5.84}$$

measured using time of flight techniques. Moreover, although it is not experimentally observable, the fidelity $F(t) = |\langle \Psi_0 | \Psi(t) \rangle|$ quantifies the distance from the initial state and is as well sensitive to the chaotic features of the Hamiltonian.

The first interesting quantity to look at is the momentum distribution versus time. At the single-particle level, the momenta should be shifted with time according to $k(t) = k - pt$ (see Chapter 3); thus, for $U = 0$, we observe in Figure 5.27 that the many-body momentum distribution exhibits Bloch oscillations at velocity p. Increasing U does not change this velocity (difficult to see in the numerics) but the main effect of the interactions is to destroy

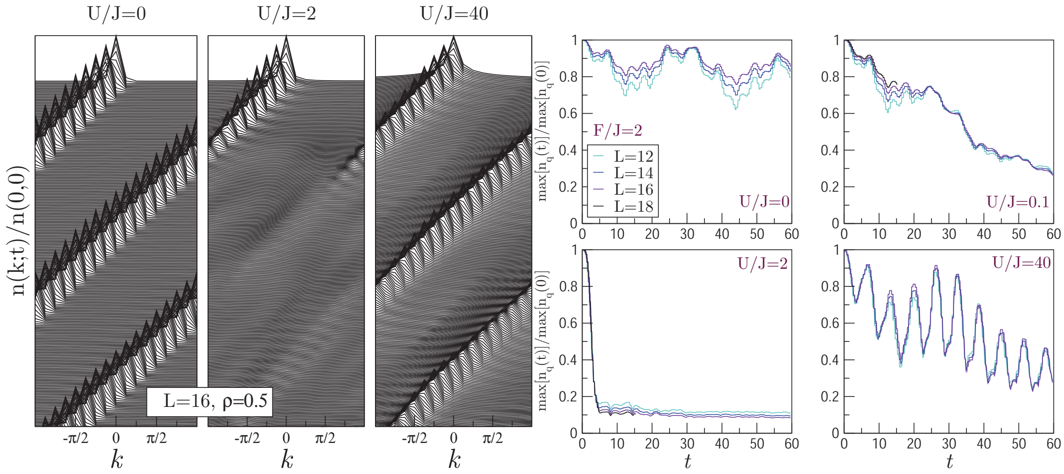

Figure 5.27: Lanczos simulations for the momentum distribution $n_k(t)$ at different time $t \in [0, 60]$ in a box with size $L = 16$ and $N = 8$ particles and slope $p \equiv F = 2J = 1$. We keep $N_{max} = N$ for correctly describing the noninteracting limit ($U = 0$). In the left figure we show the first two periods of the Bloch oscillations. Moreover, the high frequency oscillations are finite size effects associated to the momentum-space discretization ($\sim 2\pi/L$). On the right figure these finite size effects are removed by averaging over a short time windows. Notice how the $n_k(t)$ distribution is coherent over a long time for the two limiting cases ($U/J = 0$ and $U/J = 40$). Otherwise, for non-integrable system ($U/J = 2$) the signal is damped, showing a loss of coherence. On the right $\max n_k(t)$ represents the evolution of the peak and better shows the loss of coherence. All these data have been obtained in collaboration with G. Roux (LPTMS, Paris)

the central peak. Indeed, for $U = 1$, we observe a strong damping of the coherence after short times. Interestingly, increasing U brings us close to the Hard-Core Boson limit and the damping time increases again. Finally, for very large U, the central peak shape is preserved for very long times.

Another interesting point is that the zero-momentum evolution is related to the fidelity of the system in the near-integrable regimes. Indeed, we know that the momentum distribution gets back to its initial position in k-space after a period $T = 2\pi/p$. Even more, the whole many-body wave-function actually comes back close to the initial state, yielding strong revival of the fidelity. Figure 5.28 shows that the peaks in the fidelity and in the zero-momentum distribution are nicely correlated. Consequently, the zero-momentum peaks appear as a close measure of the fidelity in this setup (in the near integrable regimes).

A signature of non-integrability is also found looking at the condensate fraction $f_0(t)$, i.e. the largest eigenvalue of the correlation matrix $\langle b_i^\dagger b_j \rangle_t$ (Figure 5.29). Again, for $U = 0$ no damping is observed. When $U = 1$ a strong damping appears and $f_0(t)$ relaxes. Increasing U close to the Hard-Core boson limit, the damping time increases significantly, a signature of the integrable nature of the Hard-Core boson model.

A final remark can be done comparing $f_0(t)$ and $\max n_k(t)$ in the non-interacting regime (U=0). Indeed, the constant value of the condensed fraction $f_0(t)/f_0(0) = 1$ states that all atoms occupy the same many-body wave function for all times; nevertheless, the sudden quench at $t = 0$ affects the many-body correlations of the initial condensate and this is reflected in a non-trivial evolution of $n_k(t)$.

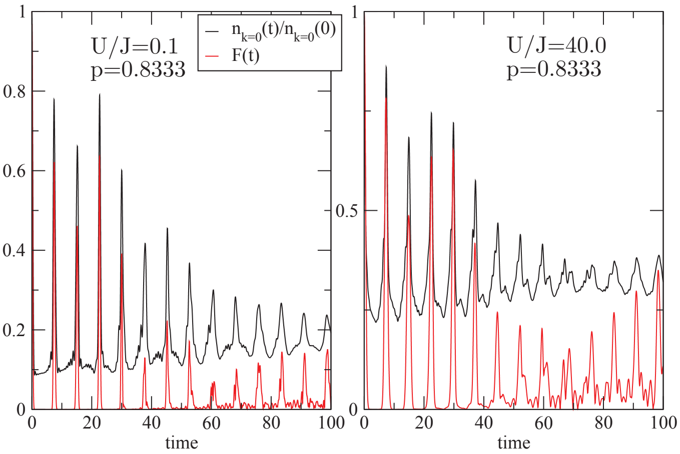

Figure 5.28: Comparison between fidelity and zero-momentum distribution. All these data have been obtained in collaboration with G. Roux (LPTMS, Paris)

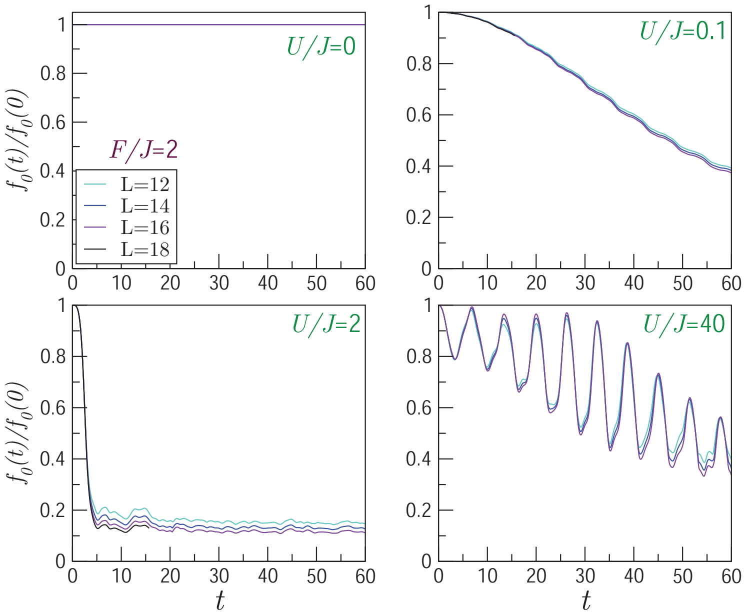

Figure 5.29: Evolution of the condensate fraction with time, showing again the role of integrability. All these data have been obtained in collaboration with G. Roux (LPTMS, Paris)

5.7 Discussion and Summary

In summary, we have analyzed the dynamics of ultra-cold bosons in tilted optical lattices. Starting from the Bose-Hubbard model, in the limit of Hard-Core bosons we developed a hydrodynamical theory which predicts the behavior of the self-trapped condensate as well as the ejected bosons. Within our hydrodynamical approach, we have derived the properties of physical quantities like the density of particles or the current of particles generated after the loading of the linear ramp. The basic ingredients of the hydrodynamical theory are the local equilibrium hypothesis, i.e. the system is locally at equilibrium with the local potential, and the motion of each phase-space point (x, q) is balistic with velocity that depends directly on the dispersion law. Using this theory we can perfectly reproduce the macroscopic bosonic oscillations over the linear ramp. Moreover, we can easily explain the total number of ejected particles as a function of the potential slope p, and we exactly reproduce the evolution of the density and current profile of the ejected particles.

Finally, using the t-DMRG and Lanczos algorithms, we have numerically investigated the dynamics generated by a sudden quench in the Bose-Hubbard model Hamiltonian. These numerical studies confirm the presence of two main frequencies located at the local interaction U and the external potential ramp p (the hopping term is fixed to $t = 1/2$). Moreover, when the system is far away from the integrability points ($U = 0$ and $U = \infty$), one can see a loss of coherence in the evolution of the trapped bosons. We have seen that, in the near integrable regime, the fidelity and the zero-momentum distribution show the same periodical revivals. In that sense, measuring the momentum distribution $n_k(t)$ turns out to be an effective tool for analyzing the properties of integrability of the model.

Chapter 6

Temperature landscape dynamics in extended quantum systems

«Three quarks for Muster Mark.»

J. Joyce

Thermodynamics and statistical mechanics are powerful tools that consent to describe in a fundamental way the classical mechanism of thermalization. The second law of thermodynamics catches the essential idea of such a mechanism: a generic isolated system, prepared in a non-equilibrium macroscopical state (in general corresponding to a set of distinct microscopical configurations) relaxes toward an equilibrium macrostate characterized by stationary macroscopic quantities. Starting from the beginning of the last century, quantum statistical mechanics has been developed to describe thermodynamics of quantum systems. In spite of the unitary evolution of the all microscopical quantum mechanical particles composing the whole system, the process governed by the second law is essentially irreversible. This irreversibility seems to be connected with two general hypothesis: (*i*) a real system consists of a huge number of atoms and its thermal-equilibrium macrostate is characterized by the largest number of different microscopical configurations with respect to any other macroscopical state; (*ii*) reality is actually complex and generic interactions between particles should reduce the number of independent constants of motion (the number of Casimir operators) imposing the Gibbs equilibrium ensemble. Nevertheless, also when we are simply working with isolated integrable systems, numerical and analytical evidence suggests that systems relax to an equilibrium characterized by a generalized Gibbs ensemble. In this generalized ensemble, the Gibbs exponent may contain a more generic linear combination of conserved quantities instead of only the energy [RDYO07, RDO08, Rig09, PDH11, KP09]. The derivation of thermodynamical phenomena from unitary quantum-mechanical dynamics is yet one of the challenges of physics. So far, physicists devoted their attentions to try to solve essentially two issues: on one side, the understanding of canonical thermalization by exploring the existence of a long-time equilibrium macrostate[Rei08, Tas98, GLTZ06, PSW06, LPSW09, EG03, VZ10, IC09, CMDO09, BCH11], and on the other side, the possibility to properly define observables suitable for out-of-equilibrium isolated quantum systems, with a special focus to the entropy[SPR11]. Indeed, quantum systems seem to show two different thermalization regimes: week thermalization occurs when, to justify the approach to a thermal state, a long-time average has to be considered; otherwise, when thermalization occurs

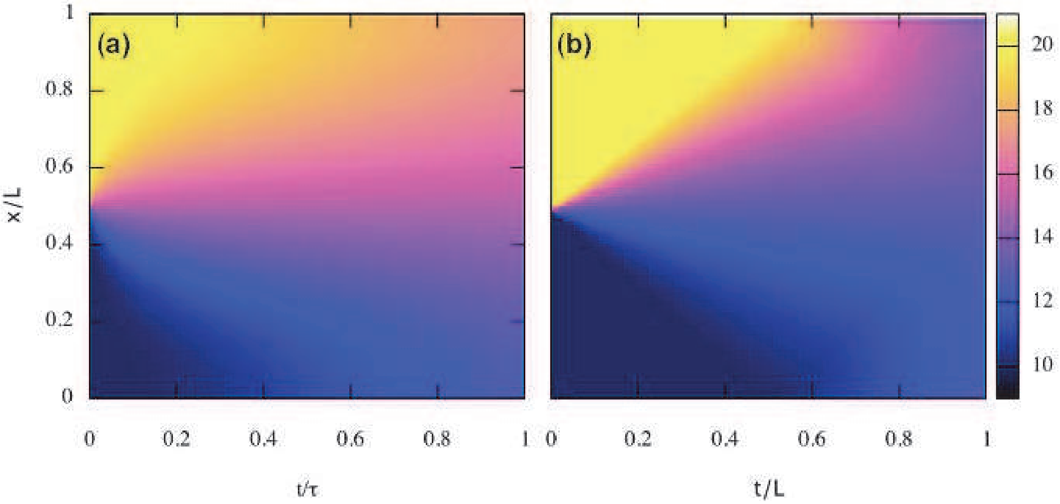

Figure 6.1: (Color online) Classical (a) versus quantum (b) temperature landscape after putting in contact the 'hot' subsystem and the 'cold' subsystem.

without any time average, we refer at this phenomenon as strong thermalization [BCH11]. However, we are still far from having really understood what is the best mechanism to explain the process of thermalization in a quantum system. Surely if such a mechanism exists, it must ensure thermalization independently of microscopic details of the Hamiltonian.

Moreover, beautiful experiments with ultra-cold atoms have attained a level of isolation and control of parameters that gives us the opportunity to analyze also the out-of-equilibrium properties of quantum systems relaxing toward equilibrium [KWW06, HLF$^+$07].

In this chapter we try to merge these goals by focusing our attention on the temporal evolution of a closed quantum system prepared in a off-equilibrium initial state. Indeed, one of the open questions arising from thermodynamics is the microscopical justification of the heat equation $\partial_t\theta = \kappa\partial_x^2\theta$. Such equation governs the temporal evolution of the temperature field $\theta(x,t)$ in a continuous one dimensional classical medium, in the hypothesis of diffusive heat conductance. Guided by some local assumptions [GMM04, CDEO08, CFM$^+$08], we build a similar quantum-mechanical theory and explore its scaling properties especially by respect to the classical ones.

6.1 Classical thermalization dynamics

Before introducing the quantum thermalization scheme, we briefly remind the classical solution of the diffusive heat equation. For that reason, let us consider a one dimensional system $\mathcal{S}$ of length L initially divided into two identical subsystems $\mathcal{S}_1$ and $\mathcal{S}_2$ of length $L/2$ with temperatures respectively θ_1 and θ_2. At time $t = 0^+$ we put $\mathcal{S}_1$ and $\mathcal{S}_2$ in contact and leave the whole system to evolve isolated from the environment. The dynamics of thermalization, in the classical diffusive hypothesis, is governed by the heat equation

$$\partial_t\theta(x,t) = \kappa\partial_x^2\theta(x,t), \tag{6.1}$$

with initial condition

$$\theta(x,0) = \theta_0(x), \ \forall x \in [0,L], \tag{6.2}$$

and free boundary conditions

$$\partial_x\theta(0,t) = \partial_x\theta(L,t) = 0,\ \forall t > 0. \tag{6.3}$$

The general solution is given by

$$\theta(x,t) = \frac{\theta_1+\theta_2}{2} + \sum_{n=1}^{\infty} c_n \cos\frac{n\pi x}{L} \exp -\frac{n^2\pi^2\kappa t}{L^2} \tag{6.4}$$

where $c_n = \frac{2}{L}\int_0^L dx\theta_0(x)\cos\frac{n\pi x}{L}$. Imposing the step-like initial condition

$$\theta_0(x) = \theta_1\Pi(0,L/2) + \theta_2\Pi(L/2,L), \tag{6.5}$$

where $\Pi(a,b) = 1$ for $x \in [a,b]$ and zero otherwise, it is straightforward to obtain $c_n = (\theta_1-\theta_2)A_n$, with $A_n = 2\sin(n\pi/2)/n\pi$. The temporal evolution of the average temperature of the subsystem $\mathcal{S}_1$ ($\mathcal{S}_2$) is given by integrating over the corresponding region $[0, L/2]$ ($[L/2, L]$); one has

$$\begin{aligned}
\theta_1(t) &= (\theta_1+\theta_2)/2 + (\theta_1-\theta_2)\sum_{n=1}^{\infty} A_n^2 \exp -\frac{n^2\pi^2\kappa t}{L^2} \equiv \bar{\theta} + \vartheta_0 f(t), &(6.6)\\
\theta_2(t) &= (\theta_1+\theta_2)/2 - (\theta_1-\theta_2)\sum_{n=1}^{\infty} A_n^2 \exp -\frac{n^2\pi^2\kappa t}{L^2} \equiv \bar{\theta} - \vartheta_0 f(t), &(6.7)
\end{aligned}$$

with $\bar{\theta} = (\theta_1+\theta_2)/2$ and $\vartheta_0 = \theta_1 - \theta_2$. The initial condition is fulfilled thanks to the normalization condition $\sum_{n=1}^{\infty} A_n^2 = 1/2$.

These equations predict an exponential evolution for the temperature equilibration, with a characteristic relaxation time τ defined by the condition $\sum_{n=1}^{\infty} A_n^2 \exp -\frac{n^2\pi^2\kappa\tau}{L^2} \simeq 1/4$ that gives the upper bound

$$\tau \simeq (L^2/\kappa\pi^2)\ln 2. \tag{6.8}$$

Finally, the scaling properties of the "equilibration temperature" $\vartheta(t) \equiv \theta_1(t) - \theta_2(t)$ are simply given by

$$\vartheta(t) = \vartheta_0\,\Theta(t/\tau), \tag{6.9}$$

where $\Theta(z)$ is an universal scaling function with scaling behavior $\Theta(0) = 1$ and $\Theta(z) \to 0$ for $z \to \infty$.

6.2 Quantum thermalization dynamics

Now we switch to the quantum counterpart of the thermalization mechanism. Let us consider a one dimensional quantum system $\mathcal{S}$ described by a continuum set of fundamental field operators ϕ_μ and suppose that initially the system splits into two spatially isolated non-interacting subsystems $\mathcal{S}_1$ and $\mathcal{S}_2$, each of them governed by the Hamiltonian H_1 and H_2, and living in the spatial domains $\mathbb{D}_1$ and $\mathbb{D}_2$ respectively. We prepare, at time $t = 0$, the whole system in a tensorial product state $\rho(0) = \rho_1(0)\otimes\rho_2(0)$, where the density matrix of each subsystems has the canonical representation

$$\rho_\alpha(0) = \exp -\beta_\alpha^0 H_\alpha/Z_\alpha, \tag{6.10}$$

with initial inverse temperature β^0_α, and $\alpha = 1, 2$. At time $t = 0^+$ we put in contact the two subsystems by switching on the interaction Hamiltonian H_I. In terms of the fundamental fields ϕ_μ the total Hamiltonian is given by integrating a local Hamiltonian density $\mathcal{H}(\phi_\mu, \partial_x\phi_\mu)$ over the whole system:

$$H = \int \mathcal{H}(\phi_\mu, \partial_x\phi_\mu)\, dx. \tag{6.11}$$

The evolution of the total density matrix is governed by the Heisenberg equation of motion

$$\partial_t\rho(t) = -i[H, \rho(t)], \tag{6.12}$$

where

$$\rho(t) = \mathrm{e}^{-iHt}\rho(0)\mathrm{e}^{iHt} \tag{6.13}$$

and we have fixed $\hbar = 1$. Supposing now a really infinite system, we look at the properties of a small subsystem $\mathcal{S}_x$ spatially located in the region $[x - \Delta x/2, x + \Delta x/2]$. The expectation value of a generic local observable $\mathcal{O}_x$ acting in such subsystem is simply given by

$$\langle\mathcal{O}_x\rangle = \mathrm{Tr}_{\mathcal{S}_x}\{\mathcal{O}_x\rho(x, t)\}, \tag{6.14}$$

where we defined the local density matrix of the subsystem,

$$\rho(x, t) = \mathrm{Tr}_{\mathcal{S}\backslash\mathcal{S}_x}\{\rho(t)\}, \tag{6.15}$$

by means of the partial trace over the rest $\mathcal{S}\backslash\mathcal{S}_x$. The hypothesis of local interactions, jointed with a specific non-degenerate dispersion relation ϵ_k of the eigenvalues of the Hamiltonian H make it possible to introduce a non-equilibrium local temperature [HMH04a, HMH04b]. Indeed, under such assumptions, the information propagates through the interval Δx in a time greater than the relaxation time of the local quantum system $\mathcal{S}_x$ but anyway much more smaller than the time that the whole system needs to reach the equilibrium; this holds especially in the limit $\Delta x \gg 1$ with $\Delta x/L \ll 1$, where L is the size of the whole system. During the evolution the local system $\mathcal{S}_x$ reacts to the external modification of the whole system and adjusts adiabatically its 'temperature'. In some sense, looking at the properties of the local quantum system $\mathcal{S}_x$, the rest of the system $\mathcal{S}\backslash\mathcal{S}_x$ plays the role of the environment: after preparing $\mathcal{S}_x$ in a specific initial state, its evolution is governed by an effective time-dependent Hamiltonian $H^{(eff)}_x(t)$ which encodes the dynamical interactions with the environment variables we have traced out. From that point of view, the hypothesis introduced above reduces into the adiabatic condition

$$|\partial_t H^{(eff)}_x(t)| \ll 1/\tau_x, \quad \forall x, t, \tag{6.16}$$

where τ_x is the typical relaxation time of the subsystem $\mathcal{S}_x$. In other words, guided by these assumptions, after introducing the local Hamiltonian

$$H_x = \int_{x-\Delta x/2}^{x+\Delta x/2} \mathcal{H}\, dx', \tag{6.17}$$

we can define the local inverse temperature $\beta(x, t)$ as the function that minimizes the distance between the real evolved reduced density matrix with respect to the canonical local density matrix $\rho_x(\lambda) = \exp(-\lambda H_x)/Z_x$ at inverse temperature λ.

To quantify the closeness of the states, we consider the distance

$$d^n(x, t, \lambda) = ||\rho(x, t) - \rho_x(\lambda)||^n, \quad n = 1, 2 \tag{6.18}$$

where norm definitions are

$$\begin{aligned} ||A|| &= Tr\{|A|\}, && (6.19)\\ ||A||^2 &= Tr\{A^\dagger A\}, && (6.20) \end{aligned}$$

the last one being deduced directly from the Hilbert-Schimdt operator norm (on bounded operators). Then, the effective local temperature at time t is defined through the minimization of the distance $d^n(x,t,\lambda)$ over the one parameter canonical family $\rho_x(\lambda)$:

$$\forall x,t \quad \beta(x,t) \,:\, d^n(x,t,\beta(x,t)) \equiv \inf_{\lambda} d^n(x,t,\lambda). \tag{6.21}$$

Despite the existence of many possible ways to define such a distance, here we have chosen to use the trace-distance because it characterizes how hard it is to distinguish two states experimentally (even given perfect measurements). Indeed, when it is small, the two states are effectively indistinguishable. More precisely, it is equal to the maximum difference in probability for any outcome of any measurement performed on the two states [PSW06, LPSW09]. Surely, we could introduce a more sophisticated trace-norm$-n$ definition of distance, where n is a generic integer exponent[1]; however, simply introducing (6.18) one may analyze the stability of the different temperature definitions that we will propose later.

It turns out that, the natural Hilbert-Schimdt definition of norm is more stable with respect to the trace-norm-1 (see Figure 6.2). In particular, using $d^2(x,t,\lambda)$, the definition (6.21) leads to the implicit equation

$$\langle H_x \Delta_\lambda \rho(x,t)\rangle^c_\lambda|_{\lambda=\beta(x,t)} = 0, \tag{6.22}$$

where $\Delta_\lambda\rho(x,t) \equiv \rho(x,t) - \rho_x(\lambda)$ and where $\langle AB\rangle^c = \langle AB\rangle - \langle A\rangle\langle B\rangle$ is the connected correlation with the canonical expectation $\langle A\rangle_\lambda \equiv Tr\{A\rho_x(\lambda)\}$ associated to the local Hamiltonian H_x.

Starting from this result, we can easily define the average temperature over the subsystem $\mathcal{S}_\alpha$ by integrating over the proper domain

$$\langle\beta\rangle_\alpha(t) = \frac{1}{V_{\mathbb{D}_\alpha}} \int_{\mathbb{D}_\alpha} \beta(x,t)dx. \tag{6.23}$$

Such a definition should be compared with an alternative global definition of temperature of system $\mathcal{S}_1$ ($\mathcal{S}_2$) arising from the minimization of the global functional

$$d^n_\alpha(t,\lambda) \equiv \mathrm{Tr}_{\mathcal{S}_\alpha}|\rho_\alpha(t) - \exp(-\lambda H_\alpha)/Z_\alpha|^n \text{ for } \alpha = 1,2, \text{ and } n = 1,2 \tag{6.24}$$

where $\rho_\alpha(t) = \mathrm{Tr}_{\mathcal{S}\setminus\mathcal{S}_\alpha}\{\rho(t)\}$. Noting that this last global definition exactly gives, at time $t = 0$, the initial subsystem temperature β^0_α. Nevertheless, some problems arise from considering a time-dependent temperature defined by looking at the evolution of an extended part of the whole system: at a given time $t > 0$ it is not sure that an extended part of the system is really described by a density matrix closes to a canonical distribution. Indeed, measuring temperature always consists in putting a small system (a thermometer) in contact to a part of the object under study. In other words, using a sufficiently reactive thermometer, we can register the changes in time of a local area of the whole system. Thus, at each time, the thermometer gives us the average temperature of the small subsystem.

---

[1] Notice that for $n \to \infty$ we fall into the maximum-norm definition.

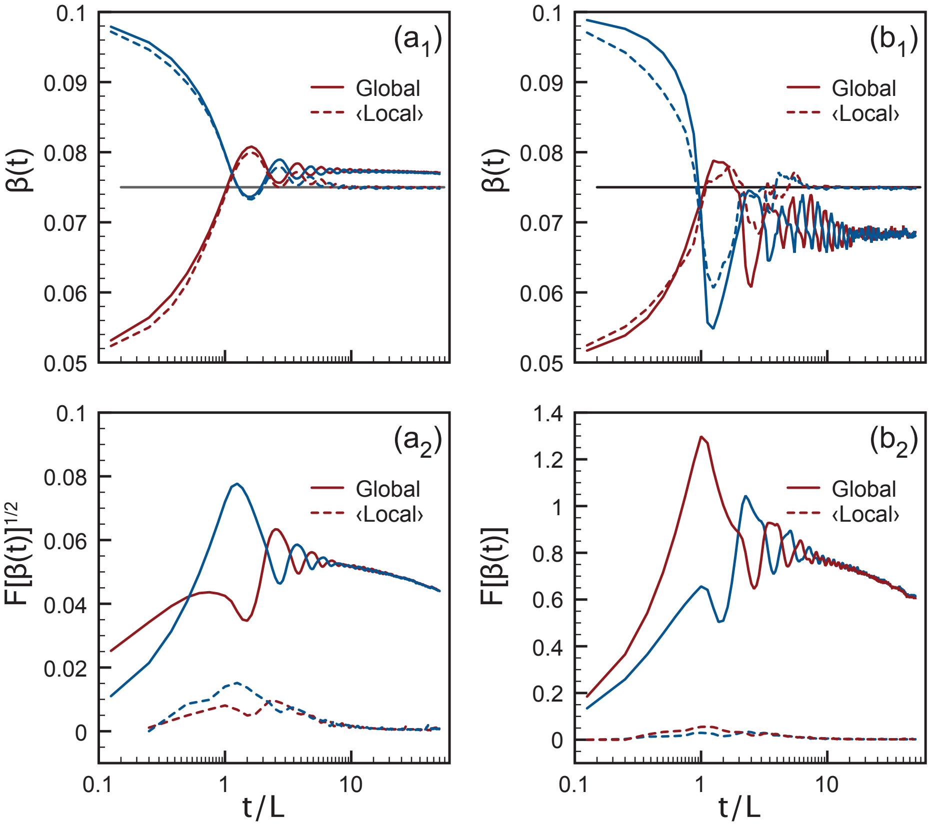

Figure 6.2: Global vs local thermal equilibration in the Hard-core boson chain initially prepared at different temperature, $\beta_1 = 0.05, \beta_2 = 0.1$. In (a_1)-(a_2) temperature is defined via the trace-norm-2; the corresponding evolution of the functional $\sqrt{d^2_\alpha(t,\beta_\alpha)}$ and $\int dx\,\sqrt{d^2(x,t,\beta(x,t))}$ calculated at the extrapolated temperatures is plotted. In (b_1)-(b_2) the same as before but using the trace-norm-1 definition of distance. The local average temperature (dashed lines) is obtained by integrating the local temperature profile over each subsytems.

6.3 Hard-Core boson model

Due to the recent experiments with boson gases loaded in optical lattice, especially with respect to the capability of experimental physicists to reproduce macroscopic inhomogeneous conditions [KWW06, HLF$^+$07, CBL$^+$09], we decide to analyze the relaxation dynamics in the one-dimensional Bose-Hubbard model, with Hamiltonian

$$H = -t\sum_i (b_i^\dagger b_{i+1} + b_{i+1}^\dagger b_i) + \frac{U}{2}\sum_i \hat{n}_i(\hat{n}_i - 1) - \mu\sum_i \hat{n}_i, \tag{6.25}$$

where $b_i^\dagger$ (b_i) are boson creation (annihilation) operators, with $\hat{n}_i \equiv b_i^\dagger b_i$ and canonical commutation relations $[b_i, b_j^\dagger] = \delta_{ij}$. In particular, we can easily manage the Hard-Core boson limit.

Thus, in the limit of strongly repulsive bosons ($U \to \infty$), the Bose-Hubbard Hamiltonian, after a Jordan-Wigner transformation, reduces in the quadratic fermion Hamiltonian

$$H_{HC} = \sum_{ij} c_i^\dagger T_{ij} c_j, \tag{6.26}$$

with

$$T_{ij} = -\mu\delta_{ij} - t[\delta_{ij+1} + \delta_{ij-1}], \tag{6.27}$$

where $c_i^\dagger$ (c_i) are fermion creation (annihilation) operators, with canonical anticommutation relations $\{c_i, c_j^\dagger\} = \delta_{ij}$. Introducing the free fermion operators $\eta_q = \sum_i \varphi_q(i) c_i$ (and $\eta_q^\dagger$), where $\sum_j T_{ij}\varphi_q(j) = \epsilon_q \varphi_q(i)$, we straightforwardly cast the Hamiltonian in diagonal form $H_{HC} = \sum_q \epsilon_q \eta_q^\dagger \eta_q$.

Now, considering a chain of L sites, due to the tensorial form of the initial density operator $\rho_1(0) \otimes \rho_2(0)$, the spatial correlation matrix at time $t = 0$ is

$$\langle c_i^\dagger c_j \rangle_0 = \sum_q \frac{\varphi_q^\alpha(i)\varphi_q^\alpha(j)}{1 + \exp \beta_\alpha \epsilon_q^\alpha} \tag{6.28}$$

for i, j in the same spatially correlated domain, otherwise is zero. For $\alpha = 1, 2$, $\varphi_q^\alpha(i)$ and ϵ_q^α are the eigenvectors and eigenvalues of the initial Hamiltonian H_α of each subsystem, and β_α is the initial inverse temperature. The evolution is governed by the total Hamiltonian

$$H = H_1 \otimes \mathbb{I}_2 + \mathbb{I}_1 \otimes H_2 - t[b_{L/2}^\dagger b_{L/2+1} + \text{h.c.}] \tag{6.29}$$

that gives

$$\langle c_i^\dagger c_j \rangle_t = R^\dagger(t) \langle c_i^\dagger c_j \rangle_0 R(t), \tag{6.30}$$

where the matrix elements of the unitary evolution operator are [PK07, PK05, Kar02]

$$R_{ij}(t) = \sum_q \varphi_q(i)\varphi_q(j) \mathrm{e}^{-i\epsilon_q t}. \tag{6.31}$$

Now, considering a generic subsystem of Δx sites around x position, by definition, the reduced density matrix $\rho(x,t)$ have to reproduce all expectation values in the subsystem. Therefore the one-particle function is

$$C_{ij}(x,t) = \mathrm{Tr}\{c_i^\dagger c_j \rho(x,t)\} \quad \text{for} \quad i, j \in \Delta x, \tag{6.32}$$

and the higher functions must factorize. According to Wick's theorem, this property holds if $\rho(x,t)$ is the exponential of a free-fermion operator

$$\rho(x,t) = \exp\Big\{-\sum_{i,j} c_i^\dagger K_{ij}(x,t) c_j\Big\}/Z_K(x,t) \equiv \exp\Big\{-\beta_0(x)\sum_{i,j} c_i^\dagger T_{ij}(x,t) c_j\Big\}/Z_T(x,t), \tag{6.33}$$

where we introduced the evolved local energy matrix $T_{ij}(x,t)$ and the initial temperature profile $\beta_0(x)$. It can be shown that matrices $C(x,t)$ and $K(x,t)$ are related by [Pes03, Pes04, EP07, EKPP08]

$$K^T(x,t) = \beta_0(x) T^T(x,t) = \ln[(\mathbb{I} - C(x,t))/C(x,t)]. \tag{6.34}$$

Using such properties, the corresponding entanglement entropy follows immediately from the spectrum $\lambda_q(x,t)$ of the local correlation matrix, $S(x,t) = -\sum_q \lambda_q(x,t) \ln \lambda_q(x,t) + [1 - \lambda_q(x,t)] \ln[1 - \lambda_q(x,t)]$.

Now, looking for the solution of the implicit equation (6.22), one needs to re-express the time evolved “Hamiltonian” operator $H_x(t)$ in the diagonal basis of the local Hamiltonian H_x:

$$H_x = \sum_{i,j} c_i^\dagger T_{ij}(x,0) c_j = \sum_{p,q}\sum_{i,j} c_i^\dagger U(x)_{ip}\Lambda(x,t)_{pq}U^\dagger(x)_{qj}c_j, \tag{6.35}$$

which leads to

$$H_x = \sum_{p,q} = \eta(x)_p^\dagger \Lambda(x,0)_{pq}\eta(x)_q = \sum_q \epsilon_q(x)\eta(x)_q^\dagger \eta(x)_q, \tag{6.36}$$

with $\eta_p(x) = \sum_i U^\dagger(x)_{pi}c_i$ the diagonal Fermi operators and where $U(x)$ is the unitary matrix diagonalizing the one-particle Hamiltonian $T(x,0) = U(x)\Lambda(x,0)U^\dagger(x)$ with diagonal one-particle energy matrix $\Lambda(x)_{pq} = \epsilon_q(x)\delta_{pq}$.

In the same way, the time evolved “Hamiltonian” operator

$$H_x(t) \equiv \sum_{i,j} c_i^\dagger T_{ij}(x,t)c_j, \tag{6.37}$$

can be diagonalized in terms of an other set of diagonal Fermi operators

$$\xi_p(x,t) = \sum_j W^\dagger(x,t)_{pj}c_j \tag{6.38}$$

where $W(x,t)$ is the unitary transformation diagonalizing $T(x,t)$ with eigen-spectrum

$$\Lambda(x,t)_{pq} = \epsilon_q(x,t)\delta_{pq}. \tag{6.39}$$

In the H_x diagonal basis the time-evolved $H_x(t)$ is given by

$$\begin{aligned} H_x(t) &= \sum_q [U^\dagger(x)T(x,t)U(x)]_{qq}\eta^\dagger(x)_q\eta(x)_q \\ &+ \sum_{p\neq q}[U^\dagger(x)T(x,t)U(x)]_{pq}\eta^\dagger(x)_p\eta(x)_q, \end{aligned} \tag{6.40}$$

where we have split the diagonal part from the off diagonal one.

Assuming that, at large enough times $t \gg \tau_x$, where τ_x is the typical relaxation time, the local system approaches a canonical state, we expand the unitary matrix $W(x,t) = U(x) + \gamma Z(x,t)$ where γ is a real small expansion parameter and $||Z(x,t)|| = \mathcal{O}(1)$. Since $W^\dagger(x,t)W(x,t) = \mathbb{I}$, on has $U^\dagger(x)Z(x,t) + Z^\dagger(x,t)U(x) = -\gamma Z^\dagger(x,t)Z(x,t)$. At the leading order in γ, the time evolved operatore $H_x(t)$ becomes

$$H_x(t) = \sum_q \epsilon_q(x,t)\eta^\dagger(x)_q\eta(x)_q + \gamma\sum_{p\neq q}\omega_{pq}(x,t)\eta^\dagger(x)_p\eta(x)_q + o(\lambda). \tag{6.41}$$

The second term allows for transition between the eigen-one-particle states of the system Hamiltonian $H_x = \sum_q \epsilon_q(x)\eta^\dagger(x)_q\eta(x)_q$, while the first leads simply to a level shift. The density matrix $\rho(x,t)$ can therefore be expanded as

$$\begin{aligned} \rho(x,t) &= \frac{1}{Z_T(x,t)}\mathrm{e}^{-\beta_0(x)\sum_q \epsilon_q(x,t)\eta^\dagger(x)_q\eta(x)_q} \\ &\times \left\{1 + \gamma\left(O - \frac{1}{2}[D,O] + \frac{1}{6}[D,[D,O]]\right)\right\}, \end{aligned} \tag{6.42}$$

where $D \equiv \sum_q \epsilon_q(x,t)\eta^\dagger(x)_q\eta(x)_q$ is the diagonal contribution and

$$O = \beta_0(x)\sum_{p\neq q}\omega_{pq}(x,t)\eta^\dagger(x)_p\eta(x)_q \tag{6.43}$$

is the off-diagonal one which does not contribute into the expectation value (6.22) defining the effective local temperature. Accordingly, equation (6.22) becomes

$$\langle H_x \Delta_\lambda \rho^{(c)}(x,t)\rangle^c_\lambda \Big|_{\lambda=\beta(x,t)} = 0, \tag{6.44}$$

with

$$\Delta_\lambda \rho^{(c)}(x,t) = \rho^{(c)}(H_x(t),\beta_0(x)) - \rho^{(c)}(H_x,\lambda), \tag{6.45}$$

where

$$\rho^{(c)}(H_x(t),\beta_0(x)) = \frac{1}{Z(H_x(t),\beta_0(x))}\exp -\beta_0(x)\sum_q \epsilon_q(x,t)\eta^\dagger(x)_q\eta(x)_q \tag{6.46}$$

is the effective canonical matrix associated to the time evolved Hamiltonian $H_x(t)$. Notice that we have explicitly introduced the apex $^{(c)}$ to denote the canonical matrix. Thus, introducing the initial canonical population $p_q(x,\lambda) = 1/[1+\exp\lambda\epsilon_q(x)]$ the implicit equation reduces to

$$\sum_q \epsilon_q(x)\langle[\eta^\dagger(x)_q\eta(x)_q - p_q(x,\lambda)]\Delta_\lambda\rho^{(c)}(x,t)\rangle_\lambda \Big|_{\lambda=\beta(x,t)} = 0. \tag{6.47}$$

Defining $\tilde{p}(u) \equiv 1/(1+\exp u)$, one obtains finally

$$\begin{aligned}\frac{Z(H_x,2\lambda)}{Z(H_x,\lambda)}\sum_q \epsilon_q(x)[\tilde{p}(2\lambda\epsilon_q(x)) - \tilde{p}(\lambda\epsilon_q(x))] \quad &= \\ \frac{Z(\tilde{H}_x(t),2\lambda)}{Z(H_x(t),\beta_0(x))}\sum_q \epsilon_q(x)[\tilde{p}(\lambda\delta_q(x,t)) - \tilde{p}(\lambda\epsilon_q(x))],&\end{aligned} \tag{6.48}$$

where

$$\lambda\delta_q(x,t) \equiv \beta_0(x)\epsilon_q(x,t) + \lambda\epsilon_q(x) \tag{6.49}$$

and

$$\tilde{H}_x(t) \equiv \frac{1}{2}\sum_q \delta_q(x,t)\eta^\dagger(x)_q\eta(x)_q. \tag{6.50}$$

At high temperature, $\beta(x,t) \sim \beta_0(x) \ll 1$, equation (6.48) drastically simplify and leads to

$$\beta(x,t) = \beta_0(x)\frac{\sum_q \epsilon_q(x)\epsilon_q(x,t)}{\sum_q \epsilon_q^2(x)}, \tag{6.51}$$

or, in terms of the non-equilibrium populations $\lambda_q(x,t) = Tr\{\eta^\dagger(x)_q\eta(x)_q\rho(x,t)\}$,

$$\beta(x,t) = \frac{1}{\sum_q \epsilon_q^2(x)}\sum_q \epsilon_q(x)\ln\frac{1-\lambda_q(x,t)}{\lambda_q(x,t)}, \tag{6.52}$$

which are the Hard-Core boson counterpart of equation (6.4).

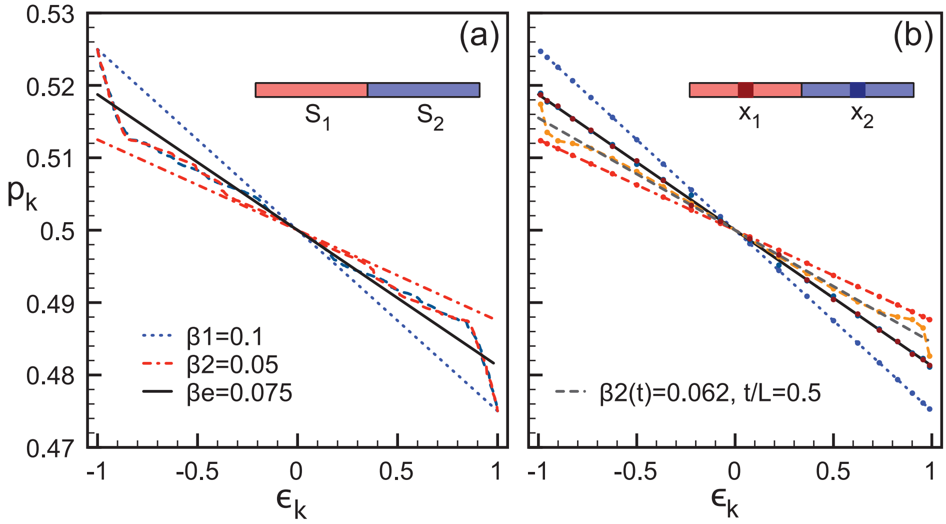

Figure 6.3: Energy level population at the beginning and after "equilibration" for the global subsystems (a) and for two symmetrical local subsystems (b). The blue and red dot-dashed lines are the initial canonical distributions; the black straight line represents the canonical distribution at the average temperature. In the local case we also plot the population of the local subsystem x_1 at the intermediate time $t/L = 0.5$ (yellow dashed line) and the canonical distribution at the extrapolated temperature (gray dashed line).

6.3.1 Numerical simulations

In Figure 6.1 we compare the evolution of the temperature profile of the Hard-Core chain with the diffusive classical behavior. For the numerical simulations we set $\gamma = 1/2$ and $\mu = 0$. The initial inverse temperatures are fixed at $\beta_1 = 1/10$ and $\beta_2 = 1/20$. For these temperatures, formula (6.52) and the numerical minimization of the non-linear functional $\mathcal{F}^{(2)}$ are indistingushable. Notice that, in the Hard-Core boson chain, time scales linearly with space. Of course, Figure 6.1 gives us simply a qualitative picture of the evolution of the temperature profile. With respect to the previous sections, in order to confirm the robustness of the local definition of temperature, we compare the two trace-norm in (6.18) for the global and local cases. In particular, we start our analysis by looking at the long-time equilibration behavior of the quantum system.

Thus, in Figure 6.2 we report the simulations we have done in a system with $L = 800$ sites. The system is initially prepared into two subsystems of equal size and initial temperatures $\beta_1 = 1/10$ and $\beta_2 = 1/20$. We extract the local temperature by fixing $\Delta x = 20$ [2]. Certainly, we expect that the thermal properties of the system still depend on the size of the subsystem that we used for calculating the profile, but this dependence will disappear with increasing the system size. Notice that the spatial average of the temperature profile (6.52) converges to the value $\beta_e = (\beta_1 + \beta_2)/2$. The convergence is quite robust since it is independent of the type of functional that is minimized to obtain the equilibrium temperature. Otherwise, this is not true for the temperature minimizing the global functional. Indeed, by minimizing the global trace-norm one obtains an equilibrium temperature above β_e or, using the global

---

[2] We checked the stability of the local properties by comparing different results obtained with $\Delta x = 10, 20, 40$.

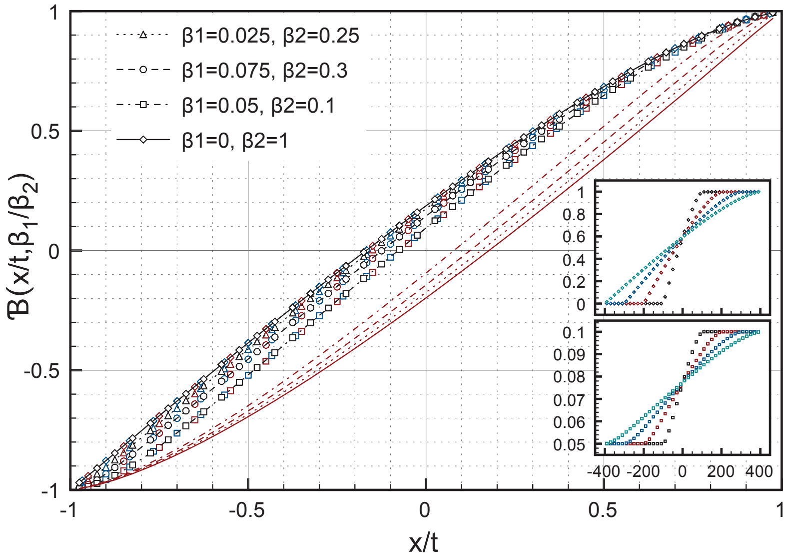

Figure 6.4: Scaling of the temperature profile in the causal region for a Hard-Core boson chain of length $L = 800$. Profiles are calculated via minimization of the local trace-norm^2 distance with $\Delta x = 20$. For each different initial temperature, curves at times $t = 200, 300, 400$ (respectively red, blue and black) show a perfect collapse. Different symbols correspond to different ratios β_1/β_2 and red lines represent the scaling for the inverse temperature ratio showing the expected symmetric property $\mathcal{B}(x/t, \beta_2/\beta_1) = -\mathcal{B}(-x/t, \beta_1/\beta_2)$. The insets represent the unrescaled profiles for $\beta_1 = 0, \beta_2 = 1$ and $\beta_1 = 0.05, \beta_2 = 0.1$.

trace-norm-2 one gets a temperature below β_e. Moreover, the thermalization temperature extracted via local functional shows really interesting features. In the early instants of the evolution, global and local temperatures (respectively dashed and full line in Figure 6.2) show a similar behavior; notice how the hot temperature (red lines) and the cold temperature (blue lines) cross each other at the same point. After that point, the global temperatures oscillate around that value, otherwise, the local temperatures deviate from that value converging to the average β_e. Furthermore, to go more inside the mechanism of thermal equilibration, we analyze $\mathcal{F}[\beta(x,t)]$ versus $\mathcal{F}_g[\beta_\alpha(t)]$. It seems evident that local thermalization better describes the real state of the system. In other words, the spatial average of local observables seems to be more robust than its global counterpart.

What we said seems to be evident also from the energy level populations. In Figure 6.3 we compare the occupation probability of the one-particle energy levels after thermal equilibration with respect to the canonical distribution for the Hard-Core boson model

$$p_k^{(can)} = \frac{1}{1 + \exp \beta \epsilon_q}. \tag{6.53}$$

Again, the system is the same as before. At the beginning the hot subsystem and the cold subsystem are prepared in a canonical state with temperature respectively $\beta_1 = 0.1$ and $\beta_2 = 0.05$ (blue and red dashed lines in Figure 6.3 (a)). After waiting a sufficiently long time, $t/L \simeq 100$, we numerically extract the energy level population for the two subsystem. Notice how the two global distributions, after equilibration, show almost the same profile. However, the distributions are not canonical: the black line, representing the canonical distribution at β_e, does not fit the numerical data.

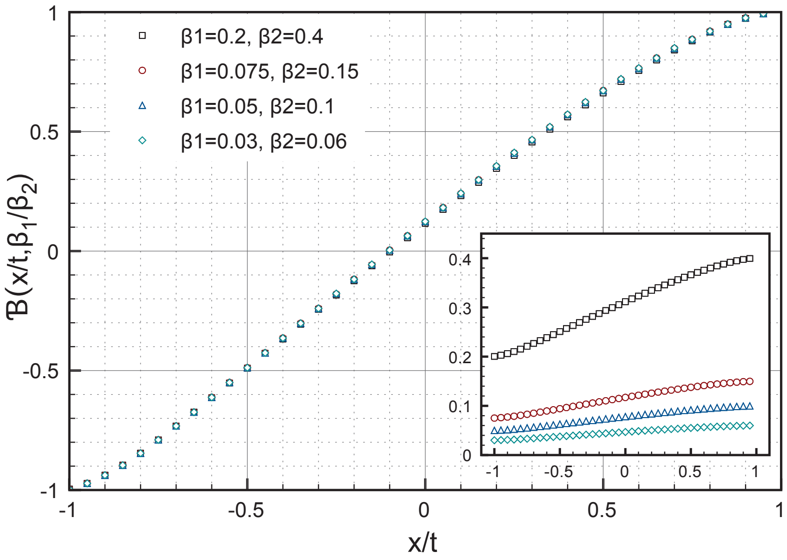

Figure 6.5: Scaling of the temperature profile as in Figure 6.4. Here different symbols represent different initial temperatures but with the same ratio $\beta_1/\beta_2 = 1/2$. Curves are taken at time $t = 400$. Inset represents the unrescaled profiles.

Otherwise, looking at the local intervals located in the middle of the two large subsystems, one obtains a completely different result. First of all, at the beginning of the evolution, the two local subsystems show a canonical distribution for the energy level population. After thermalization one observes a perfect collapse on the canonical distribution at β_e. Furthermore, the local subsystems seem to preserve the canonical distribution also during the early time of the evolution. In Figure 6.3 (b) the yellow dashed line represents the population at time $t/L = 1/2$ of the local subsystem located in x_1. Notice the good agreement with the canonical distribution at the expected temperature (dashed gray line). Again, the expected temperature is defined via minimization of the local functional $\mathcal{F}^{(2)}[\beta]$. From this analysis we can conclude that the local density matrices seems to show a quasi-Gibbs state also during the early instants of the evolution. Otherwise, the global density matrix does not show such a behavior.

Scaling of the temperature profile — For integrable systems, time evolution can cause a dephasing effect, leading for finite subsystems to steady states[CDEO08, CFM$^+$08, BS08]. In spite of that, the free modes of the global system evolve coherently up to the appearance of a sort of "dephasing" due to the repeated reflections from the boundaries. Again, in some sense, for an integrable model, the thermalization to the average temperature is a finite-size effect. Indeed, if we imagine to put in contact at $x = 0$ two semi-infinite integrable systems at different temperatures [PK07, PK05, Kar02], the coherent modification of the temperature profile will start from the contact point to the infinity, and reaches equilibration at $t \to \infty$ never hurting the boundaries. With respect to the finite counterpart (two subsystems of length $L/2$), it means that the only time window that the system will explore is $t \in [0, L/2]$, and only local thermal equilibration can be considered. Even in this case, from Figure 6.2, when $t/L \to 1$, global and local temperatures converge to a value slightly different from the average value β_e. In other words, the evolution of an infinite integrable system in general

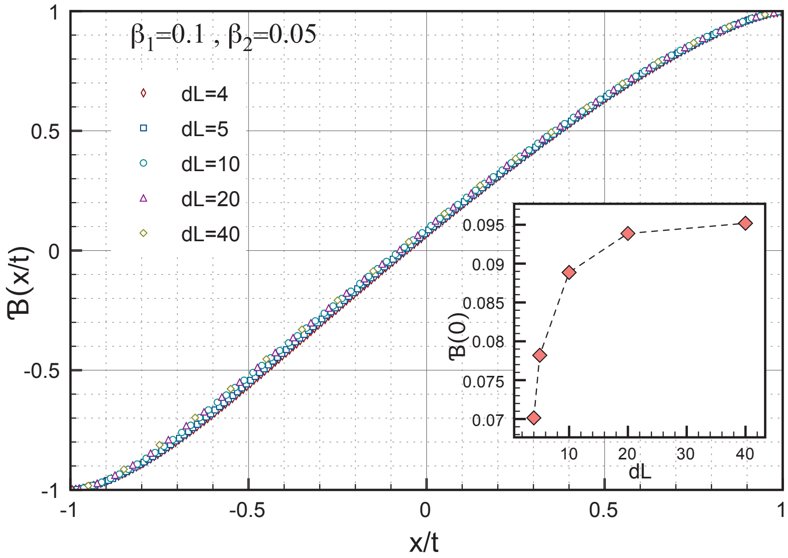

Figure 6.6: Finite-size scaling analysis of the temperature profiles. Profiles are calculated via minimization of the local trace-norm−2 distance. The inset gives the finite-size scaling of the contact point $x/t = 0$.

does not converge to a pure canonical state. Indeed, it is known that, for two semi-infinite Hard-Core boson chains put in contact, the long-time stationary state is described by the density operator [Pla08]

$$\rho \propto \mathrm{e}^{-\beta_e H_{st}}, \quad \text{with} \quad \beta_e = (\beta_1 + \beta_2)/2, \tag{6.54}$$

with

$$H_{st} = H_{HC} + \frac{\beta_1 - \beta_2}{\beta_1 + \beta_2} H_J, \tag{6.55}$$

where H_J is a non-local interaction term with the form of a current.

Of course, looking for a temperature that minimizes the distance from a pure canonical ensemble, we obtain a different result for the equilibration temperature. Coherently with the previous formula, if we consider a finite-size subsystem, for $t \to \infty$ one has $\langle H_J \rangle \to 0$ due to the repeated reflections of each mode at the boundaries: the only term that survives in the exponent of the density operator is the energy.

Guided by these considerations we analyze the scaling behavior of the temperature profile in the Hard-Core boson chain. In particular (see Figure 6.4 and Figure 6.5), considering the space-time causal cone having center into the contact point, we propose, in the high-temperature regime, the following scaling behavior

$$\beta(x,t) = \frac{\beta_1 + \beta_2}{2} \left[1 + \frac{\beta_1 - \beta_2}{\beta_1 + \beta_2} \mathcal{B}(x/t, \beta_1/\beta_2) \right], \tag{6.56}$$

really similar to the classical counterpart (6.4) except for a residual dependence from the temperatures in the scaling function $\mathcal{B}(u,v)$. We checked this dominant behavior by exploring different settings in the interval $\beta_\alpha \in [0,1]$. In Figure 6.4 we show the collapse of different curves at different times as well as its symmetries. Indeed, for two identical and

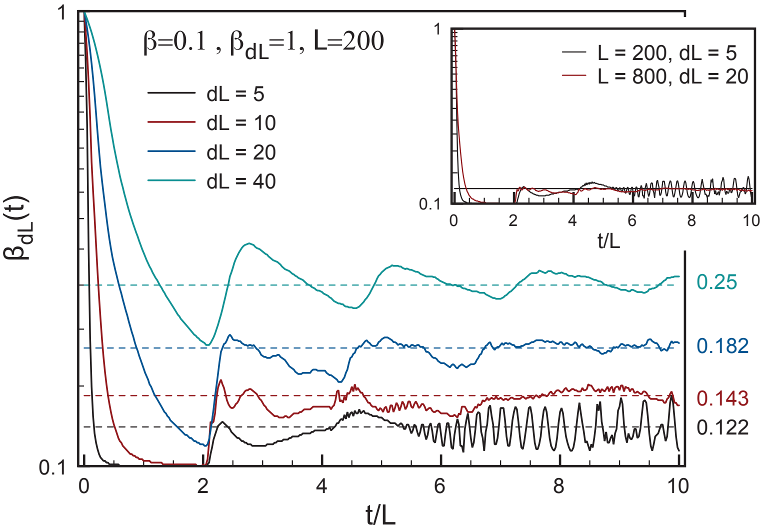

Figure 6.7: Scaling analysis of the thermalization of a thermometer put in contact with a big system. The thermometer temperature converges toward the equilibration temperature β_e except for some oscillations. Notice how these oscillations become smaller increasing the system size (inset).

symmetrical subsystems, if we exchange the two temperatures $\beta_1 \leftrightarrow \beta_2$ and we make a reflection with respect to the contact point $x \leftrightarrow -x$, the profile should remain unchanged. In Figure 6.5 we show the scaling behavior of $\mathcal{B}(u, v)$ for $t = 400$ and ratio $\beta_1/\beta_2 = 1/2$.

Finally, as we have often repeated over the course of this chapter, it is essential to analyze how the temperature profile depends on the size of the local subsystem Δx. In Figure 6.6 we study the temperature profile for different local sizes $dL = 4, 5, 10, 20, 40$. Qualitatively, one see a good collapse of the curves. In particular, a finite-size scaling analysis for the contact point $x/t = 0$ is reported in the inset. Notice the convergence for $dL \geq 20$.

Digression on a thermometer — After having analyzed the scaling properties of the temperature profile in a quantum system during the thermalization process, we would like to briefly address a question left open: it's about understanding the terms in which the thermal properties of the system under consideration depend on the choice of the size of the subsystems that we use to obtain the local temperatures. To address this issue, we simplify the problem. We will consider what for us is the definition of a "thermometer": that is, a probe, small enough not to alter the system that is brought into contact and capable to quickly react to the external changes.

Let us consider a homogeneous system with dimension L and a thermometer with dimension dL, made with the same material of the system and having the same thermal properties. In general one has $dL \ll L$. Now we suppose to probe the system at temperature β, with the thermometer at temperature β_{dL}. The expected average temperature of the whole system plus thermometer should be

$$\beta_e = \frac{L\beta + dL\beta_{dL}}{L + dL}. \tag{6.57}$$

One expect that, during the evolution, the temperature of the thermometer, extracted by minimizing the local functional, should converge towards β_e, except for some oscillations. Convergence will be more precise, the larger the size of the system and the larger the size of the thermometer, with the condition $dL/L \to 0$.

In Figure 6.7 we plot the simulations in a $L = 200$ Hard-Core boson chain put in contact to a thermometer with different sizes. The temperature of the thermometer, starting from its initial value $\beta_{dL} = 1$, falls down (it tries to reach the system temperature $\beta = 0.1$) keeping a minimum at time $t/L \simeq 2$. The energy lost by the thermometer propagates from the contact point through the system, kicks the boundary and then comes back, causing a rising of the temperature. Thus, the temperature evolution shows main oscillations with period $T = 2L$. Other oscillations related to the size of the thermometer, with higher frequencies, are added to the main behavior. Notice how the amplitude of the oscillations becomes smaller the larger is the system size. In the inset of Figure 6.7 one see that for $L = 800$ and $dL = 20$ oscillations have practically disappeared. Moreover, a further message that one keeps from Figure 6.7, is that, thermalization, for integrable systems, is actually a finite-size effect.

6.4 Discussion and Summary

In this chapter we focused our attention on the thermalization properties of an integrable quantum system. In particular, we have explored both the long-time and the short-time behavior of the temperature profile in the Hard-Core boson chain. The system is initially prepared in an out-of-equilibrium state: it is divided into two equal subsystems at different temperatures; than, the two subsystems are put in contact and left to evolve toward thermal equilibrium. We analyzed the equilibration temperature by looking at the function $\beta(x, t)$ that minimizes the distance between the evolved density operator and the canonical Gibbs distribution. We found that a local definition of distance is mandatory to ensure that the system reaches thermal equilibrium at the expected average temperature. Moreover, the local definition of temperature is stable even in the early moments of the thermalization process. Through this local definition it was possible to define the temporal evolution of the temperature profile. In particular, we made sure that this profile is sufficiently independent of the size of the subintervals in which the chain is divided. After analyzing the numerical simulations, we proposed a scaling form for that profile. It was found that the scaling properties in a thermalizing quantum system preserve large similarities with the behavior of a classical system, except for the fact that the scaling function has a residual dependence on the initial temperatures.

Finally, we should remember that the work done in this chapter is a preliminary study on the mechanisms of thermalization and on the possibility of defining an out-of-equilibrium temperature profile in a extended quantum system. Currently we are still conducting further analysis and simulations.

Chapter 7

Conclusions

In the present thesis we have investigated the dynamics of closed one-dimensional quantum systems. In particular, we have discussed different issues relating to this dynamics: the problem of adiabatically driving a system through a quantum phase transition; the dynamics of ultra-cold bosons in a tilted optical lattice; finally, the thermalization properties of an integrable quantum system.

We have addressed these issues by means of both analytical and numerical methods able to deal with strong correlated systems and non-equilibrium effects. It is well known that low-dimensional quantum systems show interesting behavior and often allows the development of analytical methods useful for simplifying the calculations; this is the reason why a good part of the models we have used fall into the category of one-dimensional integrable systems: e.g. the Ising model and the Hard-Core boson model. Nonetheless, the great part of one-dimensional quantum models are still not easily tractable by analytical methods (see for example the Bose-Hubbard model). Thus, to investigate time-dependent phenomena in one-dimensional strongly correlated systems, we developed the adaptive time-dependent density-matrix renormalization-group algorithm (t-DMRG).

After having introduced, in the first part of this manuscript, the general informations and the instruments related to our studies, we proceeded, in the second part, with our investigation on the non-equilibrium quantum dynamics.

First of all, we have analyzed in details the coherent generation of defects during an inhomogeneous adiabatic quench that drives a one-dimensional quantum system across a second order phase transition. It turned out that inhomogeneities strongly affect the equilibrium and the dynamical properties of a quantum system near a critical point. A relevant perturbation generated by a confining potential, such as a harmonic trap, changes the universality class close to the critical point. More generally, removing or loading a power-law trap smoothly in time and close to a critical point will lead to a final state carrying a nontrivial density of defects which will depend on the shape of the trap and on the temporal protocol. Such a power-law potential is relevant especially in the context of confined ultra-cold systems, where the dynamics is well described by the unitary evolution of closed systems. Thus, we have developed a scaling theory which predicts the behavior of such a quench. We have seen that the typical length scale ℓ diverges, close to the critical point, with an effective correlation length exponent $\nu_g = \nu/(1+\nu\omega)$. From this consideration, we have found that the typical time scale τ around the critical locus behaves as $\tau \sim v^{-z/y_v}$, where $y_v = z\alpha + 1/\nu_g$ is the RG dimension of the perturbation field. Within our scaling approach, we have also analyzed how the scaling properties are affected by a deviation of the space-time location of the critical locus. Moreover, using Kibble-Zurek arguments, we have derived the scaling properties of the density of defects $n \sim v^{d/y_v}$ or the energy excess $\epsilon \sim v^{(d+z)/y_v}$ generated during the loading or unloading of the power-law trap. All these predictions have been checked on the Ising quantum chain. Indeed, for the Ising quantum model, we have confirmed the scaling prediction for the energy levels as well as for the perturbation matrix elements. We have found, using the adiabatic approximation, an analytical formula for a quench of a linear trap that do not cross the critical point. Otherwise, in the general case, we have performed a finite-size scaling analysis, confirming what has been predicted by the general scaling theory. Finally we have focused our attention on the spatial properties of the local defect density as well as on the effects of a global shift of the critical point. Once again, the predictions of the general scaling theory have been confirmed within the quantum Ising model.

After that we switched our attention on the dynamics of ultra-cold bosons loaded in a tilted optical lattice. The model is described by the Bose-Hubbard Hamiltonian. At the beginning, in the impenetrable limit (Hard-Core boson model), we have developed an hydrodynamical theory which predicts the behavior of the self-trapped condensate as well as the ejected bosons. The ideas supporting this theory are essentially: the local equilibrium hypothesis, i.e. the system is locally at equilibrium with the local potential; and the ballistic motion of each phase-space point (x, q) with velocity that depends directly on the dispersion law. Under this theory, the equation of motion for the phase-space density can be summarized in

$$\rho^{\pm}(x,q,t) = \frac{1}{2}\iint dq_0 dx_0 \mathcal{G}^{\pm}(x,q,t;x_0,q_0)\rho_0(x_0,q_0), \tag{7.1}$$

with total density $\rho(x,q,t) = \rho^{+}(x,q,t) + \rho^{-}(x,q,t)$. The right and left propagators $\mathcal{G}^{\pm}$ are simply given by $\mathcal{G}^{\pm}(x,q,t;x_0,q_0) = \delta(x - x^{\pm}(x_0,q_0,t))\delta(q - q^{\pm}(x_0,q_0,t))$, where $x^{\pm}$ and $q^{\pm}$ are the equations of motion for a single particle starting in (x_0, q_0).

Using this theory we have reproduced the macroscopic bosonic oscillations over the linear ramp. Moreover, we have calculated the total number of ejected particles as a function of the potential slope p, and we have exactly reproduced the evolution of the density and current profile of the ejected particles.

Finally we have analyzed the dynamics generated by a sudden quench in the Bose-Hubbard Hamiltonian. In this case we used the t-DMRG and the Lanczos algorithms. These numerical studies have confirmed the presence of two main frequencies located at the values of the local interaction U and of the external potential slope p. Moreover, when the system is far away from the integrability points ($U = 0$ and $U = \infty$), we have seen a loss of coherence in the evolution of the trapped bosons.

The last subject treated in this thesis is about the thermalization process in the one-dimensional Hard-Core boson model. As we said before, this problem is still under investigation. However we have summarized the preliminary results that have already been achieved. Thus, we have studied the thermal equilibration dynamics after putting in contact two extended quantum system initially prepared in two different Gibbs ensembles. We have introduced the local trace-norm-n definition of distance $d^n(x,t,\beta) = \mathrm{Tr}_{\mathcal{S}_x}|\rho(x,t) - \rho_x(\beta)|^n$, for $n = 1, 2$, and we have compared them with a global definition. We have seen that thermalization occurs when local variables are taken into account. In this way, we could introduce a temperature profile $\beta(x,t)$ as in the classical case. After having developed this local definition of temperature, we have found that, in the high temperature limit, the profile behaves as

$$\beta(x,t) = \frac{1}{\sum_q \epsilon_q^2(x)} \sum_q \epsilon_q(x) \ln \frac{1-\lambda_q(x,t)}{\lambda_q(x,t)}, \tag{7.2}$$

where $\lambda_q(x,t)$ are the eigenvalues of the local correlation matrix. We have numerically investigated the scaling properties of such a profile and we have checked that the definition of $\beta(x,t)$ was stable under varying the sizes of the subintervals used to extract the local temperature. Finally we have observed that the temperature profile, in a extended quantum system, shows the scaling behavior

$$\beta(x,t) = \frac{\beta_1+\beta_2}{2}\left[1+\frac{\beta_1-\beta_2}{\beta_1+\beta_2}\mathcal{B}(x/t,\beta_1/\beta_2)\right], \tag{7.3}$$

similar to the classical counterpart, except for a residual dependence on the initial temperatures in the scaling function $\mathcal{B}(u,v)$.

Part III

Appendix

In this last part of the thesis we collect any additional information that did not fit place in the body of the thesis. As we said before, it is certainly true for the first two Appendices that give some extra information supporting the previous chapters. More precisely:

In **Appendix A** *we give a brief and simple derivation of the adiabatic perturbative expansion by combining the quantum time-independent perturbative theory in the rotating frame with Trotter decomposition of the evolution operator.*

In **Appendix B** *we present, taking as an example the case* $\omega = 1, \alpha = 2$*, the details of the calculation of the scaling prediction in the case of a "global shift to the critical point" as reported in* **Section 4.1.3**.

Otherwise we would like to spend some additional words about the **Appendix C**. *It turned out that the PhD studies have been really precious also for improving computational skills, especially with regards to the re-implementation of well know algorithms for simulating one-dimensional quantum systems; and this is the case for the DMRG and t-DMRG codes. Thus, in the last appendix we decided to summarize the theoretical framework and the technical instruments we learned during the development of such a code. In some sense, this last appendix will be more structured than the others and could be promoted as a "Chapter" of the thesis. The reader should look at this appendix in the same way he already did before for any of the central chapters of this thesis.*

Appendix A

Adiabatic perturbative expansion

We sketch briefly the demonstration of the nearly adiabatic approach used in this study. First, we discretize the time t so that we have t_0, t_1, … t_n, … $t_N = t$ with $dt = t_n - t_{n-1}$; ultimately we will take the limit $N \to \infty$, $dt \to 0$ with t fixed. The unitary time evolution operator is written as an expansion product

$$\mathcal{U}(t, t_0) = \mathcal{U}(t_N, t_{N-1}) \cdots \mathcal{U}(t_2, t_1)\mathcal{U}(t_1, t_0), \tag{A.1}$$

where, in the limit $dt \to 0$, we have essentially

$$\mathcal{U}(t_{n+1}, t_n) = \mathrm{e}^{-i\mathcal{H}(t_n)dt}. \tag{A.2}$$

Now, let us find an expression for the state after each time interval.

a. $t_0 \to t_1$

The evolution starts from the initial ground state $|\varphi(t_0)\rangle = |0(t_0)\rangle$ at the time t_0. The state at time t_1 is generated by the action of $\mathcal{U}(t_1, t_0) = \mathrm{e}^{-i\mathcal{H}(t_0)dt}$, which leads to the appearance of a phase factor:

$$|\varphi(t_1)\rangle = \mathrm{e}^{-iE_0(t_0)dt}|0(t_0)\rangle. \tag{A.3}$$

b. $t_1 \to t_2$

At the next step we have

$$|\varphi(t_2)\rangle = \mathcal{U}(t_2, t_1)|\varphi(t_1)\rangle = \mathrm{e}^{-i\mathcal{H}(t_1)dt}|\varphi(t_1)\rangle. \tag{A.4}$$

Writing

$$\mathcal{H}(t_0) = \mathcal{H}(t_1) - \frac{\mathcal{H}(t_1) - \mathcal{H}(t_0)}{dt}dt \equiv \mathcal{H}(t_1) - \mathcal{W}(t_1, t_0)dt, \tag{A.5}$$

we can expand the eigenvectors of $\mathcal{H}(t_0)$ in the basis of the eigenvectors of $\mathcal{H}(t_1)$ to first order in $\mathcal{W}(t_1, t_0)dt$:

$$|0(t_0)\rangle = |0(t_1)\rangle + dt\sum_{n\neq 0} \frac{\langle n(t_1)|\mathcal{W}(t_1, t_0)|0(t_1)\rangle}{E_n(t_1) - E_0(t_1)}|n(t_1)\rangle. \tag{A.6}$$

leading to

$$\begin{aligned}|\varphi(t_2)\rangle &= \mathrm{e}^{-i[E_0(t_0)+E_0(t_1)]dt}|0(t_1)\rangle \\ &+ \sum_{n\neq 0}|n(t_1)\rangle dt\mathrm{e}^{-iE_n(t_1)dt}\frac{\langle n(t_1)|\mathcal{W}(t_1,t_0)|0(t_1)\rangle}{E_n(t_1)-E_0(t_1)}\mathrm{e}^{-iE_0(t_0)dt}. \qquad (A.7)\end{aligned}$$

c. $t_2 \to t_3$

We can proceed in the same way as before. By using the development of the Hamiltonian $\mathcal{H}(t_1)=\mathcal{H}(t_2)-\mathcal{W}(t_2,t_1)dt$, we expand the eigenvectors

$$\begin{aligned}|0(t_1)\rangle &= |0(t_2)\rangle + dt\sum_{n\neq 0}\frac{\langle n(t_2)|\mathcal{W}(t_2,t_1)|0(t_2)\rangle}{E_n(t_2)-E_0(t_2)}|n(t_2)\rangle \\ |n(t_1)\rangle &= |n(t_2)\rangle + dt\sum_{m\neq n}\frac{\langle m(t_2)|\mathcal{W}(t_2,t_1)|n(t_2)\rangle}{E_m(t_2)-E_n(t_2)}|m(t_2)\rangle. \qquad (A.8)\end{aligned}$$

Using this expansion and taking only the first term in the development in powers of dt we obtain the evolution $|\varphi(t_3)\rangle=\mathcal{U}(t_3,t_2)|\varphi(t_2)\rangle$:

$$\begin{aligned}|\varphi(t_3)\rangle &= \mathrm{e}^{-i[E_0(t_0)+E_0(t_1)+E_0(t_2)]dt}|0(t_2)\rangle \\ &+ \sum_{n\neq 0}\mathrm{e}^{-iE_n(t_2)dt}|n(t_2)\rangle dt\Bigg\{\mathrm{e}^{-iE_n(t_1)dt}\frac{\langle n(t_1)|\mathcal{W}(t_1,t_0)|0(t_1)\rangle}{E_n(t_1)-E_0(t_1)}\mathrm{e}^{-iE_0(t_0)dt} \\ &+ \frac{\langle n(t_2)|\mathcal{W}(t_2,t_1)|0(t_2)\rangle}{E_n(t_2)-E_0(t_2)}\mathrm{e}^{-i[E_0(t_0)+E_0(t_1)]dt}\Bigg\}. \qquad (A.9)\end{aligned}$$

Now we cast the expression of $|\varphi(t_3)\rangle$ as a development on the basis of the eigenvectors at the same time t_3. Thus one obtains

$$\begin{aligned}|\varphi(t_3)\rangle &= \mathrm{e}^{-i[E_0(t_0)+E_0(t_1)+E_0(t_2)]dt}|0(t_3)\rangle \\ &+ \sum_{n\neq 0}|n(t_3)\rangle dt\Bigg\{\mathrm{e}^{-i[E_n(t_1)+E_n(t_2)]dt}\frac{\langle n(t_1)|\mathcal{W}(t_1,t_0)|0(t_1)\rangle}{E_n(t_1)-E_0(t_1)}\mathrm{e}^{-iE_0(t_0)dt} \\ &+ \mathrm{e}^{-iE_n(t_2)dt}\frac{\langle n(t_2)|\mathcal{W}(t_2,t_1)|0(t_2)\rangle}{E_n(t_2)-E_0(t_2)}\mathrm{e}^{-i[E_0(t_0)+E_0(t_1)]dt} \\ &+ \frac{\langle n(t_3)|\mathcal{W}(t_3,t_2)|0(t_3)\rangle}{E_n(t_3)-E_0(t_3)}\mathrm{e}^{-i[E_0(t_0)+E_0(t_1)+E_0(t_2)]dt}\Bigg\}. \qquad (A.10)\end{aligned}$$

Continuing along these lines, it is straightforward to prove by induction that, at t_k, we have

$$\begin{aligned}|\varphi(t_k)\rangle &= e^{-i\sum_{j=0}^{k-1}dtE_0(t_j)}|0(t_k)\rangle \qquad (A.11) \\ &+ \sum_{n\neq 0}|n(t_k)\rangle\sum_{i=1}^{k}dt\mathrm{e}^{-i\sum_{j=i}^{k-1}dtE_n(t_j)}\frac{\langle\, n(t_i)|\mathcal{W}(t_i,t_{i-1})|0(t_i)\rangle}{E_n(t_i)-E_0(t_i)}\mathrm{e}^{-i\sum_{j=0}^{i-1}dtE_0(t_j)}.\end{aligned}$$

Taking the limit $dt\to 0$ we have $\mathcal{W}(t_{n+1},t_n)\to\partial_t\mathcal{H}(t)|_{t_n}$, and one obtains finally

$$\begin{aligned}|\varphi(t)\rangle &= e^{-i\int_{t_0}^{t}dsE_0(s)}|0(t)\rangle \qquad (A.12) \\ &+ \sum_{n\neq 0}|n(t)\rangle\int_{t_0}^{t}dt'\mathrm{e}^{-i\int_{t'}^{t}dsE_n(s)}\frac{\langle\, n(t')|\partial_{t'}\mathcal{H}(t')|0(t')\rangle}{E_n(t')-E_0(t')}\mathrm{e}^{-i\int_{t_0}^{t'}dsE_0(s)}.\end{aligned}$$

Appendix B

Scaling of the propagating front: example for $\omega = 1$, $\alpha = 2$

We consider a quantum critical system with space-time deviation of the couplings with respect to its homogeneous scalar critical field h_c:

$$h(x,t) - h_c = \delta(x,t) = v|t|^{\alpha} x^{\omega} - \delta_h. \tag{B.1}$$

In other words, we suppose to add an additional homogeneous negative deviation to the original trapping potential $v|t|^{\alpha}x^{\omega}$, in order to have a shift of the critical locus:

$$h(0,t) - h_c = \delta(0,t) = -\delta_c, \quad \text{with} \quad \delta_h > 0. \tag{B.2}$$

During the evolution we open the trap: initially the system is almost totally in the disordered phase, then, a front propagates from the center of the trap toward the boundary (for fixing ideas we imagine to study an half-trap by considering the left boundary field fixed at the value $-\delta_c$). The rapidity of the adiabatic evolution is tuned by the parameter v, thus for v sufficiently small, starting at time $t_{in} = -T$ and lefting the system evolve closer and closer to "criticality", we expect that adiabatic evolution is broken when the relaxation time is too big for assuring the reaction of the system to the variation of the Hamiltonian. In other words, the typical KZ-time τ_* is found by equating the relative variation of the Hamiltonian:

$$\frac{\partial_t \mathcal{H}(t)}{\mathcal{H}(t)} \propto \frac{\partial_t \delta(x,t)}{\delta(x,t)} = \frac{\alpha v |t|^{\alpha-1} x^{\omega}}{v|t|^{\alpha} x^{\omega} - \delta_h}, \tag{B.3}$$

with the inverse of the relaxation time of the system.

In such a case, for a linear spatial profile $\omega = 1$, during the opening of the trap, the front (the crossing point $x(t) = \delta_h / v|t|^{\alpha}$ that define the spatial position of the critical region) propagates but also the gradient evaluated at $x(t)$ is evolving. The critical region is located around $x(t)$ and its length is linked to the value of the gradient $g(t)$ by trap-size scaling arguments (that we suppose are locally valid because the system up to τ_* is adiabatically evolved):

$$\xi(t) = |g(t)|^{-1/y_g}, \quad y_g = (1 + \nu\omega)/\nu. \tag{B.4}$$

The critical relaxation time (for a linear trap $\omega = 1$) is given by:

$$[\xi(t)]^z = v^{-z/y_g} |t|^{-\alpha z / y_g}. \tag{B.5}$$

Equating (B.3) and the inverse of (B.5), and taking $\nu = 1$, $\omega = 1$ (then $y_g = 2$), $x(\tau_*) = \ell_* = \tau_*^{1/z}$ and $|t| = \tau_*$ we obtain

$$\frac{\alpha v \tau_*^{\alpha-1+1/z}}{v\tau_*^{\alpha+1/z} - \delta_h} = v^{z/2}\tau_*^{\alpha z/2}. \tag{B.6}$$

Specializing this equation for $z = 1$(1d-Ising quantum chain) and $\alpha = 2$, and discarding the α factor one has

$$\frac{v\tau_*}{v\tau_*^3 - \delta_h} = v^{1/2} \Rightarrow \tau_*^3 - v^{-1/2}\tau_* - \delta_h/v = 0. \tag{B.7}$$

Notice that for $\delta_h = 0$ one has the original scaling $\tau_{KZ} \sim v^{-1/4}$. Now, supposing $\delta_h \neq 0$, we want to find the solution of that equation for $v \to 0$. In the scaling limit, we obtain the dominant behavior by posing the linear term equal to zero (for $v \to 0$ one has $v^{-1} \gg v^{-1/2}$):

$$\tau_*^{(0)}(v, \delta_h) = \left(\frac{v}{\delta_h}\right)^{-1/3}, \tag{B.8}$$

then, if we look for a solution of the form $\tau_*(v, \delta_h) = \tau_*^{(0)}(v, \delta_h) \cdot T(v, \delta_h)$ we find the equation for $T(v, \delta_h) \equiv T(\delta_h^{-2/3} v^{1/6})$:

$$T^3 - xT - 1 = 0, \quad x = \delta_h^{-2/3} v^{1/6} \tag{B.9}$$

That equation does not present divergence for $x \to 0$ thus we expect $T(x)$ analytical for $x \to 0$, with Taylor expansion:

$$T(x) = 1 + a_1 x + a_2 x^2 + \ldots \tag{B.10}$$

Substituting the expansion in the equation and keeping only the leading terms we have

$$1 + 3a_1 x - x - 1 = 0 \Rightarrow a_1 = \frac{1}{3}, \tag{B.11}$$

then finally

$$\tau_*(v, \delta_h) = \left(\frac{v}{\delta_h}\right)^{-1/3} \left(1 + \frac{1}{3}\delta_h^{-2/3} v^{1/6} + O(\delta_h^{2/3} v^{1/3})\right). \tag{B.12}$$

Now, only using the dominant behavior of the previous solution, we can verify that the position of the critical front, exactly when the adiabatic evolution break-down (remember that we are analyzing the 1d-Ising quantum chain with $\omega = 1$ and $\alpha = 2$), is:

$$\ell_* \equiv x_*(\tau_*) = \frac{\delta_h}{v\tau_*^2} = \frac{\delta_h}{v}\left(\frac{v}{\delta_h}\right)^{2/3} = \left(\frac{v}{\delta_h}\right)^{-1/3} = \tau_*. \tag{B.13}$$

In the same way we can determine the length of the critical zone around the critical front:

$$\xi_* \equiv \xi(\tau_*) = v^{-1/2}\tau_*^{-1} = \delta_h^{-1/3} v^{-1/6} = \left(\frac{\ell_*}{\delta_h}\right)^{1/2} \tag{B.14}$$

Finally, we want to study the behaviour of the spin-spin correlations in the critical zone. For accomplishing that goal, we fix the reference spin at ℓ^* and then the correlation function calculated at the distance x takes the form:

$$C(x) \sim \exp\left[-\frac{|x - \ell_*|}{\xi'(x)}\right], \tag{B.15}$$

where now $\xi'(x)$ is the local correlation length at x. In particular, $\xi'(x)$ is connected to the local deviation of the couplings from the critical value:

$$\xi'(x) \propto [v\tau_*^2|x-\ell_*|]^{-\nu} = v^{-1}\left(\frac{v}{\delta_h}\right)^{2/3}|x-\ell_*|^{-1} = \frac{\xi_*^2}{|x-\ell_*|}, \tag{B.16}$$

then finally we have

$$C(x) \sim \exp\left[-\frac{(x-\ell_*)^2}{\xi_*^2}\right], \quad \xi_* = \left(\frac{\ell_*}{\delta_h}\right)^{1/2}. \tag{B.17}$$

An interesting question is to analyze the behaviour of the maximum of the derivative of the correlation function.

$$\partial_x^2 C(x) = -\frac{2}{\xi_*^2}\partial_x(x-\ell_*)C(x) = -\frac{2}{\xi_*^2}\left(1-\frac{2(x-\ell_*)^2}{\xi_*^2}\right)C(x) = 0, \tag{B.18}$$

thus

$$1-2\delta_h\frac{(x_0-\ell_*)^2}{\ell_*} = 0, \tag{B.19}$$

and then

$$x_0 = \ell_* + \frac{1}{\sqrt{2}}\left(\frac{\ell_*}{\delta_h}\right)^{1/2} = \ell_*\left(1+\frac{1}{\sqrt{2}}(\delta_h\ell_*)^{-1/2}\right) = \left(\frac{v}{\delta_h}\right)^{-1/3}\left(1+\frac{1}{\sqrt{2}}\delta_h^{-2/3}v^{1/6}\right). \tag{B.20}$$

Appendix C

Density-Matrix Renormalization Group

«Prediction is very difficult,
especially about the future.»
N. Bohr

If we consider an object on a human scale it is impossible to obtain all dynamical information exactly. Indeed, also when we use the simplest Hamiltonians for modeling the complex behavior of quantum many-body systems, the numerical simulations are very often cumbersome and inefficient. Just for fixing the ideas, if we consider a quantum system consisting in N interacting local subsystems, each of them living in a Hilbert space of dimension D, then total Hilbert space dimension will be D^N. This number will soon exceed the available resources on a computer, already for a small value of N. In other words, the exponential growing of the Hilbert space dimension imposes a limit for the exact numerical simulation of a many-body quantum system. Although there are models whose numerical complexity can be reduced from D^N to N (see for example the XY-model), in most cases this is not possible and therefore a direct simulation is beyond question.

In order to overcame this limitation, S. R. White proposed in 1992 the Density-Matrix Renormalization Group (DMRG) method [Whi92, Whi93]. This method is essentially based on the same idea that underlies the Real Space Renormalization Group (RSRG) method. In practice, we start by considering a sufficiently small quantum system and a numerical representation of its Hamiltonian, then we add step by step other degrees of freedom, for example by enlarging the system. The key point, at each step, is to "renormalize" the original Hamiltonian by integrating out, in a proper way, the "less important" degrees of freedom. In this way, at a given step, the Hamiltonian should exhibit modified couplings with respect to those it showed previously. At the end of the process we should obtain an effective Hamiltonian which should describe the essential physics of the original system. In a sense, at the end of the algorithm, we have traced out from the original Hamiltonian all the superfluous degrees of freedom. The original White's idea, which distinguishes the DMRG from the RSRG, was actually to find "the right way" for eliminating the superfluous degrees of freedom.

In the years following the introduction of the DMRG, many efforts have been spent, from different physics research field, to improve the algorithm: quantum information theory for example has allowed to understand what are the limit of applicability of this new numerical technique. Indeed, the information theory has revealed a strong connections between the efficiency on the simulations and the entanglement behavior [Vid03, Vid04]. Among the

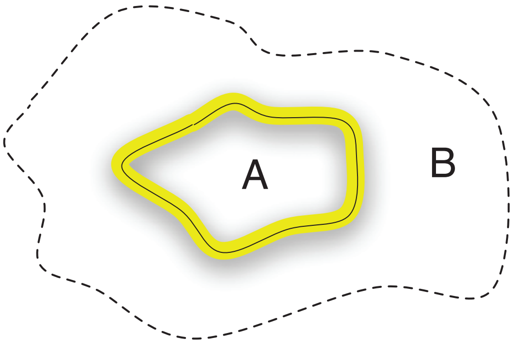

Figure C.1: Sketch of a system which is split into two subsystems. If region $\mathcal{A}$ et $\mathcal{B}$ are not correlated, e.g. by removing the yellow stripe, the wave function factorizes $|\psi_{\mathcal{A}}\rangle|\psi_{\mathcal{B}}\rangle$ and the entanglement entropy vanishes (Figure taken from [AFOV08]).

various measures, the so-called entanglement entropy is the best suited for our purposes, especially because it is easy to measure during the DMRG simulation. By considering an extended quantum system, after splitting the system into two blocks, the entanglement entropy is defined through the von Neumann entropy of the reduced density matrix $\rho_{\mathcal{A}}$ of one of the two blocks (Figure C.1) [AFOV08]. In one-dimensional critical ground states, conformal field theory (CFT) predicts, for a block $\mathcal{A}$ of length ℓ embedded in an infinite system, a logarithmic growing of the entanglement entropy:

$$S_{\mathcal{A}} \equiv -\mathrm{Tr}\rho_{\mathcal{A}} \ln \rho_{\mathcal{A}} = \frac{c}{3} \ln \ell + c' \tag{C.1}$$

where c is the central charge of the corresponding CFT and c' a non-universal constant [CC04, VLRK03, LRV04]. Away from criticality, where the system has a finite correlation length ξ, the asymptotic behavior of the entanglement entropy is bounded

$$S_{\mathcal{A}} \sim \frac{c}{3} \ln \xi \quad \text{for } \ell \gg \xi. \tag{C.2}$$

It is easy to understand the reason why the DMRG algorithm does not work very well growing the entanglement of a subsystem: indeed, for simulating strongly correlated quantum systems (at or close to a quantum critical point) it is necessary to take into account a great number of states, but otherwise, if we want to obtain some results in reasonable time, the renormalization protocol tell us to keep a moderate numbers of states looking for higher eigenvalues of the reduced density matrix. However Eq. (C.1) and (C.2) tell us that, for the ground state of one-dimensional systems, in the worst case the entanglement of a subsystem grows logarithmically with its size, so an efficient simulation with DMRG is still possible.

On the other hand, different considerations must be made with regard to the simulation of the temporal evolution of quantum systems. It has been shown that, for critical systems, the block entanglement can grow linearly with time and block size[OL04]. Therefore, the simulation of the time evolution of such systems could be definitively no more efficient.

To better understand this point, let us suppose to prepare a quantum system in an uncorrelated ground-state $|\psi^0_{g_0}\rangle$ of an Hamiltonian $\mathcal{H}_{g_0}$, where g_0 is a tunable parameter. At time $t = 0$ this parameter is suddenly changed to a different value g, and the system thus starts to evolve according to a different Hamiltonian $\mathcal{H}_g$. The time evolution is simply obtained by rewriting the initial state $|\psi^0_{g_0}\rangle$ in terms of the eigenstates $|\psi^k_g\rangle$ (with energies

ω_g^k) of the Hamiltonian $\mathcal{H}_g$. This leads to the evolved state

$$|\psi(t)\rangle = \sum_k e^{-i\omega_g^k t} \langle \psi_g^k | \psi_{g_0}^0 \rangle |\psi_g^k\rangle. \tag{C.3}$$

Then, also from an uncorrelated initial wave function one could obtain a strongly correlated state $|\psi(t)\rangle$ at some particular time.

For a complete review on the different DMRG methods, its theoretical foundations and its applications we remand to Schollwöck (2005)[Sch05] and its references.

C.1 From RSRG to DMRG

The idea underlying the DMRG method comes from some considerations about the RSRG method. This latter method, in fact, did not predict the correct results for the ground-state properties of quantum many-body systems.

What S. R. White understood was that whenever one extracts a subsystem from the whole original system, the ground-state properties should not be described by the low-energy properties of the subsystem's Hamiltonian but rather by the properties of the reduced density matrix. Indeed, the subsystem is inevitably conditioned by the environment, and the reduced density matrix takes trace in somehow of the environment properties.

For better understanding the reason that RSRG approach does not optimally work we will analyze the elementary steps of this algorithm.

As reported in [Sch05], following White's toy model of a single particle hopping on a one-dimensional lattice, we consider a box of size L. We associate at each site i the vector $|i\rangle$. The Hamiltonian is a diagonal band matrix with element $\langle i|\mathcal{H}|i\rangle = 2$, $\langle i|\mathcal{H}|i \pm 1\rangle = -1$. The RSRG recipe is the following:

1. One starts with the initial block $\mathcal{B}$ of length ℓ with Hamiltonian $\mathcal{H}_\mathcal{B}$. The system lives in a Hilbert space of dimension M.
2. Taking a symmetric copy of the initial block, we construct a super-block $\mathcal{BB}$ of length 2ℓ with total Hamiltonian $\mathcal{H}_{\mathcal{BB}} = \mathcal{I}_\mathcal{B} \otimes \mathcal{H}_\mathcal{B} + \mathcal{H}_\mathcal{B} \otimes \mathcal{I}_\mathcal{B} + \mathcal{H}_\mathcal{I}$, i.e. the two block Hamiltonian plus the inter-block interaction. The Hilbert space of the super-block has dimension M^2.
3. Find the M lowest-lying eigenstate of $\mathcal{H}_{\mathcal{BB}}$
4. Project $\mathcal{H}_{\mathcal{BB}}$ onto the subspace spanned by the previous M eigenstate. In this way, one obtains the truncated Hamiltonian $\mathcal{H}_{\mathcal{BB}} \to \mathcal{H}_{\mathcal{BB}}^{tr}$.
5. After replacing $2\ell \to \ell$, $\mathcal{BB} \to \mathcal{B}$, $\mathcal{H}_{\mathcal{BB}}^{tr} \to \mathcal{H}_\mathcal{B}$, repeat the procedure from step (2), until the desired size.

The fundamental steps in the previous RSRG recipe are the steps (3-4): reducing the Hilbert space dimension by taking the lower-energy eigenstates of $\mathcal{H}_{\mathcal{BB}}$. That means that, whenever we have to reconstruct a bigger block, we can use only the low-lying eigenstates of the previous smaller blocks. We can immediately see the failure of this method by looking at the Figure C.2. Indeed, supposing the dimension of the system sufficiently large to permit a continuous description, all the eigenfunctions of $\mathcal{B}$ should have nodes at the edges. Therefore, all the tensor products constructed from these eigenfunctions will be zero in the center of the super-block $\mathcal{BB}$. On the other hand the ground state of the super-block is different from zero right there. In practice, there is no way to reconstruct the $\mathcal{BB}$ ground state by using a limited number of eigenfunctions of the blocks $\mathcal{B}$.

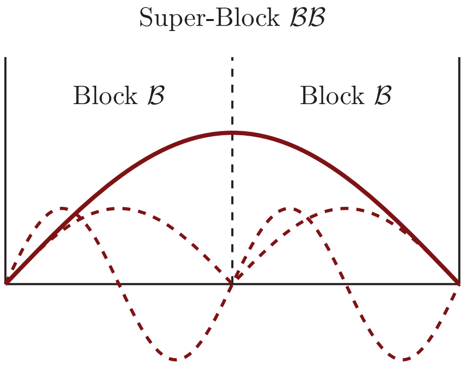

Figure C.2: The White's toy model showing how the lowest-lying eigenstates of $\mathcal{H}_{\mathcal{B}}$ (red dashed lines) are not sufficient to reproduce the ground state of the super-block (full red line). (Figure based on [Sch05])

C.1.1 Density matrices and DMRG truncation

The original aim of the DMRG was to found the best approximation of the ground state (or a given excited state) of a quantum many-body system. As we yet said, this part can be done by looking at the best block states which can be used to reconstruct a given global target state. In a sense, if we look at a part of a whole system, this should be described by the own reduced density matrix. Therefore, if our intention is to reduce the Hilbert space dimension of such a system, we should keep the most probable states in which the subsystem could be found. Before going inside the optimization protocol proposed by White in the 1998, we briefly review some elementary properties of the reduced density matrix.

We begin by considering an extended quantum system (from now on we refer to it as a super-block) which splits into two part: the system block $\mathcal{S}$ and environment block $\mathcal{E}$ (see Figure C.3). Let us suppose $|\psi_0\rangle$ the ground state of the whole system. Normally, this state carries informations about the entanglement between the block and the environment. After having introduced a basis of the system $\{|\sigma_i\rangle\}$ and of the environment $\{|\varepsilon_i\rangle\}$, we can write the global ground state as

$$|\psi_0\rangle = \sum_{i,j} \psi_{ij} |\sigma_i\rangle \otimes |\varepsilon_j\rangle \tag{C.4}$$

Whenever one considers an operator $\mathcal{O}_{\mathcal{S}}$ acting on the system block variables only, one has

$$\langle \mathcal{O}_{\mathcal{S}} \rangle = \sum_{i,j,i',j'} \psi^*_{ij} \psi_{i'j'} \langle \varepsilon_j | \otimes \langle \sigma_i | \mathcal{O}_{\mathcal{S}} | \sigma_{i'} \rangle \otimes | \varepsilon_{j'} \rangle \tag{C.5}$$

that, using the normalization condition $\langle \varepsilon_i | \varepsilon_j \rangle = \delta_{ij}$, leads to

$$\langle \mathcal{O}_{\mathcal{S}} \rangle = \sum_{i,i',j} \psi^*_{ij} \psi_{i'j} \langle \sigma_i | \mathcal{O}_{\mathcal{S}} | \sigma_{i'} \rangle . \tag{C.6}$$

In this way, we can define the reduced density operator of the system block through its matrix elements

$$\langle \sigma_{i'} | \rho_{\mathcal{S}} | \sigma_i \rangle = \sum_j \psi^*_{i,j} \psi_{i',j} \tag{C.7}$$

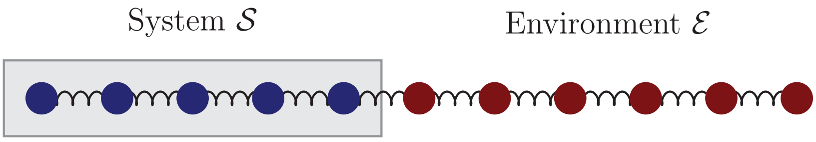

Figure C.3: Sketch of the super-block split into the system block $\mathcal{S}$ and the environment block $\mathcal{E}$.

By using this definition the expectation values can be rewritten as

$$\langle \mathcal{O}_\mathcal{S} \rangle = \mathrm{Tr}\left(\rho_\mathcal{S} \mathcal{O}_\mathcal{S}\right). \tag{C.8}$$

The reduced density operator $\rho_\mathcal{S}$ is an hermitian operator with positive spectrum and satisfying the normalization condition $\mathrm{Tr}\rho_\mathcal{S} = 1$.

Hilbert-space decimation — After having selected a super-block target state, e.g. the ground-state of a many-body quantum system, the goal of the DMRG procedure is to individuate the best representative states of both the system $\mathcal{S}$ and the environment $\mathcal{E}$ for reconstructing the original target state. Obviously, whenever one retains the entire Hilbert space for describing each part, the description of the whole system will be exact. Nevertheless, for overcoming the exponential growth of the Hilbert space dimension, it is necessary to drop out some degrees of freedom. We can do that by looking at the reduced density matrix of the system $\mathcal{S}$ (environment $\mathcal{E}$) and selecting a fixed number of states starting from the most probable ones, i.e. the states corresponding to the highest eigenvalues of the reduced density matrix $\rho_\mathcal{S}$ ($\rho_\mathcal{E}$). The formalization of such an idea is actually simple [Sch05, PHWK99].

Indeed, if we consider a bounded operator $\mathcal{O}$ acting on the system block, $\|\mathcal{O}\| \equiv c_\mathcal{O}$, its expectation value, using the density matrix eigen-basis $\rho_\mathcal{B}|w_\alpha\rangle = w_\alpha|w_\alpha\rangle$, is

$$\langle \mathcal{O} \rangle = \sum_{\alpha=1}^{D^\ell} w_\alpha \langle w_\alpha|\mathcal{O}|w_\alpha\rangle, \tag{C.9}$$

where, D is the dimension of the Hilbert space of single lattice site and ℓ is the number of the sites on the system block $\mathcal{S}$. Let us assume that the eigenstates of the density matrix are enumerated in descending order $w_1 \geqslant w_2 \geqslant \ldots \geqslant w_{D^\ell}$. If we reduce the Hilbert space dimension of the system block to the first M eigenvectors $|w_\alpha\rangle$ with the largest eigenvalues, the average value of $\mathcal{O}$ becomes

$$\langle \mathcal{O} \rangle_{tr} = \sum_{\alpha=1}^{M} w_\alpha \langle w_\alpha|\mathcal{O}|w_\alpha\rangle, \tag{C.10}$$

with an error

$$|\langle \mathcal{O} \rangle_{tr} - \langle \mathcal{O} \rangle| \leqslant c_\mathcal{O} \sum_{\alpha=M+1}^{D^\ell} w_\alpha \equiv c_\mathcal{O} \epsilon_{\rho_\mathcal{O}}. \tag{C.11}$$

In the previous equation we have introduced the so-called truncated weight

$$\epsilon_{\rho_\mathcal{S}} = 1 - \sum_{\alpha=1}^{M} w_\alpha, \tag{C.12}$$

which gives an estimation of the error that we have introduced with the Hilbert-space decimation procedure. We want to stress here that this error is a really good estimate of the accuracy of the procedure whenever we look at some local bounded observables (like local energy, magnetization, density etc.). Moreover, the equation (C.11) does not take into account the contribution from the environment truncation procedure. We will see in the next sections that the DMRG algorithm makes use of such a Hilbert-space decimation procedure for the approximative description of both the system and the environment [PHWK99].

Now we could enter into the algorithm. Basically, we can split the algorithm into two part: the “Infinite-system DMRG” wherein the system and the environment are iteratively enlarged up to the desired super-block dimension; the “Finite-system DMRG" which performs a set of iterations until the desired precision on the super-block description is achieved.

C.1.2 Infinite-system DMRG

Let us suppose that we are looking for the ground-state properties of a chain (with open boundary conditions) with short-range interactions. Henceforth we suppose each site living in a D-dimensional local Hilbert space. The idea is to start with a sufficiently small system and environment and enlarge them until the desired super-block dimension is reached. The infinite-system DMRG recipe is the following [Sch05, PHWK99, CRRM08]:

1. Consider a system block $\mathcal{S}(\ell, M_\ell)$, where ℓ is the real number of sites into the system and M_ℓ represents the number of states we use to describe the system. The Hamiltonian $\mathcal{H}_\ell^{\mathcal{S}}$ and the operators living on the system block are known. In the same way, form an environment block $\mathcal{E}(\ell, M_\ell)$. Notice that the number of sites in the environment block is the same as the system block one; in the infinite procedure this is necessary in order to enlarge the chain step by step. On the contrary, it is not necessary to keep the same number of states. [At the beginning, we usually start with a block $\mathcal{S}(1, D)$ composed of one site and described by an exact basis (the same for the environment).]

2. In the next step we construct the so-called left enlarged block $\mathcal{S}(\ell, M_\ell)\bullet$ by adding a site $\bullet$ to the right of the system block. The Hilbert space dimension of the new enlarged system $\mathcal{S}\bullet$ is $M_\ell D$, with a basis of product states. The Hamiltonian $\mathcal{H}_\ell^{\mathcal{S}\bullet}$ is constructed form the local Hamiltonians of the system block and the free site, plus the interaction
$$\mathcal{H}_\ell^{\mathcal{S}\bullet} = \mathcal{H}_\ell^{\mathcal{S}} \otimes \mathcal{I}^\bullet + \mathcal{I}_\ell^{\mathcal{S}} \otimes \mathcal{H}^\bullet + \mathcal{H}_{i\,\ell}^{\mathcal{S}\bullet}, \tag{C.13}$$
where $\mathcal{I}^{\cdots}$ stand for the identity matrices of the correspondent Hilbert spaces. Similarly, we build the right enlarged block $\bullet\mathcal{E}(\ell, M_\ell)$ by adding a site to the left of the environment block, with Hamiltonian
$$\mathcal{H}_\ell^{\bullet\mathcal{E}} = \mathcal{I}^\bullet \otimes \mathcal{H}_\ell^{\mathcal{E}} + \mathcal{H}^\bullet \otimes \mathcal{I}_\ell^{\mathcal{E}} + \mathcal{H}_{i\,\ell}^{\bullet\mathcal{E}}. \tag{C.14}$$

3. Using the two enlarged block and adding the site-site interaction, a *superblock* $\mathcal{S}\bullet\bullet\mathcal{E}$ of lenght $2\ell + 2$ is then built. The total Hilbert space dimension is $D^2 M_\ell^2$, and the Hamiltonian look as
$$\mathcal{H}^{\mathcal{S}\bullet\bullet\mathcal{E}} = \mathcal{H}_\ell^{\mathcal{S}\bullet} \otimes \mathcal{I}_\ell^{\bullet\mathcal{E}} + \mathcal{I}_\ell^{\mathcal{S}\bullet} \otimes \mathcal{H}_\ell^{\bullet\mathcal{E}} + \mathcal{I}_\ell^{\mathcal{S}} \otimes \mathcal{H}_i^{\bullet\bullet} \otimes \mathcal{I}_\ell^{\mathcal{E}}. \tag{C.15}$$
In theory we can explicitly construct the Hamiltonian $\mathcal{H}^{\mathcal{S}\bullet\bullet\mathcal{E}}$, nevertheless, we will see that it is not necessary. What we actually need is to know how to apply this Hamiltonian to a generic state vector.

4. Find the ground state $|\psi\rangle$ of $\mathcal{H}^{\mathcal{S}\bullet\bullet\mathcal{E}}$; this should be made by using Lanczos or Davidson algorithm.

5. From $|\psi\rangle$ one integrates out the right enlarged block variables obtaining the reduced density matrix $\rho^{\mathcal{S}\bullet}$ of the left enlarged block:

$$\rho^{\mathcal{S}\bullet} = \mathrm{Tr}_{\bullet\mathcal{E}}|\psi\rangle\langle\psi|. \tag{C.16}$$

   After, we determine its eigenvectors $\{|w_\alpha\rangle\}$ with descending-ordered eigenvalues w_α. In other words, we search for a unitary matrix $U^{\mathcal{S}}$ that performs a change of basis in $\mathcal{S}\bullet$ Hilbert space,

$$\rho^{\mathcal{S}\bullet} = U^{\mathcal{S}}\ \rho^{\mathcal{S}\bullet}_{diag}\ (U^{\mathcal{S}})^\dagger, \tag{C.17}$$

   whose columns are the eigenvectors of $\rho^{\mathcal{S}\bullet}$. Now, the central point of the DMRG algorithm is the Hilbert-space decimation procedure: we retain at most the first M eigenvectors. This correspond to a truncation of the $U^{\mathcal{S}}$ matrix since $M_{\ell+1} = \min(M_\ell D, M)$ number of columns (i.e.: the first $M_{\ell+1}$ eigenstates with the largest weights). Therefore we obtain the $M_\ell D \times M_{\ell+1}$ renormalization matrix $\mathcal{R}^{\mathcal{S}}_{\ell\to\ell+1}$ for the left enlarged block. In the same way, we evaluate the reduced density matrix $\rho^{\bullet\mathcal{E}}$ of the right enlarged block, diagonalize it and we obtain the matrix $\mathcal{R}^{\mathcal{E}}_{\ell\to\ell+1}$.

6. We carry out the full renormalization procedure in order to obtain a truncated enlarged block $\mathcal{S}(\ell+1, M_{\ell+1})$. In this way, the renormalized Hamiltonian of the new system block is

$$\mathcal{H}^{\mathcal{S}}_{\ell+1} = (\mathcal{R}^{\mathcal{S}}_{\ell\to\ell+1})^\dagger\ \mathcal{H}^{\mathcal{S}\bullet}_{\ell}\ \mathcal{R}^{\mathcal{S}}_{\ell\to\ell+1}, \tag{C.18}$$

   and the renormalized local rightmost operator

$$\mathcal{O}^{\mathcal{S}}_{\ell+1} = (\mathcal{R}^{\mathcal{S}}_{\ell\to\ell+1})^\dagger\ (\mathcal{I}^{\mathcal{S}}_{\ell} \otimes \mathcal{O}^\bullet)\ \mathcal{R}^{\mathcal{S}}_{\ell\to\ell+1}. \tag{C.19}$$

   Notice that the renormalization of the rightmost local operator is necessary whenever we need to construct a local interaction between the rightmost system-block site and the free site (see step 2.). We proceed in the same way for the environment in order to obtain $\mathcal{E}(\ell+1, M_{\ell+1})$.

The steps 1-6 are iterated until some desired final length is reached. Then, it is possible to calculate some ground-state properties from $|\psi\rangle$.

At the end of an infinite-system DMRG cycle the length of the chain has been increased by two sites. Otherwise, the Hilbert space dimension of a block is bounded by M. In other words, M and D set the complexity of the problem. The features of the system impose the value of D (in general, in a mixed-spin chain for example, D varies from one site to another site, so we have to use a site-dependent local Hilbert space dimension D_i for each site i), while M is normally set up by the user for obtaining a given precision (we will see that it is also possible to automatically adjust the value of M while the algorithm is running for adapting the Hilbert space dimension until the desired convergence is achieved).

C.1.3 Finite-system DMRG

In general, the accuracy on the results that one obtains after the infinite-system DMRG algorithm strongly depends on the final dimension at which we stop the algorithm. Indeed, at the end of each infinite-system DMRG step, after diagonalizing the super-block Hamiltonian, we get an approximation of the ground state of a chain with $2\ell+2$ sites. During the first steps of the infinite-system DMRG algorithm, the accuracy in the ground-state approximation is

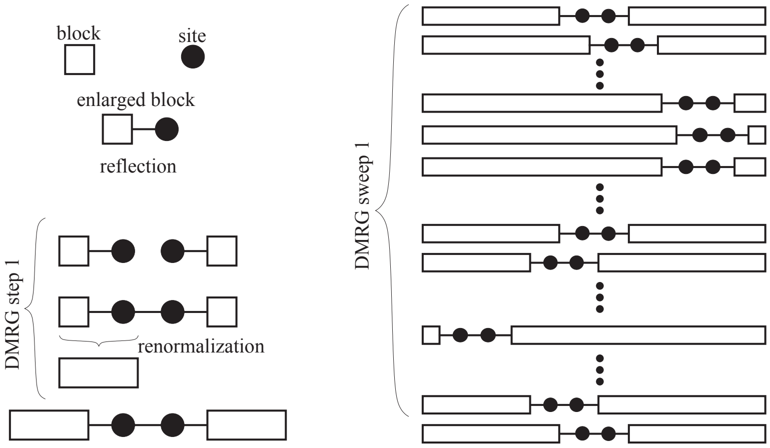

Figure C.4: Sketch of the DMRG algorithm. On the left, we show one iteration of the infinite-system DMRG. On the right, we represent one sweep of the finite-system DMRG (Figure taken from [CRRM08]).

really poor and if we stop the procedure for a fairly small super-block size, we should not obtain a good description at all. Indeed, as we have often repeated in the previous sections, the DMRG is based on the possibility that the system block has to choose its own best representation whenever it is brought into contact with different environments.

To overcame this limitation, the finite-system procedure was developed. The idea is very simple: we stop the infinite-system procedure at a given length L, then, we perform the same steps as in the infinite-system algorithm but now by keeping fixed the super-block length L. In other words, whenever the system block is growing in size the environment block is decreasing, and *vice versa*. At each step, the renormalization procedure is performed only on the growing block. Here in the following the recipe of the finite-system DMRG sweeps [CRRM08]:

1. We have the system block $\mathcal{S}(L/2, M_{L/2})$ and the environment block $\mathcal{E}(L/2, M_{L/2})$. In order to perform the sweep procedure, system and environment blocks (Hamiltonians, local operators, etc.) must have been stored previously.

2. Build the superblock of lenght L,

   $$\mathcal{S}(L/2, M_{L/2}) \bullet \bullet \mathcal{E}(L/2-2, M_{L/2-2}), \tag{C.20}$$

   and its Hamiltonian necessary for finding the ground state.

3. Operate as well as steps 4-5 of the infinite-system algorithm, but now only looking for left enlarged block renormalization matrix.

4. Use $\mathcal{R}^{\mathcal{S}}_{L/2\to L/2+1}$ to obtain a truncated enlarged block $\mathcal{S}(L/2+1, M_{L/2+1})$; then taking from memory the environment block, build the new superblock

   $$\mathcal{S}(L/2+1, M_{L/2+1}) \bullet \bullet \mathcal{E}(L/2-3, M_{L/2-3}), \tag{C.21}$$

   in order to keep costant the lenght of the chain. Now restart with step 3. Make this procedure until the enviroment block reaches its minimum size and becomes exact.

5. At the end of the left-to-right sweep the system configuration is
$$\mathcal{S}(L-3, M_{L-3}) \bullet \bullet \mathcal{E}(1, D). \tag{C.22}$$
Then we start to make growing the environment block by moving the free site from right to left.
6. The right-to-left sweep is accomplished when the system configuration look like
$$\mathcal{S}(1, D) \bullet \bullet \mathcal{E}(L-3, M_{L-3}). \tag{C.23}$$
A this point, for making sure that the ground state converges to the exact ground state of the chain, it is possible to increas the value of the maximum number of states M. In this way, when the next left-to-right sweep will start, we shall obtain a further improvement of the block description due to the increasing of the Hilbert space dimension.
7. At each DMRG sweep, we check for energy convergence. In other words, we take note of the energy difference between last ground state and previous ones.

During these sweeps we improve the ground-state approximation without changing the super-block length.

C.1.4 Measures

Using the DMRG we can extract many different features of the target state, for instance we can easily measure the expectation value of a generic observable $\mathcal{A}$. We can extract these informations by using the super-block wave function $|\psi\rangle$ at any point of the algorithm; indeed, after a suitable convergence in energy output has been obtained, all the following system configurations are only different representations of the same ground state wave function. Then, the procedure is to use the most appropriate representation of the target state in order to evaluate expectation values. For the notations adopted we remand to Section C.1.5.

One-point correlators — The easier observable we can measure is obviously a local observable $\mathcal{A}^i$, living on one single site i. In this case, for evaluating $\mathcal{A}^i$, is convenient to use the representation of $|\psi\rangle$ in which i is one of the two free sites. The average is given by
$$\langle \mathcal{A}^i \rangle = \psi^*_{g(s,\alpha,\beta,e)} \mathcal{A}^i_{\alpha\alpha'} \psi_{g(s,\alpha',\beta,e)}, \tag{C.24}$$
where i is the first free site.

Two-point correlators — Whenever we consider a non-local operator, e.g. the correlation $\mathcal{A}^i\mathcal{B}^j$, the evaluation strongly depends on where i and j belongs. Also in this case, the most convenient way to perform such a measure is to use the representation of $|\psi\rangle$ in which one of the two free sites is either i or j. If we consider a correlation between two neighboring sites $\mathcal{A}^i\mathcal{B}^{i+1}$, we can easily measure it when both i and $i+1$ are free sites. It is straightforward to obtain:
$$\langle \mathcal{A}^i\mathcal{B}^{i+1} \rangle = \psi^*_{g(s,\alpha,\beta,e)} \mathcal{A}^i_{\alpha\alpha'} \mathcal{B}^{i+1}_{\beta\beta'} \psi_{g(s,\alpha',\beta',e)}. \tag{C.25}$$

In general, when i and j are not nearest neighbor sites, the measure can be performed by firstly applying the renormalization matrices to one observable and then by performing the measure when the other one lives in a free site. For making clear the method, let us consider the case in which j is the leftmost free site and i belongs to the left block (so $i < j$). At first, starting with the system block with $i-1$ sites, we have to renormalize $\mathcal{A}^i$ in order to obtain:

$$\widehat{\mathcal{A}^i} = (\mathcal{R}^{\mathcal{S}}_{i-1\to i})^\dagger \, (\mathcal{I}^{\mathcal{S}}_{i-1} \otimes \mathcal{A}^i) \, \mathcal{R}^{\mathcal{S}}_{i-1\to i}, \tag{C.26}$$

then, at each step up to the system size will be $j-1$, we add a $D \times D$ identity matrix $\mathcal{I}^\bullet$ on the right (in DMRG sense we simply add a free site) and carry out a renormalization; the protocol then reads:

$$\begin{gathered}
(\mathcal{R}^{\mathcal{S}}_{i\to i+1})^\dagger \, (\widehat{\mathcal{A}^i} \otimes \mathcal{I}^\bullet) \, \mathcal{R}^{\mathcal{S}}_{i\to i+1} \to \widehat{\mathcal{A}^i}, \\
(\mathcal{R}^{\mathcal{S}}_{i+1\to i+2})^\dagger \, (\widehat{\mathcal{A}^i} \otimes \mathcal{I}^\bullet) \, \mathcal{R}^{\mathcal{S}}_{i+1\to i+2} \to \widehat{\mathcal{A}^i}, \\
\vdots \\
(\mathcal{R}^{\mathcal{S}}_{j-2\to j-1})^\dagger \, (\widehat{\mathcal{A}^i} \otimes \mathcal{I}^\bullet) \, \mathcal{R}^{\mathcal{S}}_{j-2\to j-1} \to \widehat{\mathcal{A}^i}.
\end{gathered} \tag{C.27}$$

At the end of this routine, $\widehat{\mathcal{A}^i}$ will live in the Hilbert space of the system block $\mathcal{S}(j-1, M_{j-1})$, and then we shall be able to perform the measure by taking the average:

$$\langle \mathcal{A}^i \mathcal{B}^j \rangle = \psi^*_{g(s,\alpha,\beta,e)} \widehat{\mathcal{A}^i}_{ss'} \mathcal{B}^j_{\alpha\alpha'} \psi_{g(s',\alpha',\beta,e)}. \tag{C.28}$$

In the same way, it is possible to perform a measure for an observable $\mathcal{B}^j$ that belongs to the environment block (the right one). We want to remark that it is also possible to evaluate measures in the case when i and j belong to the same block, but now the previous operator product representation is not correct. Indeed, such an operator should be renormalized at each DMRG step as a compound object [Sch05].

Entanglement entropy — DMRG algorithm provides an optimal representation of the super-block Hilbert space for easily measuring the von Neumann entropy, despite its non local properties. Indeed, at each DMRG step, for proceeding to the renormalization, we have to diagonalize the reduced density matrix of both enlarged system and enlarged environment. Therefore, when the system block is $\mathcal{S}(\ell-1, M_{\ell-1})$, the reduced density matrix after a DMRG step is just the density matrix of the leftmost ℓ-sites subchain:

$$\rho^\ell \equiv \rho^{\mathcal{S}\bullet}. \tag{C.29}$$

After diagonalize it, we have:

$$S(\ell) = -\sum_{n=1}^{DM_{\ell-1}} w_n \ln w_n, \tag{C.30}$$

where w_n are the eigenvalues of the reduced density matrix.

C.1.5 Technical details

Now we will analyze some technicals tricks about the implementation of DMRG algorithm. Furthermore we will give some interesting results which catch the key features of such a numerical method.

Lanczos-Davidson diagonalization — The Hamiltonian of the super-block is a matrix of dimension $D^2M^2 \times D^2M^2$. It is a very expensive procedure to diagonalize it. As we yet said, we want to know only the ground-state properties of the Hamiltonian. Thus, we can reduce the computational time by using Lanczos or Davidson methods[Dav75]. In this way, we can obtain the the ground state in much less time with respect to the time needs for accomplishing a full diagonalization routine. Moreover, it is not necessary to store the full Hamiltonian. What we need is the the way in which the Hamiltonian acts on a generic vector $|\psi\rangle$ living in a Hilbert space of dimension D^2M^2. At each DMRG step it is possible to write a generic state as:

$$|\psi\rangle = \psi_{g(s,\alpha,\beta,e)}|s,\alpha,\beta,e\rangle, \tag{C.31}$$

where Latin indexes s and e refer respectively to system and environment blocks, while Greek indexes α and β indicate free sites; in addition, the function $g(s,\alpha,\beta,e)$ is useful for storing the $|\psi\rangle$ components in a one-dimensional array whose index runs from 1 to $M_sM_eD^2$ (see at the end of this Subsection for the definition). Henceforth implicit summation convention is assumed.

With this notation, if we take a generic component $\mathcal{A}^{\mathcal{S}\bullet}\otimes\mathcal{B}^{\bullet\mathcal{E}}$ of the superblock Hamiltonian in Eq. (C.15) acting on the left and on the right enlarged block, we have to implement only this matrix multiplication:

$$\psi^{out}_{g(s,\alpha,\beta,e)} = \mathcal{A}^{\mathcal{S}\bullet}_{g(s,\alpha)g(s',\alpha')}\mathcal{B}^{\bullet\mathcal{E}}_{g(\beta,e)g(\beta',e')}\psi^{in}_{g(s',\alpha',\beta',e')}. \tag{C.32}$$

In order to make the procedure more clear we apply the matrix multiplication to the free spin interaction term appearing into the superblock Hamiltonian; in this case we have to do only the multiplication between the free sites, then the output looks like

$$\psi^{out}_{g(s,\alpha,\beta,e)} = \mathcal{H}^{\bullet\bullet}_{i\;g(\alpha,\beta)g(\alpha',\beta')}\psi^{in}_{g(s,\alpha',\beta',e)}; \tag{C.33}$$

note that the system and environment indeces of the input and the output state are the same.

Using this prescription we can save a lot of memory and number of operations, since the dimensions of a matrix that acts on a generic enlarged block are $DM \times DM$, versus $D^2M^2 \times D^2M^2$ dimensions of a super-block matrix. Finally, let us remark that this matrix multiplication used for Davidson diagonalization is quite general and we shall use it for all matrices or vectors multiplications that we should perform.

Wave function prediction — Even by using Lanczos or Davidson routine, the hardest task is still the diagonalization step. Briefly, the algorithm uses a initial vector and, after applying iteratively the matrix $\mathcal{H}^{\mathcal{S}\bullet\bullet\mathcal{E}}$, it generates a Krylov subspace in which the Hamiltonian is diagonalized; after that, it returns an approximate ground state up to some tolerance value, fixed from the user. It is obvious that if a good guess as initial state is available, the number of iterations required to converge to the solution can be reduced. In other words, with a starting state that have overlap ≈ 1 with the final state, one can substantially reduce the diagonalization time. During the infinite-system DMRG, the system changes at each step (its length grows of two site), then it is not easy to give a optimal guess as input for the diagonalization routine. Otherwise, in the case of finite-system DMRG, only the structure of the Hilbert space changes from step to step, while the physical system is left unchanged. Therefore, we can use the White's prescription to predict the ground state re-expressed in the truncated basis of the next DMRG step[Whi96]. The idea is to change the ground state representation from one basis to the next although the transformation is incomplete (one should not forget that the renormalization matrices are not square unitary matrices). In Figure C.5 we represent a system block of length ℓ and an environment block of length $L-\ell-2$.

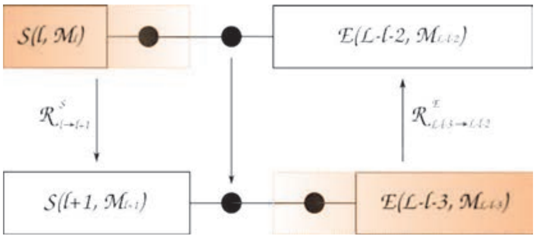

Figure C.5: Graphical representation of DMRG basis transformation in order to obtain the initial guess for the wave function.

After a Davidson diagonalization, the array elements of the target state are $\psi_{g(s,\alpha,\beta,e)}$. Now, let us assume that we are performing a left-to-right sweep in such a way that the system block is growing and the environment block is shrinking, thence we want to predict the new representation $\psi'_{g(s',\alpha',\beta',e')}$, where in both DMRG steps $|\psi\rangle$ is describing the same physical system. All what we need is to apply the matrix $\mathcal{R}^{\mathcal{S}}_{\ell\to\ell+1}$ which we know from the current DMRG iteration, and the matrix $\mathcal{R}^{\mathcal{E}}_{L-\ell-3\to L-\ell-2}$ from some previous DMRG iteration. In matrix notation, the renormalization operators act as a incomplete change of basis:

$$|s'\rangle \;\; = (\mathcal{R}^{\mathcal{S}}_{\ell\to\ell+1})_{g(s,\alpha)s'}\;|s,\alpha\rangle, \tag{C.34}$$

$$|e\;\rangle \;\; = (\mathcal{R}^{\mathcal{E}}_{L-\ell-3\to L-\ell-2})_{g(\beta',e')e}\;|\beta',e'\rangle. \tag{C.35}$$

Using Eq. (C.35) and the conjugate of Eq. (C.34) the transformed wave function then reads:

$$\psi'_{g(s',\alpha',\beta',e')} = (\mathcal{R}^{\mathcal{S}}_{\ell\to\ell+1})^*_{g(s,\alpha)s'}(\mathcal{R}^{\mathcal{E}}_{L-\ell-3\to L-\ell-2})_{g(\beta',e')e}\psi_{g(s,\alpha,\alpha',e)}. \tag{C.36}$$

Notice that the left free site is now the same as the right one just before the change of basis was carried out (see Figure C.5).

During the DMRG algorithm, we have to decide the tolerance value that we shall use for the diagonalization routine. Normally, in the infinite-system algorithm it is necessary to keep a quite small tolerance in order to avoid a wrong output target state; otherwise, in finite-system algorithm, using the White's prescription for initial wave function, it is also possible to increase the tolerance of some order of magnitude. In fact, at each step the input vector has yet a great overlap with the final state, therefore, also for a poor tolerance, there is not risk that the Davidson routine gave something wrong.

On the suitable dimension of the Hilbert space — After selecting a system where to apply the DMRG algorithm, normally the user has to tune some parameters which define the accuracy level of the simulation. Basically there are three parameters that we can set up: the tolerance of the Davidson routine, the tolerance ϵ of the energy output and the maximum value M of the Hilbert space dimension. About the diagonalization routine we have seen in the previous paragraph that, in order to obtain a good output state, it does not matter what value of tolerance has been chosen. Now, we turn our attention to the last two parameters.

The energy tolerance ϵ defines the minimum value of the energy difference between two successives DMRG sweeps. In other words, while finite-system DMRG is running, we take note of the energy value at the end of a sweep and we calculate the difference with the previous value; if this number is smaller then ϵ, we just go to stop the algorithm. A this point, it would be natural to take ϵ as error of the energy, but generally, this is not correct.

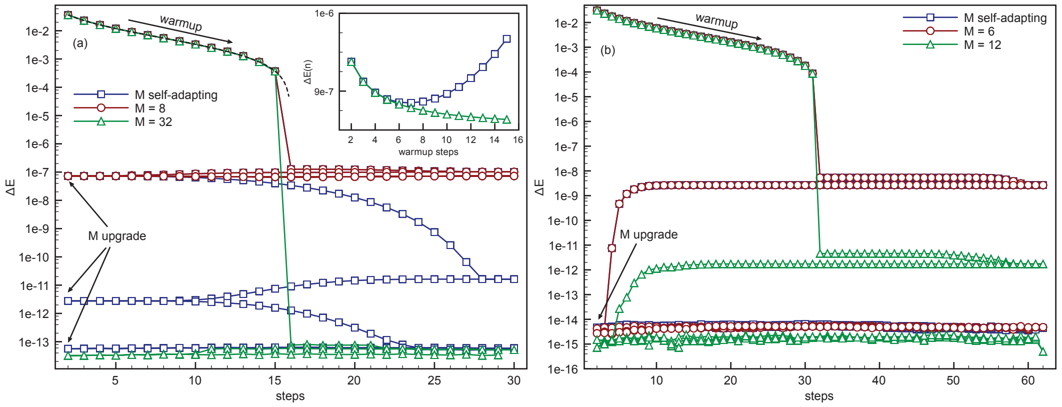

Figure C.6: Difference between DMRG and exact ground-state energy for a critical transverse Ising chain with $L = 32$ sites (a), and for a factorized XY chain ($\gamma^2 + h^2 = 1$) with $L = 64$ (b). We plot two different kind of algorithm: (red and green) - we perform the *warmup* and the *sweeps* with a fixed value of M that correspond to the starting value (red ones) and finishing value (green ones) used by M self-adapting algorithm; (blue) - now the M value grow until the same error on the energy is achieved. Only in (a), the black dot line is the exact ground energy at each warmup step refered to E_0; the inset shows the difference during the *warmup* steps.

In fact, we would take care to provide for a good M value. If M is too small for taking correctly into account all the system correlations, the energy usually converges to a value which differs from the exact ones by an amount much larger then the tolerance ϵ. It is clear that, by increasing M, the output becomes closer and closer to the exact solution, which is eventually reached in the limit of $M \sim D^L$. Normally the energy tolerance and the maximum dimension of the Hilbert space are strictly connected and it would be good to know an initial guess for M. In fact, if we use a good enough M value, ϵ give us the correct uncertainty of the energy; otherwise, it is not useful to ask for a small tolerance with a non so good M value. In answer to this request we should use the information theory. If we consider a system block which lives in a M dimensional Hilbert space, the entropy is maximum when the density matrix $\rho_{\mathcal{S}}$ has a uniform eigenvalues distribution. One has:

$$S_{\mathcal{S}} \leqslant -\sum_{i=1}^{M} (1/M)\ln(1/M) = \ln M, \tag{C.37}$$

that gives the lower limit $M \geqslant \exp(S_{\mathcal{S}})$. Now, close to a quantum critical point, the CFT predicts the scaling law

$$S(\ell) \sim \ln\left(\frac{2L}{\pi}\sin\left(\frac{\pi\ell}{L}\right)\right), \tag{C.38}$$

for the entropy of a subsystem of length ℓ embedded in a finite chain of length L. Using the maximum value $S(L/2)$ we finally obtain

$$M \gtrsim 2L/\pi. \tag{C.39}$$

Otherwise, for a system away enough from its critical points the entropy is bounded by a maximum value $S^*_{\mathcal{S}}$, then independently of the system size, M is lower-bounded by $\sim$

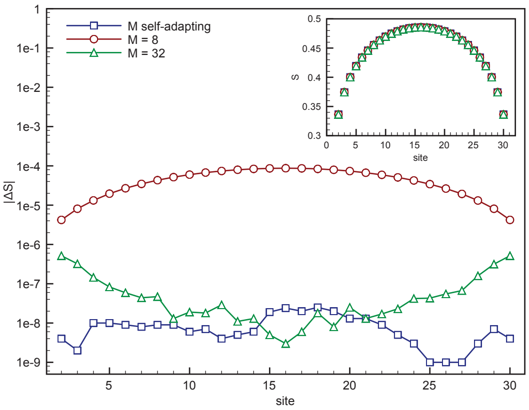

Figure C.7: Block entropy for a transverse Ising chain with $L = 32$ sites at critical point. The data are referred to the block entropy obtained by exact numerical diagonalization. The convention is the same as in Figure C.6.

$\exp(S^*_S)$. These values are only indicative and often, on depending the system we are working with, they could be very different. Moreover, it is not useful to have a great precision while finite-system DMRG is running: a better precision is recovered by using finite-system DMRG. In order to avoid this problem we perform the infinite-system algorithm with a small M, then we increase its value at each finite-system sweep looking for a energy convergence. In this way we take into account the effects of a bad starting value of M and save a lot of CPU-time. Basically, we adopt the following prescription for optimizing the energy output as well as the CPU-time:

- Perform infinite-system DMRG with a small enough $M = M_0 \lesssim L/8$.
- Run the first left to right sweep with the same value of M, then upgrade it to the $L/8$ value.
- From now on, after each DMRG sweep, increase M by M_0 for not critical systems, by $L/8$ for critical ones.

For making the discussion more clear we show in Figure C.6 the results for different solutions applied on a transverse Ising chain in a critical and not-critical regime. We perform a DMRG simulation using our prescription, then we confront the result with two other simulation accomplished with M kept fix to the starting and finishing value used by M-updating simulation. In all cases we have set the energy tolerance equale to 10^{-12}. The main plot shows the difference in the energy for a critical and a non critical system. Although the not-critical chain is much larger than the critical one, it needs for a smaller M compared to the critical one. Furthermore, in the not-critical case the algorithm is much faster and converges with higher precision; otherwise, the powerful of our prescription is better showed by the critical simulation. In fact, in this case is manifest the further improvement caused by the growth of the M value. Only for the critical case, we take note also of the warmup energy referred to the exact size-depending energy $E_0(L) = -\sin^2(\frac{\pi}{2}\frac{L}{2L+1})/\sin(\frac{\pi}{2}\frac{1}{2L+1})$; despite the difference in the value of M, the energy error rests almost unchanged, especially compared with the improvement dues to the finite-system algorithm. For the critical case, we show in Figure C.7 the block entropy behavior. We compare, as in the energy case, different algorithms and plot the result referred to the exact one. Notice that the error in

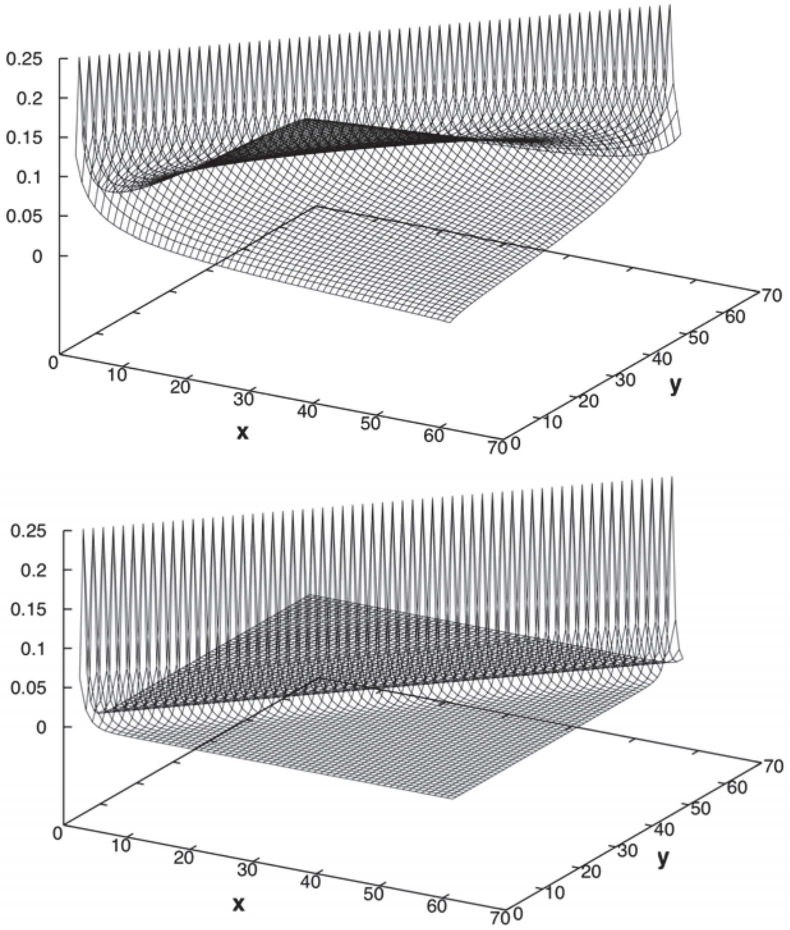

Figure C.8: Ground state correlation function $\langle \sigma_i^x \sigma_j^x \rangle$ for an Ising chain with size $L = 64$ in the critical regime $h = 1$ (top) and non critical regime $h = 2$ (bottom).

the entropy is much larger than the energy one, but again it rest quite small (on depending the energy tolerance we have set up before). Finally, as an example of two-point observable, we compare in Figure C.8 the behavior of the order parameter correlation function $\langle \sigma_i^x \sigma_j^x \rangle$ in the ground state of the Ising model both for a critical and non critical chain.

Useful storing functions — We give the storing functions used for allocate vectors and matrices during the algorithm. We have used the convention that the tensorial indexes of a vector or a matrix run from the right to the left. The first index which change is the environment, then the right free site and so on. In this way for a generic state we have

$$\psi_{s\alpha\beta e} \to \psi_{g(s,\alpha\beta,e)}, \tag{C.40}$$

with

$$g(s,\alpha,\beta,e) = e + M_{\mathcal{E}}(\beta + D(\alpha + D(s-1) - 1) - 1). \tag{C.41}$$

The index e runs from 1 to the environment dimension $M_{\mathcal{E}}$, s from 1 to the system dimension $M_{\mathcal{S}}$ and indeces α and β run from 1 to D. It is straightforward to introduce analogs functions

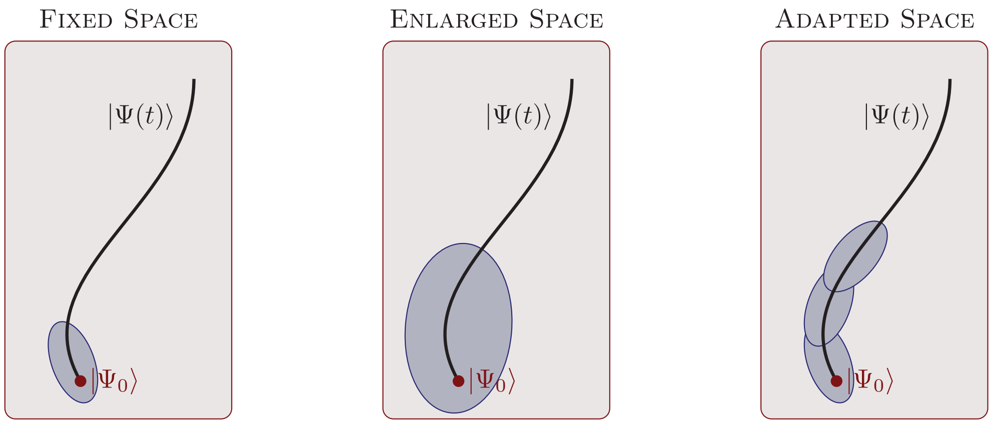

Figure C.9: In the figure different time-dependent approach are presented. In each case, the total Hilbert space (big light red squares) is truncated to a local sub-space (small light blue ellipses). From left to right we show: the FIXED SPACE approach, in which the evolution is performed taking fixed the initial truncated basis; the ENLARGED SPACE approach, in which the approximative basis is enlarged in time but the target state is always the initial one; the ADAPTED SPACE approach, in which one adapts in time the truncated Hilbert space in order to better describe the evolved vector (black full lines). In the text, we describe this latter method.

for $\mathcal{S}\bullet$, $\bullet\mathcal{E}$ and $\bullet\bullet$ subspaces

$$g(s,\alpha) = \alpha + D(s-1), \tag{C.42}$$
$$g(\beta,e) = e + M_{\mathcal{E}}(\beta-1), \tag{C.43}$$
$$g(\alpha,\beta) = \beta + D(\alpha-1), \tag{C.44}$$

and also for $\mathcal{S}\bullet\bullet$ and $\bullet\bullet\mathcal{E}$

$$g(s,\alpha,\beta) = \beta + D(\alpha + D(s-1) - 1), \tag{C.45}$$
$$g(\alpha,\beta,e) = e + M_{\mathcal{E}}(\beta + D(\alpha-1) - 1). \tag{C.46}$$

C.2 Time-dependent DMRG

In the last decade a multitude of numerical methods for implementing the time evolution in quantum systems was proposed [CM02, LXW03, CM03, Vid03, Vid04, WF04, DKSV04, FW05] but, once again, a decisive contribution came from the quantum information domain. Indeed, in 2003 G. Vidal developed the Time-Evolving Block Decimation (TEBD) algorithm which is an efficient algorithm to simulate the time-evolution of one-dimensional quantum systems. The underlying idea of such an algorithm is closely related to the DMRG method, therefore it can be easily implemented with the same DMRG language. The numerical method that comes out from the union of the TEBD with the DMRG is called "adaptive" time-dependent DMRG (t-DMRG): in practice, during the algorithm one adapts in time the reduced Hilbert space to the time-evolving target state. In this section, following [WF04,

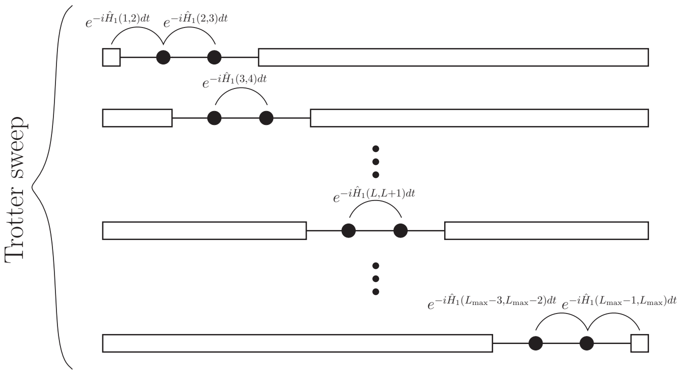

Figure C.10: Sketch of the t-DMRG algorithm. In this case the local evolution operator is implemented using the first order Trotter expansion (Figure taken from [CRRM08]).

DKSV04, SW06, CRRM08], we will describe how to implement the real time evolution into the DMRG algorithm.

Let us suppose to have found, using the static DMRG algorithm, the approximate ground state $|\Psi_0\rangle$ of some initial Hamiltonian $\mathcal{H}_0$. Then, the aim is to simulate the time-evolution of the system according to a different Hamiltonian $\mathcal{H}_1$. This goal is accomplished by introducing the Suzuki-Trotter decomposition of the evolution operator $\mathcal{U} = \mathrm{e}^{-i\mathcal{H}_1 t}$. From previous sections we know that the DMRG algorithm gives an approximate truncated basis of the Hilbert space of the system. However, the evolved state $|\Psi(t)\rangle$ changes in time, exploring different regions of the total Hilbert space, and, therefore, the initial truncated basis should be no more the better approximation to represent the actual state. As we yet said, this problem can be solved by updating such a basis during the evolution. This can be easily done in the DMRG framework: we can simply follow the DMRG renormalization procedure but now targeting the evolved state instead of the ground state of the super-block Hamiltonian.

Indeed, we can use the finite-system algorithm to perform step by step a local time evolution, then we construct a new block basis which well describes the state $|\Psi(t)\rangle$ at any time of the evolution. For accomplishing such a local evolution we needs to rewrite, at each step, the wave function $|\Psi(t)\rangle$ in the correct blocks-sites configuration in order to be able to apply the next local evolution operator on the two free sites. In other words, we have to transform the state representation between different configurations. We yet know how to do that: we need just the same White's prescription as for the static DMRG diagonalization routine [Whi96] (see paragraph "Wave function prediction"). In this case, the White's prescription is used as simple truncated-basis transformation.

As we said before, we approximately evaluate the evolution operator $\mathcal{U} = \mathrm{e}^{-i\mathcal{H}_1 t}$ using the Suzuki-Trotter decomposition. For example, the first order expansion is:

$$\mathrm{e}^{-i\mathcal{H}_1 t} \approx \left[\prod_{\ell=1}^{L-1} \mathrm{e}^{-i\mathcal{H}_1(\ell) dt} \right]^N , \tag{C.47}$$

where we have introduced the small time interval dt and the number of time steps $N = t/dt$. $\mathcal{H}_1(\ell)$ is the local interaction Hamiltonian between site ℓ and $\ell + 1$, in such a way that $\mathcal{H}_1 = \sum_\ell \mathcal{H}_1(\ell)$ and L is the size of the system. Of coarse, we can introduce higher-order approximations: for example, if we split the total Hamiltonian as $\mathcal{H}_1 = \mathcal{H}_e + \mathcal{H}_o$, where

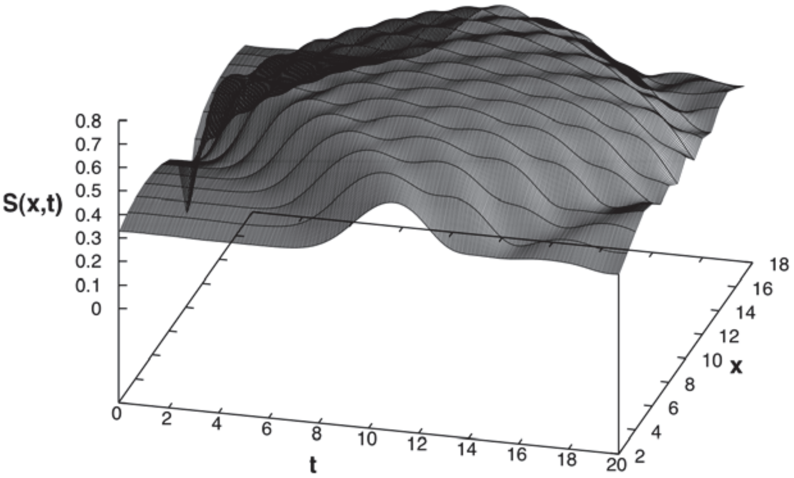

Figure C.11: Temporal evolution of the entanglement entropy $S(\ell, t)$ of a L = 20 critical Ising chain after switching on the interaction term in the middle. Here we used $dt = 0.05$.

$\mathcal{H}_e = \sum_{\ell\,\text{even}} \mathcal{H}_1(\ell)$ contains only even bonds and $\mathcal{H}_o = \sum_{\ell\,\text{odd}} \mathcal{H}_1(\ell)$ only odd bonds, since $[\mathcal{H}_e, \mathcal{H}_0] = 0$ one obtains the second-order expansion:

$$\mathrm{e}^{-i\mathcal{H}_1 t} \approx \left[\mathrm{e}^{-i\mathcal{H}_e dt/2}\mathrm{e}^{-i\mathcal{H}_o dt}\mathrm{e}^{-i\mathcal{H}_e dt/2}\right]^N . \tag{C.48}$$

Notice that the second order Trotter decomposition corresponds to apply, for a single time-step, the operator

$$\mathrm{e}^{-i\mathcal{H}_1 dt} \approx \mathrm{e}^{-i\mathcal{H}_1(1)dt/2} \cdots \mathrm{e}^{-i\mathcal{H}_1(L-1)dt/2}\mathrm{e}^{-i\mathcal{H}_1(L-1)dt/2} \cdots \mathrm{e}^{-i\mathcal{H}_1(1)dt/2}, \tag{C.49}$$

giving reversible (in the sense left/right) time evolution. The idea is to apply $\mathrm{e}^{-i\mathcal{H}_1(1)dt/2}$ at DMRG step 1, then $\mathrm{e}^{-i\mathcal{H}_1(2)dt/2}$ at step 2, etc., up to the end of the usual left-to-right sweep, then to repeat the same procedure but in the inverse order following the right-to-left sweep.

In theory it is possible to improve the algorithm by using successive order expansions. Nevertheless, the main source of errors also in the t-DMRG algorithm is still the truncation error. Indeed, it is not useful to have a perfect time evolution if we have a poor approximation of the wave function. What we need is a good compromise between the maximum number of states kept M, the order of the Trotter decomposition and the number of Trotter steps N. For more details on the t-DMRG errors see [GKSS05, SW06].

In the following paragraph we summarize the adaptive time-dependent DMRG algorithm which incorporates the TEBD.

C.2.1 Adaptive t-DMRG recipe

1. Find the ground state $|\Psi_0\rangle$ of $\mathcal{H}_0$ by using the static DMRG algorithm.

2. Follow the same finite-system procedure, but now, at each step ℓ, apply the operator $\mathrm{e}^{-i\mathcal{H}_1(\ell)dt/2}$ (second order Trotter expansion) to the system state. For first, from left to right, then from right to left using the inverse sequence.

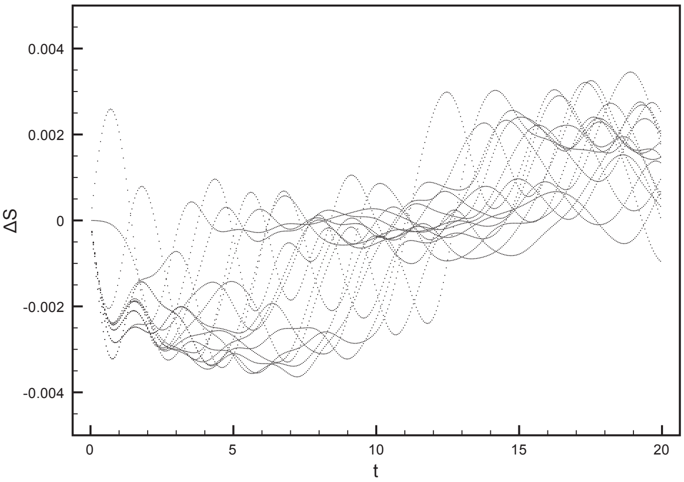

Figure C.12: Entropy difference between DMRG and exact dynamics, $\Delta S \equiv S_{DMRG}(\ell, t) - S_{ex}(\ell, t)$. Each curve represents different subsystem size ℓ.

3. Renormalize the system block and the environment block storing the matrices $\mathcal{R}^{\mathcal{S}}$ and $\mathcal{R}^{\mathcal{E}}$ for the following steps.

4. Use the White's prediction to change the state representation.

5. Repeat points 3 to 4, until a complete sweep (left-to-right plus right-to-left) is accomplished.

As we yet said, the White's prescription is already included in the static DMRG recipe, then implementing the TEBD method in the DMRG code is straightforward: at each DMRG step ℓ, we need to apply the local evolution operator $\mathrm{e}^{-i\mathcal{H}_1(\ell)dt/2}$ to the super-block state vector. To be more clear, we explicitly give an example of the procedure using the Trotter expansion (C.49). In this case, for accomplishing the evolution from t to $t + dt$ one needs one entire sweep: we perform the usual left-to-right half sweep applying at each step the local representation of the operator $\mathrm{e}^{-i\mathcal{H}_1(\ell)dt/2}$ to the two free site ℓ and $\ell + 1$. Notice that this operator, in the representation in which the sites ℓ and $\ell + 1$ are the two free sites, is described by an exact $D^2 \times D^2$ matrix. Once the left-to-right half sweep is accomplished, we apply the same operators in the reversed order following the right-to-left half sweep. At the end of this procedure we obtain the vector $|\Psi(t + dt)\rangle$. Just one remark: whenever we arrive to the border, e.g. the configuration $\mathcal{S}(L-3, M_{L-3}) \bullet \bullet \mathcal{E}(1, D)$ at the end of the left-to-right half sweep, we have to use the same representation of the wave function to perform the evolution of both the two free sites and the block. Finally, we want to stress again that during the whole procedure we have to renormalize the corresponding growing block using as a target state the partially evolved super-block state. In this way, we take into account the modification of the truncated Hilbert space. In addition, we can also change the maximum size M of the block Hilbert space during the time evolution. By doing that, it is possible to take into account any growth in the system correlations (see next paragraph). In Figure C.10 we give a sketch of such a procedure for one half sweep.

Now, we give a simple example of a simulation performed with the t-DMRG. We consider a quantum critical Ising chain $\mathcal{H}_{TI}[L] = -\sum_{i=1}^{L-1} \sigma_i^x \sigma_{i+1}^x - \sum_{i=1}^{L} \sigma_i^z$, where L is the system size. We first run the finite-system DMRG algorithm to obtain the ground state $|\Psi_0\rangle$ of

$\mathcal{H}_0 = \mathcal{H}_{TI}[10] + \mathcal{H}_{TI}[10]$, that is two unconnected Ising chain with size $L = 10$. Then we switch on the central site interaction, performing the t-DMRG algorithm with $\mathcal{H}_1 = \mathcal{H}_{TI}[20]$. In Figure C.11 we plot the entanglement entropy profile $S(\ell, t)$ for the leftmost subsystem of size ℓ embedded in the whole chain. By comparing t-DMRG evolution with the exact numerical diagonalization one can see that, during the evolution, $|S_{DMRG}(\ell, t) - S_{ex}(\ell, t)| \lesssim dt^2$ (see Figure C.12).

Enlarging the Hilbert space in time — To conclude this section, we give some technical details about the adaptive calculation of the maximal Hilbert space dimension. Once again, we use the information theory to link the dimension of the Hilbert space to the entanglement entropy. The idea is to state, also for time evolved system: $S(t) \sim \ln M(t)$; where $S(t)$ is the time-dependent entropy, and $M(t)$ represents the maximal Hilbert space dimension at time step t. In practice, after a complete evolution from $t - dt$ to t, we know the entanglement entropy profile $S(\ell, t)$. Using the entropy difference calculated at the maximum value

$$dS(t) = S_{MAX}(t) - S_{MAX}(t - dt), \tag{C.50}$$

we perform the upgrading for the next step

$$M(t + dt) = \mathrm{int}\left[M(t)\mathrm{e}^{dS(t)}\right]. \tag{C.51}$$

Bibliography

[ABS11] F. C. Alcaraz, M. I. Berganza, and G. Sierra, *Entanglement of low-energy excitations in conformal field theory*, Phys. Rev. Lett. **106** (2011), 201601.

[AFOV08] L. Amico, R. Fazio, A. Osterloh, and V. Vedral, *Entanglement in many-body systems*, Rev. Mod. Phys. **80** (2008), 517.

[AL95] D. B. Abraham and F. T. Latrémolière, *Corner spontaneous magnetization*, J. Stat. Phys. **81** (1995), 539.

[Alv10] Juan Felipe Carrasquilla Alvarez, *The bose-hubbard model with disorder in low-dimensional lattices*, Ph.D. thesis, SISSA, 2010.

[BC04] B. Berche and C. Chatelain, *Order, disorder and criticality*, World-Scientific, Singapore, 2004.

[BCH11] M. C. Bañuls, J. I. Cirac, and M. B. Hastings, *Strong and weak thermalization of infinite nonintegrable quantum systems*, Phys. Rev. Lett. **106** (2011), 050405.

[BDZ08] I. Bloch, J. Dalibard, and W. Zwerger, *Many-body physics with ultracold gases*, Rev. Mod. Phys. **80** (2008), 885.

[Bin83] K. Binder, *Phase transitions and critical phenomena*, Academic Press, London, 1983.

[BJZ$^+$08] J. Billy, V. Josse, Z. Zuo, A. Bernard, B. Hambrecht, P. Lugan, D. Clément, L. Sanchez-Palencia, P. Bouyer, and A. Aspect, *Direct observation of anderson localization of matter waves in a controlled disorder*, Nature **453** (2008), 891.

[Blo28] F. Bloch, *Über die quantenmechanik der elektronen in kristallgittern*, Z. Phys. **52** (1928), 555.

[BM71a] E. Barouch and B. McCoy, *Statistical mechanics of the* XY *model.* II. *spin-correlation functions*, Phys. Rev. A **3** (1971), 786.

[BM71b] ———, *Statistical mechanics of the* XY *model.* III, Phys. Rev. A **3** (1971), 2137.

[BMA71] E. Barouch, B. McCoy, and D. B. Abraham, *Statistical mechanics of the* XY *model.* IV*. time-dependent spin-correlation functions*, Phys. Rev. A **4** (1971), 2331.

[BMD70] E. Barouch, B. McCoy, and M. Dresden, *Statistical mechanics of the* XY *model.* I, Phys. Rev. A **2** (1970), 1075.

[Bos24] S. N. Bose, *Plancks gesetz und lichtquantenhypothese*, Zeitschrift für Physik **26** (1924), 178.

[BP08] R. A. Barankov and A. Polkovnikov, *Optimal nonlinear passage through a quantum critical point*, Phys. Rev. Lett. **101** (2008), 076801.

[BPP84] M. N. Barber, I. Peschel, and P. A. Pearce, *Magnetization at corners in two-dimensional ising models*, J. Stat. Phys. **37** (1984), 497.

[BS08] T. Barthel and U. Schollwöck, *Dephasing and the steady state in quantum many-particle systems*, Phys. Rev. Lett. **100** (2008), 100601.

[Car83] J. L. Cardy, *Critical behaviour at an edge*, J. Phys. A: Math. Gen. **13** (1983), 3617.

[Car84] ———, *Conformal invariance and surface critical behavior*, Nucl. Phys. B **240** (1984), 514.

[Car96] ———, *Scaling and renormalization in statistical physics.*, Cambridge Lecture Notes in Physics, 1996.

[CBL+09] J. Catani, G. Borontini, G. Lamporesi, F. Rabatti, G. Thalhammer, F. Minardi, S. Stringari, and M. Inguscio, *Entropy exchange in a mixture of ultracold atoms*, Phys. Rev. Lett. **103** (2009), 140401.

[CC04] P. Calabrese and J. L. Cardy, *Entanglement entropy and quantum field theory*, J. Stat. Mech. (2004), P06002.

[CDDZ07] F. M. Cucchietti, B. Damski, J. Dziarmaga, and W. H. Zurek, *Dynamics of the bose-hubbard model: Transition from a mott insulator to a superfluid*, Phys. Rev. A **75** (2007), 023603.

[CDEO08] M. Cramer, C. M. Dawson, J. Eisert, and T. J. Osborne, *Exact relaxation in a class of nonequilibrium quantum lattice systems*, Phys. Rev. Lett. **100** (2008), 030602.

[CFM+08] M. Cramer, A. Flesch, I. P. McCulloch, U. Schollwöck, and J. Eisert, *Exploring local quantum many-body relaxation by atoms in optical superlattices*, Phys. Rev. Lett. **101** (2008), 063001.

[CGKS+05] P. Cladé, S. Guellati-Khélifa, C. Schwob, F. Nez, L. Julien, and F. Biraben, *A promising method for the measurement of the local acceleration of gravity using bloch oscillations of ultracold atoms in a vertical standing wave*, Europhys. Lett. **71** (2005), 730.

[CH04] S.-A. Cheong and C. L. Henley, *Many-body density matrices for free fermions*, Phys. Rev. B **69** (2004), 075111.

[CK10] M. Collura and D. Karevski, *Critical quench dynamics in confined systems*, Phys. Rev. Lett. **104** (2010), 200601.

[CK11] ______, *Nonlinear quenches of power-law confining traps in quantum critical systems*, Phys. Rev. A **83** (2011), 023603.

[CKT09] M. Collura, D. Karevski, and L. Turban, *Gradient critical phenomena in the ising quantum chain: surface behaviour*, J. Stat. Mech. (2009), P08007.

[CL06] R. W. Cherng and L. S. Levitov, *Entropy and correlation functions of a driven quantum spin chain*, Phys. Rev. A **73** (2006), 043614.

[CM02] M. A. Cazalilla and J. B. Marston, *Time-dependent density-matrix renormalization group: A systematic method for the study of quantum many-body out-of-equilibrium systems*, Phys. Rev. Lett. **88** (2002), 256403.

[CM03] ______, *Cazalilla and marston reply:*, Phys. Rev. Lett. **91** (2003), 049702.

[CMDO09] A. C. Cassidy, D. Mason, V. Dunjko, and M. Olshanii, *Threshold for chaos and thermalization in the one-dimensional mean-field bose-hubbard model*, Phys. Rev. Lett. **102** (2009), 025302.

[CMV] P. Calabrese, M. Mintchev, and E. Vicari, *Entanglement entropies in free fermion gases for arbitrary dimension*, arXiv:1110.6276v1.

[CMV11] ______, *Entanglement entropy of one-dimensional gases*, Phys. Rev. Lett. **107** (2011), 020601.

[CP01] M.-C. Chung and I. Peschel, *Density-matrix spectra of solvable fermionic systems*, Phys. Rev. B **64** (2001), 064412.

[CRRM08] G. De Chiara, M. Rizzi, D. Rossini, and S. Montangero, *Density matrix renormalization group for dummies*, J. Comput. Theor. Nanosci. **5** (2008), 1277.

[CV09] M. Campostrini and E. Vicari, *Critical behavior and scaling in trapped systems*, Phys. Rev. Lett. **102** (2009), 240601.

[CV10] ______, *Trap-size scaling in confined-particle systems at quantum transitions*, Phys. Rev. A **81** (2010), 023606.

[CW98] Eric A. Cornell and Carl E. Wienman, *The bose-einstein condensate*, Scientific American **278** (1998), 40 – 45.

[Dam05] B. Damski, *The simplest quantum model supporting the kibble-zurek mechanism of topological defect production: Landau-zener transitions from a new perspective*, Phys. Rev. Lett. **95** (2005), 035701.

[Dav75] E. R. Davidson, *The iterative calculation of a few of the lowest eigenvalues and corresponding eigenvectors of large real-symmetric matrices*, Journal. Comp. Phys. **17** (1975), 87.

[DKSV04] A. J. Daley, C. Kollath, U. Schollwöck, and G. Vidal, *Time-dependent density-matrix renormalization-group using adaptive effective hilbert spaces*, J. Stat. Mech. (2004), P04005.

[DLZ99] J. Dziarmaga, P. Laguna, and W. H. Zurek, *Symmetry breaking with a slant: Topological defects after an inhomogeneous quench*, Phys. Rev. Lett. **82** (1999), 4749.

[DP97] B. Davies and I. Peschel, *A unified treatment of ising model magnetizations*, Ann. Phys. Lpz. **6** (1997), 187.

[DPK08] S. Dorosz, T. Platini, and D. Karevski, *Work fluctuations in quantum spin chains*, Phys. Rev. E **77** (2008), 051120.

[DPR$^+$96] M. B. Dahan, E. Peik, J. Reichel, Y. Castin, and C. Salomon, *Bloch oscillations of atoms in an optical potential*, Phys. Rev. Lett. **76** (1996), 4508.

[DR10a] J. Dziarmaga and M. M. Rams, *Adiabatic dynamics of an inhomogeneous quantum phase transition: the case of a* $z > 1$ *dynamical exponent*, New J. Phys. **12** (2010), 103002.

[DR10b] ———, *Dynamics of an inhomogeneous quantum phase transition*, New J. Phys. **12** (2010), 055007.

[DZ06] B. Damski and W. H. Zurek, *Adiabatic-impulse approximation for avoided level crossings: From phase-transition dynamics to landau-zener evolutions and back again*, Phys. Rev. A **73** (2006), 063405.

[DZ07] ———, *Dynamics of a quantum phase transition in a ferromagnetic bose-einstein condensate*, Phys. Rev. Lett. **99** (2007), 130402.

[DZ09] ———, *Quantum phase transition in space in a ferromagnetic spin-1 bose–einstein condensate*, New J. Phys. **11** (2009), 063014.

[Dzi05] J. Dziarmaga, *Dynamics of a quantum phase transition: Exact solution of the quantum ising model*, Phys. Rev. Lett. **95** (2005), 245701.

[Dzi10] ———, *Dynamics of a quantum phase transition and relaxation to a steady state*, Adv. Phys. **59** (2010), 1063.

[EG03] M. Esposito and P. Gaspard, *Spin relaxation in a complex environment*, Phys. Rev. E **68** (2003), 066113.

[Ein25] A. Einstein, *Quantentheorie des einatomigen idealen gases*, Sitzungsberichte der Preussischen Akademie der Wissenschaften **1** (1925), 3.

[EKPP08] V. Eisler, D. Karevski, T. Platini, and I. Peschel, *Entanglement evolution after connecting finite to infinite quantum chains*, J. Stat. Mech. (2008), P01023.

[EP07] V. Eisler and I. Peschel, *Evolution of entanglement after a local quench*, J. Stat. Mech. (2007), P06005.

[FA05] F. Franchini and A. G. Abanov, *Asympotic of toeplitz determinants and the emptiness formation probability for the* XY *spin chain*, J. Phys. A **38** (2005), 5069.

[Fag08] M. Fagotti, *Dinamica di non-equilibrio dell'entanglement e delle correlazioni in una catena di spin*, Master's thesis, Università di Pisa, 2008.

[FGG$^+$01] E. Farhi, J. Goldstone, S. Gutmann, J. Lapan, A. Lundgren, and D. Preda, *A quantum adiabatic evolution algorithm applied to random instances of an np-complete problem*, Science **292** (2001), 472.

[FPST06] G. Ferrari, N. Poli, F. Sorrentino, and G. M. Tino, *Long-lived bloch oscillations with bosonic sr atoms and application to gravity measurement at micrometer scale*, Phys. Rev. Lett. **97** (2006), 060402.

[FS78] E. Fradkin and L. Susskind, *Order and disorder in gauge systems and magnets*, Phys. Rev. D **17** (1978), 2637.

[FW05] A. E. Feiguin and S. R. White, *Time-step targeting methods for real-time dynamics using the density matrix renormalization group*, Phys. Rev. B **72** (2005), 020404.

[FWGF89] M. P. A. Fischer, P. B. Weichman, G. Grinstein, and D. S. Fisher, *Boson localization and the superfluid-insulator transition*, Phys. Rev. B **40** (1989), 546.

[GB97] U. Grimm and M. Baake, *The mathematics of long-range aperiodic order*, Kluwer, Dordrecht, 1997.

[GBP08] C. De Grandi, R. A. Barankov, and A. Polkovnikov, *Adiabatic nonlinear probes of one-dimensional bose gases*, Phys. Rev. Lett. **101** (2008), 230402.

[GHM$^+$08] M. Gustavsson, E. Haller, M. J. Mark, J. G. Danzl, G. Rojas-Kopeinig, and H.-C. Nägerl, *Control of interaction-induced dephasing of bloch oscillations*, Phys. Rev. Lett. **100** (2008), 080404.

[GKSS05] D. Gobert, C. Kollath, U. Schollwöck, and G. Schütz, *Real-time dynamics in spin-1/2 chains with adaptive time-dependent density matrix renormalization group*, Phys. Rev. E **71** (2005), 036102.

[GLTZ06] S. Goldstein, J. L. Lebowitz, R. Tumulka, and N. Zanghi, *Canonical typicality*, Phys. Rev. Lett. **96** (2006), 050403.

[GME$^+$02] M. Greiner, O. Mandel, T. Esslinger, T. W. Hänsch, and I. Bloch, *Quantum phase transition from a superfluid to a mott insulator in a gas of ultracold atoms*, Nature **415** (2002), 39.

[GMG09] V. N. Golovach, A. Minguzzi, and L. I. Glazman, *Dynamic response of one-dimensional bosons in a trap*, Phys. Rev. A **80** (2009), 043611.

[GMM04] J. Gemmer, M. Michel, and G. Mahler, *Quantum thermodynamics*, Lecture Notes in Physics, vol. **657**, Springer, 2004.

[GRS88] J. F. Gouyet, M. Rosso, and B. Sapoval, *Fractal structure of diffusion and invasion fronts in three-dimensional lattices through the gradient percolation approach*, Phys. Rev. B **37** (1988), 1832.

[Her76] J. A. Hertz, *Quantum critical phenomena*, Phys. Rev. B **14** (1976), 1165.

[HLF$^+$07] S. Hofferberth, I. Lesanovsky, B. Fischer, T. Schumm, and J. Schmiedmayer, *Non-equilibrium coherence dynamics in one-dimensional bose gases*, Nature **449** (2007), 324.

[HMH04a] M. Hartmann, G. Mahler, and O. Hess, *Existence of temperature on the nanoscale*, Phys. Rev. Lett. **93** (2004), 080402.

[HMH04b] ———, *Local versus global thermal states: Correlations and the existence of local temperatures*, Phys. Rev. E **70** (2004), 066148.

[HMMR+09] F. Heidrich-Meisner, S. R. Manmana, M. Rigol, A. Muramatsu, A. E. Feiguin, and E. Dagotto, *Quantum distillation: Dynamical generation of low-entropy states of strongly correlated fermions in an optical lattice*, Phys. Rev. A **80** (2009), 041603.

[HvL81] H. J. Hilhorst and J. M. J. van Leeuwen, *Nonuniversal and anomalous decay of boundary spin correlations in inhomogeneous ising systems*, Phys. Rev. Lett. **47** (1981), 1188.

[IC09] A. Iucci and M. A. Cazalilla, *Quantum quench dynamics of the luttinger model*, Phys. Rev. A **80** (2009), 063619.

[IKR98a] F. Iglói, D. Karevski, and H. Rieger, *Comparative study of the critical behavior in one-dimensional random and aperiodic environments*, Eur. Phys. J. B **5** (1998), 613.

[IKR98b] ———, *Random and aperiodic quantum spin chains: A comparative study*, Eur. Phys. J. B **1** (1998), 513.

[IPT93] F. Iglói, I. Peschel, and L. Turban, *Inhomogeneous systems with unusual critical behaviour*, Adv. Phys. **43** (1993), 683.

[IR00] F. Iglói and H. Rieger, *Long-range correlations in the nonequilibrium quantum relaxation of a spin chain*, Phys. Rev. Lett. **85** (2000), 3233.

[JBC+98] D. Jaksch, C. Bruder, J. I. Cirac, C. W. Gardiner, and P. Zoller, *Cold bosonic atoms in optical lattices*, Phys. Rev. Lett. **81** (1998), 3108.

[JW28] P. Jordand and E. Z. Wigner, Z. Phys. **47** (1928), 631.

[JZ05] D. Jaksch and P. Zoller, *The cold atom hubbard toolbox*, Ann. of Phys. **315** (2005), 52.

[Kar02] D. Karevski, *Scaling behaviour of the relaxation in quantum chains*, Eur. Phys. J. B **27** (2002), 147.

[Kar06] ———, *Ising quantum chains*, arXiv:cond-mat/0611327 (2006).

[KCT+02] M. Kenzelmann, R. Coldea, D. A. Tennant, D. Visser, M. Hofmann, P. Smeibidl, and Z. Tylczynski, *Order-to-disorder transition in the* XY*-like quantum magnet* Cs_2CoCl_4 *induced by noncommuting applied fields*, Phys. Rev. B **65** (2002), 144432.

[Kib76] T. W. B. Kibble, *Topology of cosmic domains and strings*, J. Phys. A **9** (1976), 1387.

[Kib80] ———, *Some implications of a cosmological phase transition*, Phys. Rep. **67** (1980), 183.

[KLR$^+$01] D. Karevski, Y-C. Lin, H. Rieger, N. Kawashima, and F. Iglói, *Random quantum magnets with broad disorder distribution*, Eur. Phys. J. B **20** (2001), 267.

[KLT97] D. Karevski, P. Lajkó, and L. Turban, *Corner exponents in the two-dimensional potts model*, J. Stat. Phys. **86** (1997), 1153.

[Kog79] J. B. Kogut, *An introduction to lattice gauge theory and spin systems*, Rev. Mod. Phys. **51** (1979), 659.

[Kol03] A. R. Kolovsky, *New bloch period for interacting cold atoms in 1d optical lattices*, Phys. Rev. Lett. **90** (2003), 213002.

[KP09] D. Karevski and T. Platini, *Quantum nonequilibrium steady states induced by repeated interactions*, Phys. Rev. Lett. **102** (2009), 207207.

[KPT95] D. Karevski, G. Palagyi, and L. Turban, *Local critical behaviour at aperiodic surface extended perturbation in the ising quantum chain*, J. Phys. A: Math. Gen. **28** (1995), 45.

[KT73] J. M. Kosterlitz and D. J. Thouless, *Ordering, metastability and phase transitions in two-dimensional systems*, J. Phys. C **6** (1973), 1181.

[KV97] T. W. B. Kibble and G. E. Volovik, *On phase ordering behind the propagating front of a second-order transition*, JETP Lett. **65** (1997), 102.

[KWW06] T. Kinoshita, T. Wenger, and D. S. Weiss, *A quantum newton's cradle*, Nature **440** (2006), 900.

[LL03] Lev D. Landau and Evgenij M. Lifstis, *Meccanica quantistica - teoria non relativistica. fisica teorica 3*, Editori Riuniti, 2003.

[LPSW09] N. Linden, S. Popescu, A. J. Short, and A. Winter, *Quantum mechanical evolution towards thermal equilibrium*, Phys. Rev. E **79** (2009), 061103.

[LRV04] J. I. Latorre, E. Rico, and G. Vidal, *Ground state entanglement in quantum spin chains*, Quant. Inf. Comp. **4** (2004), 48.

[LSA$^+$07] M. Lewenstein, A. Sanpera, V. Ahufinger, B. Damski, A. Sen, and U. Sen, *Ultracold atomic gases in optical lattices: mimicking condensed matter physics and beyond*, Adv. Phys. **56** (2007), 243.

[LSM61] E. Lieb, T. Schultz, and D. Mattis, *Two soluble models of an antiferromagnetic chain*, Ann. of Phys. **16** (1961), 407.

[LXW03] H. G. Luo, T. Xiang, and X. Q. Wang, *Comment on "time-dependent density-matrix renormalization group: A systematic method for the study of quantum many-body out-of-equilibrium systems"*, Phys. Rev. Lett. **91** (2003), 049701.

[Mes62] A. Messiah, *Quantum mechanics*, vol. 2, North-Holland, Amsterdam, 1962.

[MMP06] R. MacKenzie, E. Marcotte, and H. Paquette, *Perturbative approach to the adiabatic approximation*, Phys. Rev. A **73** (2006), 042104.

[OL04] R. Orus and J. I. Latorre, *Universality of entanglement and quantum-computation complexity*, Phys. Rev. A **69** (2004), 052308.

[Ovc07] A. A. Ovchinnikov, *Fisher-hartwig conjecture and the correlators in xy spin chain*, Phys. Lett. A **366** (2007), 357.

[PA09] D. Patanè and L. Amico, *Adiabatic dynamics of a quantum critical system coupled to an environment: Scaling and kinetic equation approaches*, Phys. Rev. B **80** (2009), 024302.

[PDH11] A. V. Ponomarev, S. Denisov, and P. Häggi, *Thermal equilibration between two quantum systems*, Phys. Rev. Lett. **106** (2011), 010405.

[Pes85] I. Peschel, *Some more results for the ising square lattice with a corner*, Phys. Lett. A **110** (1985), 313.

[Pes03] ———, *Calculation of reduced density matrices from correlation functions*, J. Phys. A: Math. Gen. **36** (2003), L205.

[Pes04] ———, *On the reduced density matrix for a chain of free electrons*, J. Stat. Mech. (2004), P06004.

[PG08] A. Polkovnikov and V. Gritsev, *Breakdown of the adiabatic limit in low-dimensional gapless systems*, Nature Physics **4** (2008), 477.

[PHWK99] I. Peschel, K. Halberg, X. Wang, and M. Kaulke, *Density matrix renormalization: a new numerical method*, Lecture Notes in Physics, vol. **528**, Springer, 1999.

[PK05] T. Platini and D. Karevski, *Scaling and front dynamics in ising quantum chains*, Eur. Phys. J. B **48** (2005), 225.

[PK07] ———, *Relaxation in the xx quantum chain*, J. Phys. A: Math. Theor. **40** (2007), 1711.

[PKT07] T. Platini, D. Karevski, and L. Turban, *Gradient critical phenomena in the ising quantum chain*, J. Phys. A **40** (2007), 1467.

[Pla08] T. Platini, *Chaînes de spins quantiques hors de l'équilibre*, Ph.D. thesis, Université Henri Poincaré, 2008.

[Pol05] A. Polkovnikov, *Universal adiabatic dynamics in the vicinity of a quantum critical point*, Phys. Rev. B **72** (2005), 161201(R).

[PSA+08] D. Patanè, A. Silva, L. Amico, R. Fazio, and G. E. Santoro, *Adiabatic dynamics in open quantum critical many-body systems*, Phys. Rev. Lett. **101** (2008), 175701.

[PSSV11] A. Polkovnikov, K. Sengupta, A. Silva, and M. Vengalattore, *Colloquium: Nonequilibrium dynamics of closed interacting quantum systems*, Rev. Mod. Phys. **83** (2011), 863.

[PSW06] S. Popescu, A. J. Short, and A. Winter, *Entanglement and the foundations of statistical mechanics*, Nature Physics **2** (2006), 754.

[PTI91] I. Peschel, L. Turban, and F. Iglói, *Critical behaviour in parabolic geometries*, J. Phys. A: Math. Gen. **24** (1991), L1229.

[PWT+11] N. Poli, F.-Y. Wang, M. G. Tarallo, A. Alberti, M. Prevedelli, and G. M. Tino, *Precision measurement of gravity with cold atoms in an optical lattice and comparison with a classical gravimeter*, Phys. Rev. Lett. **106** (2011), 038501.

[RDF+08] G. Roati, C. D'Errico, L. Fallani, M. Fattori, C. Fort, M. Zaccanti, G. Modugno, M. Modugno, and M. Inguscio, *Anderson localization of a non-interacting bose–einstein condensate*, Nature **453** (2008), 895.

[RDO08] M. Rigol, V. Dunjko, and M. Olshanii, *Thermalization and its mechanism for generic isolated quantum systems*, Nature **452** (2008), 854.

[RDYO07] M. Rigol, V. Dunjko, V. Yurovsky, and M. Olshanii, *Relaxation in a completely integrable many-body quantum system: An ab initio study of the dynamics of the highly excited states of 1d lattice hard-core bosons*, Phys. Rev. Lett. **98** (2007), 050405.

[Rei08] P. Reimann, *Foundation of statistical mechanics under experimentally realistic conditions*, Phys. Rev. Lett. **101** (2008), 190403.

[RGS85] M. Rosso, J. F. Gouyet, and B. Sapoval, *Determination of percolation probability from the use of a concentration gradient*, Phys. Rev. B **32** (1985), 6053.

[RGS86] ———, *Gradient percolation in three dimensions and relation to diffusion fronts*, Phys. Rev. Lett. **57** (1986), 3195.

[Rig09] M. Rigol, *Breakdown of thermalization in finite one-dimensional systems*, Phys. Rev. Lett. **103** (2009), 100403.

[Sac00] S. Sachdev, *Quantum phase transitions*, Cambridge University Press, 2000.

[Sch05] U. Schollwöck, *The density-matrix renormalization group*, Rev. Mod. Phys. **77** (2005), 259.

[SHL+06] L. E. Sadler, J. M. Higbie, S. R. Leslie, M. Vengalattore, and D. M. Stamper-Kurn, *Spontaneous symmetry breaking in a quenched ferromagnetic spinor bose condensate*, Nature **443** (2006), 312.

[SMS+04] T. Stoferle, H. Moritz, C. Schori, M. Kohl, and T. Esslinger, *Transition from a strongly interacting 1d superfluid to a mott insulator*, Phys. Rev. Lett. **92** (2004), 130403.

[SPP07] I. B. Spielman, W. D. Phillips, and J. V. Porto, *Mott-insulator transition in a two-dimensional atomic bose gas*, Phys. Rev. Lett. ***98*** (2007), 080404.

[SPR11] L. F. Santos, A. Polkovnikov, and M. Rigol, *Entropy of isolated quantum systems after a quench*, Phys. Rev. Lett. **107** (2011), 040601.

[SRG85] B. Sapoval, M. Rosso, and J. F. Gouyet, *The fractal nature of a diffusion front and the relation to percolation*, J. Phys. Lett. **46** (1985), L149.

[SSM08] D. Sen, K. Sengupta, and S. Mondal, *Defect production in nonlinear quench across a quantum critical point*, Phys. Rev. Lett. **101** (2008), 016806.

[ST99] G. M. Schütz and S. Trimper, *Relaxation and aging in quantum spin systems*, Europhys. Lett. **47** (1999), 164.

[SW06] U. Schollwöck and S. R. White, *Methods for time dependence in* DMRG, vol. Effective models for low-dimensional strongly correlated systems, G. G. Batrouni and D. Poilblanc (eds.), Melville, New York, 2006.

[Tas98] H. Tasaki, *From quantum dynamics to the canonical distribution: General picture and a rigorous example*, Phys. Rev. Lett. **80** (1998), 1373.

[Vid03] G. Vidal, *Efficient classical simulation of slightly entangled quantum computations*, Phys. Rev. Lett. **91** (2003), 147902.

[Vid04] ———, *Efficient simulation of one-dimensional quantum many-body systems*, Phys. Rev. Lett. **93** (2004), 040502.

[VLRK03] G. Vidal, J. I. Latorre, E. Rico, and A. Kitaev, *Entanglement in quantum critical phenomena*, Phys. Rev. Lett. **90** (2003), 227902.

[VZ10] L. C. Venuti and P. Zanardi, *Unitary equilibrations: Probability distribution of the loschmidt echo*, Phys. Rev. A **81** (2010), 022113.

[WBM$^+$96] S. R. Wilkinson, C. F. Bharucha, K. W. Madison, Q. Niu, and M. G. Raizen, *Observation of atomic wannier-stark ladders in an accelerating optical potential*, Phys. Rev. Lett. **76** (1996), 4512.

[WF04] S. R. White and A. E. Feiguin, *Real-time evolution using the density matrix renormalization group*, Phys. Rev. Lett. **93** (2004), 076401.

[Whi92] S. R. White, *Density matrix formulation for quantum renormalization groups*, Phys. Rev. Lett. **69** (1992), 2863.

[Whi93] ———, *Density-matrix algorithms for quantum renormalization groups*, Phys. Rev. B **48** (1993), 10345.

[Whi96] ———, *Spin gaps in a frustrated heisenberg model for* $\mathrm{CaV_4O_g}$, Phys. Rev. Lett. **77** (1996), 3633.

[Yuk09] V. I. Yukalov, *Cold bosons in optical lattice*, Laser Physics **19** (2009), no. 1, 1–110.

[ZD08] W. H. Zurek and U. Dorner, *Phase transition in space: how far does a symmetry bend before it breaks?*, Phil. Trans. R. Soc. A **366** (2008), 2953.

[ZDZ05] W. H. Zurek, U. Dorner, and P. Zoller, *Dynamics of a quantum phase transition*, Phys. Rev. Lett. **95** (2005), 105701.

[Zen32] C. Zener, *Non-adiabatic crossing of energy levels*, Proc. Roy. Soc. A **137** (1932), 696.

[ZS86] R. M. Ziff and B. Sapoval, *The efficient determination of the percolation threshold by a frontier-generating walk in a gradient*, J. Phys. A: Math. Gen. **19** (1986), L1169.

[Zur85] W. H. Zurek, *Cosmological experiments in superfluid helium?*, Nature **317** (1985), 505.

[Zur09] ———, *Causality in condensates: Gray solitons as relics of bec formation*, Phys. Rev. Lett. **102** (2009), 105702.

Résumé

Dans cette thèse, nous avons répondu à certaines questions ouverts dans le domaine de la dynamique hors équilibre des systèmes quantiques unidimensionnels fermés. Durant ces dernières années, les avancées dans les techniques expérimentales ont revitalisé la recherche théorique en physique de la matière condensée et dans l'optique quantique. Nous avons traité trois sujets différents et en utilisant des techniques à la fois numériques et analytiques. Dans le cadre des techniques numériques, nous avons utilisé des méthodes de diagonalisation exacte, l'algorithme du groupe de renormalisation de la matrice densité en fonction du temps (t-DMRG) et l'algorithme de Lanczos. Au début, nous avons étudié la dynamique quantique adiabatique d'un système quantique près d'un point critique. Nous avons démontré que la présence d'un potentiel de confinement modifie fortement les propriétés d'échelle de la dynamique des observables en proximité du point critique quantique. La densité d'excitations moyenne et l'excès d'énergie, après le croisement du point critique, suivent une loi algébrique en fonction de la vitesse de la trempe avec un exposant qui dépend des propriétés spatio-temporelles du potentiel. Ensuite, nous avons étudié le comportement de bosons ultra-froids dans un réseau optique incliné. En commençant par l'hamiltonien de Bose-Hubbard, dans la limite de Hard-Core bosons, nous avons développé une théorie hydrodynamique qui reproduit exactement l'évolution temporelle d'une partie des observables du système. En particulier, nous avons observé qu'une partie de bosons reste piégée, et oscille avec une fréquence qui dépend de la pente du potentiel, au contraire, une autre partie est expulsée hors de la rampe. Nous avons également analysé la dynamique du modèle de Bose-Hubbard en utilisant l'algorithme t-DMRG et l'algorithme de Lanczos. De cette façon, nous avons mis en évidence le rôle de la non-intégrabilité du modèle dans son comportement dynamique. Enfin, nous avons abordé le problème de la thermalisation dans un système quantique étendu. À partir de considérations générales, nous avons introduit la notion de profil de température hors équilibre dans une chaîne des bosons à cœr dure. Nous avons analysé la dynamique du profil de temperature et, notamment, ses propriétés d'échelle.

MOTS CLÉS: Mécanique quantique, phénomènes critiques quantiques, transitions de phase quantiques, théorie d'échelle, dynamique adiabatique, mécanisme de Kibble-Zurek, densité de défauts, modèle XY quantique, modèle de Bose-Hubbard, intrication quantique, entropie, bosons ultra-froids, oscillations de Bloch , auto-piégeage, thermalisation quantique, profil de température quantique.